DAMAGED RESPONSE IN NATURAL FIBRE REINFORCED COMPOSITES:

Characterisation and Modelling under Quasi-static and Fatigue conditions

by

Ziauddin Mahboob
B.Eng. in Aerospace Engineering, Ryerson University, 2007
M.A.Sc. in Aerospace Engineering, Ryerson University, 2009

A dissertation
presented to Ryerson University
in partial fulfilment of the requirements
for the degree of

Doctor of Philosophy
in the program of
Mechanical and Industrial Engineering

Toronto, Ontario, Canada, 2018

AUTHOR'S DECLARATION FOR THE ELECTRONIC SUBMISSION OF A DISSERTATION

I hereby declare that I am the sole author of this dissertation. This is a true copy of the dissertation, including any required final revisions, as accepted by my examiners.

I authorise Ryerson University to lend this dissertation to other institutions or individuals for the purpose of scholarly research.

I further authorise Ryerson University to reproduce this dissertation by photocopying or by other means, in total or in part, at the request of other institutions or individuals for the purpose of scholarly research.

I understand that my dissertation may be made electronically available to the public.

DAMAGED RESPONSE IN NATURAL FIBRE REINFORCED COMPOSITES:
CHARACTERISATION AND MODELLING UNDER QUASI-STATIC AND FATIGUE CONDITIONS

Ziauddin Mahboob
Doctor of Philosophy, Mechanical and Industrial Engineering, Ryerson University, 2018

Abstract

'Natural' fibrous material are subjects of accelerated research on account of the non-renewability and environmental costs of traditional 'synthetic' engineering fibres like Carbon and Glass. Of all candidates, *Flax* plant fibres have been found to offer composite reinforcement similar, or even superior, to Glass fibres in specific mechanical properties. Despite repeated evidence of its potential from independent studies, industry adoption of natural fibre reinforcement for load-bearing applications is still negligible, owing to their relatively immature body of research that discourages confidence in their long-term strength, durability, and predictability. This work contributes original findings on the complex damaged-condition response of natural fibre composites (NFC), and proposes modelling approaches to simulate the same. Material properties and mechanical behaviour of several Flax-epoxy composites are determined under tensile and compressive static loading, and correlated to internal damage mechanisms observed by micrography. Stiffness degradation and accumulated permanent strain are quantified along principal in-plane orthrotropic directions, which are used to develop a Continuum Damage Mechanics-based mesoscale model wherein constitutive laws are specifically formulated to reproduce NFC quasi-static response, including their highly nonlinear fibre-direction stiffness loss and inelasticity progression. Current progress of fatigue research is critically and extensively reviewed. Reported fatigue endurance and progressive damage behaviour of several NFC laminates are analysed. Existing knowledge on NFC fatigue damage is found to be insufficient and ambiguous, therefore inadequate for engineering design consideration. The unique fatigue-stiffening phenomenon reported for Flax-epoxy specimens is argued to be a misleading consequence of increasing strain-rate under *constant stress-amplitude* cycling. To minimise the influence of a varying strain-rate, original *constant strain-amplitude* fatigue tests are conducted on Flax-epoxy laminates, where no evidence of stiffening is observed. Considering this sensitivity to strain-rate, strain-amplitude controlled fatigue tests may be better suited for NFC investigation. Strain-controlled fatigue lives of Flax-epoxy can be modelled by a linearised strain/log-life relationship. Evolution of several material properties and dissipation phenomena (inelastic strain, peak stress, stiffness, hysteresis energy, superficial temperature) are measured, and correlated with SEM-observed damage mechanisms in the microstructure. An evolution/growth model is proposed to simulate laminate-scale stiffness degradation and cumulative inelastic strain as a function of applied peak strain and fatigue cycles, and is found to well-capture experimental trends for Flax-epoxy. The combined contribution of this work provides much-needed original data on the damaged-condition mechanical behaviour of Flax-epoxy and other NFCs under a variety of loading conditions, clarifies contradictory aspects of critical NFC behaviour, and proposes numerical methods to replicate observed progressive damage and failure in NFCs.

Acknowledgements

I am deeply indebted to my advisor, Dr. Habiba Bougherara, for her trust, continual support, and unfailing optimism over the last few years. I am grateful to Dr. Zouheir Fawaz for his encouragement, advice, and easy-going wisdom. Through them both, my research was supported in part by Natural Sciences and Engineering Research Council of Canada – Discovery Grants program (NSERC-DG).

I have been fortunate to collaborate with Dr. Yves Chemisky of the *Laboratoire d'étude des microstructures et de mécanique des matériaux* (Arts et Métiers ParisTech – ENSAM, Metz, France) on computational modelling aspects of this research, and I am grateful for his passionate participation and friendship. I thank Mr. Saeed Manteghi, MASc, Mr. Constantin Nicolinco, MASc, Ms. Zainab Al Hajjaj, MSc, Mr. Ahmed Sarwar, MASc, and Dr. Hamid Ghaemi, all of Ryerson University (Toronto, ON, Canada), for their kind assistance with computational and/or mechanical testing tasks. My gratitudes to Mr. Roland Pelland and Mr. Kourosh Abdi of Bombardier Aerospace (Toronto, ON, Canada) for technical assistance and advice on composite manufacturing and strain-measurement techniques. I gratefully acknowledge Hunstman Corporation (The Woodlands, TX, USA) and LECO Instruments ULC (Mississauga, ON, Canada) for supplies of matériel and equipment essential to this work.

My thanks to the many examiners and reviewers of my work over the years, including: Dr. Ziad Saghir, Dr. Siyuan He, Dr. Ahmad Ghasempoor, Dr. Krishnan Venkatakrishnan, Dr. Ayşe Bener, Dr. Radovan Zdero (Mechanical and Materials Engineering, Western University), Dr. Fodil Meraghni (Arts et Métiers ParisTech, France); Dr. Julia Spaniol (Psychology, Ryerson University) for chairing my dissertation defense; Dr. Seyed Hashemi (Aerospace Engineering, Ryerson University) and Dr. Hossam Kishawy (Automotive, Mechanical and Manufacturing Engineering, UOIT) for serving as external members of the examining committee, and the extraordinarily patient Ms. Adriana Gaertner.

A special note of thanks to my friend and colleague Dr. Ihab El Sawi, for his instruction on experimental and theoretical topics, and for his humorous outlook on academia. To my family and friends – you remain a source of variety, colour, and richness in my otherwise rigorously predictable life. My regrets for inconveniencing you all many a time during the course of my academic pursuits.

Dedication

To my beloved parents.
And to my younger brothers, who bring much meaning and purpose to my life.

Table of Contents

List of Tables

List of Figures

Chapter 1

Introduction

Fibre reinforced polymer composites are known to provide favourable specific strength (i.e., strength-to-weight or strength-to-density ratios) over metals, and have replaced metals in aerospace, automotive, biomedical, construction, and marine engineering applications. Given the continual pursuit of 'lightweighting' in engineering design, fibre-composites will remain a popular class of engineering material. It follows that their end-of-life disposal and the sustainability of their constituent materials is of significant concern to the engineering designer. Synthetic fibres such as Aramid, Carbon, and Glass are still dominant in the current market for fibre-composites [1; 2], however, an awareness of their non-renewability, hazardous disposability, energy-intensive manufacturing, and eventual scarcity of source material has accelerated interest in bio-based composites [1; 3–6]. Renewable alternatives for composite reinforcement can be found from natural sources: (i) plants (jute, hemp, kenaf, flax, sisal, ramie, bamboo etc) [7–11], (ii) animals (wool, hair, silk, etc) [12; 13], or (iii) minerals (asbestos) [6; 12]. Of these, asbestos silicates are now well known to be carcinogenic after prolonged inhalation, and protein-based animal fibres (where collagen or keratin is the major structural component) offer less mechanical stiffness at relatively higher production costs than cellulose-based plant fibres [6]. Therefore, in the context of composite reinforcement, current natural fibre research appears intensively directed towards the abundant and relatively inexpensive plant fibres (alternatively, *vegetal* fibres), evidenced by the recent high volume of academic publications on the subject. The original research described in the following chapters augments existing understanding of natural fibre composite behaviour in the presence of accumulating damage by quantifying the progression of damage indicators, and proposing means to model the same. Note that, from now on, the term 'natural fibre' will refer exclusively to fibres derived from plants, particularly the 'bast layer' of the plant stem (to be elaborated later).

1.1 Motivation

The common advantages typically attributed to natural fibres, when compared to synthetic fibres, are:

1. Good specific mechanical properties (due to their lower density; see Figure 1.1) [3; 4; 7; 14]
2. Good thermal and acoustic insulation [7]
3. Greater energy absorption under high strain rates (impact loading) [15]
4. Renewable / sustainable resource [5; 7]
5. Low cost [10]
6. Easier handling [7], non-abrasive tooling [16]
7. Low toxicity to human health during processing [16; 17]
8. Lower energy consumption in production [17]
9. Recyclable [5], or can be safely incinerated without toxic residue [16]
10. Can store CO_2 during growth, reducing atmospheric concentration [17–19]
11. Lower environmental impact [4; 9; 18; 20]; CO_2-neutral [16]

Disadvantages of natural fibres identified in published studies are:

1. Lower absolute tensile strengths (i.e., when not normalised by density), compared to conventional Carbon or Glass fibres [10; 21; 22]
2. Natural fibres exhibit complex anisotropic, ductile response in tension [23; 24], compared to brittle-failing Carbon or Glass fibres that can be reasonably modelled as isotropic, linear elastic
3. Lower fatigue strengths (without factoring density) [25]
4. Scatter in mechanical properties data due to non-uniform geometry (variable fibre diameters within the same fibre strand and between fibre bundles) [14; 26]
5. Scatter in mechanical properties data due to defects [27–30]
6. Poor 'wettability' by non-polar matrix material [31]
7. Flammable; lower resistance to ignition [7; 16]
8. Limited range of operating temperatures [7]
9. Susceptible to rotting (bacterial and fungal action) if not effectively protected [7; 16]
10. Prone to water uptake [32–34]
11. For the purpose of engineering application, quality control of post-harvest fibre processing has to be stringent to produce fibres with consistent and reliable mechanical properties

Despite research increasingly indicating that natural fibre composites (NFC) have (i) mechanical properties comparable to Glass-composites [3; 25; 35–39], and (ii) long-term economic-environmental benefits [4; 18], large-scale industry adoption has been slow. While NFCs have found use in non-structural components (packaging, piping, door panels, trunk liners), it is rare to find them being considered for load-bearing applications beyond limited use in sporting equipment [1; 6], and in civil engineering construction repair solutions (e.g. in hybridised cement-based structures [40–45]). To blame is a lack of confidence in the structural performance of NFCs on account of their many challenges (as listed in the previous section), and the relative deficiency of data on mechanical behaviour – particularly under compressive, off-axis, creep, and fatigue loading conditions [2]. The relative novelty of NFCs has meant that research is far behind

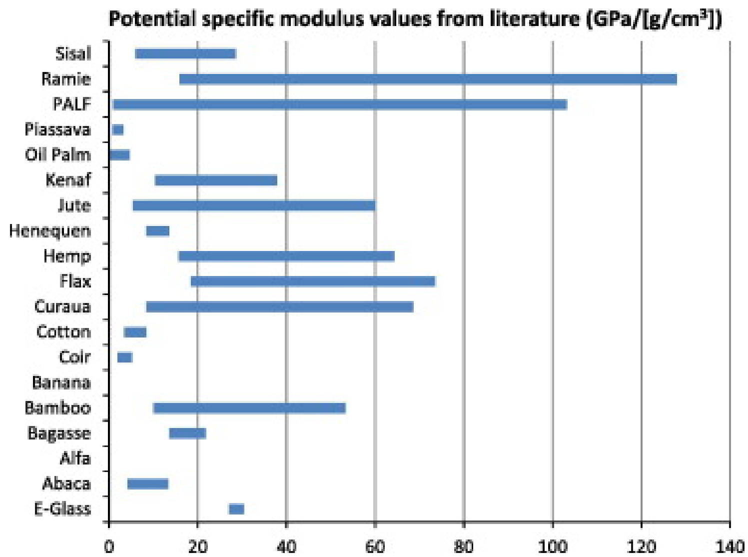

Figure 1.1: Range of specific moduli for several natural fibres, compared to E-Glass. Reproduced with permission from [7].

the maturity enjoyed by composites of Carbon or Glass fibre. There also remains a noticeable absence of validated predictive tools to model the complex loading response of NFCs, which, if demonstrated or made available, would readily allow for the design of reliable natural fibre reinforced engineering components.

Amongst all natural fibres, those harvested from the stem of Flax plant (*Linum usitatissimum*) have been found to have the best, most cost-effective, mechanical properties [7; 46]. Flax fibres have been shown to be comparable, or even exceed, Glass fibres in aspects of strength, cost, and energy requirement, as summarised in Table 1.1. Currently, Flax is commercially grown for its fibre in Russia, Ireland, Belgium,

Table 1.1: Comparing Flax and Glass fibre

		Flax fibre	Glass fibre
1	density [7] (g/cm^3)	1.4-1.5	2.5-2.6
2	specific strength [7] ($MPa/g\text{-}cm^{-3}$)	245-1333	800-1351
3	specific modulus [7] ($GPa/g\text{-}cm^{-3}$)	20-67	28-30
4	elongation at failure [7] (%)	1.2-3.3	1.8-4.8
5	cost-savings[a]:		
	• by weight [7] (USD/kg)	0.50-1.50	1.60-3.25
	• per length of fibre-bundle required to resist 100 kN [7] (USD/m)	0.05-0.65	0.1-0.4
6	production energy-consumption [17] (MJ/kg)	11.4-38.6	49-122.6

[a] 2012 estimates

the Netherlands, USA, and Canada [47]. Canada has been the largest producer and exporter of Flax in the world since 1994 [46].

1.2 Research objectives

Considering that (i) Flax-based NFCs demonstrate promising potential as substitutes for Glass-composites in high-performance applications [48; 49], but that (ii) much data on mechanical properties remain unavailable, and (iii) many aspects of their damage-sustaining behaviour appear ambiguous or inconclusively understood (as will be demonstrated in subsequent chapters), the research compiled in this dissertation expands the body of knowledge on NFC *mechanical behaviour* by *characterising* and *modelling* their response in the presence of damage, with particular focus on a *Flax fibre reinforced epoxy* composite.

The objectives of the proposed research are to:

I. manufacture representative Flax-epoxy composites and measure orthotropic material properties,

II. quantify the nonlinear elasto-plastic loading response of Flax-composites (in terms of damage accumulation) under static and fatigue conditions,

III. correlate the damaged-condition response with observed microscopic physical damage, and

IV. develop numerical models to simulate observed progressive damage evolution and failure.

As will be seen in later chapters, addressing the above objectives has resulted in original mechanical data and validated techniques to predict material behaviour, which are expected to better enable design of Flax-composite components as replacements for Glass-composites in load-bearing applications.

1.2.1 Research approach

The above objectives are pursued as individual sub-projects (organised herein as separate chapters) that address shortcomings in the mechanical characterisation of Flax-composites and in the state-of-the-art for engineering design using NFCs. The sub-objectives and expected contributions are described in brief, as follows:

1. **Manufacturing composite plates:** Flax fibre reinforced epoxy plates are to be manufactured using an 'in-house'-developed compression moulding setup. Manufacturing parameters (e.g. compression pressure) are optimised by trial-and-error until fabricated plates have a ∼50% fibre volume fraction, with minimal void content. Mechanical tests on manufactured specimens will confirm whether material properties agree with published data from other independent sources, in order to demonstrate that specimens are representative of typical Flax-epoxy composites – and therefore appropriate for further investigative research.

2. **Static response, mechanical:** The majority of published research on Flax-composites reports only fibre-direction properties and behaviour, under tensile conditions – which is insufficient even for preliminary prototyping of engineering structures made from Flax-reinforced material. To remedy the limited supply of reliable mechanical data under a variety of loading conditions (compression, off-axis, shear), extensive tests are conducted to determine tensile and compressive properties (modulus,

strength, failure strain, Poisson's ratios, nonlinear response) along orthotropic axes of a representative unidirectional (UD) continuous Flax fibre reinforced epoxy laminate, and for several 'standard' symmetric layup architectures (Chapter 5).

3. **Static response, progressive damage:** A necessary precondition of designing load-bearing components from Flax-reinforced material is knowledge of its many damage mechanisms, the initiation and progression characteristics of damage, and the development of failure conditions. Existing studies tend to focus on damage phenomena within the natural fibre only, but with scant information on the mechanical effects of degradation on the overall composite response. An intensive quantification is conducted of evolving stiffness and accumulating inelasticity within UD Flax-epoxy composites, under both tensile and compressive quasi-static loading, along the fibre-direction, perpendicular-to-fibre direction, and in-plane shear – all complemented by identification of damage mechanisms via microstructure observation of internal crack propagation and of fracture surfaces (Chapter 5).

4. **Static response model:** Unlike synthetic fibres, natural fibres demonstrate complex nonlinear tensile deformation in the fibre-direction – a phenomenon that also carries over to their derived composites. Existing models for Carbon or Glass fibre composites tend to simplify fibre-direction behaviour as linear elastic and brittle, which is unsatisfactory to represent NFC response. Realistic predictive models of damaged-condition NFC behaviour have only recently begun appearing in research publications, and are very few in number. In order to offer a model that not only predicts failure, but also interim progressive damage and accumulating permanent deformation, a mesoscale model based on damage mechanics and irreversible thermodynamics is developed to simulate tensile in-plane response of multi-orientation, multi-ply NFC laminates (Chapter 6).

5. **Fatigue response, stress-amplitude controlled:** Fatigue is an important failure mode in structural components, whereby periodic loading at well below ultimate strengths can still lead to failure. The few fatigue studies to date (all published over the last 5–7 years, and all tested under constant stress amplitude loading) involve various NFC fibre architectures (multi-orientation UD, woven twill fabric, random orientation short fibre) tested under different fatigue parameters (frequency, loading ratio). There is a need to compile the results of these disparate studies so that a holistic description of NFC endurance (S-N data) and progressive stiffness degradation is possible. Such a 'review and analysis' study is conducted, and the limitations of existing knowledge are identified (Chapter 7).

6. **Fatigue response, strain-amplitude controlled:** To date, NFC fatigue studies were mostly conducted under *constant frequency* and *constant stress amplitude*, during which the *strain amplitude* was found to progressively increase (due to significant accumulation of residual strain) – i.e. the strain rate experienced by the specimen was continually increasing. Based on a review of existing stress-controlled fatigue studies, it is reasoned that a varying strain rate introduces an unnecessary, potentially influential variable which affects the observed mechanical properties, and may in turn affect the resulting deductions and derived conclusions. Original fatigue tests are conducted under *constant strain amplitude* on several Flax-epoxy and comparable Glass-epoxy laminates to determine (i) strain-life fatigue endurance (ϵ-N curves), (ii) evolution trends of material properties and damage indicators, and (iii) microstructural cracking damage (Chapter 8).

7. **Fatigue response model, strain-amplitude controlled:** To the best of the author's knowledge,

no attempt appears to have been made to model the progression of stiffness degradation, or any other damage-indicating material property, in NFCs. This may partially be due to the complexity of fibre-direction behaviour observed under constant stress amplitude fatigue, where laminates with fibres along loading axis appear to *increase in modulus*, i.e. demonstrate negative stiffness damage, as cycling progresses [25; 50]. A phenomenological approach to predict progressive damage accumulation and failure will be developed based on *strain-controlled* fatigue tests, so that damage indicators (residual stiffness, permanent strain) can be predicted as a function of fatigue cycles (Chapter 9).

1.3 Dissertation organisation

Review of current knowledge on Flax fibre structure and composite behaviour is compiled in **Chapter 2**. Theoretical background on quantifying damage and damage mechanics are given in **Chapter 3**. Details of composite design and manufacturing techniques used to fabricate laminates and test specimens for this study are provided in **Chapter 4**. Experimental equipment and methods adopted in this research work are also described in the same **Chapter 4**. Relevant literature review of Flax-epoxy static behaviour, details of original testing of monotonic/quasi-static mechanical properties, and the results are elaborated in **Chapter 5**. Quantification of evolving stiffness and accumulating inelasticity within Flax-composites, and identification of damaging mechanisms are also discussed in **Chapter 5**. Critical review of existing quasi-static progressive damage models, details of original model development and validation, and predictions of proposed model are given in **Chapter 6**. **Chapter 7** details the analysis of existing *stress-amplitude controlled* fatigue data on (i) stress-life (S-N), (ii) evolution of damage indicators, and (iii) influence of fatigue test parameters on observed behaviour. **Chapter 8** describes original fatigue tests under *constant strain amplitude* cycling conducted for several Flax-epoxy and two comparable Glass-epoxy laminates, identified fatigue endurance (ϵ-N curves), and evolution of material properties in conjunction with microstructure observations of physical damage. **Chapter 9** details the development of proposed growth models that offer a phenomenological means to simulate progressive fatigue damage (strain-amplitude controlled) as a function of fatigue cycles. **Chapter 10** summarises the conclusions from all phases of this research, and discuses possible avenues of future investigation. Supplementary data is provided in the **Appendices**.

Chapter 2

Literature review

This chapter summarises the multi-scale structure and constitution of Flax and other ligno-cellulosic plant fibres, their mechanical properties, and their highly nonlinear behaviour under tensile and compressive loading. The multiple complex damage mechanisms in plant fibres and their composites are discussed. Evidence for observed and speculated damage mechanisms are presented. The reported sequence of damage in elementary fibre structure, from initial loading until failure, is summarised.

2.1 On Flax and other cellulosic fibres

2.1.1 Structure and constituents

The multi-scale breakdown of Flax plant structure is given in Figure 2.1.

Flax fibres are complex hierarchical structures of cellulosic polymers, extracted from the outer *bast layer* of the plant stem [23; 24] which can grow up to 90 cm in length and 1-3 mm in diameter [46; 54], as shown in Figure 2.1(a)-(b). The fundamental tubular unit in the bast layer is the *elementary fibre* (alternatively, *ultimate fibre* or *monofilament*) that has a polygonal cross section (dia. 10-30 μm) with a hollow central *lumen* [23] (see Figure 2.1(d)). About 10-40 elementary fibres are are held together by pectins [54] in bundles (dia. 50-200 μm) called *technical fibres* [23; 51; 54; 55] (see Figure 2.1(c)).

The cells of elementary fibres have multiple concentric layers of *cell walls* (Figure 2.1(e)) that provide necessary structural rigidity to the plant stem [56]. The primary chemical component in cell walls is the polysaccharide *cellulose*, a non-branched polymer chain of glucose molecules (Figure 2.2(a)) with chain-direction stiffness and strength reported to be 74–167 GPa [57; 58] and 1–15 GPa [56; 58], respectively. These crystalline cellulose chains are arranged in aggregate bundles called *microfibrils*, and their close arrangement is possibly maintained via hydrogen bonds between adjacent H and O atoms. The numerous hydroxyl (OH) groups in cellulose (3 from each glucose monomer) gives it a *hydrophilic* character, which is why natural fibres have poor resistance to moisture absorption [57].

The cellulose microfibrils are highly ordered in the *secondary cell wall* layers (5–15 μm thick), but not quite so in the *primary cell wall* (0.2 μm thick) [54]. Microstructure studies reveal that the microfibrils in

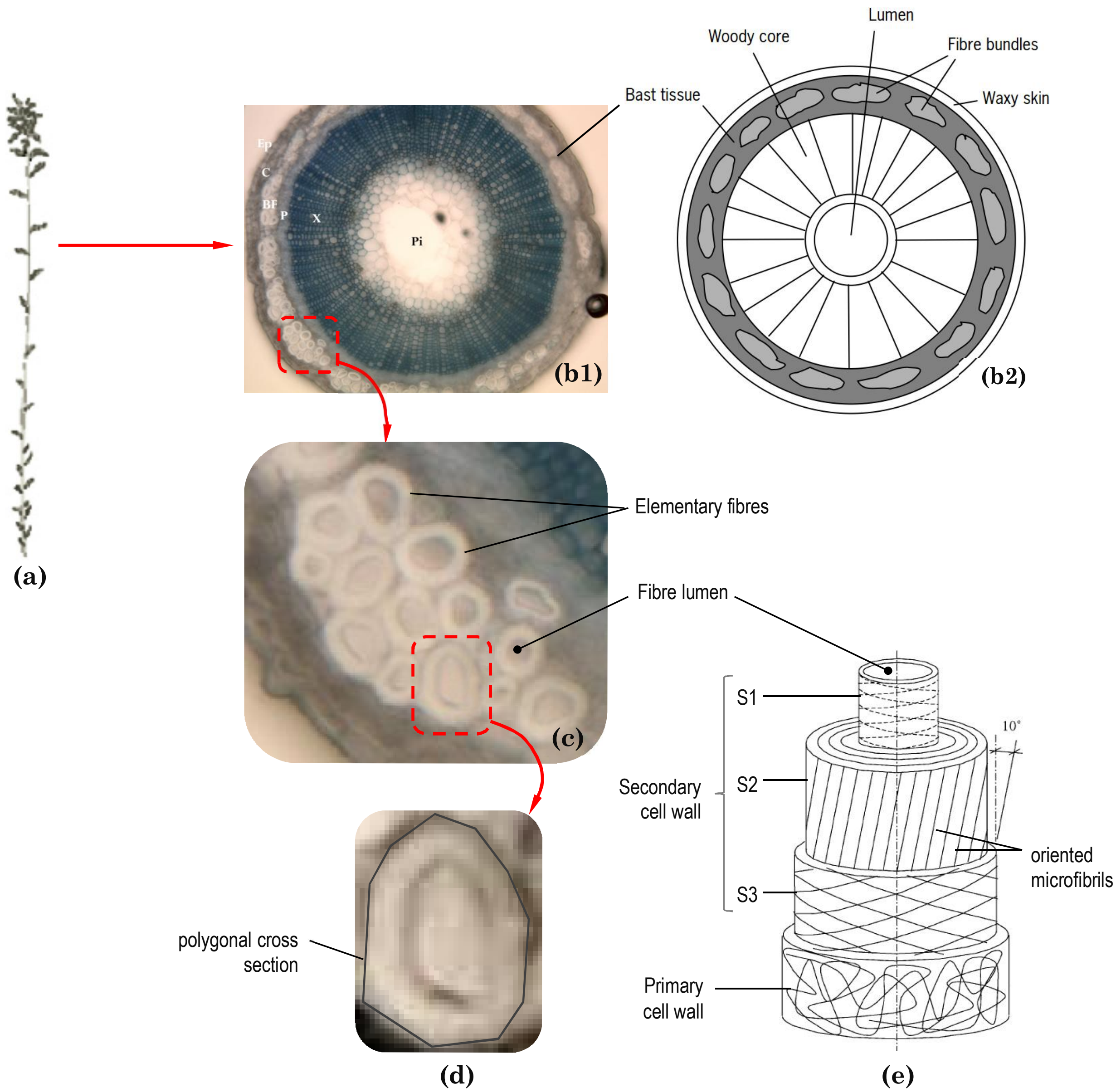

Figure 2.1: Structure of Flax plant stem: (a) Flax plant, length ~90 cm; (b) Stem cross-section, ⌀1-3 mm; (c) Fibre bundle (*technical fibre*), ⌀50-200 μm; (d)-(e) Elementary fibre cross section and schematic, ⌀10-30 μm. Reproduced with permission: (a) from [51], (b1) and (c)-(d) from public domain [52], (b2) from [53], and (e) from [23].

S2 cell wall of most natural fibres are arranged in a helical angled orientation to the fibre axis, as shown in Figure 2.2(b). This orientation is approximately 10° in flax (Figure 2.1(e)), 8° in jute, 7.5° in ramie, 6.2–11° in hemp, and 20° in sisal [61; 62].

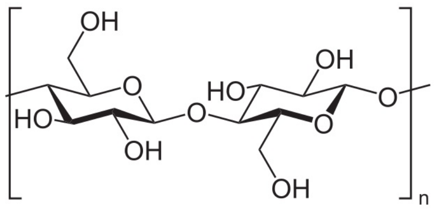

(a)

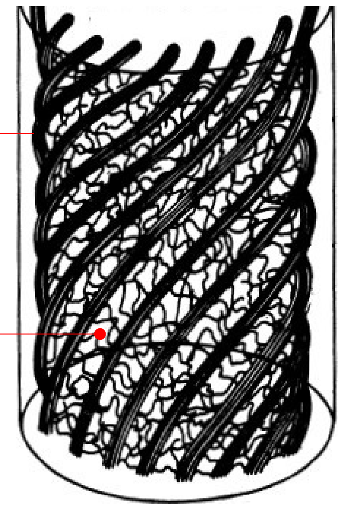

(b)

Figure 2.2: (a) Cellulose is a linear polymer of glucose units (two shown); from public domain source [59]. (b) Representation of S2 secondary cell wall in elementary fibre, showing helically-oriented cellulose microfibrils in an amorphous matrix; reproduced with permission from [60].

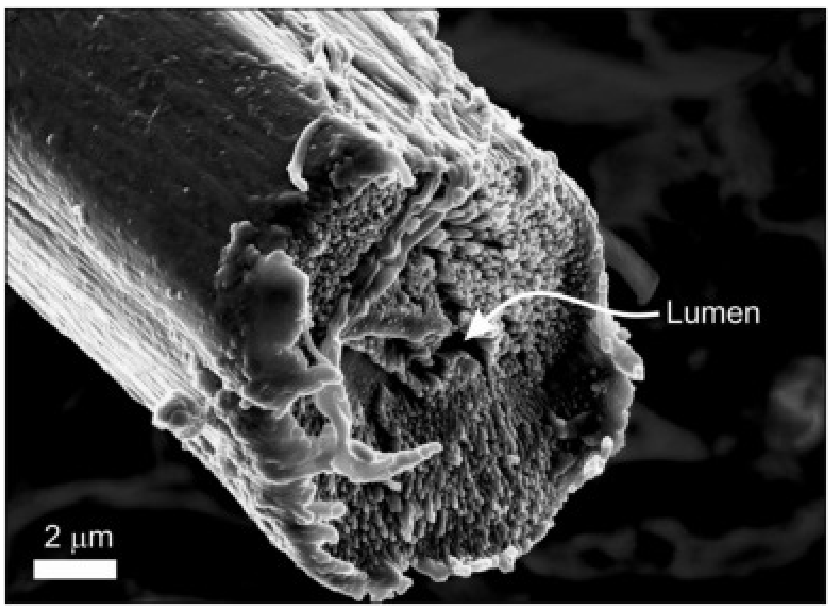

Figure 2.3: Transverse fracture surface of single Flax elementary fibre showing lumen and microfibrils. Reproduced with permission from [63].

In both primary and secondary cell walls, microfibrils (seen in Figure 2.3) are embedded in a matrix of hemicelluloses, pectins, and possibly crosslinked lignins and some amorphous cellulose [54; 57; 64; 65]. The amorphous hemicellulose is understood to mostly coat the microfibrils, while the pectin and lignin fills the spaces in between (Figure 2.4) [62].

Hemicellulose, despite its name, is not a form of cellulose. It is a class of polysaccharide made from several types of sugar units (not just glucose), with considerable chain branching, and a degree of polymerisation that is 10–100 times less than in cellulose [57]. Modulus of amorphous hemicellulose is reported to be 0.02–2 GPa [66]. *Pectin* is a collective name for heteropolysaccharides rich in galacturonic acid (an oxidised form of galactose sugar), and is soluble in water after a partial neutralisation by ammonium hydroxide or alkalis [57]. *Lignin* covers a group of complex branched hydrocarbons that contain both aromatic and aliphatic groups [57], with a reported modulus range of 2.5–3.7 GPa [58]. The remaining chemical constituents in Flax (and all natural fibres) are waxy materials and moisture [46; 54; 57]. *Waxes* consist of different alcohols of poor water solubility [57]. In all, Flax fibres consist of about 70% cellulose, 15% hemicellulose, 9% moisture, and the rest split nearly evenly between pectin, lignin, and wax (∼2% each) [46].

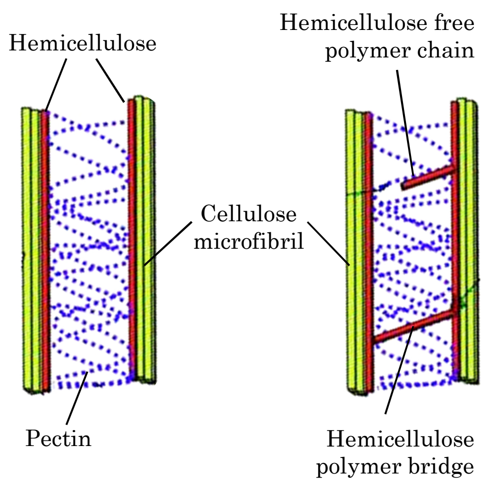

Figure 2.4: Schematic representations of structural arrangement in S2 secondary cell wall. Relative thicknesses not to scale, and space between microfibrils is exaggerated. Reproduced with permission from [62].

2.1.2 Mechanical properties and behaviour

Differences in growth conditions, genetic pool of crop, harvesting practices, processing techniques, and moisture/humidity affect the physical structure and chemistry of natural fibres, resulting in highly variable mechanical properties, when compared to synthetic fibres [56; 62; 67–70]. Davies and Bruce [67] showed that accumulating defects and increasing ambient humidity had the effect of reducing fibre modulus and strength, as shown in Figure 2.5. Pillin et al. [71] and Bourmaud et al. [62] reported on the influence of fibre variety and harvest year on fibre properties. Tables 2.1–2.3 compile reported tensile and compressive mechanical properties of Flax fibres, respectively.

2.1.2.1 Tension

Reported range of Flax fibre tensile modulus, strength and failure strain are 27–91 GPa, 300–1,834 MPa, and 0.95-3.27%, respectively, as seen in data compiled in Tables 2.1–2.2. In general, *elementary fibres*

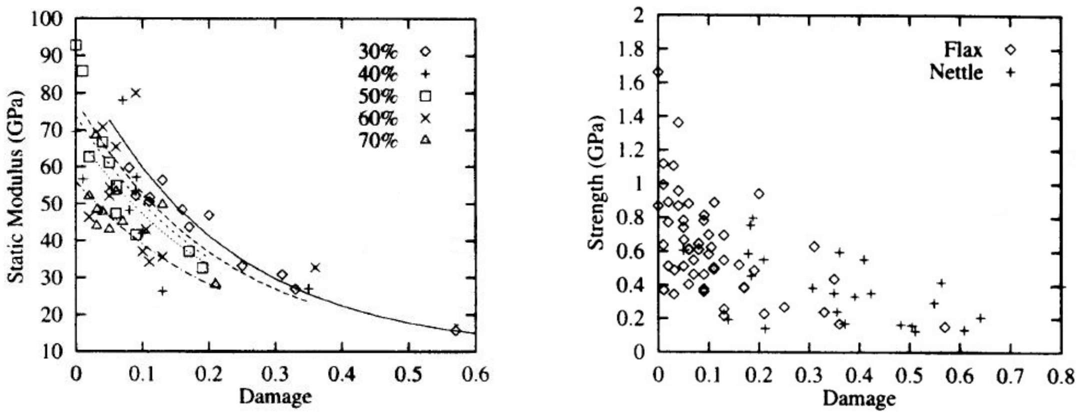

(a)

(b)

Figure 2.5: Influence of defects on tensile (a) modulus and (b) strength of elementary Flax fibre. Defect regions were distinguished by polarised microscopy, and quantified as a fraction of total fibre length. Percentage values in (a) indicate relative ambient humidity. Reproduced with permission from [67].

tested individually tend to produce higher strength data than *technical fibre bundles*[1] – the reason being that bundle strength is an average of the elementary fibres contained within. For similar reasons, tests on shorter fibre gauge lengths tend to produce higher strength and stiffness values than those on longer gauge lengths. Charlet et al. [54] showed that individual Flax fibre mechanical properties vary lengthwise, with the middle portion of the harvested fibres demonstrating the highest tensile strength, stiffness, and failure strain. In a related later study, Charlet et al. [82] showed that fibre properties varied depending on what location on Flax plant stem they were extracted from. Fibres from the middle of the stem showed the highest tensile stiffness and strength, though failure strain appeared the same for all stem locations.

Stiffness measurement for Flax fibres is sensitive to fibre diameter, as shown by Lamy et al. [26; 27], where higher stiffness values are derived for smaller diameters: 60-80 GPa for 7-20 μm diameters, compared to 40-55 GPa for 24-35 μm diameters. Charlet et al. [54] also found similar correlation of mechanical properties with fibre diameter – fibres of increasing diameter have proportionally decreasing stiffness and strength, but no conclusive influence on failure strain is seen (see Figure 2.6). However, since these diameter

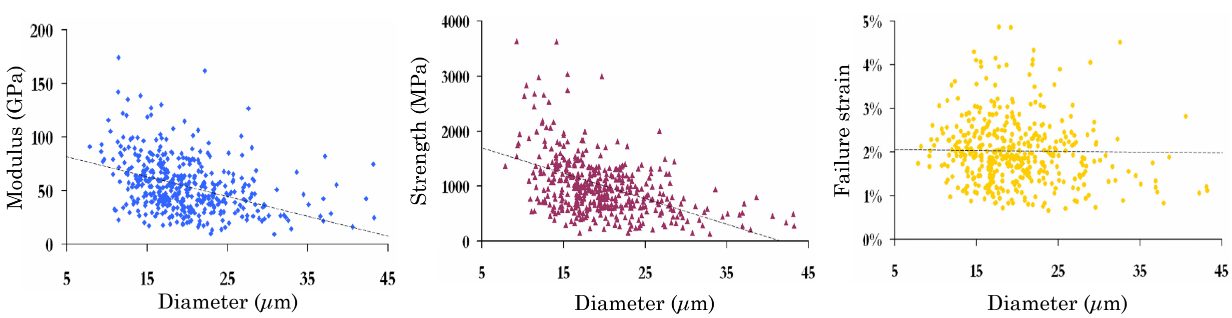

Figure 2.6: Flax fibre tensile modulus (*left*), strength (*centre*), and failure strain (*right*) as a function of fibre diameter. Reproduced from [49].

[1] Distinction between elementary and technical fibre was discussed in the previous section.

Table 2.1: Reported tensile properties of untreated elementary Flax fibre

Study	Year	Fibre configuration	Gauge length (mm)	Modulus (GPa)	Strength (MPa)	Failure strain (%)
[24]	1999	elementary	–	50	–	–
[26]	2000	elementary	–	58.64	–	–
[23]	2002	elementary	10	54.08 ±15.13	1339 ±486	3.27 ±0.84
[27]	2002	elementary	–	58.65	–	–
[72]	2003	elementary	5	89 ±35	1300 ±300	–
[73]	2004	elementary	10	54.080 ±15.128	1339 ±486	3.27 ±0.84
			1	–	1030 ±383	–
[74]	2005	elementary	10	69 ±20	–	2.375 ±1.625
			20	64 ±21	–	1.8 ±1.5
[54]	2007	elementary:	10			
		upper fibre		59.1 ±17.5	1129 ±390	1.9 ±0.4
		middle fibre		68.2 ±35.8	1454 ±835	2.3 ±06
		lower fibre		46.9 ±15.8	755 ±384	1.6 ±0.5
[48]	2010	elementary	10	from 54 ±49 (initial) to 62 ±32 (final)	1253 ±619	2.35 (typical)
[75]	2011	elementary, unmodified	–	31.4 ±16.2	974 ±419	3 ±0.65
		elementary, hackled	–	33.1 ±11.6	760 ±392	2.27 ±0.63
[62]	2013	elementary, varieties:	10			
		2003 Agatha		57.0 ±29.0	865 ±413	1.8 ±0.7
		2003 Oliver		47.2 ±21.3	751 ±414	1.7 ±0.6
		2005 Everest		41.0 ±12.5	663 ±307	1.8 ±0.5
		2006 Alaska		46.3 ±12.1	691 ±253	1.8 ±0.6
		2006 Hivernal		67.5 ±23.7	1119 ±490	1.9 ±0.5
		2008 Everest		75.0 ±21.6	1232 ±554	2.1 ±0.8
[76]	2013	elementary	25-30	48.9 ±12.0	1066 ±342	2.8 ±3.8
				48.3 ±13.8	841 ±300	2.2 ±0.8
				57.1 ±15.5	1135 ±495	2.1 ±0.6

sensitivity studies calculate fibre cross-section area based on outer diameter only without accounting for the hollow lumen, it is reasonable to consider the larger-diameter moduli and strengths to be underestimated; i.e. since larger-diameter fibres are likely to have larger lumens, their effective load-bearing cross-section area is overestimated. Thomason et al. [81] and Aslan et al. [75] also observed this significant source of error in calculating area, and consequently, the modulus.

The diameter-dependence of natural fibre modulus was investigated by Placet et al. [83] using a theoretical model based on 3D elastic theory that incorporated a multi-layered cylindrical geometry and oriented microfibrils. Their model confirmed that fibre modulus is depenedent on lumen and outer diameters, but they find that geometric factors are not sufficient to explain the large dispersion of reported modulus as a function of fibre diameter. The authors conclude that 'ultrastructural' parameters, i.e. micro- and nanostructure aspects such as degree of cellulose crystallinity and movement of fibre constituents should

Table 2.2: Reported tensile properties of untreated technical Flax fibre (bundle)

Study	Year	Fibre configuration	Gauge length (mm)	Modulus (GPa)	Strength (MPa)	Failure strain (%)
[61]	1986	*unspecified*	20	–	780	2.4
[67]	1998	technical	–	51.7 ±18.2	621 ±295	1.33 ±0.56
[77]	1998	technical	70	34 ±4	975 ±525	2.25 ±0.75
[10]	1999	*unspecified*	–	27	344	–
[21]	2002	technical, scutched & hackled	3	58.65	1522 ±400	–
		technical, hand decorticated	3	–	1834 ±900	–
[55]	2003	technical	20	–	613 ±442	–
			40	–	454 ±231	–
			80	–	264 ±127	–
[53]	2004	technical, unmodified	3.2	–	750 ±131	–
		technical, dewaxed	3.2	–	820 ±52	–
[78]	2006	technical	–	91 ±10	1000 ±100	–
[79]	2007	technical, unmodified	5	–	906.4 ±246.3	2.25 (typical)
			8	–	736.8 ±208.6	
			10	–	602.6 ±198.4	
		technical, dew retted	5	–	678.9 ±216.2	1.9 (typical)
			8	–	523.7 ±175.3	
			10	–	468.3 ±211.6	
[80]	2009	technical	75	30 ±11	300 ±100	1.1 ±0.4
[81]	2011	technical	10	38.43 ±2.17	613.00 ±75.74	0.95 ±0.02
			15	45.90 ±2.55	723.67 ±149.91	1.10 ±0.30
			20	51.43 ±1.96	812.00 ±176.23	1.25 ±0.33
			25	56.47 ±3.04	641.33 ±368.71	1.01 ±0.51
			30	57.53 ±5.12	649.67 ±285.55	1.07 ±0.40

be the main factors causing the large scatter in data [83].

Flax fibre tensile response can show variable nonlinearlity [23; 49; 51; 76; 80]. Charlet [49] observed three types of tensile response in elementary Flax fibres, with up to as many linear 'zones' in the stress-strain response curve, shown in Figure 2.7. The number of linear zones in the response appear to positively correlate with failure strain, but have no discernible influence on failure stress. Usually, the reported modulus for Flax fibre (as those listed earlier in Table 2.1) is the slope of the last linear portion of the stress-strain response.

Load-unload tests demonstrate that Flax fibres undergo *stiffening*, and *inelastic deformation* in tension [23; 49], inferred from residual strain observed in response curves like Figure 2.8(a), which may be explained by the straightening S2 microfibrils that do not return to their original 10°-oriented state once

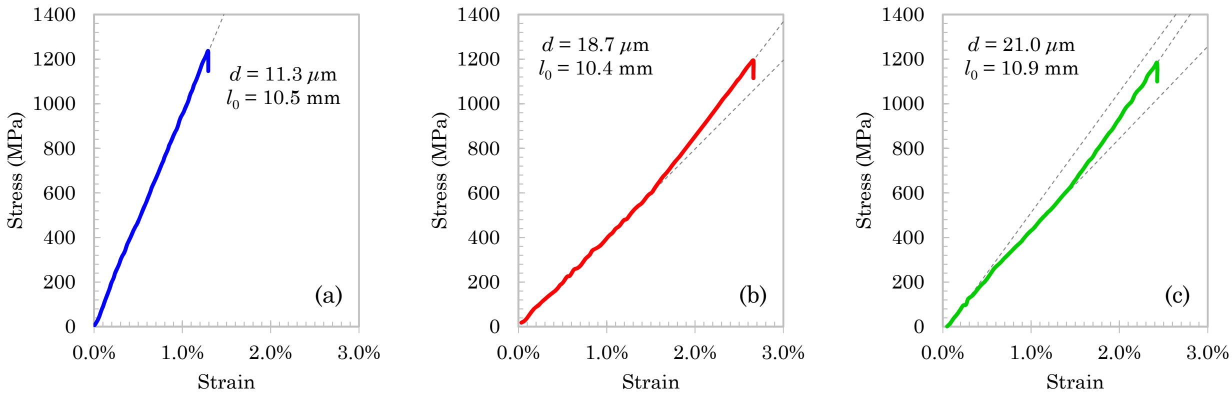

Figure 2.7: 3 types of Flax elementary fibre response observed: (a) Almost completely linear response; (b) 2 linear zones, 1 inflection point; (c) 3 linear zones, 2 inflection points. Figure diameter d and gauge length l_0 shown. Smaller diameter (∼10 μm) fibres can show linear response, but larger diameters (∼20 μm) show nonlinear response. Data from [49].

unloaded. Tensile tests by Kecker et al. [84] have confirmed that this permanent deformation in natural

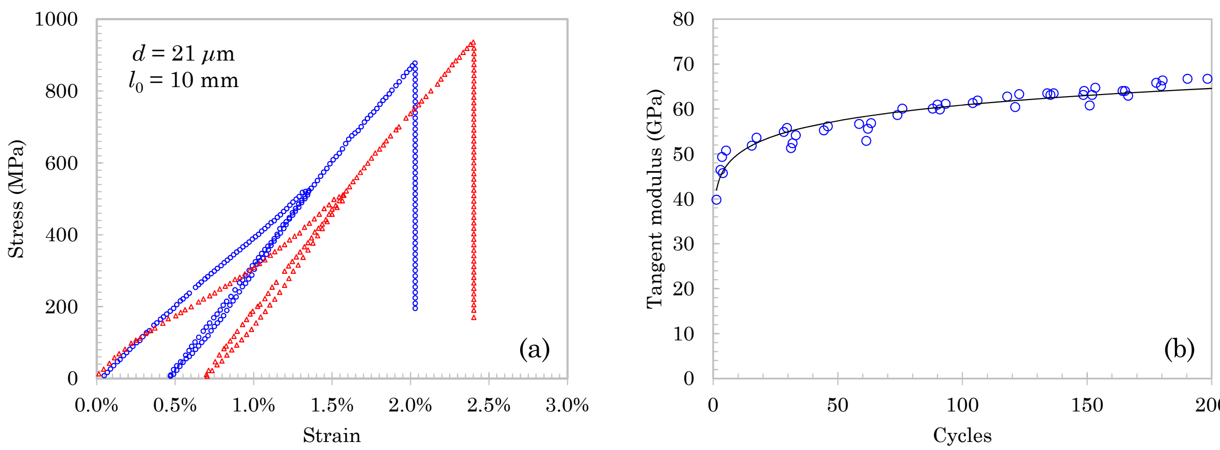

Figure 2.8: Flax elementary fibre cycled tensile response: (a) Residual strain and stiffening, loading rate 1 mm/min; data from [49]. (b) Evolution of tangent modulus under fatigue (peak load 0.2 N, load ratio R=0, frequency 0.05 Hz); data from [23].

fibres essentially occurs in the secondary cell wall, with contribution from reorienting microfibrils. Furthermore, load-controlled *fatigue tests* on single elementary fibres by Baley et al. [23] indicated an increase in stiffness as cycling progressed (see Figure 2.8(b)), suggesting that MFA was steadily approaching 0° with every cycle.

Studies on other cellulosic bast fibres like Hemp also provide insight applicable to Flax. Hemp elementary fibres have a structure and S2 layer MFA similar to Flax [61; 62], and demonstrate similar variable nonlinearity, increase in modulus, and inelastic deformation under tension, as shown by the insightful investigation of Placet et al. [65]. Under cycled progressive loading, Hemp elementary fibres show a clear hysteretic response, accumulation of residual strain, and increasing secant modulus[2] (Figure 2.9(a)). Inter-

[2] Secant modulus is the slope of hysteresis loop major axis, i.e. line from maximum to minimum stress-strain datapoint,

estingly, it was also shown that a fraction of residual strain may be recovered and stiffness increase may be somewhat reversed after every loading cycle, and the extent of this recovery depends on the time allowed for it (Figures 2.9(b)–2.9(c)). The authors conclude that although a major fraction of residual strain is permanent, a minor fraction remains time-dependently reversible [65]. This time-dependent recovery of residual strain has the effect of reducing the measured secant modulus.

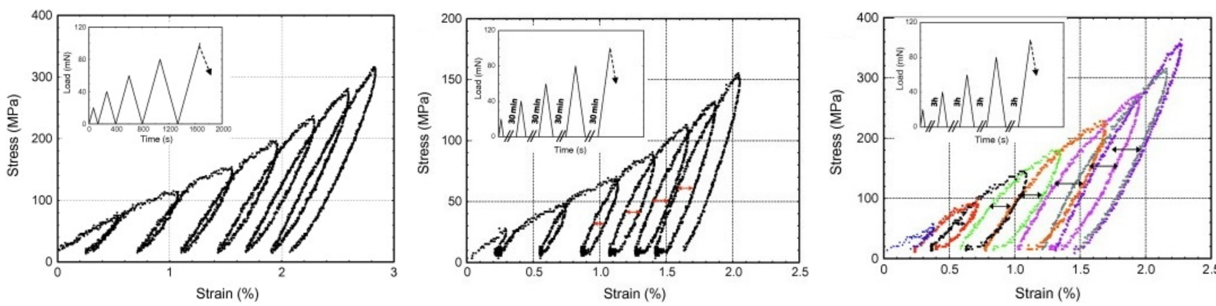

(a) (b) (c)

Figure 2.9: Hemp elementary fibre tensile response (gauge length l_0=10 mm, loading rate 0.3 mN/s) under (a) continuous cycled progressive loading; or held at constant minimum load for (b) 30 mins and (c) 3 hr between successive cycles. Reproduced with permission from [65].

2.1.2.2 Compression

Compression testing of fibres is not trivial, so data for Flax fibre is very limited – as can be seen from Table 2.3. Reported values for compression strength of Flax are either theoretical estimates [53], or data from

Table 2.3: Reported compression properties of untreated Flax fibre

Study	Year	Fibre configuration	Modulus (GPa)	Strength (MPa)	Failure strain (%)
[24]	1999	elementary	50 (assumed)	1300	–
[21]	2002	elementary	50 (assumed)	1200 ±370	–
[53]	2004	technical	–	400 (estimated)	–

special *elastica loop tests* [21; 24] originally developed by Sinclair [86] to determine tensile properties of Glass fibres and subsequently adapted for fibre compression properties in [87; 88]. Bos et al. [53] provide a rough lower-bound estimate for Flax fibre compressive strength of 400 MPa, reverse-calculated from tested Flax-epoxy composite properties. Elastica loop tests by Bos et al. [21] report that *yielding*, i.e. plastic deformation, initiates at an estimated 1200 ±370 MPa compressive stress, which is ∼70% of its tensile strength. It is notable that the difference between compressive and tensile strength in Flax is not as much as that for synthetic fibres, e.g. the compressive strength of Kevlar is only 15–20% of its tensile [89].

Bos et al. [21] also find that the presence of *kink bands* (alternatively, *nodes* [90]) in Flax fibres influence compressive properties, with higher count of this defect type correlating with lower strength. Kink bands are areas of locally buckled cell wall, as shown in Figure 2.10. Other transverse defects called *slip planes*

as defined by Hahn and Kim [85]

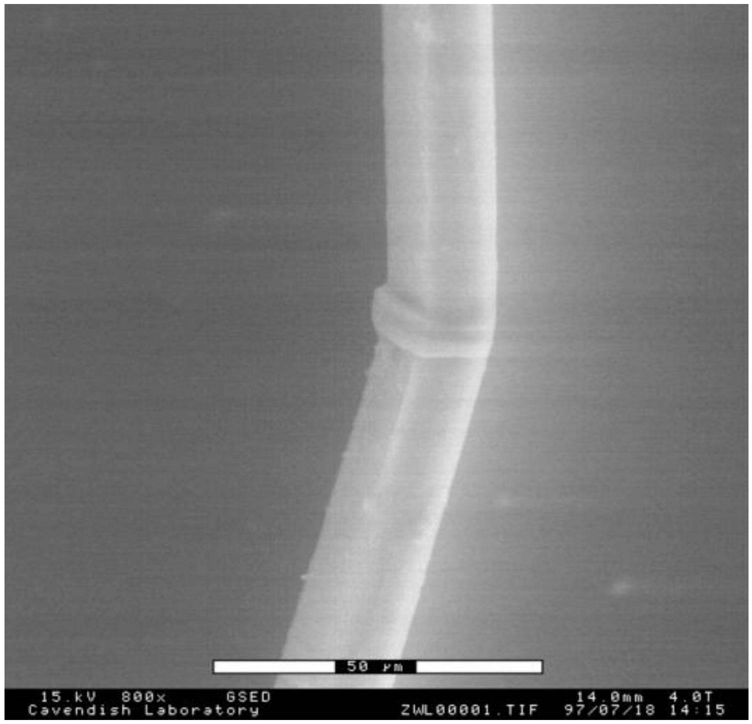

Figure 2.10: SEM micrograph at ×800 of a fully developed kink band defect in Flax elementary fibre. Scale bar shows 50 μm. Reproduced with permission from [21].

(shown later in Figure 2.17) have similar influence on compressive properties. The loop test calculations of Bos et al. [21] involve an assumed compressive modulus of 50 MPa – taken to be the same as the median tensile modulus. There appears to be no reported value for failure strain in compression.

2.2 Damage mechanisms in NFCs

Generally, failure in fibre composites is rarely a consequence of a few dominant cracks propagating across the material, as is the case in traditional engineering materials like polymers and metals [91]. Instead, several different damage modes progressively accumulate at possibly different rates, and these mechanisms may be independent of each other or influence each other [92–94]. The complex damage response is further compounded in NFCs due to the hierarchical-composite structure, intrinsic structural variations within natural fibres, and the probability of post-processing defects. In the context of damage response, the most prominent feature that sets NFCs apart from synthetic fibre composites is the complex fibre-direction behaviour.

Physical and chemical processes that degrade mechanical properties or cause permanent deformation in natural fibre laminates occur at different scales, from the laminate level (macroscale) down to the scale of polymer chains in the fibre (nanoscale). The following sections summarise all currently known, proposed, hypothesised, or evidenced mechanisms at the different scales within NFCs.

2.2.1 Laminate and ply

NFCs may be expected to show all the classically identified macroscale damage modes that characterise fibre-composite behaviour. At the scale of the lamina (ply level), fibre-direction tensile behaviour and strength is governed by fibre properties and fibre fracture (Figure 2.11(b)). Composites of synthetic fibres

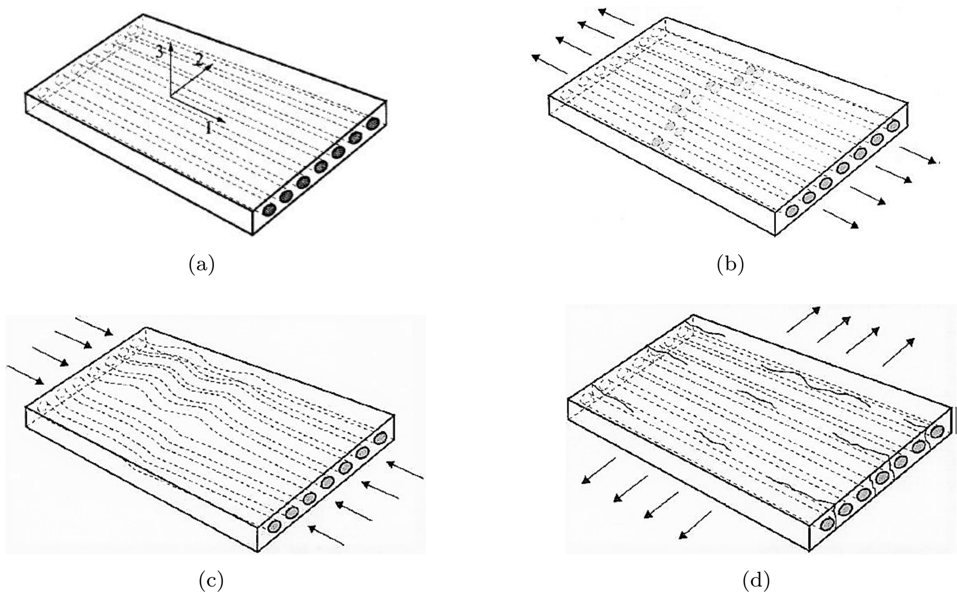

Figure 2.11: Unidirectional (UD) continuous fibre reinforced lamina: (a) principal axes; (b) loaded in tension along fibre-direction (*11*), showing internal fibre fracture; (c) loaded in compression along fibre-direction (*11*), showing fibre buckling; and (d) loaded in tension along transverse direction (*22*), showing matrix cracking and fibre-matrix debonding. Reproduced with permission from [91].

like Glass and Carbon tend to demonstrate elastic-brittle response in the fibre-direction with minimal plasticity, but NFC response generally have the same nonlinear and ductile quality of individual natural fibres [90]. Competing mechanisms like breakdown in fibre-matrix adhesion or matrix cracking can limit fibre-direction strength or stiffness. Compression along fibre-direction may also be fibre dependent, but with greater interaction with matrix behaviour. In fibre-composites, fibre buckling (Figure 2.11(c)) can be alleviated by the surrounding matrix acting as a physical support, so lamina compression strength is a function of fibre-matrix adhesion and ability of matrix to brace against fibre buckling [91]. Fibre-matrix debonding and matrix cracking also appear in a lamina under transverse tensile (Figure 2.11(d)), transverse compressive, or shear forces [91].

In a study on thermoplastic starch reinforced by Flax as UD and crossply laminate specimens, Romhány et al. [95] found that the dominant failure modes change during tensile loading, and that the failure sequence depends on fibre content fraction and ply orientation. At low load levels, fibre-matrix separation (Figure 2.12) is reported to occur simultaneously with separation of elementary fibres (elaborated in the next section on fibre bundle mechanisms). At higher loads, fibre pull-out and transverse fibre cracks become dominant. When failure is imminent, multiple fibre fractures occur that cascade into final fracture of laminate.

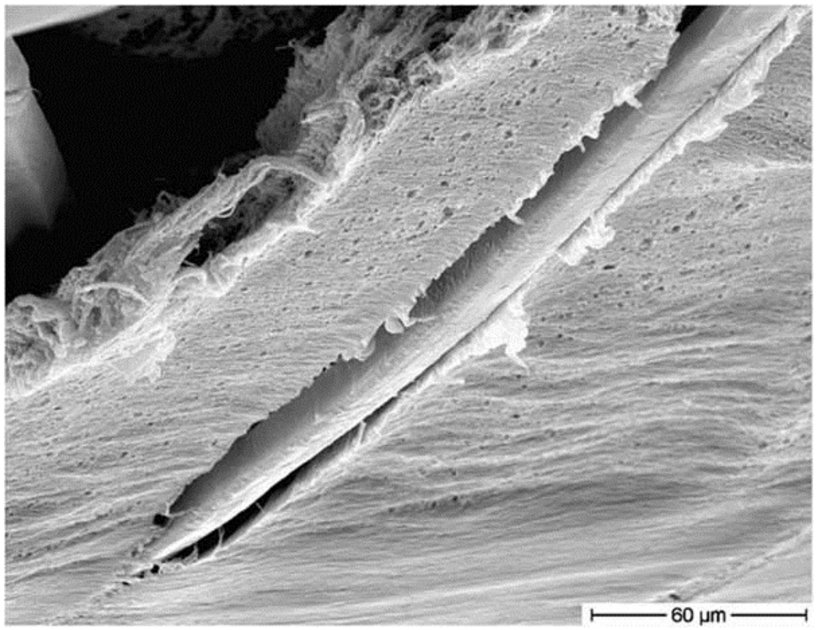

Figure 2.12: SEM image of debonding between Flax elementary fibre and thermoplastic starch matrix. Reproduced with permission from [95].

At the scale of a laminate with multiple plies of different fibre orientations, interlaminar damage phenomena like delamination may develop (i) in tension due to the differing Poisson ratios from ply to ply (Figure 2.13(a)), and (ii) in compression due to plies buckling separately (Figure 2.13(b)). All above individual mechanisms in each ply interact and influence each other in complicated sequences, which may either pause or accelerate the degradation of laminate mechanical properties before final failure [91].

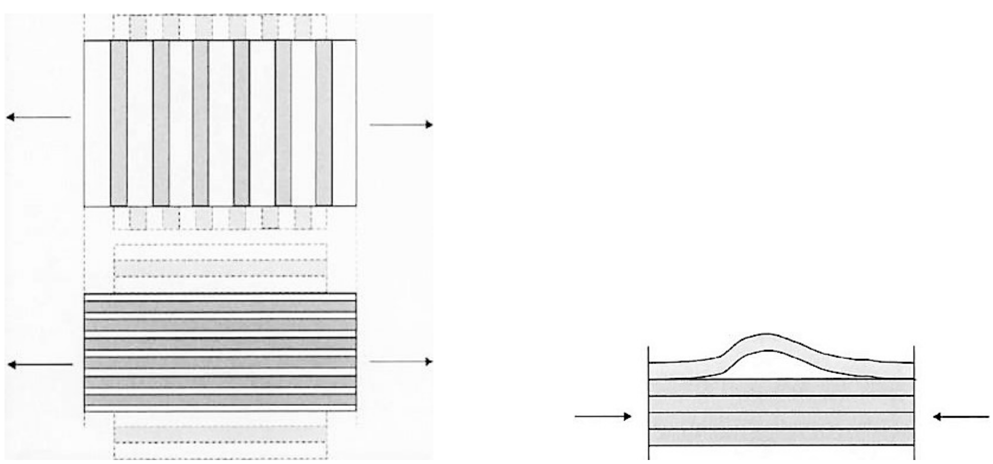

(a) (b)

Figure 2.13: Delamination (a) in tension caused by differences of Poisson effect between plies, where initial dimensions are identical but the divergent deformation results in damaging stress gradients at the ply interface; and (b) in compression due to ply buckling. Reproduced with permission from [91].

2.2.2 Fibre bundle and elementary fibre

2.2.2.1 Compression

Recall that the presence of pre-existing circumferential kink bands result in lower compression yield strength in Flax fibres [21]. The authors Bos et al. [21] noted that these pre-existing kinks are not formed during natural growth, but are damage caused during extraction and processing of the fibre. In subsequent loop tests, the same authors observed that the damaging mechanism in compression is also the development of similar new kinks, which appear to be locally buckling primary cell walls, as shown in Figure 2.14. The same kink-buckling mechanism is known to appear in other synthetic fibres with highly oriented crystalline structure, such as Carbon or Aramid fibres [24].

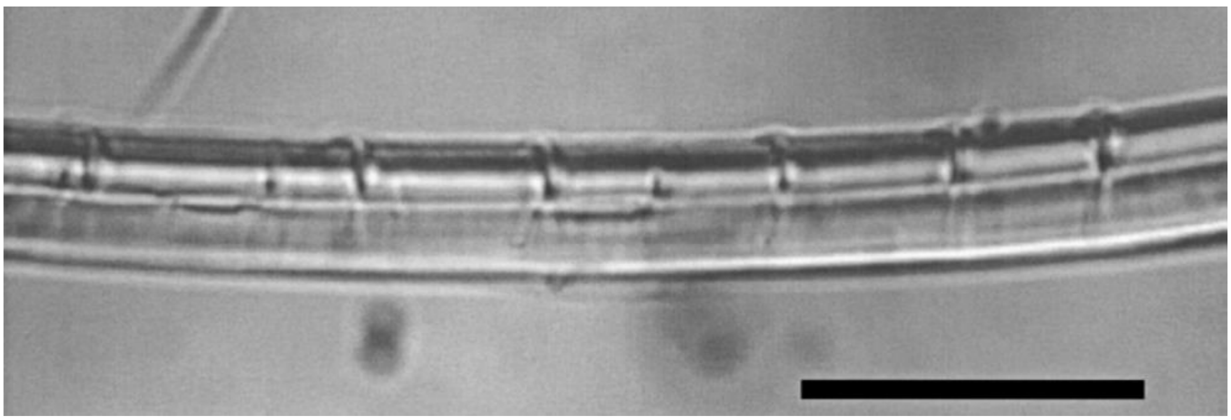

Figure 2.14: Flax elementary fibre forced into a loop, showing development of local cell wall buckling (kinks) on the compression side. Scale bar shows 50 μm. Reproduced with permission from [21].

2.2.2.2 Tension

Romhány et al. [55; 95] investigated the failure modes in Flax fibre bundles using *in situ* scanning electron microscopy (SEM) and acoustic emission (AE). Also considering other studies on Flax fracture [21; 75], the tensile failure sequence can be distinguished into three stages, shown in Figures 2.15–2.16 and summarised as follows:

I. Failure starts with *fibrillation*, or the axial separation of elementary fibres. This is due to a breakdown in pectin adhesion (Figure 2.15(b)) between fibres in a bundle. The AE signal for this event was measured at <35 dB [55]. Once separated, the elementary fibres are individually loaded and free to extend independently of each other. Recall that helically-arranged microfibrils within the S2 cell wall layer are oriented at 10° to fibre axis, which now begin to straighten towards the loading axis. Reoriented microfibrils may not return completely to their original orientation when the tensile load is released (this will be elaborated in the next section on damage mechanisms at the microfibril scale).

II. Upon continued loading, *transverse circumferential cracks* are observed across the outer cell wall (Figures 2.15(c) and 2.16(b)). These cracks registered a 35-60 dB AE signal [55]. Aslan et al. [75]

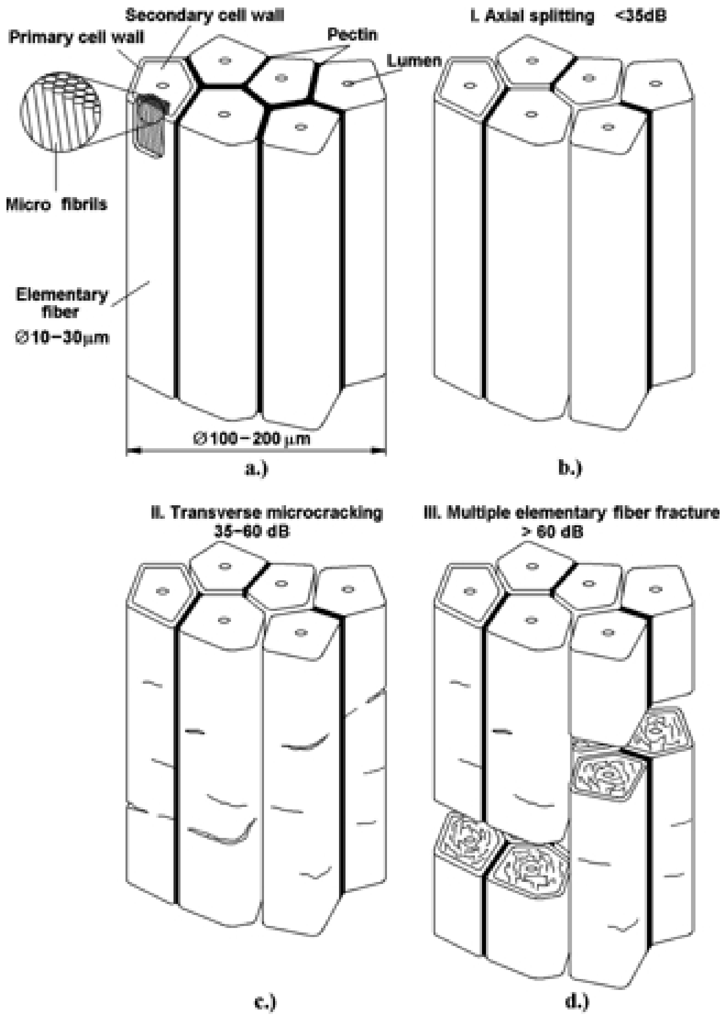

Figure 2.15: Failure sequence in a Flax fibre bundle under tension. Reproduced with permission from [95].

showed that these cell wall cracks are more likely to initiate at defect locations (see Figure 2.17). The accumulation of these transverse cracks further augment the inelastic elongation of fibre.

III. The fibrillation and transverse cracking redistribute local stresses, creating stress concentrations and subsequent tearing at other locations. These multiple transverse cracks and axial splits merge, appearing like a 'zig-zag' advance of cracks (Figure 2.15(d) and 2.16(c)-(d)). This allows cracks to further progress from the outer primary cell wall to the internal secondary cell wall, and fracture the microfibrils – which may also be in a complex zig-zag pattern (Figure 2.17). Fibre fractures were registered at >60 dB [55]. Bos and Donald [24] showed that, during tensile fracture, the primary cell wall could separate (peel away) from the secondary. The primary cell wall (amorphous pectin, hemicellulose, and crosslinked lignin) was observed to fracture in brittle manner, while the fibrillar secondary cell wall exhibited coarse crack progressions, presumably on account of their differing composition and morphology.

Hughes et al. [90] studied the development of damage events in UD Flax-polyester composite [0] lam-

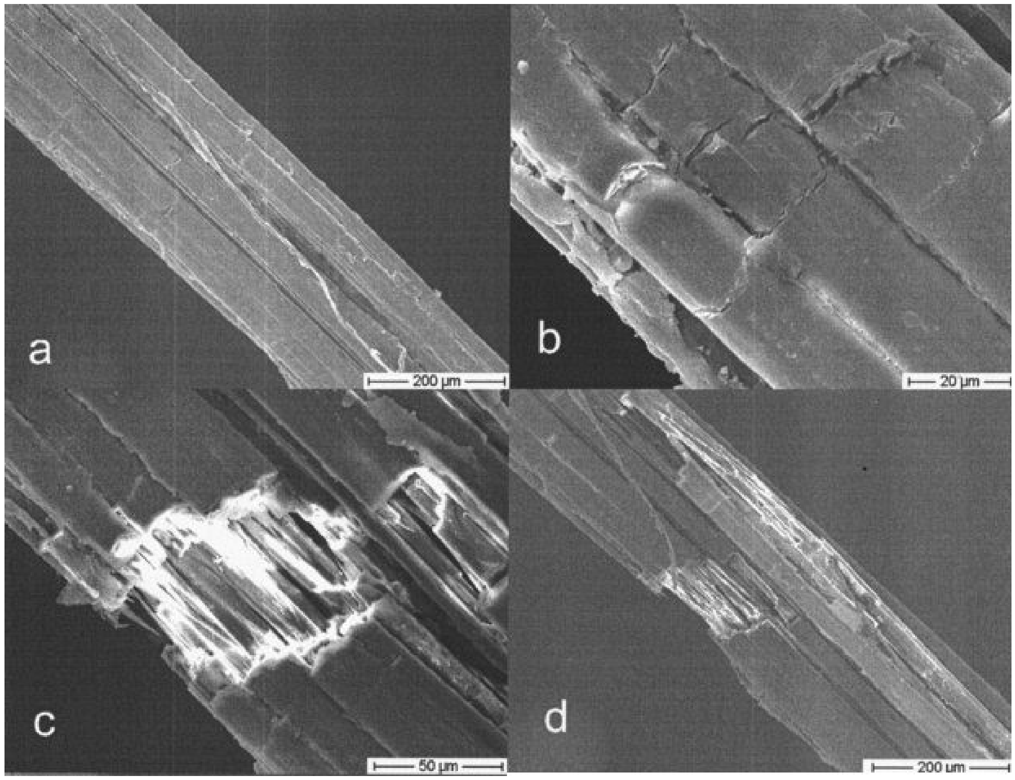

Figure 2.16: SEM images of tensile failure progression in technical Flax fibre bundle: (a) longitudinal debonding and separation of elementary fibres, (b) transverse (circumferential) cracking, (c) tearing across fibres exposing internal microfibrils, (d) fracture of microfibrils and fibre. Reproduced with permission from [55].

inates by measuring acoustic emissions (AE) during monotonic tensile tests. A nonlinear and inelastic fibre-direction deformation is observed. The authors suggest that physical changes of defect geometry in reinforcing fibres contribute towards the composite inelasticity observed. The authors consider the bulging kinked regions (as was shown in Figure 2.10) to be less stiff than the defect-free regions, and suggested that these micro-compressed regions will elongate first under tensile forces. Interfacial stress concentrations are expected to develop primarily around these kink regions, initiating fibre-matrix debond cracks when shear stresses exceed a critical value [69; 90]. Acoustic emissions (AE) were detected starting at fairly low tensile strains of $\sim$0.06% (see Figure 2.18), and the AE range with the most numerous events ($<$19.2 dB) appears to initiate at the 'yield' point (first inflection) of the stress-strain curve. The most energetic AE events ($>$43 dB) occurred during the latter half of response, between 0.9% and failure strain.

Newman et al. [96] studied loss and recovery of strain energy in a plain-woven Flax-polyester laminate under progressive cyclic tensile loading. The authors observed that, upon holding a constant tensile strain for 30 s, the required stress relaxed – and this relaxation is more pronounced at higher strain levels (see Figure 2.19(a)). Such viscoelastic behaviour in the fibre direction was attributed to viscous flow and reorganisation in amorphous hemicellulose regions of Flax fibre, thought to occur as microfibrils reorient. Several cycled quasi-static tests (5 cycles) were conducted at progressively increasing max loads, to measure the ratio of dissipated to recovered energy (i.e. ratio of hysteresis loop area to area under unloading curve)

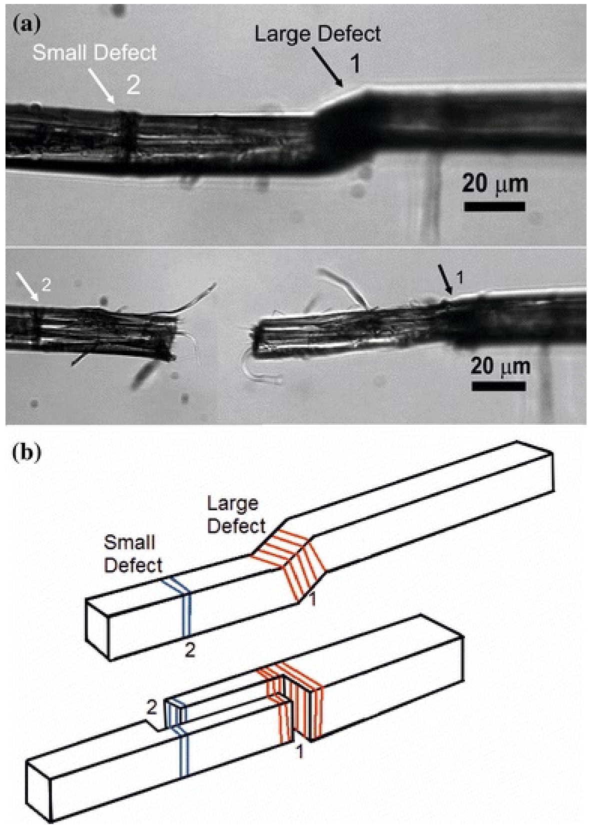

Figure 2.17: Flax elementary fibre fracture influenced by pre-existing transverse defect zones: (a) Optical micrographs before and after tensile fracture; (b) Schematic represenation of the same fibre failure. Reproduced with permission from [75].

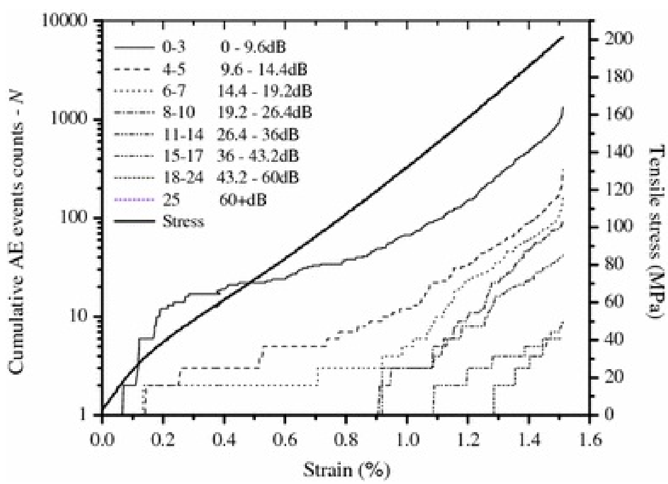

Figure 2.18: Cumulative trend of acoustic events (left vertical axis) and stress-strain response at 10 mm/min loading rate (right vertical axis) for UD Flax-polyester [0] laminate, $v_f = 0.576$. Reproduced with permission from [90].

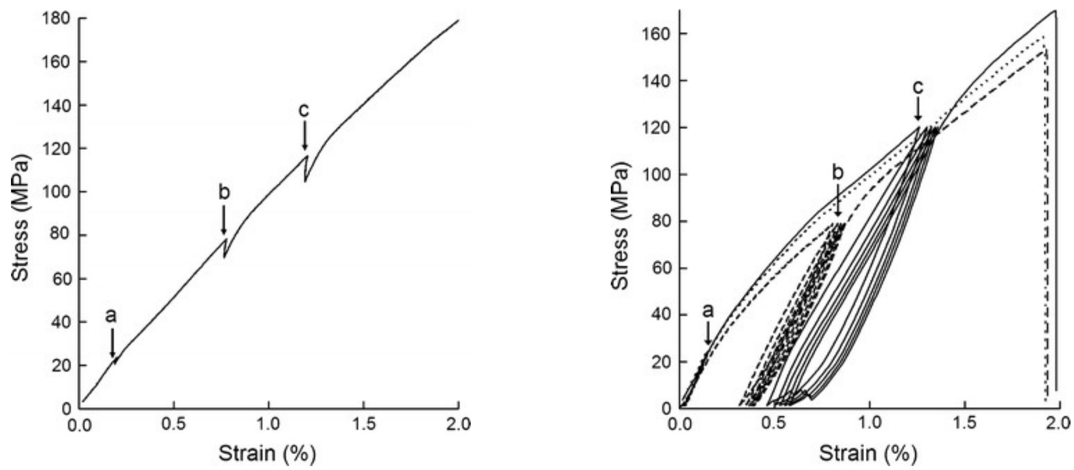

(a) (b)

Figure 2.19: Tensile response of plain-weave Flax fabric reinforced polyester specimens: (a) 1 test with load held for 30 s at 15%, 50%, and 75% of expected failure (points a, b, and c respectively); (b) 3 tests under quasi-cycled loading, each with with 5 cycles applied at 15% (dotted), 50% (dashed), and 75% (solid) of expected failure, respectively. Reproduced with permission from [96].

for each cycle. Results indicated that the highest proportion of lost strain energy always occurs at the first cycle, thereafter reducing to a near constant for remaining cycles. The high energy loss ratio during initial loading is attributed to fibre-matrix debonding, and subsequent changes in fibre microstructure (irreversible microfibril movement), resulting in permanent deformation. The authors assume that debonding initiates first at fibre defect locations (based on partial debonding observed via SEM), hypothesising that bulging kink bands become taut and slim under tensile loading, thereby causing separation from surrounding matrix. Further testing indicated that initial inelasticity-causing damage must occur *after* the 'yield' point, between 0.2%–0.8% strain, i.e. between points 'a' and 'b' in Figure 2.19(b).

The above hypothesised mechanism of micro-compressed kink regions elongating was later evidenced by Placet et al. [65] on Hemp elementary fibres. Hemp fibres were observed under a polarised light microscope as they elongated in tension. The bulky kink regions appear bright and opaque, as seen in Figure 2.20. As tensile forces increase, these regions appear to elongate, get dimmer and more translucent like the remaining non-defected regions (see Figure 2.20(a)). This indicates that kink band elongations (i) involve internal structural reorganisation, (ii) contribute to overall fibre strain, and (iii) when in a bundle or composite configuration, may very likely cause initiation of fibre separation or fibre-matrix debonding. Further testing also indicated that once tensile load is released, the strained fibre tends to recover and the kink regions slowly reappear, as can be seen in Figure 2.20(b).

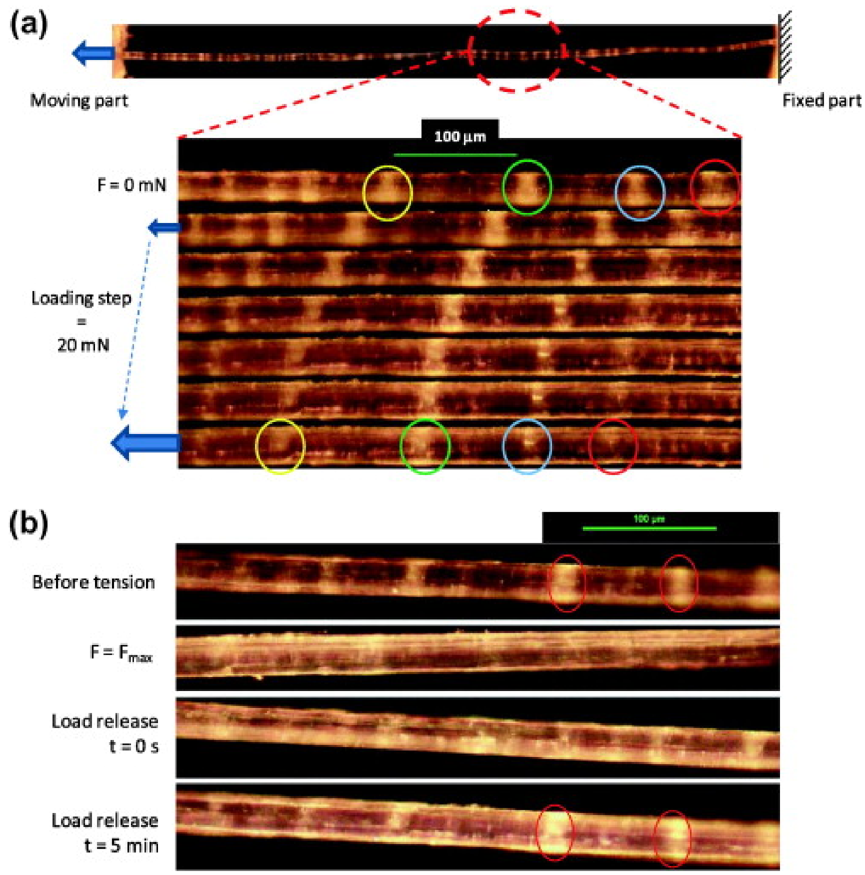

Figure 2.20: Tensile deformation of Hemp elementary fibres under polarised microscope. Kink bands appear as bright, opaque regions that become more translucent as the fibre elongates. Reproduced with permission from [65].

2.2.3 Mirofibrils and constituent polymers

2.2.3.1 Compression

Recall that under compression, elementary fibres show localised cell wall buckling. In the buckled kink regions, the primary cell wall is not observed to actually crack [24]. Bos et al. [21] propose a that under compression, the helically wound microfibrils in secondary cell wall 'come apart', much like a twisted bundle of steel cables under compression (this behaviour was also proposed for Carbon fibre deformation by Williams et al. [97]). The amorphous pectin-hemicellulose-lignin matrix within the fibre is thought to keep the microfibrils glued together even as they buckle outwards, but this adhesion eventually fails as lateral stresses increase, causing the microfibrils to separate. Still, since the primary cell wall does not break, the microfibrils remain contained within the cell walls [21; 24].

2.2.3.2 Tension

Several hypotheses have been proposed by now to explain the nonlinear response, stiffening, and permanent deformation in natural fibres under tension. At present, there is evidence that all the following mechanisms contribute to natural fibre behaviour, discussed in the following paragraphs.

Microfibril reorientation. As noted earlier, cellulose microfibrils in Flax S2 cell wall are arranged in a helical orientation of $\sim 10°$ to the fibre axis [23; 24; 61; 62]. Upon tensile loading, the microfibrils tend to re-orient and straighten towards the loading axis (i.e. to $0°$), as shown in Figure 2.21. This

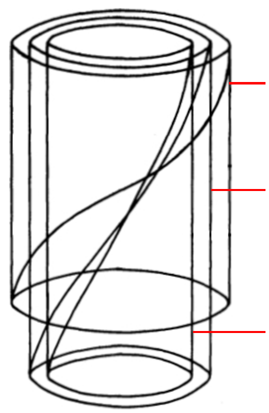

Figure 2.21: Extension of a helical structure. Reproduced with permission from [60].

varying orientation is understood to contribute to the aforementioned stiffness variation observed in Flax fibres under tensile loading. The direct relation between applied loading, extension, decreasing MFA, and increasing modulus in plant fibres is a well-evidenced phenomenon, confirmed via polarisation microscopy [98], X-ray scattering [99; 100], and X-ray diffraction [62; 84].

Tests by Kecker et al. [84] on wood fibres have shown that tensile extension is not uniform over the length of fibre, where some regions exhibit large deformations and almost zero S2 microfibrillar angle (MFA), while other regions are less deformed. A detailed study on a variety of Flax fibres by Bourmaud et al. [62] showed that smaller MFAs in S2 cell wall correlate with higher moduli, supporting the hypothesis that an increase in elementary fibre modulus is related to steepening MFA. The study also found no significant correlation between initial MFA and tensile failure strain, which is reasonable considering that by time failure is imminent, microfibrils should be close to parallel with the loading axis (i.e. MFA would be minimal), in which case the initial orientation would be irrelevant.

Stick-slip 'velcro' mechanics. Irreversible straining in cellulosic natural fibres is attributed to the *irreversible* reorientation of helically-wound microfibrils in the S2 layer. In order to reorient, the cellulosic microfibrils must first break bonds with the surrounding hemicellulose-pectin matrix. However, unlike helical springs that may recover their initial dimensions once load is released, any elastic recovery in microfibrillar angle (MFA) is thought to be arrested by new bonds formed with the matrix that prevent a slide back to original configuration. The currently preferred hypothesis for this microfibril sliding and bond recovery, based on almost real-time observations of MFA under loading, is one proposed by Keckes et al. [84], and shown in Figure 2.22.

Keckes et al. [84] observed that, during progressive load-unload tensile tests, the overall stiffness of individual wood fibres does not degrade after yield points, even as residual strains accumulate and MFA

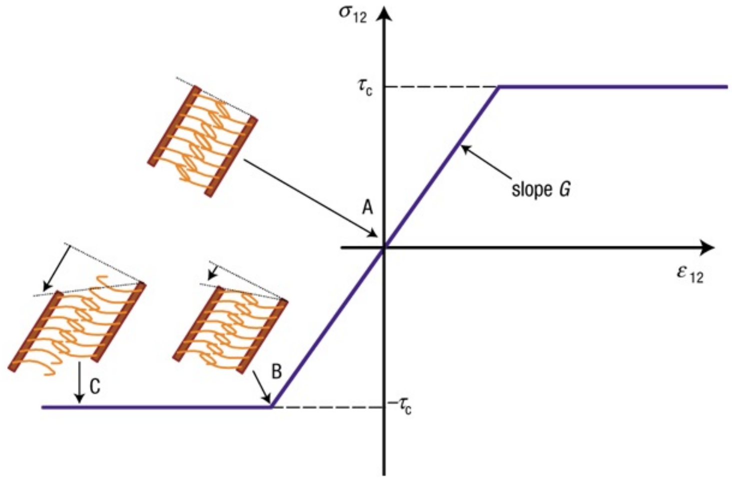

Figure 2.22: 'Velcro' mechanics: Proposed mechanism of microfibril 'stick-slip' movement and idealised evolution of shear stress-strain in amorphous matrix between microfibrils, that results in irreversible extention of overall elementary fibre. Reproduced with permission from [84].

decreases – indicating that there is a recovery mechanism that reforms microfibril-matrix bonds, thereby maintaining tensile mechanical properties. The authors imagine molecular bonding between microfibrils and surrounding amorphous matrix to be in the form of 'hooks' (point A in Figure 2.22). Shear stresses are transmitted between adjacent microfibrils through viscous flow in the amorphous hemicellulose-pectin matrix, wherein shear deformation is considered linear until a threshold τ_c is reached (point B in Figure 2.22). Beyond this critical stress, shear deformation is considered constant, the 'hook' linkages come apart and microfibrils slide relative to one another – but do not slide back upon unloading because new linkages are formed between microfibrils and matrix (point C in Figure 2.22). The critical shear stress occurs at the yield point of fibre stress-strain response [96]. Subsequent loading re-initiates this process (back to point A in Figure 2.22). The sliding movement between points B and C in Figure 2.22 corresponds to inelastic deformation similar to dislocation gliding in metals undergoing plastic deformation.

This proposed 'stick-slip' movement can explain natural fibres' permanent elongation without degrading stiffness, or without initiating cracking in amorphous matrix regions. The authors call this *'velcro' mechanics* [84; 101], on account of the hypothesised hook linkages behaving much like Velcro attachments in the nanoscale.

Strain-induced crystallisation. As discussed above, the amorphous matrix is forced to deform by the reorienting helical microfibrils. Astley and Donald [102] conducted *in situ* small- and wide-angle X-ray scattering tests of technical Flax fibres under tensile forces. The authors interpreted their evolving peak intensity data during fibre deformation to mean that some non-crystalline, disordered cellulose chains are present within the fibre that become crystallised along fibre axis (i.e. deforms or reorganises into an ordered arrangement) due to the enforced tensile strains. This process increases the amount of crystalline cellulose in the fibre, thereby contributing to overall longitudinal stiffening.

Proposed sequence of intra-fibre events. Placet et al. [65] proposed a detailed sequence of damage events based on known fibre mechanisms and original observations on Hemp elementary fibre deformation. Considering that Flax fibre structure and tensile response is very similar to that of Hemp, the same sequence can reasonably be expected for Flax fibre. From the 2-inflection-point Flax fibre response shown in Figure 2.23, the tangent modulus is seen to decrease after the *first inflection point* (0.25-0.5% strain), then increase after the *second inflection point* (∼1.4% strain), then remains constant until failure.

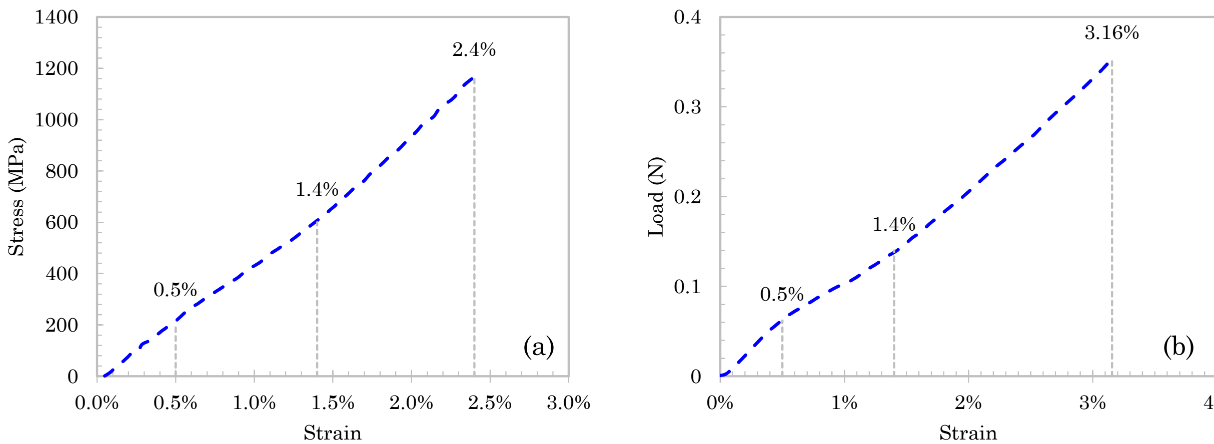

Figure 2.23: Flax elementary fibre monotonic response (gauge length 10 mm, test speed 1 mm/min) from two sources: (a) [49], and (b) [23]. Response shows two inflection points at similar strain loading.

The sequence of shear-induced crystallisation, stick-slip sliding, and eventual permanent microfibril reorientation is shown schematically in Figure A.2, and summarily tabulated in Table A.1.

2.3 Fatigue studies on NFCs

Most available fatigue studies to date on Flax-composites are based on constant stress amplitude, tension-tension uniaxial tests. These studies are discussed in the following paragraphs.

2.3.1 Flax-epoxy composites

Liang et al. [25] compared the fatiguing behaviour of Flax-epoxy (FE) and Glass-epoxy (GE) laminates of similar volume fractions, considering two symmetric layup architectures for each: crossply $[0/90]_{3S}$ and angled-crossply $[\pm 45]_{3S}$. All tests were conducted at 5 Hz and loading ratio $R = 0.1$. Strain was not measured directly from a dedicated transducer, instead it was estimated from the ratio of crosshead displacement to gauge length. The study found that all laminates demonstrated a continually increasing total strain response under a constant stress amplitude (as expected), generally following a three-stage sigmoidal trend (all except FE [0/90]). FE [0/90] experiences a larger strain increase than GE (see Figure 2.24(a)), but interestingly in the case of [±45], GE showed a much more pronounced strain increase for a similar loading amplitude (see Figure 2.24(b)). The authors did not quantify the inelastic portion of strain, however after inspecting Figure 2.24(b) it can be concluded that for an *angled* crossply [±45] layup, GE tends to accumulate more permanent strain than equivalent FE.

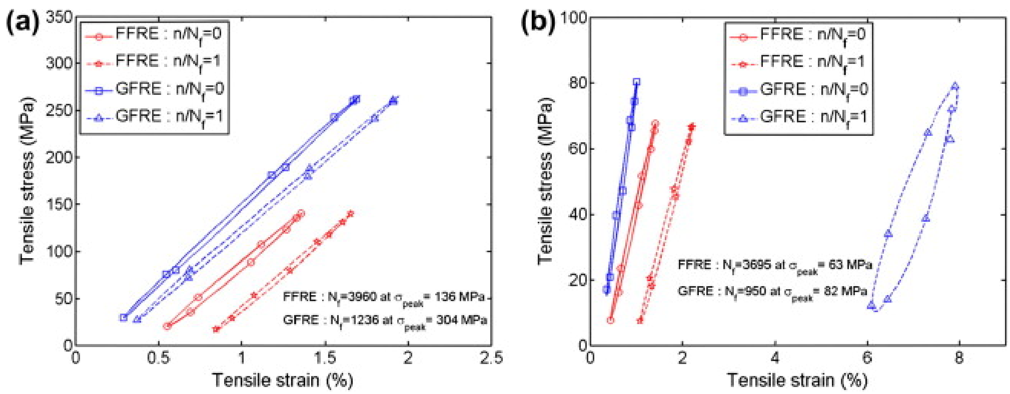

Figure 2.24: Increasing strain response of Flax-epoxy (FFRE) and Glass-epoxy (GFRE) laminates under constant stress amplitude fatigue at $\sigma_{\max} = 0.8$UTS for: (a) $[0/90]_{3S}$, and (b) $[\pm 45]_{3S}$. Reproduced with permission from [25].

The same study [25] revealed that FE [0/90] specimens *increased* in stiffness under constant-stress amplitude fatigue. The evolution trend is uniquely distinctive (Figure 2.25(a)), showing a very short-lived (0-0.015N_f) initial decrease followed by a progressive *stiffening* (at $\sim$2%/N_f) until 0.6N_f, after which the stiffness remains steady. This stiffening effect was attributed to the (i) re-organisation of microfibrils in Flax cell wall, and (ii) straightening of 'waviness' in fibre strands. In contrast, both GE layups and FE [±45] experienced a progressively *degrading* stiffness (Figure 2.25). The comparative FE vs GE stress-life (S-N) curves are analysed in conjunction with results from other fatigue studies in a later section (Chapter 7.2).

In a later study, the same research group Liang et al. [50] examined the fatigue response of two more FE laminates: $[0]_{12}$ and $[90]_{12}$, in addition to those previously studied. The stress-life (S-N) curves are

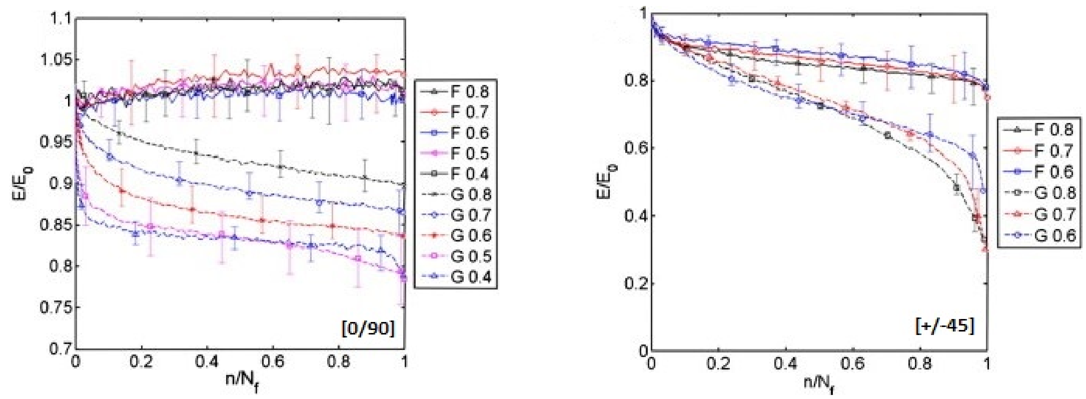

(a) (b)

Figure 2.25: Comparing Flax-epoxy (F) and Glass-epoxy (G) modulus evolutions under constant stress amplitude fatigue for: (a) $[0/90]_{3S}$ (0.4-0.8UTS), and (b) $[\pm45]_{3S}$ (0.6-0.8UTS). Reproduced with permission from [25].

discussed in conjunction with results from other fatigue studies in a later section. Damage kinetics was monitored by following the evolution of several *damage indicators* over the fatigue lifetime: (i) residual, or permanent, strain, (ii) dynamic, or secant, modulus (slope of hysteresis loop, similar to E_i in Figure 5.1(a)), (iii) fatigue modulus (peak stress-to-strain ratio), (iv) hysteresis energy density (area within hysteresis loop), and (v) crack density. Strain was derived from crosshead displacement measurements. It is seen that laminates with fibres aligned in the loading direction (fibre-dominant, [0] and [0/90]), tend to behave differently than those where response is arguably more influenced by matrix or interface properties (matrix-dominant, [90] and [±45]). *Permanent strain* is seen to continuously increase with increasing cycles, for all laminates, at all tested load levels (see Figure 2.26). However, fibre-dominant layups show a 2-stage evolution (initially accelerated, then steady accumulation), while the others have an additional third stage (also of accelerated accumulation) just before failure. *Secant modulus* evolution trends are generally *increasing* for fibre-dominant layups (similar to the Flax-composite curves in Figure 2.25(a)), but decreases rapidly as failure becomes imminent. This behaviour is further analysed later in Section 7.3. For matrix-dominant layups, the secant modulus is continuously *decreasing* following a 3-stage trend. *Fatigue modulus* is continuously decreasing for all laminates, at all load levels, following a 3-stage degradation trend. However, the first stage of accelerated degradation is more pronounced for the fibre-dominant layups. *Hysteresis energy density* typically decreases for fibre-dominant layups, but increases over fatigue life for matrix-dominant layups. *Crack density* was measured from micrographs of specimen edges, and appears to correlate well with permanent strain evolution. Cracks were seen to typically progress around fibres, but no cracking was observed in matrix-rich regions.

At about the same time, El Sawi et al. [103] conducted constant stress amplitude fatigue tests on Flax-epoxy laminates $[0]_{16}$ and $[\pm45]_{4S}$ to (i) develop *S*-*N* plots, (ii) observe evolving material properties, and (iii) record specimen surface temperature over test duration by infra-red (IR) imaging. As with the previously reviewed studies, the *S*-*N* plots are discussed in a later section. The mean strain for both laminates follows a 3-stage continuously increasing evolution at all tested stress levels. Like Liang et al. [50], the authors showed that dynamic modulus *increased* for [0] specimens until about 80% of fatigue life ($0.8N_\mathrm{f}$), after which the stiffening phenomenon reversed. In contrast, the modulus *decreased*

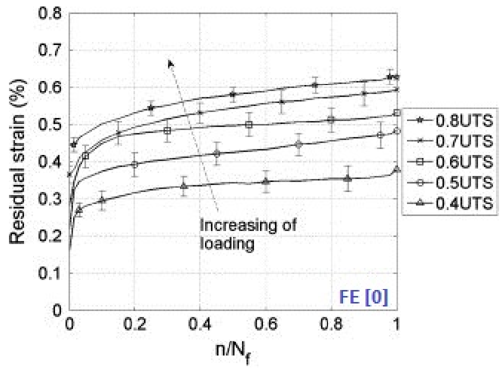

(a)

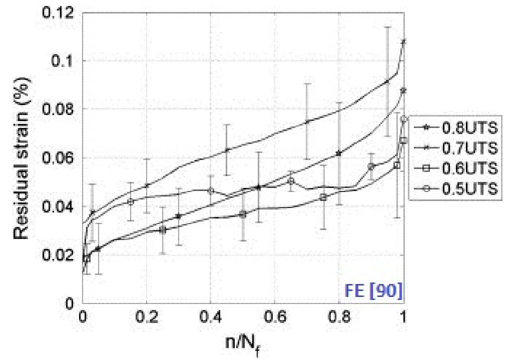

(b)

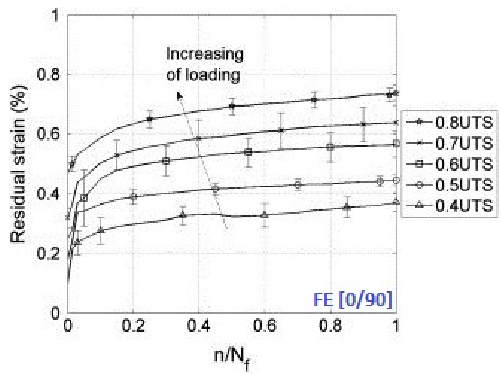

(c)

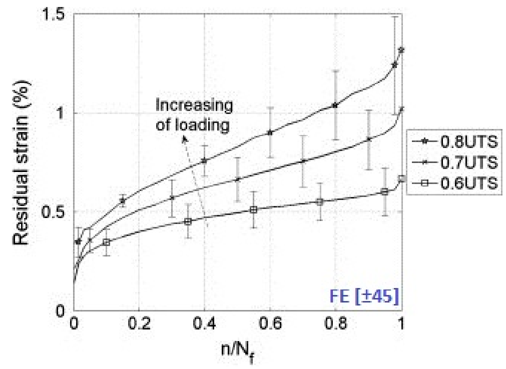

(d)

Figure 2.26: Residual (inelastic) strain evolution under constant stress amplitude fatigue for Flax-epoxy laminates: (a) $[0]_{12}$, (b) $[90]_{12}$, (c) $[0/90]_{3S}$, and (d) $[\pm 45]_{3S}$. Reproduced with permission from [50].

for [±45] over fatigue life. The stiffening of [0] laminates was attributed to reorientation/straightening of microfibrils in Flax fibre cell wall. Additional fatigue tests were conducted for both layups at 70% ultimate strength, interrupted at ⅓ and ⅔ of fatigue life for destructive SEM examination of specimen cross-section. Microcracks were seen to initiate within Flax fibre bundles, eventually progressing out either into the matrix or around the fibre bundle along fibre-matrix interface. Observed microcrack areas were measured as a fraction of total image area. The increase in measured areal crack percentage was found to correspond very well with the mean strain increase (also similar to finding in [50]). This suggests that the increasing strain amplitude (deformation) may be caused by an accumulation of cracks within the material. IR measurement during constant stress amplitude fatigue testing indicates that the specimen temperature initially increases, then stabilises after about 4,000 cycles. This stable temperature is found to be proportional to the applied peak stress, i.e. higher peak stress produces a higher surface temperature after stabilisation – and this correlation is bilinear, as shown in Figure 2.27 (plots T_{stable} vs peak stress $S_{\max}$). Further investigation enabled the authors to conclude that the inflection point in these plots occur at the high cycle fatigue strength (HCFS) of the material. Upon combining this T-S with S-N curve data, the authors propose a relationship between overall temperature rise ΔT and fatigue life $\log(N_{\mathrm{f}})$:

$$\Phi = \Delta T \times \log(N_{\mathrm{f}}) \tag{2.1}$$

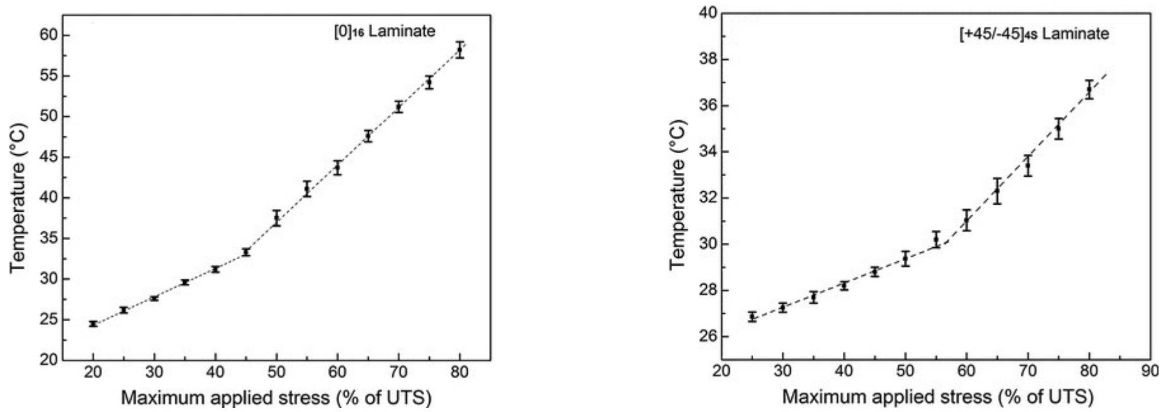

(a) (b)

Figure 2.27: Specimen surface temperature after stabilisation T_{stable} plotted as a function of applied peak stress for Flax-epoxy (a) $[0]_{16}$; and (b) $[\pm 45]_{4S}$. Curves are bilinear, wherein slope is constant for specific range of $S_{\max}$. Inflection point (knee) corresponds to high cycle fatigue strength. Reproduced with permission from [103].

where $\Delta T = T_{\text{stable}} - T_0$, and Φ is almost constant for specific ranges of applied peak load. Similar relationships for temperature rise as a function of fatigue life have been previously reported for metals [104] and woven Carbon fibre composites [105].

Ueki et al. [106] investigated the influence of cycling frequency on fatigue response of [0] Flax-epoxy specimens. Their S-N plot is discussed in a later section along with data from other sources. Tests were conducted at constant stress amplitude $R = 0.1$, and five loading frequencies: 0.25, 0.5, 1, 2, and 5 Hz. The residual strain and stiffness evolutions were observed to be similar to those reported in earlier fatigue studies by El Sawi et al. [107] and Liang et al. [50]: continuously increasing permanent strain, and increasing stiffness until $\sim$0.8-0.9N_{f}. It is noted that the stiffening correlates with increase in permanent strain. Loading frequency is found to have a significant influence on fatigue life and overall stiffening at least up to 2 Hz, above which the effect appears inconclusive from Figure 2.28 – though the authors report that there is no noticeable effect on fatigue endurance between 2 and 5 Hz. As shown in Figure 2.28: increasing frequencies (i) produce slightly lower stiffness increases, (ii) but longer fatigue lives (Figure 2.28(a)), and (iii) the correlation between residual strain and stiffness becomes less linear and less steep (for the same stiffness rise, the residual strain accumulation is higher, see Figure 2.28(b)). The authors have yet to investigate the micromechanical causes for this behaviour.

Asgarinia et al. [108] studied the fatigue behaviour of Flax-epoxy laminates made from three different textile (woven twill) Flax fabrics: (i) $[0]_6$ made from prepreg 200 g/m^2 fabric, (ii) [0/90/0] made from prepreg 550 g/m^2 fabric, and (iii) and $[0]_5$ made from 224 g/m^2 fabric through a VARTM[3] procedure. The authors designed a [0/90/0]-layup for the 550 g/m^2 specimens because they noticed a significant disparity in crimp[4] between the warp and weft weaves, so adding a 90°-rotated layer was a means to ensure equivalent biaxial properties in the laminate. All tests were conducted at $R = 0.1$ and 5 Hz – except the 224 g/m^2 specimens were cycled at 1, 1.5, and 3 Hz. The fatigue endurance and S-N plot

[3] vacuum-assisted resin transfer moulding

[4] *Crimp* is the shortening of yarn length in fabrics, that may result from a compressed, wavy, or non-taut weave.

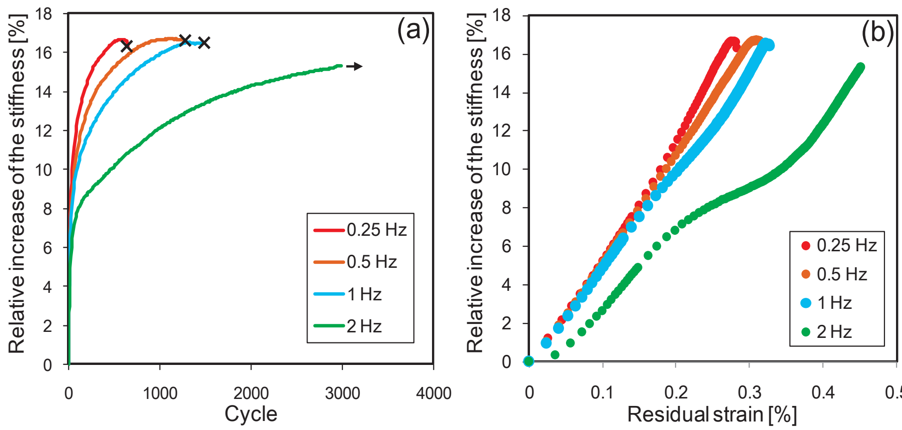

Figure 2.28: Influence of cycling frequency on fatigue behaviour of [0] Flax-epoxy specimens, showing that increasing frequency (a) slightly reduces overall stiffening but improves endurance, and (b) produces a more irregular correlation between stiffening and residual strain, where the same stiffness increase develops with more accumulated permanent strain. Reproduced with permission from [106].

are discussed in a later section along with data from other sources; however it must be noted here that no significant influence of cycling frequency is observed on fatigue life – which is somewhat in contrast to the findings on [0] specimens by Ueki et al. [106], discussed earlier. Based on the differences in fatigue endurance between the different woven specimens and microscopic observations of cracking, the authors conclude that (i) increased crimp encourages damage mechanisms, and damage intensity, during fatigue loading, and (ii) linear yarn density has a directly proportional relationship with fabric strength; therefore (iii) the best fatigue endurance can be obtained with 'flatter' fibre bundles/fabrics, or high tex (twist) yarn as they would have the least amount of crimp.

Bensadoun et al. [109; 110] studied the fatigue behaviour of several Flax-epoxy (FE) architectures: 4 UD-based laminates, 3 reinforced by woven twill fabrics, and 1 laminate each of plain-weave reinforced and random-short-fibre reinforced (*mat*-reinforced). Tests were conducted at 5 Hz and constant stress amplitude with $R = 0.1$, up to a maximum of 1 million cycles. Additionally, some specimens are tested only up to 500,000 cycles to study their post-fatigue static properties. To compare fatigue endurance, Glass-epoxy (GE) laminates of select architectures (UD-based, woven fabric, random mat) were also tested. The authors find that stacking sequence, ply orientation, and weave type have an impact on fatigue endurance, though this influence seems to disappear at low loading stress levels ($\leq$0.3UTS). The S-N plots of all FE and GE specimens are discussed in a later section, along with data from other sources. *Secant modulus* trend shows an initial short-lived (100-150 cycles) period of increasing stiffness in *all* tested FE specimens, including the random mat laminate. The authors suggest that this fibre-direction stiffening may be due to (i) the reorientation of helical microfibrils towards loading axis, and/or (ii) increase in crystallinity (thus increasing modulus) of amorphous viscoplastic cellulose in elementary fibres. The stiffening phenomenon is lesser for most twill woven laminates compared to UD, crossply and plain-weave laminates. Interestingly, monotonic tensile modulus and strength after 500,000 cycles at 0.3$\times$UTS appears to be statistically identical to undamaged mechanical properties for all specimens (see comparison bar-charts in Figure 2.29) except for low-twist twill (where the decrease is $\sim$20%); however the effect on failure strain appears inconclusive. Such similarity between pre- and post-fatigue properties have also

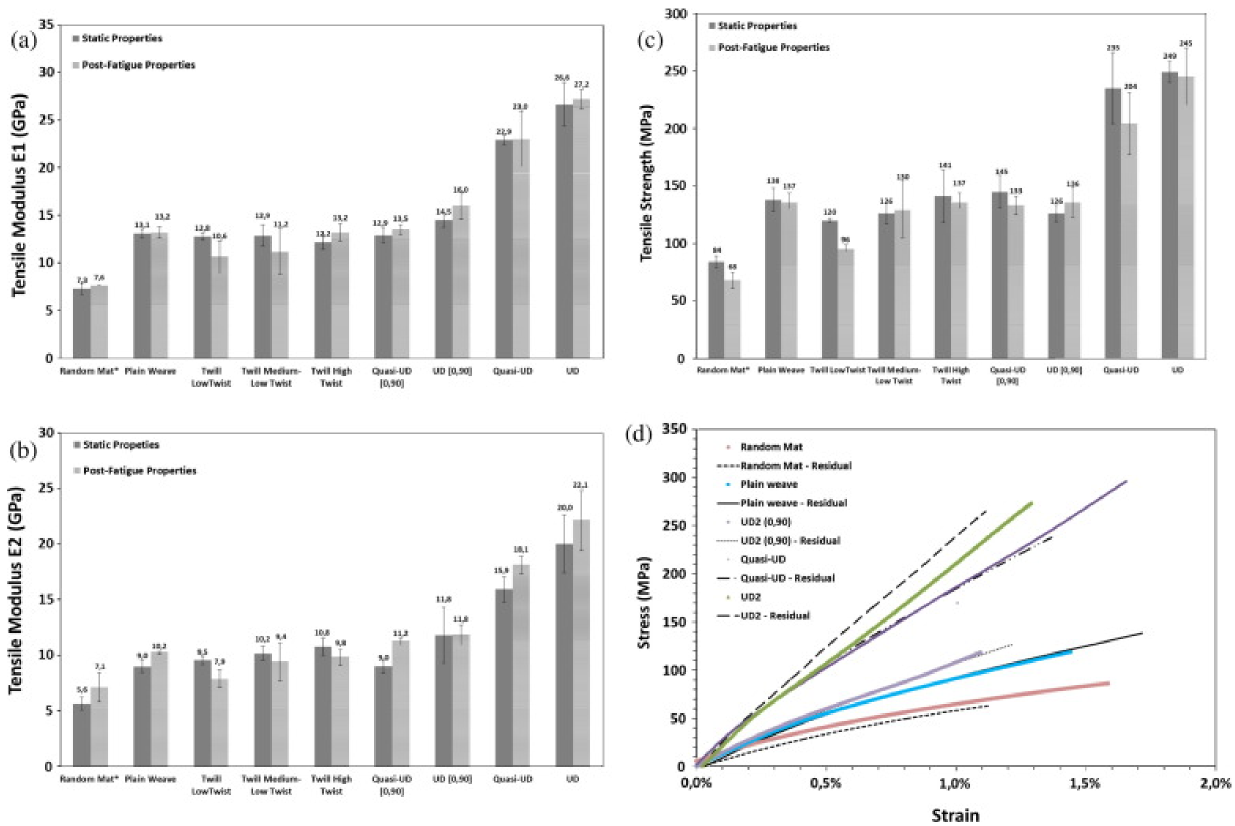

Figure 2.29: Insignificant difference observed in monotonic tensile properties of several Flax-epoxy architectures before and after 500,000 fatigue cycles at 0.3UTS: (a) Initial modulus E_1, (b) Secondary modulus E_2 (second linear portion of bilinear stress-strain curve), (c) Strength, and (d) Stress-strain response. Reproduced with permission from [109].

been reported for non-crimp textile Carbon-epoxy composites [111]. To explain this, the authors postulate that fatigue-related damage mechanisms may have *postponed* the development of failure-causing damage mechanisms, which eventually manifest during the static tests post-500,000-cycle-fatigue. *Hysteresis loops* for UD [0] laminates showed the smallest energy dissipation, and shortest shift to the right, compared to the crossply and woven laminates – indicating that in-fibre damage mechanisms are not as intensive as other mechanisms (delamination, interfacial debonding etc). As also concluded from previously reviewed studies, specimens of higher static strength (due to architecture, fibre alignment) demonstrate longer fatigue lives, delayed damage initiation, and slower damage progression. *Residual strain* is seen to increase continuously in a 2-stage power-law type trend for all specimens, and the quickest accumulation is seen in plain-weave and low-twist twill specimens. Most permanent strain accumulation occurs early in the fatigue life. The source of this irreversible deformation is suggested to be (i) movement of un-impregnated elementary fibres within the fibre bundle, (ii) breakdown of low-strength pectin adhesion in the *middle lamellae* region of fibre bundle, (iii) weak adhesion between fibre surface and epoxy, and (iv) plastic deformation of the matrix (cracking damage in fibre cell walls is not mentioned). Contrary to the findings of Asgarinia et al. [108], no evidence is found of crimp influencing fatigue response.

Sodoke et al. [112] studied the fatigue behaviour of ‘quasi-isotropic’ $[0_2/90_2/\pm45]$ Flax-epoxy specimens before and after water ageing (immersion in water bath at 60℃ until saturation). Fatigue tests were conducted at 5 Hz and constant stress amplitude $R = 0.1$, up to a maximum of 2 million cycles. Damage was followed by observing the evolution of hysteresis loops, secant modulus, surface temperature, and total strain amplitude. Acoustic Emission (AE) measurements were taken for specimens tested at 0.7-0.8UTS, to detect acoustic events that are correlated with different damage modes. The specimens were found absorb 26% of their original weight until saturation point (no further increase), within 25-30 hours – which the authors consider to be rapid, and attribute to the high fibre volume fraction of 0.68. Modulus decreased to 40% of original within 48 hours, then remained stable. As in the previously reviewed studies, cumulative *permanent straining* is observed. *Fatigue life* of aged specimens is noticeably lower than that of dry unaged specimens. The comparative S-N data is further discussed in a later section. *Hysteresis loops* are seen to narrow as the test progresses, consistent with reports from previously reviewed studies. The authors attribute the initial wider hysteresis loop to the higher damage events during the early period of fatigue cycling (Stage I). Water-aged specimens demonstrate more energy dissipation than dry specimens, indicating that water absorption increases internal damage activity. *Secant modulus* was observed to be 'fairly constant' until failure, prompting the authors to suggest that progressive fibre-stiffening balances the modulus-degrading effect of cracking damage. Since hysteresis (dissipated) energy and secant modulus are seen to stabilise early in the fatigue life, these properties were not considered to be useful failure criteria. The authors propose *minimum-strain* (strain at minimum cyclic load) as the most appropriate indicator of damage kinetics. For both dry and aged specimens, the highest percentage of AE events were in the low 35-40 dB range, which the authors claim is the signature range for matrix cracking. Interestingly, aged specimens register a relatively higher count of AE events in 50-60 dB range, than dry specimens. This is understood to be the typical range for fibre-matrix debonding and fibre pull-out, thereby suggesting that impregnation by water degrades fibre-matrix adhesion, resulting in increased debonding and expedited specimen failure.

2.3.2 Other NFCs

While the preceding section reviewed Flax-epoxy-related publications, fatigue studies on other cellulosic-fibre based NFCs have also reported noteworthy damage behaviour.

Towo and Ansell reported in two separate studies [113; 114] the fatigue response of polyester and epoxy composites reinforced by continuous Sisal fibres. The effect of treating fibres with alkali (0.06 M solution[5] of NaOH) was also studied. The constant stress amplitude fatigue cycles were enforced at 200 MPa/s loading-unloading rate in one set of tension-tension tests (T-T, R=0.1) [114], and at 400 MPa/s in another set of T-T and tension-compression (T-C, R=−1) tests [113]. Note that (i) cycle frequency was constant for each tested specimen, but not the same from specimen to specimen, and (ii) T-C tests were only conducted on Sisal-epoxy specimens. The authors report that alkali treatment of Sisal fibres increased the static strength of polyester-based specimens by 28.5%, while the epoxy-based specimens show a more modest 1.7% increase. The treated Sisal-polyester specimens typically show considerably longer T-T *fatigue lives* than untreated specimens, but since the treated-specimens' S-N curve is steeper, this difference is almost eliminated at stress levels <100 MPa. However, the treated Sisal-epoxy specimens showed an insignificant difference in T-T fatigue endurance when compared to their untreated counterparts.

[5] molar concentration, 1 M = 1 mole/litre

In contrast to T-T behaviour, the alkali treated Sisal-epoxy specimens demonstrate longer T-C fatigue lives, but this difference is reduced at low stress levels <50 MPa. The *fracture profile* in polyester specimens have a 'brushier' appearance with evident separation of individual fibres, but the epoxy specimens showed 'stepped' longitudinal brittle fracture and delamination. The failure in T-C specimens showed a wedge or 'kink' type deformation of the specimen. Under T-T tests, the measured *hysteresis loop area* for both polyester and epoxy based composites is larger initially than towards the end of fatigue life. The authors note that the initial large loop areas support other studies' findings of high early-life damage activity. In contrast, for T-C tests, the hysteresis loop areas for both composite types *increase* over the fatigue life. It is also seen that the compression-side of loop is wider (larger in area) than the tension-side. The authors conclude that Sisal fibres form stronger bonds with epoxy resin than with polyester, explained to be in the form of strong hydrogen bonds between epoxy and hydroxyl groups on fibre surface. This results in better load transfer between fibre-matrix, and the more brittle (or less defibrillated) failure modes seen in UD Sisal-epoxy composites. This finding also negates the need for improving fibre-matrix adhesion in epoxy based composites by alkali treatment of fibres.

Shah et al. [115] investigated the effect of fibre type/static strength, fibre volume fraction, textile architecture, and loading ratio on fatigue behaviour of several polyester-based NFCs. Tension-tension tests on several unidirectional (UD) [0] laminates (Flax-, Hemp-, and Jute-polyester) confirm that higher static strengths result in longer fatigue endurance, but this difference in data all but disappears when loading stress is divided by ultimate strength – indicating fibre-direction endurance of cellulose-based NFCs is identical when loaded at the same fraction of their ultimate strengths (all other test parameters being equal). The authors therefore reason that fatigue mechanisms and strength degradation is independent of plant/yarn type, on account of the structural similarity (cellulose content and crystallinity, degree of polymerisation, microfibril orientation) of the constituent plant fibres. Fatigue lives of tested NFCs are generally found to be shorter-lived than a comparable E-Glass-polyester composite, however when loading stress is normalised by ultimate strength, the NFCs exceed the Glass composite in endurance. Tests on Flax-polyester [0], $[\pm 45]_{\mathrm{nS}}$, and [90] laminates show that the more off-axis ply orientations are, the lower the static strength and fatigue endurance, as expected. On normalising by ultimate strength, it is seen that off-axis layups have a steeper stress-life plot than [0]. Tests on [0] Hemp-polyester at 5 different loading ratios (1 tension-compression, 3 tension-tension, 1 compression-compression) reveal that higher ratios result in longer fatigue lives and less steep stress-life curves (Figure 2.30(a)). The authors hypothesise that, since higher loading ratios imply smaller absolute loading amplitudes, the material experiences lower stress gradients between fibre and matrix phases, thereby alleviating crack initiation and progression along the interface. Tests on [0] Jute-polyester of fibre volume fractions ranging from 17-38% showed that increasing fibre content improved fatigue endurance – at least for fibre volume fractions up to ∼40% (Figure 2.30(b)).

Fatigue damage in plain-woven Hemp-epoxy was observed by de Vasconcellos et al. [116] through: (i) mechanical properties measurement, (ii) high-resolution imaging and (iii) optical microscopy of specimen surface, (iv) X-ray computed tomography (CT), (v) infra-red (IR) imaging, and (vi) acoustic emissions (AE) measurement. Tension-tension tests were conducted on $[0/90]_{\mathrm{nS}}$ and $[\pm 45]_{\mathrm{nS}}$ specimens at 1 Hz and a low loading ratio of R=0.01. An empirical power law based relationship is used to model fatigue life as a function of peak stress, loading stress ratio, and tensile strength. As also reported for other NFCs, [±45] specimens show longer fatigue endurance than [0/90]. Failure modes in fatigue were found to be similar to those under static loading: matrix cracking, fibre-matrix interface damage, and fibre fracture.

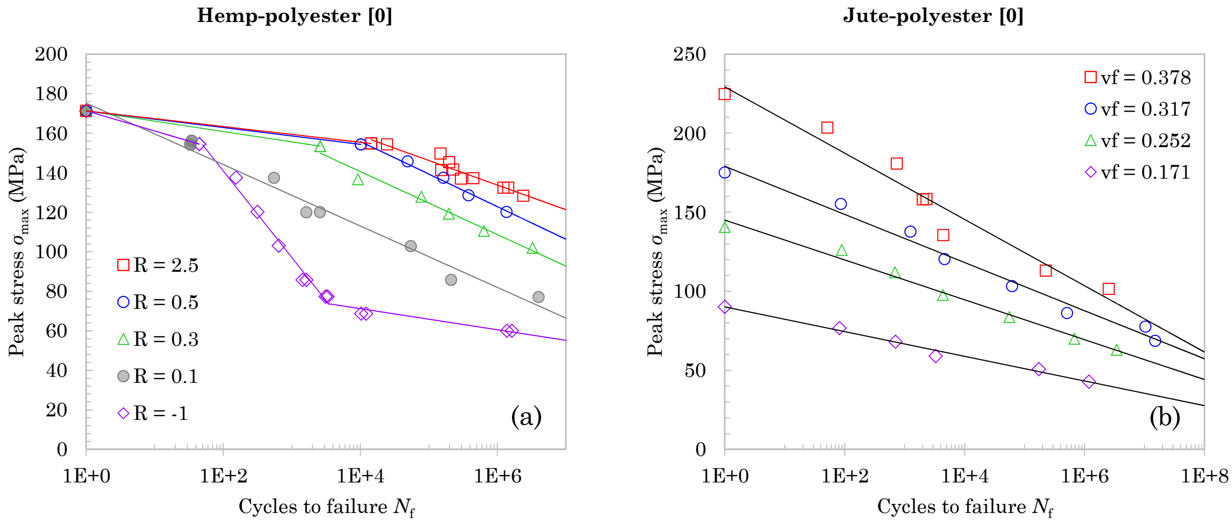

Figure 2.30: Influence on fatigue life of (a) loading ratio $R = \frac{\sigma_{\min}}{\sigma_{\max}}$ on Hemp-polyester, where $R = -1$ implies fully-reversed tension-compression fatigue, $R = \{0.1, 0.3, 0.5\}$ are tension-tension, and $R = 2.5$ is compression-compression; and (b) fibre volume fraction v_f on Jute-polyester. Data obtained from [115].

Secant modulus for both laminates were seen to degrade continuously in a 3-stage trend characteristic of fibre-composites. The [±45] specimens show a higher modulus degradation (−60%) than [0/90] specimens (−22%). *Minimum cycle strain* increases continuously for both laminates following a 3-stage trend, with [±45] specimens showing a higher increase (+1.8-3%) than [0/90] specimens (+0.3-0.9%). The differences in mechanical properties evolution is attributed to the more ductile response of [±45]. Hi-res imaging, micrography, and CT measurements indicated that [±45] specimens accumulated significantly higher *defect counts* than [0/90]. IR imaging revealed a progressive increase of *superficial temperature* at concentrated 'hot zones' where fractures eventually occur. Figure 2.31 sketches the damage modes observed by the authors. Based on methods and results of previous acoustic studies on Hemp-epoxy damage by Bonnafous

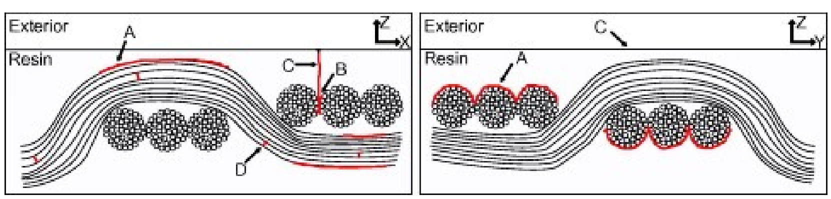

Figure 2.31: Diagram of damage in plain-weave biaxial laminates, showing the same crack types viewed across (a) X-Z plane (longitudinal cross-section, X is loading axis) and (b) Y-Z plane (transverse cross-section). A is interface debonding, B is separation of bundles, C is through-crack progressing to surface, and D is fibre fracture. Reproduced with permission from [116].

et al. [36; 117], three decibel ranges were identified that correlate to different damage modes: 35-53 dB for epoxy cracking, 58-63 dB for interface cracking, and 66-100 dB for Hemp fibre fracture. AE monitoring showed that damage events within the acoustic range of *matrix cracking* occurred throughout the entire fatigue life of both laminate types (Figure A.1). *Interface damage* acoustic events seem to manifest during the early (0-0.2N_f) and late (0.8-1N_f) cycles. *Fibre fracture* events are recorded during early and late fatigue life for [0/90], but are barely noticed for [±45].

Fotouh et al. [94; 118] studied moisture-absorption effects on fatigue of high-density polyethylene (HDPE) reinforced by short-chopped Hemp fibres (<5 mm). Micrographic examination confirmed that the short fibre distribution and orientation were variable and random. Specimens of neat HDPE, and two different fibre volume fraction composites, 13.5% and 30.1%, were tested under tension-tension constant stress amplitude cycling at 3 Hz and loading ratio R=0.1. Additional tests were conducted on specimens of v_f=13.5% composite at R=0.8, and after water immersion for 35 days. The v_f=30.1% specimens show the longest fatigue lives of all tested specimen types. Higher fibre-fraction is seen to extend fatigue life, while moisture exposure has a reducing effect. As expected, specimens cycled at R=0.8 showed shorter fatigue lives than those at lower R=0.1. The unreinforced, neat HDPE performance appears to match that of v_f=13.5% specimens at loading peak-stress levels >22 MPa, below which neat HDPE begins to endure longer. All composite specimens showed brittle failure, irrespective of fibre or moisture content. Post-mortem micrography of water aged specimens showed a separation of fibres from matrix, indicating that moisture absorption degrades fibre-matrix adhesion. Based on their tests, the authors propose a fatigue life prediction model that accounts for fibre fraction, loading ratio, and strain rate.

Yuanjian and Isaac [119] studied the fatigue performance of random-mat Hemp-polyester specimens before and after impact damage. To compare, asymmetric Glass-polyester $[\pm 45]_4$ specimens were also tested. Tension-tension constant stress amplitude tests were conducted at 1 Hz and R=0.1. The short fibre Hemp-composites generally showed better *fatigue performance* than the crossply Glass-reinforced specimens of similar fibre volume fraction, for peak stress loading levels >25 MPa (for below this stress level, data is insufficient). The Glass-composites showed visible *cracking* transverse to loading axis, but no such cracking was observed for Hemp-composites (note, no optical magnification used). *Residual modulus* of Glass-composites was found to decrease during early fatigue life by 80%, but Hemp-composite residual modulus appeared unaffected and constant until sudden final fracture – as shown in Figure 2.32(a). As expected, *impact damage* significantly reduces the fatigue life and residual modulus of Hemp-composites.

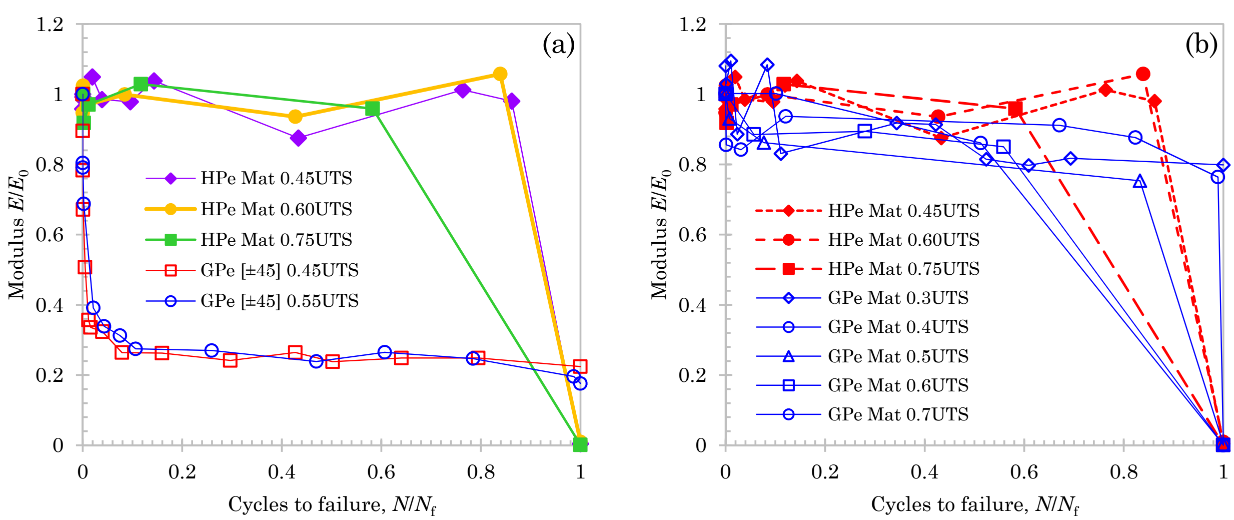

Figure 2.32: Residual modulus evolution over fatigue life for (a) short-fibre Hemp-polyester (HPe) and $[\pm 45]_4$ Glass-polyester (GPe), data adapted from [119]; (b) the same short-fibre HPe compared with short-fibre GPe, data adapted from [38].

A related study by Shahzad and Isaac [38] compared the same short-fibre Hemp-polyester as above [119] with the fatigue performance of short-chopped Glass fibre reinforced polyester under the same tension-tension (T-T) test parameters (1 Hz, R=0.1). In addition, fully reversed tension-compression (T-C) fatigue tests at R=−1 were also conducted on the Hemp-polyester specimens. The authors found that, while short fibre Hemp specimens have shorter *fatigue lives* than equivalent Glass specimens at the same absolute stress level, this difference was significantly minimised when stress level is normalised by ultimate strength. The T-T Hemp specimens showed higher fatigue endurance than T-C tested specimens. It should be noted that *residual modulus* evolution in short fibre Glass specimens is similar to that of short fibre Hemp specimens (2.32(b)), though showing a gently progressing degradation of ∼20%.

A summary of the findings in this review on existing NFC fatigue studies is compiled in Chapter 7.

2.4 In conclusion

1. Natural fibres are themselves composite structures, with highly ordered crystalline cellulose chains, at different orientations in different cell wall layers, reinforcing an amorphous matrix of pectin, hemicellulose and lignin [56; 57]. In contrast, synthetic fibres have a simpler, monolithic internal structure: Glass fibres are mostly composed of amorphous silica (silicon dioxide SiO_2), while Carbon fibres are made of stacked graphene (planar crystalline hexagonal arrangement of carbon atoms) layers [56; 120; 121].

2. The mechanical response of cellulose-based fibres are generally dependent on (i) cellulose content and (ii) microfibril spiral angle in the S2 layer of secondary cell wall (which is the bulk of the cell wall structure) [56; 57; 61]. Fibres with larger proportions of crystalline cellulose have higher stiffness and strength, and those with higher microfibril orientation angles will demonstrate more nonlinearity (stiffness variation) in their response.

3. The hierarchic multi-layer nature of fibre structure, the different constituent materials present in varying proportions, the ability of internal crystalline constituents to reorganise and some amorphous constituents to become crystalline under loading, contributes to the highly anisotropic, nonlinear deformation and complex damage progression behaviour seen in natural fibres and their composites. As such, the numerical simulation of NFC laminates must allow for nonlinear elasto-plastic response along all orthotropic planes.

4. Fatigue studies of NFCs published to date are all very recent. Reported studies are not always conducted under similar testing parameters, and may involve different plant fibres and laminate configurations. So, a holistic examination of all reported studies is needed to summarise existing knowledge on NFC fatigue endurance and damage accumulation, identify limitations, and recommend avenues of future investigation.

Chapter 3

Theory review

This chapter offers a brief primer on mechanical failure theories and the many approaches to multi-scale damage modelling. Damage mechanics concepts of damage, effective stress, strain equivalence, state variables, and thermodynamic potential are introduced. A damage-coupled elastoplastic modelling framework, in relation to the Mesoscale Damage Theory of Ladevéze et al. [122–124], is summarised.

3.1 On failure theories and damage modelling

As noted earlier, the design of reliable fibre-laminate structures depend on accurate predictions of damage initiation, damage progression, and development of failure conditions. Damage may be thought of as surface discontinuities (microcracks) and volume discontinuities (microvoids) [124]. *Damage progression* (alternatively, *evolution* or *accumulation*) is the initiation and growth of these discontinuities resulting in continuously developing, irreversible structural changes by various damage mechanisms. The evolution of distributed defects causes a progressive degradation of material stiffness, which results in nonlinear constitutive behaviour and strength reduction [124]. *Failure* is a subjective condition, typically defined as a loss of a desired load-carrying capacity – a condition that may not necessarily coincide with physical fracture. Heterogenous structures like fibre-composites tend to develop multiple local failures prior to physical fracture [125]. As noted earlier, at the *microscale* (scale of constituent fibre or matrix), fibre-composite damage mechanisms are fibre rupture (tension) or fibre buckling (compression), typically accompanied by microcracking in the matrix. At the *mesoscale* (scale of the ply), the typical damage mechanism is transverse matrix cracking due to coalescence of matrix microcracks, and fibre-matrix debonding. At the *macroscale*, observed damage is typically delamination, where a macroscopic debonding of the meso-constituents (delamination) occurs [124].

From a survey of the literature, it appears that existing failure prediction approaches in fibre-composite laminates broadly fall under the following: (i) Failure criterion, (ii) Progressive failure analysis (PFA), (iii) Fracture mechanics, and (iv) Damage mechanics. These approaches will be briefly discussed in the following paragraphs.

3.1.1 Failure criteria

The failure criterion approach of failure prediction simply compares the current macroscopic state of stress (or strain) with a criterion that describes the chosen failure definition. The simplest failure criteria are the *Maximum Stress* and the *Maximum Strain* criteria, which predict failure when the current stress or strain components reach pre-determined limits or maximum allowables. These criteria are *non-interactive*, since the combined effect of the individual stress or strain components are not captured. Examples of *interactive* criteria are the well-known *Tsai-Hill* [126], *Tsai-Wu* [127], and *Hashin* [128] criteria, all of which are polynomial criteria and are currently the most frequently used in fibre-composite failure prediction [91]. Such criteria are not generally based on the physics of damage or failure mechanisms; instead they are mathematical relationships that attempt to better correlate analytical predictions with experimental observations by combining all components of stress in interactive equations.

Predicting failure by comparison to a failure criterion is a rather conservative approach to composite design, since failure of a lamina does not necessarily imply a complete loss of load-resistance by the laminate. In addition, such approaches have no concept of following the progression of damage in either the lamina or laminate level. Predicting damage evolution and failure is a feature of the other techniques discussed as follows.

3.1.2 Progressive failure analysis

Progressive failure analysis (PFA) are procedures where the material properties of a composite laminate are degraded (typically, components of the laminate stiffness matrix) when a failure criterion (e.g. Tsai-Wu or Hashin) is locally satisfied [91]. The Hashin criteria appear to be the most commonly applied failure criteria in PFA methods [91]. The stiffness degradation approach tends to model sudden and brittle failures, i.e. the appropriate stiffness matrix components are forced to zero upon activation of a particular failure mode criterion. Stresses in the laminate are then recalculated using the new global stiffness matrix. PFA methods usually start with a determination of *first ply failure*, eventually determining the final collapse load of the laminate structure – which may prove to be much higher than the first ply failure load. A review of various existing PFA methods may be found in [129; 130].

The main advantage of PFA methods is practicality, owing to their simplicity in numerical implementation. However, the sudden stiffness-reduction approach may lead to difficulties in convergence. In addition to this disadvantage, failure criterion-based PFA methods do not capture the effect of stress concentrations around flaws or notches that may compromise the validity of stress-based criteria [91].

3.1.3 Fracture mechanics

Fracture mechanics methods for composite laminates allow an assessment of strength in the presence of defects by simulating crack propagation that drives the damage mechanisms of matrix cracking and delamination. Fracture mechanics is a discipline that "quantifies the conditions under which a load-bearing body can fail due to the enlargement of a dominant crack contained in that body" [91]. Well established numerical fracture mechanics procedures exist for composite laminate applications [91], but this approach as a whole is at a fundamental disadvantage in the context of damage modelling – *a defect must be pre-existing* at the start of the analysis procedure – which implies that damage *initiation* cannot be modelled. In addition, the state of diffuse damage in loaded laminates where many small cracks propagate and interact (as opposed to the assumption of one dominant crack) tend to be outside the scope of fracture mechanics methods [91].

3.1.4 Damage mechanics

Damage mechanics methods are an alternative approach to failure modelling that allows the prediction of damage initiation and overall evolution, upto and including rupture [125]. Simply put, damage mechanics techniques aim to predict:

- material response in the presence of damage, and
- conditions that lead to physical rupture [131].

To describe material damage evolution, such techniques apply nonlinear constitutive models defined in the context of continuum media, wherein damage is quantified by internal state variables that represent, directly or indirectly, the distribution or density of microdefects [91; 132]. Called *Continuum Damage Mechanics* (CDM), these techniques represent microscale damage (cracks) evolution by modelling macroscale effects (e.g. stiffness degradation, accumulation of plastic strain), within a framework of irreversible thermodynamics [132]. Several CDM-based methods of fibre-composite damage modelling and failure prediction have been proposed roughly over the last two decades [91; 122; 133–138]. A survey of recent publications indicate considerable ongoing activity in innovating or improving CDM-based techniques that model the damaged response of fibre-composites [91; 137; 139].

Since damage mechanics techniques are able to:

1. make predictions of damage initiation within plies from an undamaged state, unlike fracture mechanics approaches that require a pre-existing crack; and
2. capture the *evolution* of interim diffuse damage within each ply upto rupture, unlike the failure-criteria-based PFA approaches that only track ply failures (that, too, as sudden brittle failures),

the simulation of static tensile damage accumulation in Flax-composites, as developed for this study and described in Chapter 6, is best accomplished by applying a CDM-based model.

3.1.4.1 The Mesoscale Damage Theory (MDT)

Chapter 6 will elaborate the development of a CDM model that simulates damaged mechanical response in Flax-laminates by modifying an existing mesoscale framework developed at the *Laboratoire de Mécanique et Technologie*, Cachan, France (LMT-Cachan[6]), described by Ladevèze and others [122; 124; 140]. Named the Mesoscale Damage Theory (MDT) by Herakovich [124], it is the basis for a large number of CDM models

[6] LMT-Cachan, established 1975, is a research institution operated jointly by *École normale supérieure Paris-Saclay* (formerly *École normale supérieure de Cachan*), French National Centre for Scientific Research (*Centre national de la recherche scientifique*, CNRS), and the *Université Pierre-et-Marie-Curie* (UPMC); `http://lmt.ens-paris-saclay.fr/`.

in literature, and has been shown to be robust in predicting damaged response of composite structures under a variety of conditions [123; 124; 136; 141–154]. *Meso*-scale implies that the scale of analysis is between that of *micromechanics* (the level of constituents) and laminate analysis, i.e. *macroscale*. The main assumption in this framework is that laminate response under any loading until fracture can be predicted by modelling two elementary mesoscale entities: the ply and the interface, and a constitutive law is developed for each that includes inelasticity and damage. Typically, the interface layer is idealised as a mechanical surface that connects two plies, and only included in the model when delamination or out-of-plane deformation is of interest [141; 142; 144].

The following sections introduce concepts of damage mechanics that are relevant to understanding the MDT.

3.2 Damage mechanics preliminaries

Considering that it is rather difficult to distinguish between a volume element with significant internal damage and one that is undamaged, it is necessary to hypothesise *internal variables* and principles to help represent the deteriorated state of matter in the element [132; 155, p.348]. The *method of local state* postulates that the thermodynamic state of a material at a given point can be defined by a set of variables, uniquely dependent on that point, at any instant [132]. These *state* variables (also called *thermodynamic* or *independent* variables) represent mechanical properties that are either directly measurable (*observable* variables, e.g. total strain, temperature)[7] or may be hypothesised and inferred (*internal* variables, e.g. damage, elastic and plastic components of strain, inelastic hardening parameters) [132; 157]. The choice of appropriate state variables, especially internal variables, is somewhat subjective (dependent on the material medium, damage mechanisms studied, and researcher experience and inclination), which has so far resulted in an arbitrary variety of CDM models, but the method still remains popular since it allows flexible formulation of theories to simulate many different damage phenomena [132; 155]. In phenomenological damage mechanics formulations, some internal variables and principles relevant to this study are summarised as follows.

3.2.1 Damage

Following the Lemaitre and Chaboche [132, pp.349-350] definition of damage as the surface density of physical discontinuities (microvoids or microcracks), damage D in direction $\overrightarrow{n}$ is defined as the ratio of crack area S_D to total area S (both areas normal to $\overrightarrow{n}$, as shown in Figure 3.1):

$$D = \frac{S_D}{S} \tag{3.1}$$

Then, the *effective area of resistance* $\tilde{S}$ in the presence of damage is:

$$\tilde{S} = S - S_D = S(1 - D) \tag{3.2}$$

[7] In thermo-elastic materials, strain and temperature are the only two naturally observable state variables, and are therefore sometimes called *natural* or *canonical* state variables [156, p.553].

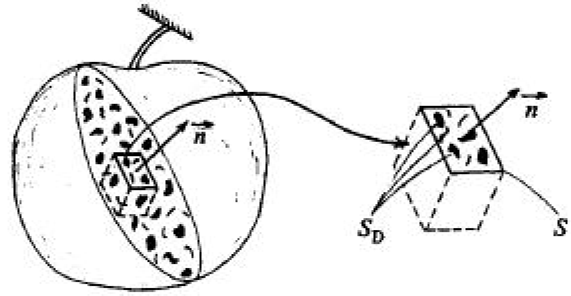

Figure 3.1: Damaged volume element, showing damage areas S_D on a reference surface area S. Reproduced with permission from [155].

3.2.2 Effective stress

For a simple case of uniaxial load F on a representative volume element, the usual stress satisfying equilibrium is $\sigma = \frac{F}{S}$. However, in the presence of microcracks or microvoids, since the area available to resist F is reduced, an *effective stress* $\tilde{\sigma}$ is defined:

$$\tilde{\sigma} = \frac{F}{\tilde{S}} = \frac{F}{S\,(1-D)} = \frac{\sigma}{1-D} \tag{3.3}$$

3.2.3 Strain equivalence

Assuming that *elastic deformation* behaviour of a material is only affected by damage in the form of effective stresses, Lemaitre and Chaboche [132, pp.349-350] hypothesise:

> "any deformation behaviour, whether uniaxial or multiaxial, of a damaged material is represented by the constitutive laws of the undamaged material in which the usual stress is replaced by the effective stress"

Therefore, the linear elastic law written in terms of elastic strain ϵ^e and undamaged elastic modulus E^0 is (shown for a uniaxial case):

$$\varepsilon^e = \frac{\tilde{\sigma}}{E^0} = \frac{\sigma}{(1-D)E^0} \tag{3.4}$$

This concept of *strain equivalence* between damaged and equivalent undamaged material is demonstrated in Figure 3.2.

3.2.4 Measuring damage

Rearranging (3.4):

$$\sigma = E^0(1-D)\cdot\varepsilon^e \tag{3.5}$$

where the term $(1-D)E^0$ is the damaged-condition elastic modulus E:

$$E = (1-D)E^0 \tag{3.6}$$

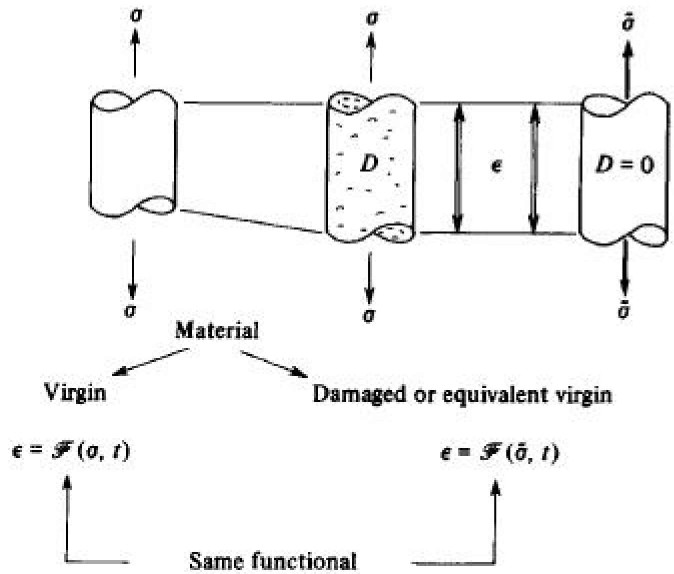

Figure 3.2: Equivalence in strain and hypothesised effective stress $\tilde{\sigma}$. Reproduced from [132, pp.351].

Rearranging in terms of damage variable D:

$$D = 1 - \frac{E}{E^0} \tag{3.7}$$

The damaged elastic modulus E can be experimentally determined from response curves of progressive load-unload tests, such as in the tensile example shown in Figure 3.3. Thus, damage can be calculated for every unload-reload cycle using (3.7) if the initial undamaged modulus E^0 is known.

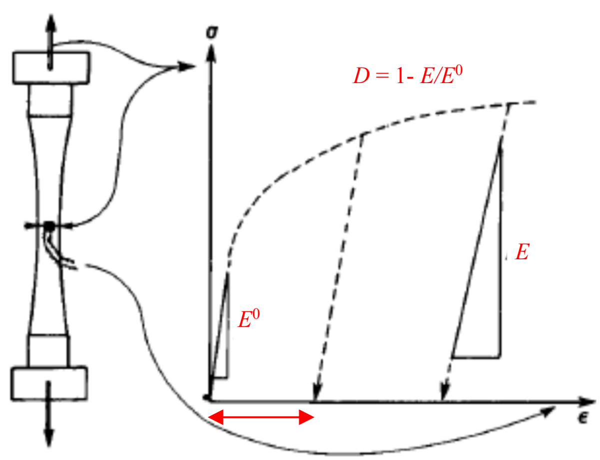

Figure 3.3: Monitoring damage by calculating damaged modulus from load-unload response curve of tensile test specimen. Reproduced from [132, pp.353].

Note that the above derivations (3.1)-(3.7) are intended to define damage as a function of crack area S_D, which leads to a related definition in terms of effective stress $\tilde{\sigma}$ and degraded modulus E. However, the accumulation of physical discontinuities in a material affects the value of several material properties, all of which may serve as observable state variables, and measured experimentally as a means of quantifying damage [157, p.7]: creep strain rate, density, elastic modulus, electrical resistance, hardness, inelastic strain, ultrasonic waves velocity, yield stress, etc.

3.2.5 Thermodynamics of damage modelling

A continuum which possesses both thermal and mechanical energy is called a *thermodynamic continuum*. The thermodynamic state of a system is known if all state variables are known. The transition from one thermodynamic state to another, i.e. a *thermodynamic process*, is reversible if the system and its surroundings can be brought back to their initial conditions [158, p.530] – e.g. elastic deformation of a solid. An irreversible process, therefore, is a one that is not reversible – e.g. inelastic deformation. If there is no change in state variables over time, the system is in *thermodynamic equilibrium*. A system at equilibrium has no tendency to change (has uniform temperature, no deformation) when it is isolated from its surroundings. A process that remains close to a thermodynamic equilibrium at all times is a *quasi-static process* [159]. The deformation of a test specimen under quasi-static mechanical loading may be thought of as a sequence of successive, but different, equilibrium states. As discussed in the previous chapter, it is known that natural fibres and their NFCs under quasi-static loading demonstrate inelastic deformation after an initial 'yield' point, but approximately elastic deformation upon unload-reloading[8], so the thermodynamic treatment of this deformation process may be considered as separate reversible and irreversible components.

The thermodynamics of irreversible processes allows for the modelling material behaviours in, broadly, three steps [157, p.7]:

- Define relevant *state variables* (as discussed in the previous section) which are chosen according to experimental observations of deformation and damage mechanisms, each contributing to the description of the current state.
- Define an appropriate state *thermodynamic potential*, which is a function of all state variables involved, from which state laws may be derived (e.g. thermo-elasticity), and would allow the definition of other *associated variables*.
- Define *dissipation potentials*, from which the evolution laws for the state variables may be derived, based on the dissipation mechanisms involved.

The above three steps are evident in the formulation of the standard Mesoscale Damage Theory (MDT) [122–124], which is the basis of the laminate progressive damage model developed in Chapter 6. The MDT considers the response of a damaged layer at any instant to be a function of elastic modulus degradation and accumulating permanent deformation due to cracking or plasticity effects. The subsequent sections summarise concepts that allow the development of this mesoscale model for stiffness-degrading elasto-plastic laminate response within the framework of irreversible thermodynamics.

[8] Recall that unload-reload hysteresis loop slope (secant modulus) is linear, and may be considered to remain constant until the previous maximum load is surpassed. This approximation should be valid as long as the load-unload cycle count is very low so as to avoid fatigue effects.

3.2.6 Thermodynamic potential

Just as potential energy is the capacity to do work (from classical mechanics), *thermodynamic potentials* are a measure of the 'useful' or process-initiating work that can be obtained from a thermodynamic system [132; 158]. Once appropriate state variables are defined, the existence of a state potential is postulated, from which *evolution laws* for the chosen state variables may be derived. For thermo-mechanical systems (e.g. a thermo-elastic solid), the *Gibbs Free Energy* and *Helmholtz Free Energy* are two famous functions that have been proposed in the past to serve as convenient potentials. Helmholtz Free Energy is the maximum amount of work a closed system can perform in a thermodynamic process in which *volume and temperature are held constant.* Gibbs Free Energy is the maximum reversible work that may be performed by a thermodynamic system at a *constant temperature and pressure* [132; 158].

In the literature on damage mechanics for anisotropic materials like fibre-composites, a reduced thermodynamic potential (derived from the aforementioned Gibbs or Helmholtz functions) is used to build lamina damage models for purely mechanical deformation under isothermal conditions, which is a Free Energy *Density* function $\rho\Psi$, typically formulated as the sum of elastic and inelastic contributions [91, p.488]:

$$\begin{aligned} \rho\Psi = W_D + f_p &= \frac{1}{2}\{\varepsilon^e\}^\top [\mathcal{L}(d)]\{\varepsilon^e\} \quad + \quad f(\tilde{p}) \\ &= \frac{1}{2}\{\sigma\}^\top [\mathcal{L}(d)]^{-1}\{\sigma\} \quad + \quad f(\tilde{p}) \end{aligned} \tag{3.8}$$

where ρ is the mass density, W_D is the Elastic Strain Energy Density function (the potential for elasticity with stiffness damage), f_p is the plastic potential function that governs the kinematics of plastic deformation, $\tilde{p}$ is the internal state variable quantifying overall multi-dimensional plasticity; while $\{\varepsilon^e\}$, $\{\sigma\}$, and $[\mathcal{L}]$ are the elastic strain, stress, and stiffness tensors, respectively; and d represents damage variables that influence the stiffness matrix components.

The following sections further discuss the damage-coupled elastic and inelastic terms of the above thermodynamic potential.

3.2.7 Damage-coupled elasticity

In the case of quasi-static mechanical deformation of a solid under isothermal and isobaric conditions, where the quasi-static process is sufficiently slow that enough time remains to equalise temperature of the material and its surroundings, dynamic heating effects are negligible (thus, equilibrium), and material density may be considered to remain constant (small strain assumption), the Free Energy functions may be reduced and expressed as the *Elastic Strain Energy Density* function W_D [156, p.554], which is a measure of the stored energy in the system[9] [158]. This function is the basis of the preferred thermodynamic potential in many different CDM models proposed for fibre-reinforced laminate deformation [123; 124; 136; 141–154].

[9] To follow the application of Helmholtz Free Energy function as a thermodynamic potential while satisfying the first and second laws of thermodynamics, and special-case conditions that allow its reduction into the Strain Energy Density function, please refer to Ottosen and Ristinmaa [158], and Lemaitre and Chaboche [160].

For an undamaged orthotropic ply, the Elastic Strain Energy Density function may be formulated in terms of the principal axes of orthotropy as:

$$
\begin{aligned}
2W_D = \{\sigma\}^\top[\mathcal{L}]^{-1}\{\sigma\} =& \frac{\sigma_{11}^2}{E_1} + \frac{\sigma_{22}^2}{E_2} + \frac{\sigma_{33}^2}{E_3} + \frac{\sigma_{12}^2}{G_{12}} + \frac{\sigma_{13}^2}{G_{13}} + \frac{\sigma_{23}^2}{G_{23}} \\
&- \left(2\frac{\nu_{12}}{E_1}\right)\sigma_{11}\sigma_{22} - \left(2\frac{\nu_{13}}{E_1}\right)\sigma_{11}\sigma_{33} - \left(2\frac{\nu_{32}}{E_3}\right)\sigma_{22}\sigma_{33}
\end{aligned}
\tag{3.9}
$$

where $\{\sigma\}$ is the stress tensor, $[\mathcal{L}]$ is the stiffness tensor, and per common practice [160, p.127] the following symmetry conditions are assumed:

$$
\frac{\nu_{12}}{E_1} = \frac{\nu_{21}}{E_2}, \quad \frac{\nu_{13}}{E_1} = \frac{\nu_{31}}{E_3}, \quad \frac{\nu_{32}}{E_3} = \frac{\nu_{23}}{E_2}
$$

For a *damaged* ply, the elastic modulus terms may be replaced by their damaged-condition counterparts, as shown in (3.6) (or, equivalently, the stress terms σ may be replaced by effective stress $\tilde{\sigma}$). Furthermore, for an in-plane loading condition, (3.10) retains only the in-plane terms, and thus reduces to:

$$
\begin{aligned}
2W_D &= \{\sigma\}^\top[\tilde{\mathcal{L}}]^{-1}\{\sigma\} \\
&= \frac{\sigma_{11}^2}{(1-d_{11})E_1^0} - \left(2\frac{\nu_{12}^0}{E_1^0}\right)\sigma_{11}\sigma_{22} + \frac{\sigma_{22}^2}{(1-d_{22})E_2^0} + \frac{\sigma_{12}^2}{(1-d_{12})G_{12}^0}
\end{aligned}
\tag{3.10}
$$

where $\tilde{\mathcal{L}}$ is the damaged-condition stiffness tensor, and d_{11}, d_{22}, and d_{12} are in-plane damage components along the fibre direction *11*, perpendicular to fibre direction (transverse) *22*, and shear plane *12*, respectively.

Considering that material properties in othotropic media are typically represented in ply coordinates, it follows that material damage may also be conveniently quantified along principal ply coordinates. The three in-plane damage variables d_{11}, d_{22}, and d_{12} are thus measures of their respective modulus degradation along *11*, *22*, and *12*. Note that the standard MDT model [122–124] defines damage variables only for transverse and shear planes. Since it was originally formulated for synthetic fibre composites where the reinforcing fibres tend to be linear-elastic and brittle materials (Glass, Carbon, etc.), fibre-direction modulus degradation is not typically defined. As will be seen later in Chapter 5, tests conducted for this study confirm that Flax-composites exhibit progressive modulus degradation in the fibre-direction – therefore it is necessary to amend the standard model and define a fibre-direction damage component d_{11}, as is done in Chapter 6.

Thus, the experimentally observed interaction between damage and elasticity is modelled through the principle of strain equivalence and resulting concept of effective stress $\tilde{\sigma}$.

3.2.7.1 Damage force, or Damage energy release rate

An *associated variable*, or *conjugate*, to the damage variable is defined, called the *thermodynamic damage force* Y. The standard MDT model [122–124] defines only in-plane transverse and shear damage variables, and their damage conjugates are derived from the Elastic Strain Energy Density function as follows:

$$Y_{22} = \frac{\partial W_D}{\partial d_{22}} = \frac{1}{2} \frac{\sigma_{22}^2}{E_2^0(1-d_{22})^2} \tag{3.11a}$$

$$Y_{12} = \frac{\partial W_D}{\partial d_{12}} = \frac{1}{2} \frac{\sigma_{12}^2}{G_{12}^0(1-d_{12})^2} \tag{3.11b}$$

The above derivation of Y (as the changing energy density ∂W_D with respect to damage increment ∂d) is the reason for its alternative name *damage energy release rate*. Y governs damage development the same way that the energy release rate K governs crack propagation in fracture mechanics. A previous maximum value of some function of the damage forces Y_{ij} has to be exceeded if new damage is to occur.

3.2.7.2 Damage evolution laws

The evolution of othotropic damage in a single ply is defined by laws relating the principal damage variables d_{ij} to some function of the damage force variables Y_{ij}. These functions are material-specific, and their formulation is determined from experimental observations of laminate response. First, a *coupled damage force* Y_{ts} is defined, which allows transverse and shear damage to influence each other:

$$Y_{ts} = \sqrt{Y_{12} + b \cdot Y_{22}} \tag{3.12}$$

where b is a coupling parameter to be determined experimentally. Then, the evolution this coupled damage force is defined as a function of each damage variable separately, assumed to be linear relationships in the standard MDT:

$$Y_{ts}(d_{22}) = Y_t^c \cdot d_{22} + Y_t^0 \tag{3.13a}$$

$$Y_{ts}(d_{12}) = Y_s^c \cdot d_{12} + Y_s^0 \tag{3.13b}$$

where Y_t^c and Y_s^c are the slopes of the linear functions, and Y_t^0 and Y_s^0 are the intercepts (that serve as initiation thresholds for damage along *22* and *12*, respectively). From the above evolution functions (3.13), it is evident that positive damage values initiate only when Y_{ts} from (3.12) surpasses the thresholds Y_t^0 or Y_s^0.

The standard MDT does not allow for stiffness degradation damage in the fibre-direction (response treated as linear-elastic and brittle), so it does not provide an evolution function for any fibre-direction damage. Since the NFCs tested for this study demonstrate fibre-direction stiffness degradation (see Chapter 5), a fibre-direction damage evolution law will be proposed in Chapter 6 based on observations of UD Flax-epoxy [0] specimens.

3.2.8 Damage-coupled inelasticity

Inelastic strains may develop for many reasons, including inherent plasticity of the material, cracking damage, creep etc. To simulate the inelastic component of deformation, inelastic behaviour is modelled such that it is also coupled with the effects of permanent damage. The MDT follows the formalism of classical *plasticity theory.* An *elastic domain*, or *yield surface*, f is defined as a function of the multiaxial effective stresses $\tilde{\sigma}_{ij}$, which is analogous to the elastic limit, or yield stress, in uniaxial stress space (σ_y in Figure 3.4). This domain defines the stress space within which all stress variations generate only elastic strain variations. Stress increments at or beyond the elastic domain boundary generate inelastic strains (*plastic flow*). As will be seen later in Chapter 5, Flax-based NFCs clearly accumulate residual strain, and the apparent yield point increases under repeated progressive unload-reload cycles for all in-plane directions – i.e. they demonstrate apparent *plastic hardening*, indicating (i) the existence of an elastic domain (ii) that is not constant in size, but instead (iii) expands with plastic flow.

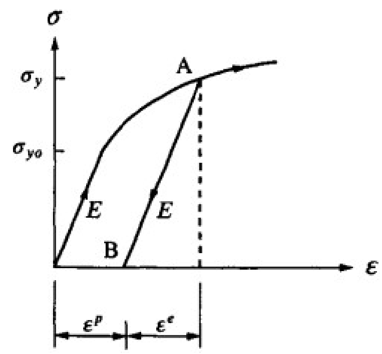

Figure 3.4: Uniaxial hardening response of elasto-plastic material. Reproduced from [158, p.203].

3.2.8.1 Strain decomposition and effective inelastic strain

The total strain is the sum of elastic and inelastic strain components, expressed here in incremental form:

$$\dot{\varepsilon}_{ij} = \dot{\varepsilon}^{e}_{ij} + \dot{\varepsilon}^{p}_{ij} \tag{3.14}$$

The effective inelastic strain *increment* or *rate* is derived such that the rate of work (mechanical dissipation of energy) by effective stress and effective inelastic strain rate is identical to that of actual stress and inelastic strain rate [124]:

$$\tilde{\boldsymbol{\sigma}}^{\top}\dot{\tilde{\boldsymbol{\varepsilon}}}^{p} = \boldsymbol{\sigma}^{\top}\dot{\boldsymbol{\varepsilon}}^{p} \tag{3.15}$$

In the standard MDT model, where no plasticity is allowed for in the fibre-direction, effective inelastic strain increments $\dot{\varepsilon}^{p}_{ij}$ are only defined in transverse and shear:

$$\dot{\tilde{\varepsilon}}^{p}_{22} = \dot{\varepsilon}^{p}_{22}(1 - d_{22}) \tag{3.16a}$$

$$\dot{\tilde{\varepsilon}}^{p}_{12} = \dot{\varepsilon}^{p}_{12}(1 - d_{12}) \tag{3.16b}$$

3.2.8.2 Yield surface, plastic potential, and hardening

In the standard in-plane MDT model for an orthotropic ply [122–124], the *yield surface* is defined only in terms of transverse and shear effective stresses (fibre-direction stress contribution was neglected since synthetic fibre composites show negligible plastic effects along fibre-direction):

$$f_p = \sqrt{\tilde{\sigma}_{12}^2 + a^2 \cdot \tilde{\sigma}_{22}^2} = R \tag{3.17}$$

As can be seen from (3.17), the form of the yield surface in $\tilde{\sigma}_{22}$–$\tilde{\sigma}_{12}$ space is assumed to be an ellipse of size R, with a *coupling effect* between transverse and shear stresses via a scalar constant coupling factor a^2. When expressed as the inequality (3.18), the function then describes the *elastic domain*, or the *plastic potential function* [161]:

$$f = \sqrt{\tilde{\sigma}_{12}^2 + a^2 \cdot \tilde{\sigma}_{22}^2} - R \leq 0 \tag{3.18}$$

The hardening (i.e. the increase in size of elastic domain) is assumed to be isotropic in $\tilde{\sigma}_{22}$–$\tilde{\sigma}_{12}$ space (centre of the elastic domain remains at the origin), as shown in Figure 3.5. In the standard MDT model, the size of the expanding yield surface is given by the function:

$$R = R_0 + R_H(\tilde{p}) = R_0 + \beta(\tilde{p})^\alpha \tag{3.19}$$

where R_0 is the initial size of the yield surface (plasticity threshold), and $R_H(\tilde{p})$ is a material-specific hardening function that depends on the *accumulated effective plastic strain* $\tilde{p}$. For a uniaxial case (e.g. Figure 3.4), this $\tilde{p}$ is simply the inelastic component of effective strain ($\tilde{\varepsilon}^p$), but for a multiaxial case, $\tilde{p}$ is a function of all orthotropic inelastic contributions $\tilde{\varepsilon}_{ij}^p$ formulated according to the yield criteria assumed [162, p.10], i.e. it is a measure of total plasticity accumulated. At loading beyond the yield surface, the hardening evolution is expected to follow a power law $R_H = \beta(\tilde{p})^\alpha$, based on experimental observations of Carbon-epoxy laminate response [122–124]. The parameters β and α are material-specific, and determined experimentally. In the uniaxial case, once plasticity develops, the yield point is equal to the highest value

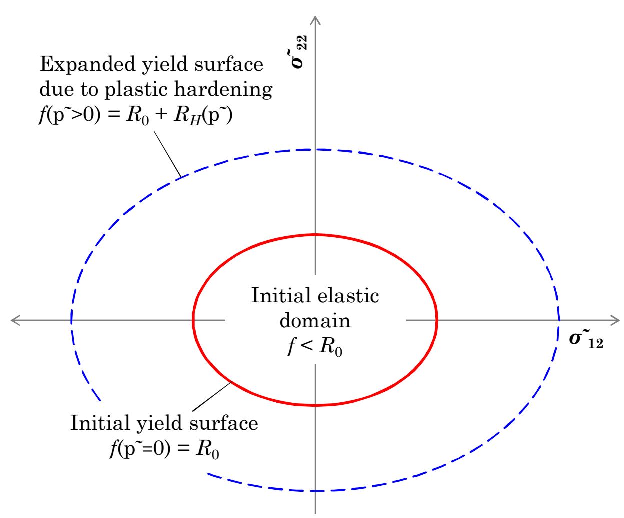

Figure 3.5: Isotropic hardening of yield surface in $\tilde{\sigma}_{22}$–$\tilde{\sigma}_{12}$ space, as assumed in standard MDT model [122–124].

of stress previously attained, so unloading does not affect the yield point. Similarly, for a multiaxial stress state, the yield surface remains at the highest value of R previously attained.

According to the generalised *normality hypothesis* associated with instantaneous dissipative phenomena for *standard materials* [124; 160, p.193], the inelastic strain increment is required to be normal to the yield surface f per:

$$\dot{\tilde{p}} = -\dot{\lambda}\frac{\partial f}{\partial R} = \dot{\lambda} \tag{3.20}$$

$$\dot{\tilde{\varepsilon}}^p_{ij} = \dot{\lambda}\frac{\partial f}{\partial \tilde{\sigma}_{ij}} \tag{3.21}$$

where $\dfrac{\partial f}{\partial \tilde{\sigma}_{ij}}$ is the *direction vector* of the inelastic increment $\dot{\tilde{\varepsilon}}^p$ (normal to the yield surface), and $\dot{\lambda}$ is a scalar *multiplier* that can be thought of as scaling factor which determines the magnitude of the plastic increment. The flow direction vector $\dfrac{\partial f}{\partial \tilde{\sigma}_{ij}}$ in the standard MDT for in-plane ply deformation can be derived from (3.18):

$$\frac{\partial f}{\partial \tilde{\sigma}_{ij}} = \begin{Bmatrix} \dfrac{\partial f}{\partial \tilde{\sigma}_{11}} \\ \dfrac{\partial f}{\partial \tilde{\sigma}_{22}} \\ \dfrac{\partial f}{\partial \tilde{\sigma}_{12}} \end{Bmatrix} = \begin{Bmatrix} 0 \\ \dfrac{a^2 \cdot \tilde{\sigma}_{22}}{\sqrt{S}} \\ \dfrac{\tilde{\sigma}_{12}}{\sqrt{S}} \end{Bmatrix} \tag{3.22}$$

where $\sqrt{S} = \sqrt{\tilde{\sigma}_{12}^2 + a^2 \cdot \tilde{\sigma}_{22}^2}$, or alternatively from (3.18)–(3.19), $\sqrt{S} = R_0 + \beta(\tilde{p})^{\alpha}$. Note that $\dfrac{\partial f}{\partial \tilde{\sigma}_{11}} = 0$ since, in the standard MDT [122–124], fibre-direction deformation is assumed to produce no plastic contribution, and thus no fibre-direction terms were included in the yield surface f formulation (3.18). Therefore, the incremental transverse and shear inelastic strains are computed from (3.20)–(3.22) as:

$$\dot{\tilde{\varepsilon}}^p_{ij} = \dot{\lambda}\frac{\partial f}{\partial \tilde{\sigma}_{ij}} = \dot{\lambda} \begin{Bmatrix} \dfrac{\partial f}{\partial \tilde{\sigma}_{11}} \\ \dfrac{\partial f}{\partial \tilde{\sigma}_{22}} \\ \dfrac{\partial f}{\partial \tilde{\sigma}_{12}} \end{Bmatrix} = \dot{\tilde{p}} \begin{Bmatrix} 0 \\ \dfrac{a^2 \cdot \tilde{\sigma}_{22}}{\sqrt{S}} \\ \dfrac{\tilde{\sigma}_{12}}{\sqrt{S}} \end{Bmatrix} \tag{3.23}$$

3.3 In conclusion

From the above discussion of damage mechanics, it is understood that the chosen progressive damage modelling framework (MDT) is essentially a phenomenological constitutive law that is able to capture material degradation (via stiffness and inelasticity evolution), starting from an undamaged state at the beginning of load application until just before failure, without the need to follow visible cracks to measure damage and predict failure (as is necessary in fracture mechanics).

Chapter 4

Materials, manufacturing and equipment

Most of the original work reported in the following chapters is based on mechanical tests on composite plates manufactured specifically for this dissertation work. This chapter discusses the raw materials and fabrication procedure used to manufacture composite plates in the laboratory, the measurement of constituent fractions (fibre, matrix, porosity) in the resulting composites, and the preparation of specimens for all types of mechanical testing conducted.

4.1 Introduction

A variety of fabrication techniques have been tried to manufacture Flax-composites: hand layup, resin transfer moulding (RTM), compression moulding, vacuum infusion, film stacking, and pultrusion [46]. A review of typical factors affecting manufacturing of NFCs can be found in [12; 46]. As will be described later, the specimen composites for the studies proposed herein will be fabricated by hand-layup and hot-platen compression – a procedure that is labour intensive but straightforward and inexpensive.

4.2 Constituent materials

4.2.1 Matrix material

Both synthetic and natural polymers have been tried as matrix material for Flax-composites. From the literature surveyed, tested polymers may be categorised into following (with a non-exhaustive list of examples):

- *Biodegradables*: Polylactic acid (PLA) [163; 164], Poly-L-lactide (PLLA) [163], Soy protein isolate resin (SPI) [165], Polyhydroxybutyrate (PHB) [163; 166]
- *Thermoplastics*: Polypropylene (PP) [14; 28; 164; 167], Polyethylene [168], Polystyrene (PS) [169]

- *Thermosets*: Epoxy resins [25; 27; 32; 107; 170; 171], Vinylester (VE) [72; 172], Polyester (PE) [72; 173–175]

Biodegradable polymers have the advantage of being very environmentally friendly, but currently happen to cost 3-5 times more than thermoplastics [46]. *Thermoplastic* polymers appear to be the most commonly studied matrix material for Flax-composites (particularly PP) on account of their (i) low density, (ii) high temperature resistance, (iii) good impact resistance, and (iv) ease of moulding complex shapes. However, research on thermoplastics (e.g. those of PP) is limited by their processing temperature, which should be less than 230℃ to avoid any natural fibre degradation [46]. *Thermoset* polymers surpass thermoplastics in (i) mechanical properties, (ii) thermal stability, (iii) chemical resistance, (iv) general environmental durability, and (v) can be cured at temperatures well within the safe range for natural fibres [46].

Considering that thermosets have been found to provide the best mechanical and durability properties to natural fibre composites, the studies conducted in the following chapters will use thermoset Epoxy resin-based composite specimens. A hot-curing epoxy system is used to manufacture the Flax composite plates, which is a combination of low-viscosity epoxy resin Araldite® LY 1564 and a cycloaliphatic polyamine hardener Aradur® 22962 (Huntsman Corporation, Advanced Materials, The Woodlands, TX, USA). The epoxy-hardener ratio is 4:1 by weight, per supplier specifications.

4.2.2 Flax fibre

In the last decade or so, Flax fibres of various architectures have been tested as reinforcements in polymer resins. A survey of published research on Flax-composites reveals that, in addition to its bundle and elementary forms, Flax fibres have also been further processed into short-fibre mats, yarns, rovings, and woven fabrics. *Mats* are non-woven layers of finite-length fibre bundles (technical fibres) that are interlaced by a punch-needling process [21; 47]. The fibres may be either randomly oriented or specifically oriented (e.g. unidirectional). *Rovings* are typically clumps of technical fibres bound or twisted by hand [164; 172]. *Yarns* are twisted continuous threads made from technical fibres [31]. Fibre bundles, rovings and yarns can be further processed into *woven fabrics*, that may or may not be *balanced* [27; 33; 176]. For the studies described in the following chapters, a UD fabric is chosen since it can be hand-cut to desired fibre-orientations, and thus allowing the highest flexibility in manufacturing composite specimens of desired layups.

The reinforcing Flax material used is a commercially available dry UD fabric roll FlaxPly® (Lineo NV, Belgium, [177]; see Figure 4.1) of area-weight 150 g/m^2 per supplier specifications. Based on measurements at our laboratory, the average density of the Flax fabric is 1.473 g/cm^3 (Table 4.1). The FlaxPly® fabric architecture consists of fibre bundles predominantly in the warp direction (0°), held together by a periodic cross-weave (90°), as shown in Figure 4.2. The ratio of 0° to 90° fibres is 40:3, i.e. for every 40 strands in the 0°-direction there are 3 across, within a unit-squared area of fabric. Each strand is a twisted bundle of elementary fibres with a twist rate of ∼5 turns/cm, measured from optical micrographs. Note that, while the fabric is not perfectly unidirectional (due to the presence of cross-weave), tests on the derived composites (detailed later in Chapter 5 and in [178]) demonstrate that the mechanical properties compare very well with existing published data on unidirectional continuous-fibre Flax composites – thus indicating

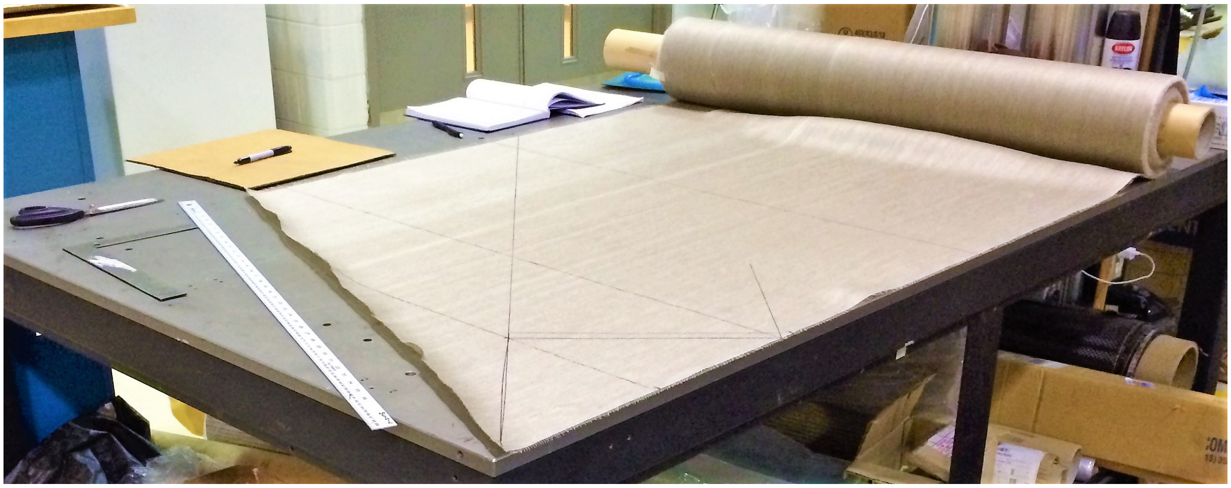

Figure 4.1: UD FlaxPly® fabric roll from Lineo NV, Belgium, shown prepared for cutting on a flat table.

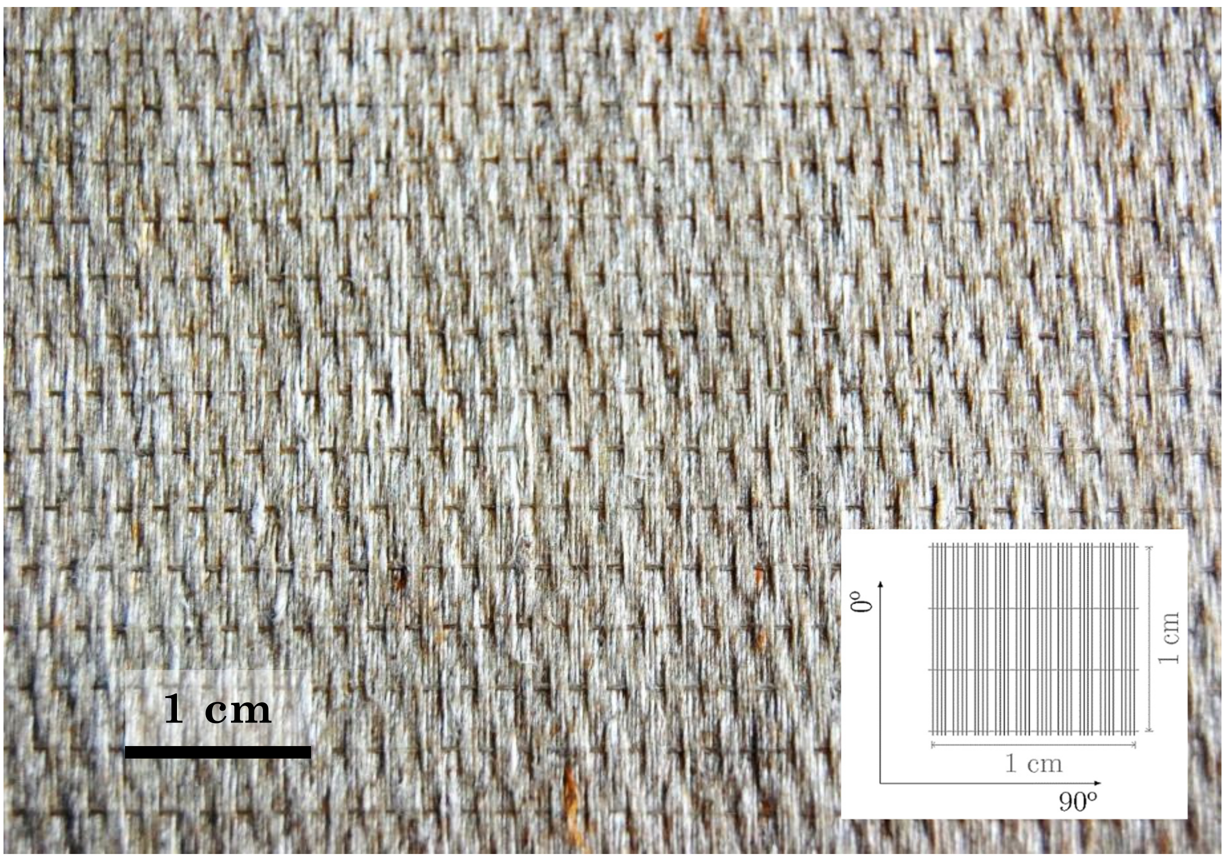

Figure 4.2: FlaxPly® is predominantly unidirectional, held together by a periodic cross-weave. Ratio of 0° strands to 90° cross-weave strands is 40:3.

that the cross-weaves do not have a significant influence on the bulk composite response, and that the fabric may be considered practically unidirectional in nature.

Microscopy observations of the eventual Flax-composite cross-section indicate that the fibre bundles measure 150-300 μm in diameter (see Figure 4.3), and they consist of individual Flax fibres of diameter 10-30 μm. Individual elementary fibres have a polygonal cross-section, with about 5-8 sides. These observations are consistent with published descriptions in other studies [23; 51; 55].

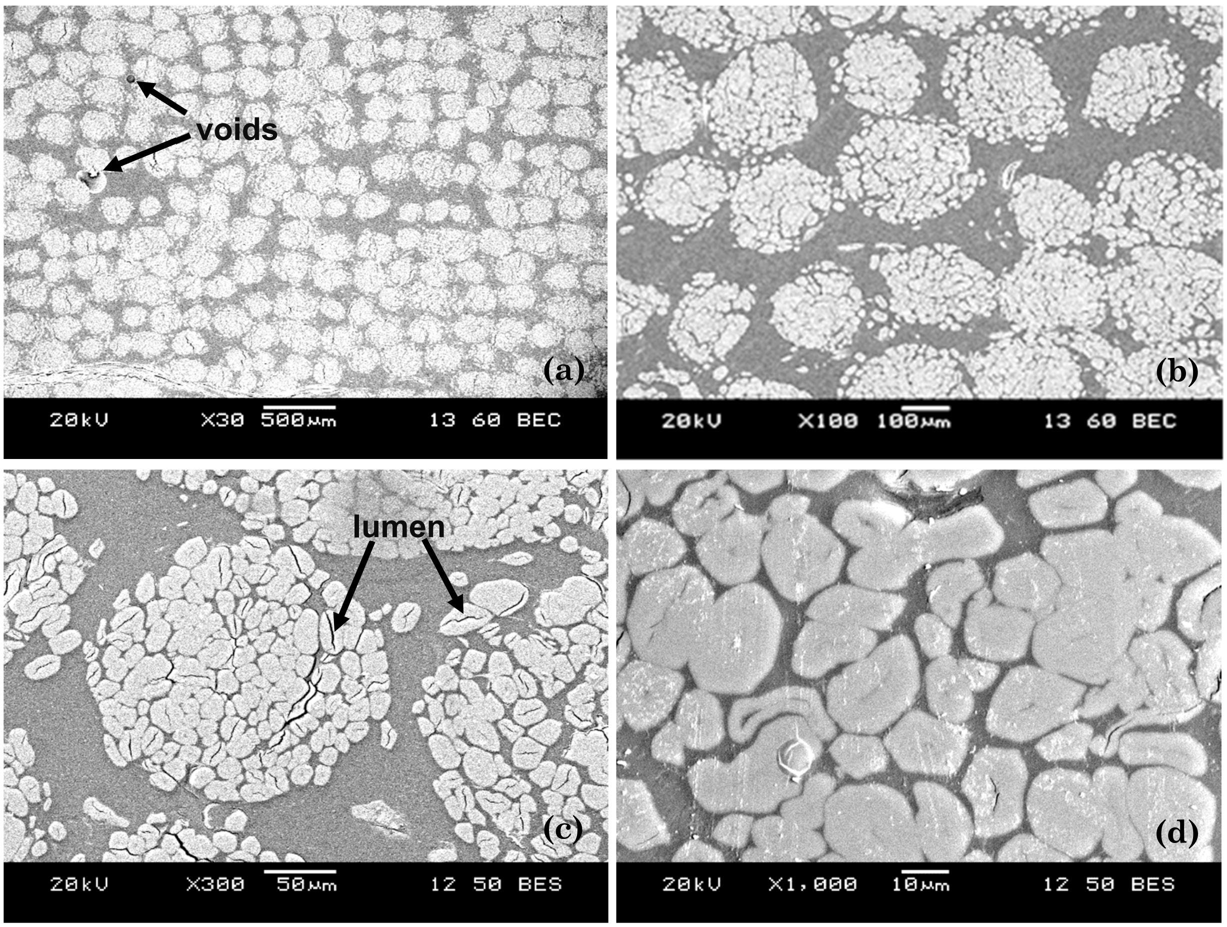

Figure 4.3: Cross-section SEM images of undamaged Flax-epoxy composite: (a) at ×30, Flax fibre bundles in light grey, matrix in dark; (b) at ×100, showing bundles where individual elementary Flax fibres are discernible; (c) at ×300, collapsed lumen visible in elementary fibres; (d) at ×1000, showing polygonal cross-section of elementary fibres

4.2.3 Glass fibre

Commercially available E-Glass (14-oz ×12" Model 1115 supplied by Composites Canada, Mississauga, ON, Canada) was used to manufacture the Glass-epoxy composites tested under fatigue for this study. Individual Glass fibres are closely bundled and held together in a loose 'fabric' by an overlaid mesh layer of the same Glass fibres, as shown in Figure 4.4. Micrographs indicate that the Glass fibres are cylindrical with circular cross-sections of diameter 16 ±2 μm (see Figure 4.5) – the same order of magnitude as that of elementary Flax fibres.

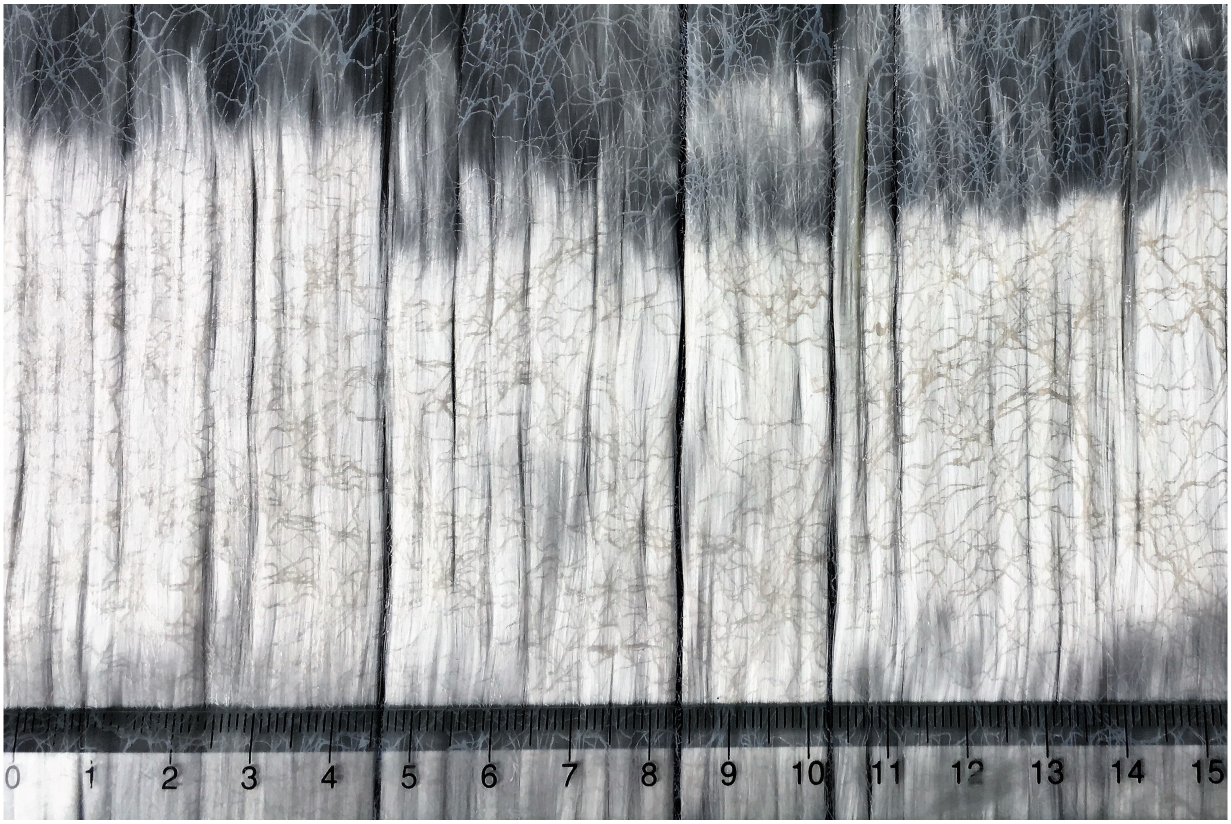

Figure 4.4: E-Glass continuous fibres held together in a loose 'fabric' by a random mesh of the same fibre. Shown scale is in cm.

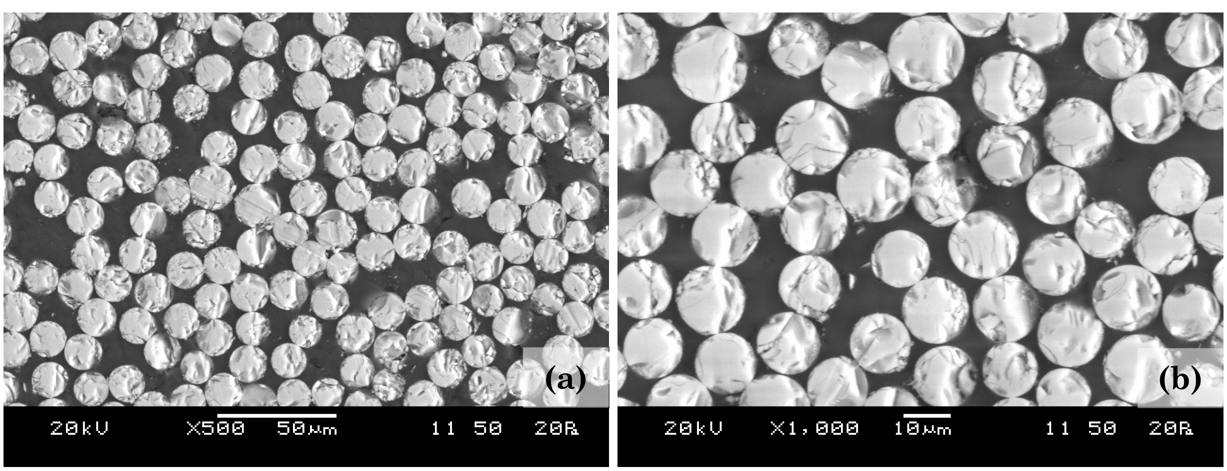

Figure 4.5: SEM images of undamaged Glass-epoxy composite, showing circular cross-section E-Glass fibres (lighter shade) in epoxy matrix (darker shade): (a) at $\times 500$, and (b) at $\times 1000$.

4.3 Manufacturing

The Flax-fabric plies were hand-layed, the matrix hand-poured and evenly spread across the stack-up, and final laminate plates were press-manufactured by heated-platen compression in a small-scale laboratory setup. For the cure cycle parameters of temperature and duration (specified later), specifications by the the matrix manufacturer were followed as detailed in the datasheet for epoxy/hardener system Araldite® LY 1564 / Aradur® 22962[10]. For other manufacturing variables, such as the number of plies and appropriate compression pressure, decisions were made based on (i) previous practice documented in existing publications on composites made from the same FlaxPly® fabric [103; 107], (ii) published research by Gning et al. [176] of the influence of ply number and compression pressure on Flax-epoxy properties, and (iii) repeated trial-and-error manufacturing in order to obtain ∼50% fibre content with minimal porosity, and a minimum plate thickness of 3–4 mm for convenience of mechanical testing (e.g. to prevent crushing at the grips; to resist buckling due to accidental compressive forces during cyclic tests, etc.).

Gning et al. [176] found that Flax-epoxy specimen properties are correlated with the number of plies, manufacturing compression pressure, and ambient temperature during testing. However, these factors appear to have differing degrees of influence depending on the stacking sequence orientation. In general, increasing the number of plies from 2 to 10 tends to produce higher modulus values at room temperature – though this appears less true for $[0/90]_{\mathrm{nS}}$ longitudinal modulus than for shear modulus from $[\pm 45]_{\mathrm{nS}}$ specimens, as can be deduced from Figure 4.6. Furthermore, Gning et al. [176] also showed that increasing the compression pressure generally results in higher fibre fractions, but thinner plates, for Flax-epoxy crossply laminates, as shown in Figure 4.7. Increasing the number of plies at the same pressure boosts the fibre fraction (Figure 4.7(a)), and total laminate thickness (Figure 4.7(b)). From Figure 4.7, the highest fibre volume fraction $v_f \simeq 0.45$ is found for the 10-ply laminate manufactured at 6.7 bars pressure (0.67 MPa), and the same combination of plies and pressure produces the thickest plate at ∼3.6 mm.

Considering that higher pressure and ply-count increases fibre content, Figure 4.7(a) suggests that attaining v_f=0.5 will require more than 10 plies, but the appropriate pressure range cannot be conclusively determined from this study by Gning et al. [176] alone – so a trial-and-error manufacturing study was conducted to determine an acceptable combination of manufacturing pressure (3–6 bars) and number of plies (>10) that will produce the desired v_f=0.5, given the manufacturing setup in the laboratory.

Since it was pre-determined in the research objectives that a quasi-isotropic layup $[0/+45/90/-45]_{\mathrm{nS}}$ would be one of the many Flax-epoxy laminates considered for this study, the total number of plies in such a symmetric laminate would have to be in multiples of 8. Thus, a 16-layer configuration was chosen, since 16 is the next multiple of 8 that is >10. 16 layers was also preferred in some previous Flax-epoxy studies that used the same FlaxPly® fabric [103; 107]. Repeated trials of fabricating 16-ply UD Flax-epoxy laminates revealed that a pressure of 5 bars (0.5 MPa) resulted in $v_f \simeq 0.5$, porosity $v_p \simeq 3.3$ (see Table 4.1 later), with a plate thickness ∼4 mm.

[10] The datasheet for this epoxy/hardener combination is public-access, and easily searchable online.

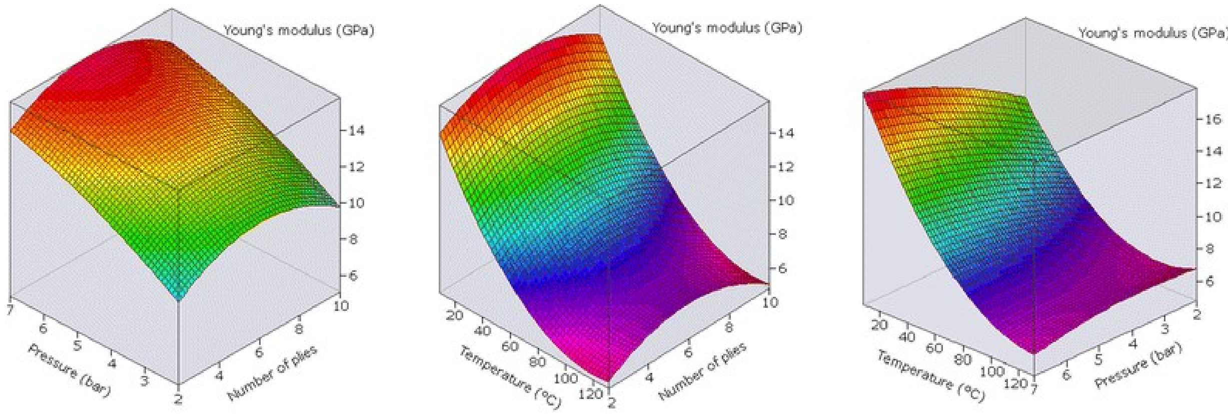

(a)

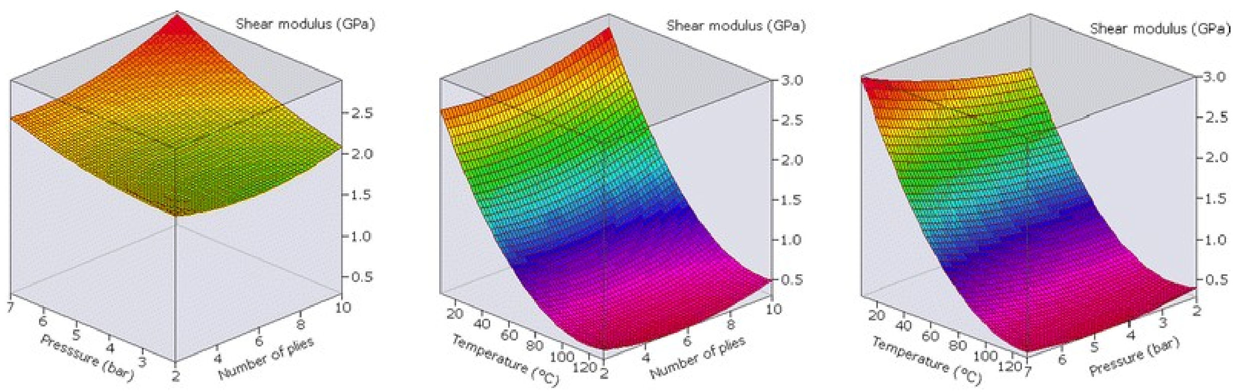

(b)

Figure 4.6: Surface plots showing influence of manufacturing compression pressure, number of plies, and ambient temperature during testing on (a) modulus of $[0/90]_{nS}$, and (b) shear modulus derived from $[\pm 45]_{nS}$ tensile tests. Reproduced with permission from [176].

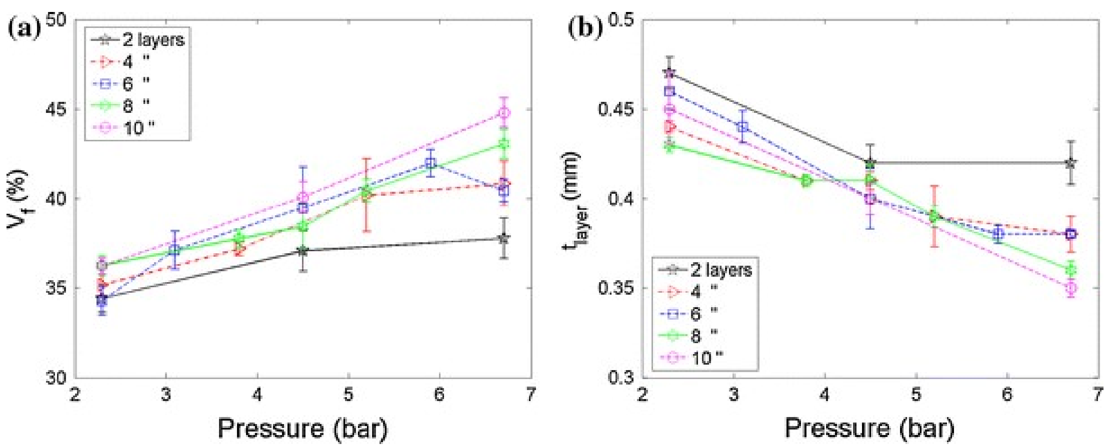

Figure 4.7: Reported effect of manufacturing compression pressure on (a) fibre volume fraction and (b) thickness per ply (not laminate), with increasing number of plies, for Flax-epoxy crossply laminates. Reproduced with permission from [176].

4.3.1 Composite laminate

All laminates tested in this study (Flax- and Glass-composites) are of symmetric stacking sequence. As noted earlier, the overall manufacturing technique is a hand-layup followed by heated-platen compression moulding procedure. The Flax and Glass UD fabrics were stored at room temperature, and not subjected any particular treatment process pre-manufacture. The fabrication steps are as follows:

- A flat-plate 'mould' is prepared using 15×15×0.125" Aluminium plates lined along the edges with 6-mm thick low-tack silicone, as shown in Figure 4.8. As such, the top and bottom of this 'mould' are flat and rigid, and the relatively deformable silicone edges allow excess resin to escape during compression.
- Regular square-shape sheets are cut out from the fabric roll, typically 12×12". Since Flax fibres are structurally heterogenous and liable to contain more defects than the regular cross-section Glass fibres, more layers of Flax (16 plies) are used in Flax-epoxy plates than in Glass-epoxy (12 plies), so as to minimise the effect of fibre defects and encourage a consistent bulk response from Flax-epoxy under mechanical testing.

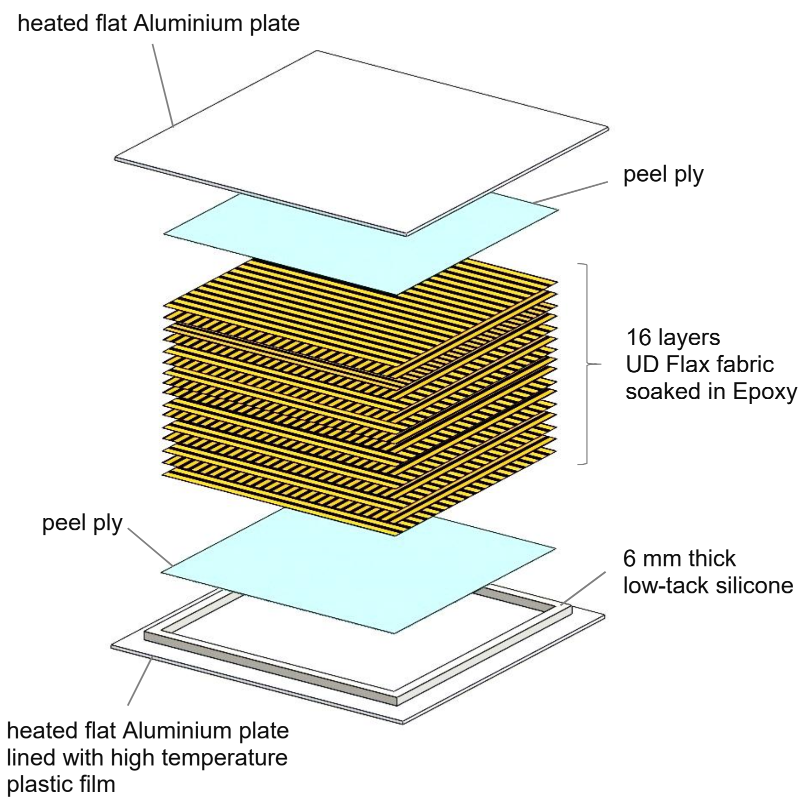

Figure 4.8: Setup for composite plate manufacture. Flax-epoxy $[0/90]_{4S}$ shown as example.

- The epoxy/hardener LY1564/22962 combination is prepared at ratio 4:1 by weight, following supplier specifications.
- Heat-resistant peel plies are placed on either side of the fabric stack.

- The fabric sheets are placed in the mould at the desired orientation stacking sequence, and resin is poured onto the fabric layer by layer until completely soaked. Since the resin is viscous, a uniform impregnation of the fibres is ensured by frequently spreading the thick resin over the fabric using a fine brush and roller.
- The mould is placed in a hot compression apparatus (Carver Inc., Wabash, IN, USA), shown in Figure 4.9. The temperature and pressure sequence is programmed.

Figure 4.9: Self-containing press with heating/cooling platens for compression per ASTM D1928; Carver Inc. Auto-Series, Wabash, IN, USA.

- The applied curing temperature cycles follows supplier specifications for the epoxy system: 15 mins at 120℃, followed by 2 hours at 150℃ – which results in a glass transition temperature (T_g) of 130-140℃ (per supplier datasheet, Huntsman Advanced Materials, The Woodlands, TX, USA).
- The compression pressure is held at 2.5 bar (0.25 MPa) until end of the 120℃ stage, followed by 5 bar (0.5 MPa). As discussed earlier, these pressures were determined after repeated laboratory trials indicated that, when using low-tack silicone edge-liners (6 mm total thickness), applying a 5 bar holding pressure produced Flax-epoxy plates of around 50-50 fibre-matrix ratio with a low void content (see Table 4.1).
- The same temperature and pressure parameters are adopted to fabricate Glass-epoxy plates.

- Heating is suspended after the 2-hour 150°C stage, but pressure is held at 5 bar as the platens/mould are air-cooled down to room temperature. Pressure is released once temperature reaches 30°C. The plate is not subjected to further post-curing heat treatment.

The resulting plate thickness is around 4 mm for Flax-epoxy, and 3.5 mm for Glass-epoxy. Observations from SEM micrographs indicate very good contact between fibre and matrix (see Figure 4.3); however interfacial strength is not empirically evaluated.

4.3.2 Neat epoxy

Dogbone specimens of pure matrix material were manufactured by pouring the epoxy resin into open-faced moulds, and curing them per the same supplier specification described above for composite manufacture.

4.4 Optical method for constituent fraction measurement

Conventional standardised techniques of volume fraction evaluation for engineering fibre composites, e.g. as specified by ASTM D3171 [179], are completely unsuitable for natural fibre composites. As these techniques involve matrix digestion in acids (e.g. hydrochloric acid or sulphuric acid/hydrogen peroxide) or matrix burnoff in a furnace, application of these methods will severely degrade the natural fibres, making a reliable measurement of fibre weight impossible. An alternative optical method is adopted – similar to that used by Phillips et al. [180] and El Sawi et al. [107] to estimate the constituent fractions – whereby microscopic images of specimen cross-sections are examined using open-source image-analysis software *ImageJ* (Image Processing and Analysis in Java, developed by National Institutes of Health, USA). Provided sufficient contrast is obtained such that the fibre, matrix, and void or crack regions are distinctly identifiable, an image can be analysed to calculate area fractions of any region of interest (see Figure 4.10).

Specimen cross-sections are prepared for microscopy by grinding and polishing, with the final two polishing stages conducted using 1 micron and 0.05 micron abrasive powders. Laboratory trials indicated that images from electron microscopy are better suited for this method of constituent fraction measurement, compared to those from optical microscopy where image clarity tends to be more sensitive to superficial flaws and traces from grinding-polishing. Samples from 5 random locations on each manufactured composite plate are imaged. An average of area fraction measurements from at least 50 images is considered to be an indicator of the volume fraction.

Table 4.1 lists the average fibre and void content of UD and cross-ply plates manufactured for this study. Flax-epoxy (FE) plates manufactured per specifications described in the previous section result in fibre content of $\sim$50% and $\sim$3.4% porosity; while Glass-epoxy (GE) plates have $\sim$60% fibre and $\sim$1% porosity by volume. Density of the constituent materials and resulting composites were measured using the buoyancy method.

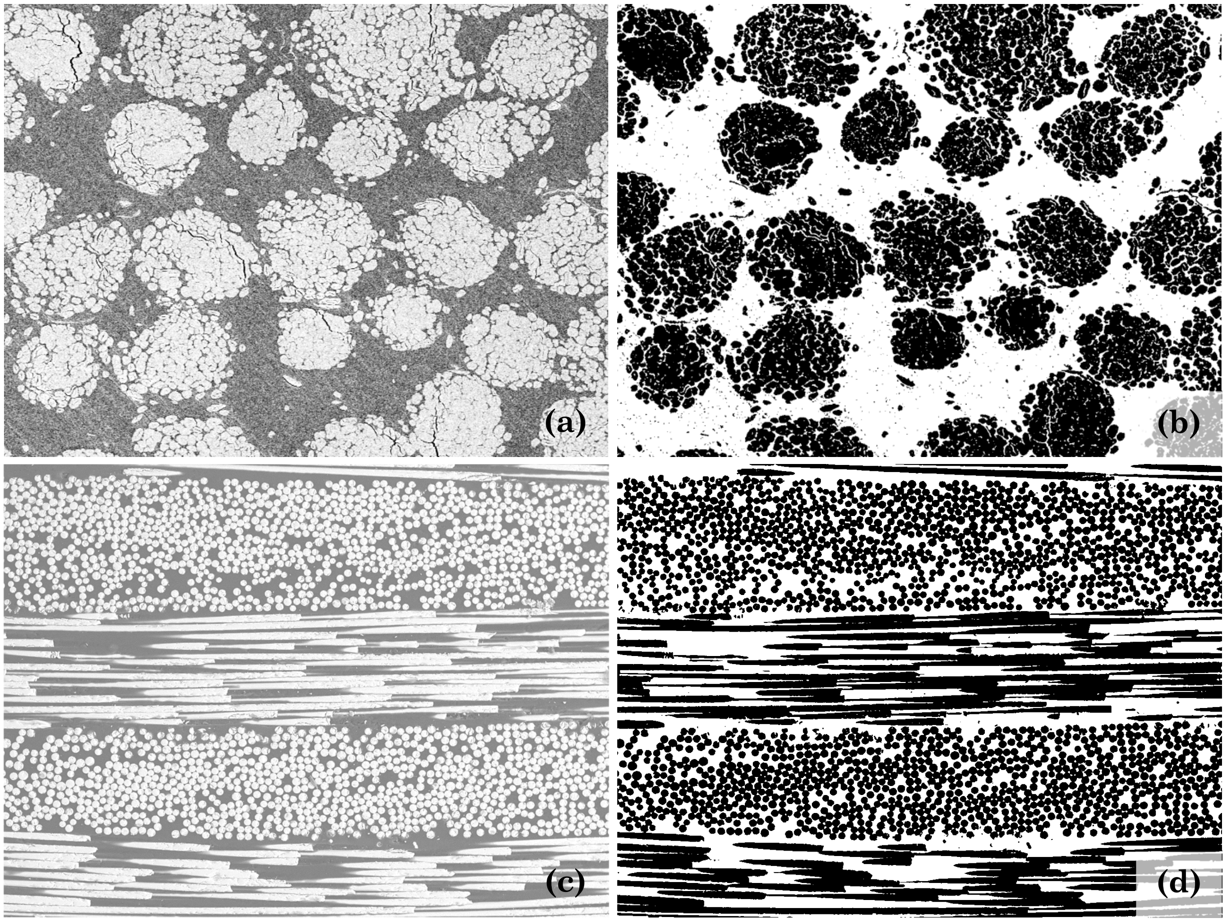

Figure 4.10: Example ×100 SEM images of FE [0] (*top*) and GE [0/90] (*bottom*) cross-sections; showing 8-bit greyscale image (*left*), and the same image 'binarised' into black and white (*right*). Area fraction of black region (fibre) is computed to be 49.82% in (b), and 54.73% in (d).

Table 4.1: Measured densities and fractions of constituent materials, Flax-epoxy (FE) and Glass-epoxy (GE) composites

	Flax fibre	Glass fibre	Epoxy neat	FE UD [0], [90], [45]	FE Crossply [0/90], [±45]	GE Crossply [0/90], [±45]
Density ρ (g/cm^3)	1.47 ±0.24	2.537 ±0.060	1.15 ±0.04	1.256 ±0.020		1.840 ±0.041
Fibre volume fraction v_f (%)	–	–	–	50.97 ±3.92	49.79 ±2.33	49.58 ±3.57
Porosity v_p (%)	–	–	–	3.35 ±2.62	3.31 ±3.01	0.12 ±0.04

4.4.1 Validation using classical relations

From Berthelot [92], an ideal composite with *no porosity* has a density given by the classical relation:

$$\rho_{cc} = \rho_f v_f + \rho_m(1 - v_f) \tag{4.1}$$

where ρ_{cc} is density of the ideal composite, ρ_f and ρ_m are densities of the fibre and matrix, respectively, and v_f is the fibre volume fraction. This calculated density may differ from that measured experimentally due to the presence of voids, so the void content may be estimated from [92]:

$$v_p = \frac{\rho_{cc} - \rho_{cx}}{\rho_{cc}} \tag{4.2}$$

where ρ_{cc} is the calculated ideal-composite density from (4.1), and ρ_{cx} is the experimentally measured density of the manufactured composite.

Using the laboratory-measured data (Table 4.1), the experimental values of density and porosity can be compared with those calculated by (4.1) and (4.2), shown in Table 4.2.

Table 4.2: Comparing optically measured and calculated porosities

	ρ_{cx} experimental (g/cm^3)	ρ_{cc} from (4.1) (g/cm^3)	v_p from optical method (%)	v_p from (4.2) (%)
Flax-epoxy	1.26 ±0.02	1.31	3.33 ±2.82	4.20
Glass-epoxy	1.84 ±0.04	1.85	0.12 ±0.04	0.17

As can be seen from Table 4.2, the porosities measured using the optical method compare well with those estimated from classical relation (4.2), thus suggesting that the optical method of measuring volume fraction is a reliable alternative.

4.5 Specimen preparation

All composite specimens were cut from the manufactured plates using a fine-cutting 0.35 mm diamond-edged saw, followed by grinding to produce a flat edge finish. As noted earlier, the heated compression manufacturing process results in plates that are 4 mm thick. As will be seen in the following chapters, specimens are prepared to test:

a) Flax-epoxy (FE) tensile quasi-static
b) FE compressive quasi-static
c) FE tensile fatigue
d) Neat epoxy tensile quasi-static
e) Neat epoxy compressive quasi-static
f) Glass-epoxy (GE) tensile quasi-static
g) GE tensile fatigue

Static tension, FE and GE For tensile quasi-static tests on FE and GE specimens, rectangular 250×25 mm specimens were prepared from the manufactured plates (∼3.5-4 mm thick) within the guidelines of ASTM D3039 [181]. The composite specimens were tabbed with 64 mm long tapered Aluminium tabs, as shown in Figure 4.11(*top*).

Static tension, Neat epoxy Epoxy tension specimens were manufactured in open-faced moulds of dogbone shape dimensions described in ASTM D638 [182] for plastic tensile testing.

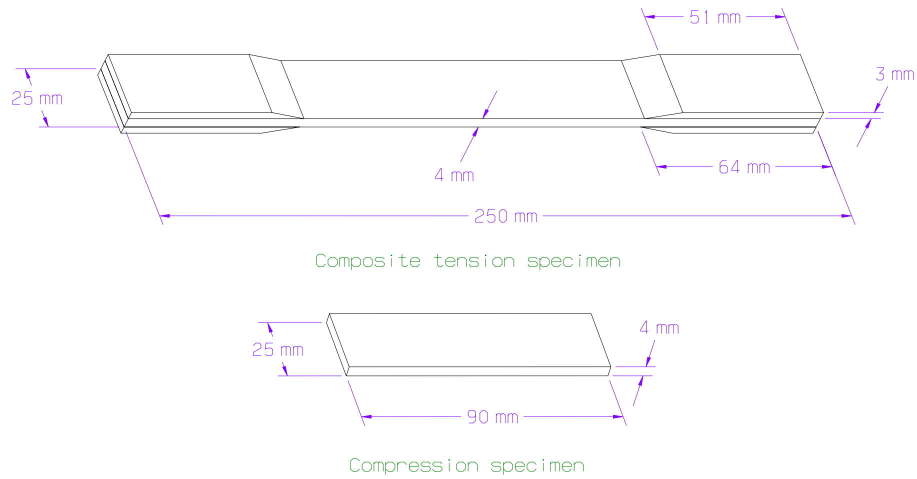

Figure 4.11: Specimen geometry for monotonic/quasi-static testing; *top:* FE and GE tension, *bottom:* all compression specimens

Static compression, FE and neat epoxy For all compression tests, shorter rectangular 90×25 mm composite specimens were used with no tabs, shown in Figure 4.11(*bottom*), where the un-gripped gauge length was about 18 mm.

Fatigue tension, FE and GE The fatigue specimen dimensions are identical to those of static specimens, however the tabs used are not tapered or made of Aluminium, but rectangular 64×25×3 mm (l×w×t) tabs of Flax-epoxy material instead. Laboratory trials indicated that specimens fitted with tapered aluminium tabs often fractured near the grips during fatigue testing, while those with Flax-epoxy tabs (quasi-isotropic layup) always fractured in the middle gauge section.

4.6 Mechanical testing

Tensile and compressive mechanical tests were conducted in a servo-hydraulic MTS 322 (Eden Prairie, MN, USA) test frame at room temperature and pressure laboratory conditions. Humidity was not monitored. *Static tests* are conducted at a displacement rate of 2 mm/min. For most tensile tests, longitudinal strain is measured using a uniaxial extensometer of gauge length 0.5 in (12.7 mm), transverse strain is measured using 350Ω strain gauges (Figure 4.12(a)). For all compression specimens and $[\pm 45]_{4S}$ tensile specimens strain is measured using a Digital Image Correlation (DIC) setup, explained in further detail shortly. *Fatigue tests* are conducted using the same test frame. Tensile-tensile fatigue tests at constant strain amplitude were run at a commanded frequency of 5 Hz and strain ratio $R_\epsilon = \frac{\epsilon_{\min}}{\epsilon_{\max}} = 0.1$. For fatigue tests, typically only longitudinal strain is measured, using the same extensometer as for quasi-static tests. The testing procedure for each study compiled here (e.g. cycled progressive loading quasi-static tests, fatigue testing sequence, etc) are discussed in further detail in their respective chapters.

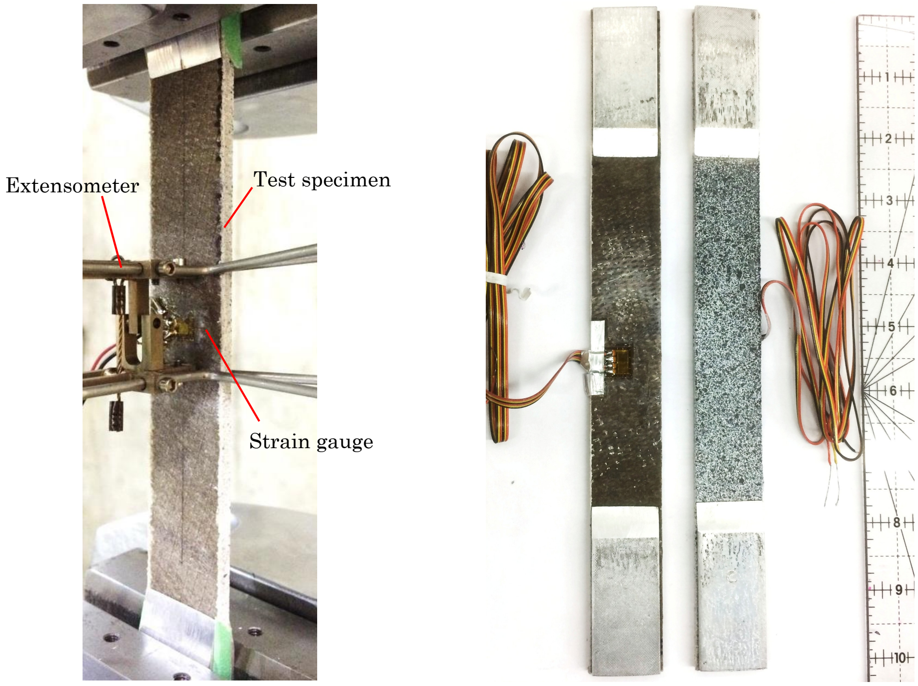

(a) (b)

Figure 4.12: Tensile specimens showing: (a) extensometer for longitudinal strain measurement, and strain gauge for transverse; and (b) speckled pattern for DIC on one side, and strain gauges on the other.

4.6.1 Digital Image Correlation (DIC)

As noted earlier, strain measurements for compression and $[\pm 45]_{4S}$ specimens were taken using a Digital Image Correlation (DIC) setup supplied by Correlated Solutions (Irmo, SC, USA). Speckle patterns are spray-painted on the test specimen (Figure 4.12(b)), which are imaged during the tests at 20-50 frames per second, i.e. one image every 0.02-0.05 s (shorter-duration tests, such as compressive tests, are imaged at the more frequent rate).

Since the DIC method enables capturing complete images of the speckled specimen surface, full-field strain may be derived by 'correlating' successive images and measuring change in the displacement of the speckle pattern. This correlation and measurement is performed using the commercial software VIC-2D™ [183]. Applying DIC methods is advantageous for compression and angled crossply specimens since:

(i) direct, full-field measurement of principal strains and shear strain is possible from the same set of images, and
(ii) very large strains can be conveniently measured, uninhibited by the physical limitations of traditional strain transducers.

To confirm reliable strain measurement, careful calibration and validation of the DIC-based setup was conducted by comparing results from both DIC and a strain transducer (extensometer or strain gauge) from the same specimen tests (see Figure 4.12(b)), with excellent correlation observed (R^2 between 0.9859-0.9998).

Chapter 5

Quasi-static response of Flax-epoxy composites

This chapter conducts quasi-static (monotonic and low-cycle progressive loading) tests to evaluate, characterise, and discuss the in-plane mechanical properties and related evolution of stiffness, permanent strain, and physically observable damage in Flax-epoxy composites, under tensile and compressive loading. The literature survey and studies described in this chapter are published in part in the following peer-reviewed article [178]:

Z. Mahboob, I. El Sawi, R. Zdero, Z. Fawaz, and H. Bougherara. Tensile and compressive damaged response in Flax fibre reinforced epoxy composites, *Composites Part A: Applied Science and Manufacturing* 92 (2017) 118-133. doi: 10.1016/j.compositesa.2016.11.007.

5.1 Introduction

Flax fibre is understood to be one the strongest natural fibre candidates in the pursuit of replacing synthetic fibres like Glass, for reasons discussed in the introductory Chapter 1. As such, compared to other natural fibres like jute, hemp, kenaf, sisal, bamboo, etc., Flax-composites have been a popular focus of interest over the last decade [7; 46; 48]. Despite this, some obvious gaps can yet be identified in the publicly-available data on Flax-composites that would limit an aspiring engineering designer:

1. Not considering woven-fabric-reinforced composites, the overwhelming majority of published research reports only fibre-direction tensile properties for composites (Table 5.1) which is insufficient to attempt design of Flax reinforced components. Data on off-axis, transverse, shear, and compressive response, as well as Poisson's ratios (all of which may be extrapolated to predict behaviour of woven Flax-composites) are limited. A first goal of this static response study is to provide data on these in-plane material properties from quasi-static tensile and compressive testing of relevant specimens ($[0]_{16}$, $[90]_{16}$, $[\pm 45]_{4S}$), and offer supplementary data on some common laminate layups ($[45]_{16}$, $[0/90]_{4S}$, $[0/+45/90/-45]_{2S}$).

2. Reliable engineering design depends on the prediction of damage initiation, damage progression, and the development of failure conditions. Available sources either describe damage evolution in only Flax fibres [21; 24; 55], or if the focus is on Flax-composites, tend to examine only fibre-direction and tensile damage (observation or quantification of microcracking [50; 103; 184], acoustic emissions [90; 185], plasticity evolution [186], tangent modulus evolution [175; 185]). The static response study in this chapter will identify damage mechanisms by micrography, and measure damage effects in all principal in-plane directions (fibre-direction, transverse, and shear) of an orthotropic Flax-composite, under both tensile and compressive loading, by measuring the material stiffness degradation and accumulation of inelastic strain (permanent deformation).

5.1.1 Flax-epoxy composite behaviour

In developing feasible Flax-composites, a better understanding of Flax fibre mechanical properties and damaging mechanisms has been the essential first step – these topics were covered in some depth earlier in Chapter 2. Flax fibre mechanical properties from all sources accessible to the authors were listed earlier in Tables 2.1–2.3. Flax fibre structure has been shown to directly influence the derived composite behaviour and damage mechanisms [48]. There has been a growing body of research on Flax-composites since the 2000s, including UD and woven fibre configurations, using a variety of different matrix material, for specimens of varying fibre volume fractions. To serve as a means of comparison in this study, a summary of UD Flax continuous-fibre reinforced epoxy composite mechanical properties is given in Tables 5.1–5.4.

Charlet et al. [54] studied the tensile response of Flax-monofilament reinforced epoxy composites, and found that for increasing fibre volume fraction, the modulus and strength increase proportionally; while the failure strain remains almost constant beyond a 0.15 fibre volume fraction. The same influence of fibre volume fraction on modulus and strength is also reported by Romhány et al. [95] for UD and crossply Flax-starch laminates. Further study by Charlet et al. [48] tested both individual Flax fibres and polyester-composites reinforced by the same batch of Flax. The study showed that the variable modulus characteristic of Flax fibres also carries over to the composites derived from them, in that the composites exhibit similar changes in stiffness at nearly the same loading or strain levels. The study also found that the generally high tensile properties of Flax fibres do not translate into similarly high composite properties. The authors concluded that not all fibres in the Flax-composite are able to contribute towards reinforcement, hypothesising the following causes: (i) thermal damage to fibres during composite manufacturing, or (ii) slippage between individual fibres upon tensile loading [48].

Shah et al. [186] showed that classical laminate theory and failure criteria can be applied to closely predict tensile modulus, strength, and failure strain for a UD Flax-polyester composite of any fibre orientation (0° to 90°). The authors also showed that fibre-direction permanent strains may not develop before a loading strain of 0.146%. A similar Flax-polyester composite was examined by Shah [175] to follow the evolution of tangent modulus in fibre-direction as a measure of damage progress, where tangent modulus was defined as the stress-strain plot slope at a given fibre-direction strain loading. Repeated load-unload-reload tests at increasing peak loads revealed a strain hardening behaviour, which the author detected as an alternating loss and recovery of tangent modulus between successive load and reload stages.

Table 5.1: Reported fibre-direction (*11*) properties of continuous Flax fibre reinforced epoxy composites

Study	Year	Fibre volume fraction v_f	Tension: Modulus E_{11} (GPa)	Tension: Strength σ_{11}^{tu} (MPa)	Tension: Fail strain ε_{11}^{tu} (%)	Tension: Major Poisson's ratio ν_{12}	Compression: Modulus E_{11}^{c} (GPa)	Compression: Strength σ_{11}^{cu} (MPa)	Compression: Fail strain ε_{11}^{cu} (%)
[170]	2001	0.21	22 ±4	193 ±30	0.9	–	–	–	–
		0.32	15 ±0.6	132 ±4.5	1.2	–	–	–	–
		0.42	35 ±3	280 ±15	0.9	–	–	–	–
		0.47	39 ±6	279 ±15	0.8	–	–	–	–
[27]	2002	0.4	24.6 ±0.5	–	–	–	–	–	–
[53]	2004	0.25	23.3 ±3.3	249 ±25	–	–	–	–	–
		0.25 (dewaxed)	18.5 ±1	242 ±28	–	–	–	–	–
		0.438	–	–	–	–	30	119 ±2	–
		0.438 (dewaxed)	–	–	–	–	30	137 ±13	–
[171]	2006	0.4	26 ±1	190 ±10	–	–	–	–	–
		0.48	32 ±1	268 ±26	–	–	–	–	–
[32]	2011	0.4	∼35	380	1.8	–	–	–	–
[76]	2013	0.22	13 ±0.3	208 ±21	1.2 ±0.2	–	–	–	–
		0.23	11 ±1.9	165 ±11	1.1 ±0.08	–	–	–	–
		0.36	20 ±3	207 ±8	1.2 ±0.09	–	–	–	–
		0.36	24 ±1.8	271 ±32	1.3 ±0.01	–	–	–	–
		0.42	22 ±0.6	362 ±19	1.3 ±0.13	–	–	–	–
		0.48	31 ±1.5	348 ±28	1.2 ±0.1	–	–	–	–
		0.51	26 ±2	408 ±36	1.3 ±0.05	–	–	–	–
		0.51	28 ±3.6	290 ±22	1.1 ±0.15	–	–	–	–
		0.54	34 ±3	364 ±14	1.3 ±0.09	–	–	–	–
[107]	2014	0.48	25	307	1.2-1.6	–	–	–	–
[103]	2014	0.48	∼33.3	304	1.6	–	–	–	–
[185]	2015	0.47 ±0.02	27.2 ±0.52	296 ±0.5	1.65 ±0.055	–	–	–	–
[22]	2015	0.439 ±1.5	24.7 ±0.6	318 ±12	1.65 ±0.05	0.434 ±0.084	–	136 ±2	2.41 ±0.27
[110]	2016	∼0.4 (prepreg)	23.7 ±1.13	259 ±31	1.22 ±0.07	–	–	–	–
		0.44 (not prepreg)	26.6 ±2.3	249 ±9	1.16 ±0.1	–	–	–	–
[187]	2016	0.461	31.6 ±0.96	311 ±13.9	1.50 ±0.12	0.36 ±0.02	–	–	–
		0.456	30.0 ±1.3	319 ±20	1.59 ±0.14	0.34 ±0.02	–	–	–
		0.450	27.7 ±0.3	327 ±9.8	1.45 ±0.15	0.36 ±0.02	–	–	–

Kersani et al. [185] found that, for Flax-epoxy layups wherein tensile response is fibre-dominant, the non-linearity in the tensile stress-strain plot (corresponding to decrease in tangent modulus) roughly coincides with the onset of acoustic activity >40 dB (signals below this were filtered out as noise). Note that this filter cut-off level eliminates acoustic emissions due to splitting of elementary fibres, which typically register <35 dB (as shown by Romhány et al. [55], discussed earlier in Chapter 2). Noticing that the

Table 5.2: Reported in-plane transverse (*22*) properties of continuous Flax fibre reinforced epoxy composites

			Tension				Compression		
Study	Year	Fibre volume fraction v_f	Modulus E_{22} (GPa)	Strength σ_{22}^{tu} (MPa)	Fail strain ε_{22}^{tu} (%)	Minor Poisson's ratio ν_{21}	Modulus E_{22}^{c} (GPa)	Strength σ_{22}^{cu} (MPa)	Fail strain ε_{22}^{cu} (%)
[171]	2006	0.4	0.2-0.6	4-12	–	–	–	–	–
		0.48	3.7-4.3	17-19	–	–	–	–	–
[22]	2015	0.439 ±1.5	5.93 ±0.27	26.1 ±0.6	0.622 ±0.036	0.084 ±0.0.011	–	100 ±4	3.27 ±0.12
[187]	2016	0.461	4.71 ±0.33	31.2 ±0.84	0.96 ±0.08	0.07 ±0.01	–	–	–
		0.456	4.69 ±0.74	30.0 ±1.3	0.99 ±0.16	–	–	–	–
		0.450	4.80 ±0.25	27.7 ±0.3	1.00 ±0.15	0.06 ±0.006	–	–	–

Table 5.3: Reported in-plane shear (*12*) properties of continuous Flax fibre reinforced epoxy composites

Study	Year	Fibre volume fraction v_f	Modulus G_{12} (GPa)	Strength τ_{12}^{u} (MPa)	Fail strain γ_{12}^{u} (%)
[176]	2011	0.372 ±0.4	2.10 ±0.09	37.9 ±1.5	3.8 ±0.9
		0.377 ±0.5	2.07 ±0.06	45.6 ±1.9	4.7 ±0.1
		0.420 ±0.8	2.34 ±0.17	43.4 ±1.3	4.0 ±0.8
[22]	2015	0.431 ±0.6	1.96 ±0.17	39.7 ±3.3	6.23 ±1.08

count of acoustic events was proportional to the number of fibres along the loading axis (0°), the authors hypothesise that most of the detected damage activity after 0.5% loading strain is somehow fibre-related – which subsequent optical microscopy suggest to be due to fibre-matrix interface cracking. The authors report that matrix cracks do not make an appearance until just before failure.

Panamoottil et al. [184] measured the density of identifiable in-plane cracks (crack length per imaged area, mm/mm^2) from optical micrographs of a Flax-polypropylene composite in tension, and developed a continuum damage model where damage variables are a function of normalised crack densities. The micrographs were taken only between 70-100% tensile failure load, at 5% intervals (corresponds to 1% strain until failure at 1.55%), and seemed to indicate that cracking initiates within Flax bundles or at the Flax-polypropylene interface. Matrix cracks were not evidenced, and were thought to either be non-existent or simply difficult to detect.

In addition to offering alternative strategies of quantifying damaged response that can confirm or contrast findings in existing reports on fibre-direction tensile behaviour discussed above, this static response study will extend the examination of Flax-composite damage into in-plane transverse, shear, and compressive response.

Table 5.4: Reported mechanical properties of select symmetric Flax-epoxy laminates

Laminate	Study	Year	Fibre volume fraction v_f	Modulus E (GPa)	Strength σ^{tu} (MPa)	Fail strain ϵ^{tu} (%)	Poisson's ratio ν_{LT}
$[0/90]_{nS}$	[176]	2011	0.372 ±0.4	12.74 ±0.91	130.0 ±5.4	1.3 ±0.1	0.12 ±0.04
			0.377 ±0.5	12.98 ±1.31	148.1 ±19.3	1.44 ±0.23	0.108 ±0.020
			0.420 ±0.8	15.61 ±0.38	150.0 ±10.7	1.3 ±0.1	0.13 ±0.02
	[50]	2014	0.437	14.3 ±0.8	170.0 ±19.6	1.72 ±0.30	0.17 ±0.05
	[185]	2015	0.47 ±0.02	15.7 ±0.15	158 ±2	1.62 ±0.5	0.126 ±0.014
	[110]	2016	∼0.4 (prepreg)	12.75 ±0.9	149 ±14	1.58 ±0.06	–
			0.39 (not prepreg)	14.5 ±0.8	126 ±7	1.08 ±1.6	–
			0.38 (plain weave)	12.6 ±0.4	135 ±18	1.69 ±0.32	–
$[\pm 45]_{nS}$	[103]	2014	0.48	6-7	64-69	4.6-8.4	–
	[50]	2014	0.437	6.5 ±0.7	79.0 ±6.6	3.8 ±0.6	0.75 ±0.04
	[185]	2015	0.47 ±0.02	5.7 ±0.11	85 ±4	7.47 ±0.415	0.566 ±0.064
Quasi-isotropic $[0/90/\mp 45]_S$	[185]	2015	0.47 ±0.02	11.9 ±0.6	126 ±7.5	1.76 ±0.15	0.319 ±0.259
$[0_2/90_2/\pm 45]_S$ [a]	[112]	2016	0.4-0.43 [b]	19.64 ±0.76	145.55 ±7.21	0.98 ±0.04	–

[a] not a true quasi-isotropic laminate, since twice as many 0° and 90° plies as there are +45° and −45°
[b] estimated from reported vendor data: Flax areal density 100 g/m^2 and epoxy weight fraction 50%

5.2 Manufacturing and methods

5.2.1 Materials and manufacturing

The details of manufacturing composite plates for this study were elaborated earlier in Chapter 4. The epoxy matrix material and reinforcing UD Flax fabric used are described in Sections 4.2.1–4.2.2. The Flax-epoxy composite plates were fabricated as described in Section 4.3. Composite and neat epoxy specimens were prepared as described in Section 4.5.

5.2.2 Mechanical testing

Tensile and compressive tests are conducted on epoxy specimens, $[0]_{16}$, $[90]_{16}$, $[45]_{16}$, $[0/90]_{4S}$, $[\pm 45]_{4S}$, and $[0/+45/90/-45]_{2S}$ laminate specimens. All tests were conducted under room temperature conditions in a servo-hydraulic MTS 322 (Eden Prairie, MN, USA) test frame at a displacement rate of 2 mm/min. Fibre direction (*11*) properties are derived from tests on $[0]_{16}$ and $[0/90]_{4S}$ specimens. In-plane transverse (*22*) properties are derived from tests on $[90]_{16}$ specimens. Shear (*12*) properties are derived from tests on $[\pm 45]_{4S}$ tension specimens, per ASTM D3518 [188] (except that the large strains are not truncated at 5%). For all the above, at least 3 specimens of each laminate are tested in tension and compression.

5.2.2.1 Strain measurement & Digital Image Correlation

For all tension specimens except $[\pm 45]_{4S}$, the longitudinal and transverse strains were measured using a uniaxial extensometer (gauge length 0.5 in) and 350Ω strain gauge, respectively. For compression and

$[\pm 45]_{4S}$ specimens, strain measurements were taken using a Digital Image Correlation (DIC) setup supplied by Correlated Solutions (Irmo, SC, USA). A speckle pattern on the test specimen is imaged at regular intervals throughout the test duration, and a commercially-available image correlation software VIC-2D™ [183] is used to calculate strains based on deformation of the speckle pattern. Applying DIC methods is advantageous for compression and angled crossply specimens since:

(i) direct, full-field measurement of principal strains and shear strain is possible from the same set of images, and
(ii) very large strains can be conveniently measured, uninhibited by the physical limitations of traditional strain transducers.

As noted earlier in Section 4.6.1 To confirm reliable strain measurement, careful calibration and validation of the DIC-based setup was conducted by comparing results from both DIC and a strain transducer (extensometer or strain gauge) from the same specimen tests (see Figure 4.11), with excellent correlation observed (R^2 between 0.9859-0.9998).

5.2.2.2 Load-unload tests

Damage and stiffness degradation. To measure evolving damage and its effects, test specimens are subjected to a repeated quasi-static 'load-unload' sequence at progressively increasing maximum loads until failure (see Figure 5.1). As discussed earlier in Section 3.2, damage is understood to be the density of physical discontinuities in a material, which results in the degradation of stiffness properties. Damage can thus be defined as a function of elastic modulus based on the principle of *strain equivalence* [160], given by the following relation:

$$D = 1 - \frac{E}{E_0} \tag{5.1}$$

where E_0 is the undamaged initial modulus, and E is the modulus at a future damaged state.

Figure 5.1(a) shows how a typical load-unload response plot may be utilised to determine stiffness damage per relation (5.1). Note that E is not a tangent modulus, but the damaged-condition modulus of the material after loading. The Flax-epoxy specimens studied here generally exhibit some hysteresis as they are fully unloaded (Figure 5.1(b)); however, for the purposes of measuring damaged modulus, the load-unload cycle can be approximated as linear elastic (dashed line in Figure 5.1(a)).

Inelasticity. Another obvious symptom of internal structural damage is the apparent plasticity in the response of a composite material. This permanent deformation in the composite may be caused by several irreversible mechanisms: (i) inherent plasticity of the matrix polymer, (ii) structural re-organisation within Flax fibre bundles, (iii) cracks in the matrix and fibre phases, or (iv) fibre-matrix debonding. In addition to observing stiffness evolution, load-unload tests also expose an accumulation of permanent strain (ε^p, measured at the intersection point of the hysteretic loop slope and horizontal strain axis, as shown in Figure 5.1(a)). Thus, recording stiffness degradation and permanent strain accumulation allows for a complete description of the damaged-condition response of the composite material.

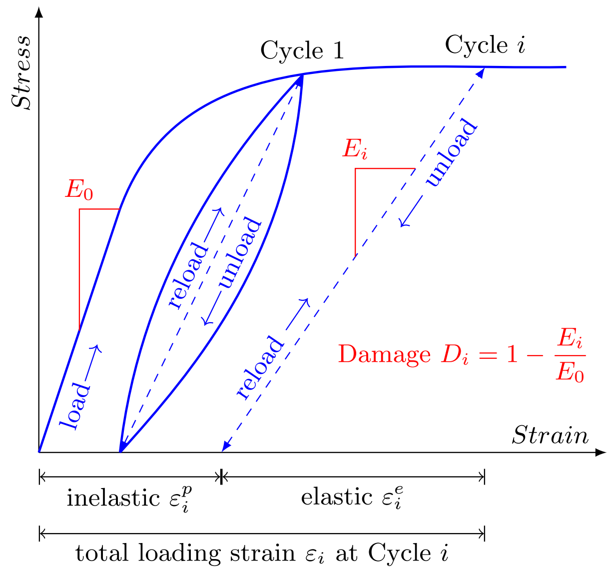

(a)

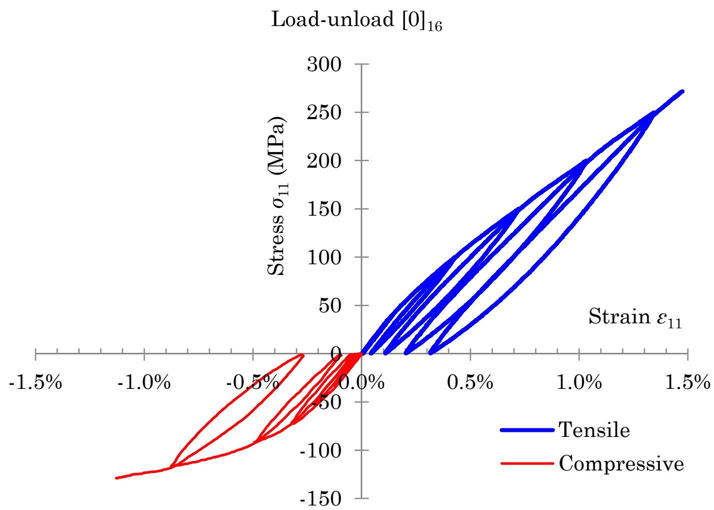

(b)

Figure 5.1: (a) Load-unload hysteretic response diagram showing damage D calculation; elastic and inelastic portions of strain (ε^e and ε^p, respectively); (b) Typical load-unload plot for [0] laminate longitudinal response showing hysteresis

5.3 Results and Discussion

5.3.1 Mechanical response

The tested mechanical properties of neat epoxy and Flax-epoxy laminates are listed in Table 5.5.

The tested in-plane orthotropic mechanical properties of a Flax-epoxy UD ply are given in Table 5.6. The mechanical response from tension and compression tests are plotted in Figures 5.2, 5.4 and 5.5, omitting the unload-reload segments to preserve clarity. For the same reason, response plots of only two

Table 5.5: Tested mechanical properties of neat epoxy and Flax-epoxy laminates

	Tension				Compression			
	Modulus, initial E_0 (GPa)	Strength σ^{tu} (MPa)	Fail strain ε^{tu} (%)	Poisson's ratio	Modulus, initial E_0^c (GPa)	Strength σ^{cu} (MPa)	Fail strain ε^{cu} (%)	Poisson's ratio
Epoxy (datasheet)[a]	2.7-2.9	75-80	3.5-8.0	–	–	–	–	–
Epoxy[b]	3.03 ±0.46	67.17 ±2.45	3.61 ±0.23	0.403 ±0.007	3.57 ±0.38	73.99 ±4.64	3.72 ±0.95	0.411 ±0.013
$[45]_{16}$	5.00 ±0.29	44.92 ±2.79	1.46 ±0.16	0.302 ±0.027	6.20 ±0.32	95.35 ±3.70	7.99 ±2.03	0.419 ±0.028
$[0/90]_{4S}$	16.69 ±0.72	155.78 ±9.56	1.57 ±0.08	0.111 ±0.027	17.40 ±1.68	96.89 ±3.75	2.84 ±0.28	0.095 ±0.008
$[\pm 45]_{4S}$	6.42 ±0.41	74.28 ±3.56	11.04 ±0.40	0.620 ±0.073	6.01 ±1.03	86.47 ±1.05	6.23 ±1.80	0.555 ±0.046
Quasi-isotropic[c]	13.09 ±1.44	124.60 ±3.25	1.70 ±0.02	0.357 ±0.050	12.48 ±1.48	88.17 ±2.81	2.01 ±0.18	0.289 ±0.004

[a] reported by supplier
[b] tested for this study
[c] $[0/+45/90/-45]_{2S}$

tests (representing highest and lowest failure strain) are shown for each case.

Table 5.6: Fibre-direction (*11*), in-plane transverse (*22*), and shear (*12*) properties of Flax-epoxy composite derived from tests on $[0]_{16}$, $[90]_{16}$, and $[\pm 45]_{4S}$ laminates, respectively

	Tension				Compression			
	Modulus, initial (GPa)	Strength (MPa)	Fail strain (%)	Poisson's ratio	Modulus, initial (GPa)	Strength (MPa)	Fail strain (%)	Poisson's ratio
	E_{011}	σ_{11}^{tu}	ε_{11}^{tu}	ν_{12}	E_{011}^c	σ_{11}^{cu}	ε_{11}^{cu}	ν_{12}^c
11	31.42 ±1.47	286.70 ±13.30	1.53 ±0.07	0.353 ±0.011	30.32 ±3.04	127.11 ±5.08	1.60 ±0.29	0.396 ±0.046
	E_{022}	σ_{22}^{tu}	ε_{22}^{tu}	ν_{21}	E_{022}^c	σ_{22}^{cu}	ε_{22}^{cu}	ν_{21}^c
22	5.58 ±0.5	33.86 ±1.35	1.36 ±0.18	0.067 ±0.003	5.70 ±0.71	79.94 ±9.95	2.61 ±0.53	0.066 ±0.010
	G_{012}	τ_{12}^{u}	γ_{12}^{u}		G_{012}^c	τ_{12}^{cu}	γ_{12}^{cu}	
12	2.07 ±0.13	37.35 ±1.78	14.92 ±2.57	–	1.63 ±0.25	43.24 ±0.52	9.79 ±2.63	–

5.3.1.1 Fibre direction

Tension In tension, Fibre direction (*11*) strength and initial modulus are found to average 287 MPa and 31 GPa, respectively, obtained from tests on $[0]_{16}$ specimens (Table 5.6 and Figure 5.2(a)). These

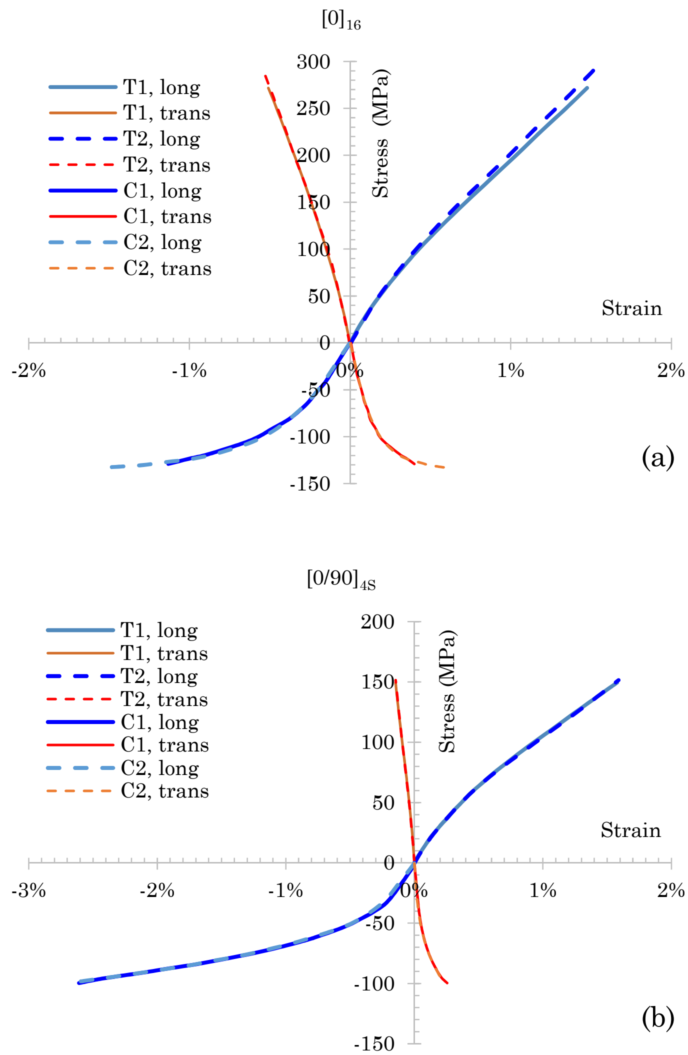

Figure 5.2: Response plots for specimens of (a) $[0]_{16}$, and (b) $[0/90]_{4S}$ laminate; T = tensile test, C = compressive test

results agree well with published data on epoxy composites reinforced by continuous Flax fibre (compare with Table 5.1). The Poisson's ratio (ν_{12}) typically varies through the duration of the test, from a high of ∼0.5-0.6, then tending rapidly towards a value of 0.353. A variation is observed in tangential modulus after an initial linear response up to 0.2-0.25% strain, which is consistent with reported Flax fibre tensile behaviour (discussed earlier) [23; 51; 80]. However, no further significant non-linearity is evidenced after this point. The response is highly linear after 0.35% strain, indicating that microfibrillar re-orientation within the Flax fibres may be complete by this stage. The tensile failure strain is found to average 1.53%, which is also within the reported range observed for flax bundle failure (see Table 2.2) – confirming that the tensile response is fibre-dominant. Considering this, failure strain is better estimated from tests on crossply $[0/90]_{4S}$ specimens, as their fibre direction deformation should be less sensitive to defects in the laminate. The [0/90] specimens fail at a slightly higher average strain of 1.55%. As expected, the [0/90] specimens have around half the initial modulus, and fail at about half the stress as that of [0] specimens (since [0] specimens have twice as much Flax reinforcement in the loading direction within the same cross section area). The observed [0/90] properties (Table 5.5) are in good agreement with published data (Table 5.4).

Applying tested epoxy and fibre-direction properties, the classical rule-of-mixtures method (Figure 5.3(a)) estimates a Flax fibre modulus of 60 GPa, which is in very good agreement with published data on Flax technical fibres (Table 2.2). Similar application of a rule-of-mixtures fit estimates the fibre strength

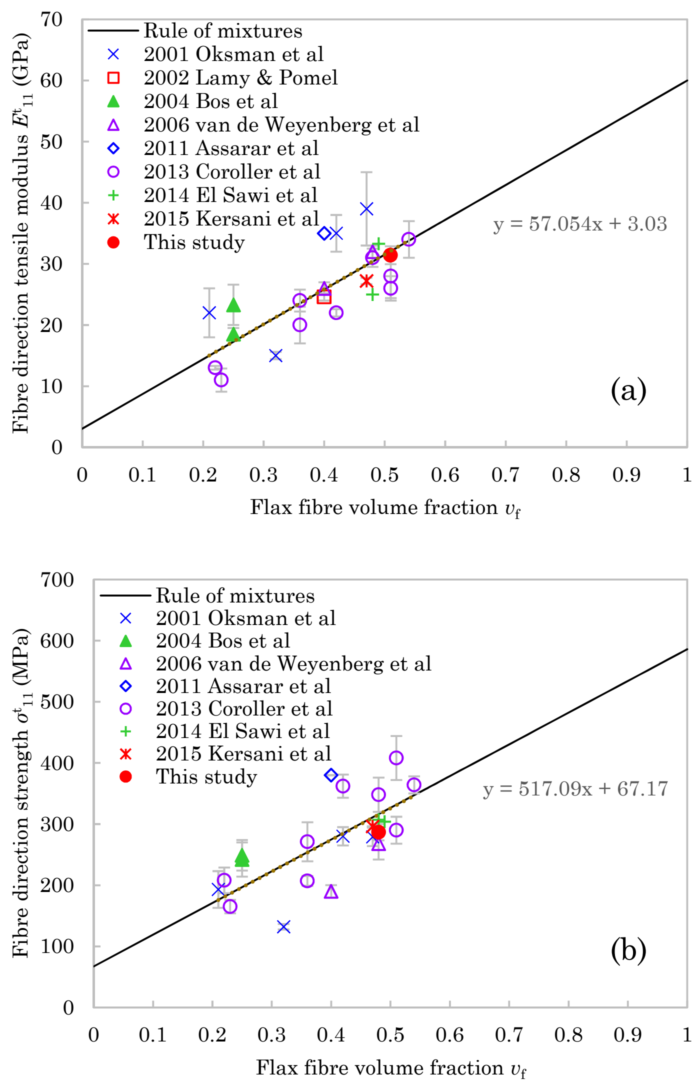

Figure 5.3: Fibre direction (a) tensile modulus (b) and strength as a function of fibre volume fraction; refer to Tables 5.1 and 2.1–2.2 for data from other sources

to be 585 MPa (Figure 5.3(b)) – also well within the range of strengths reported for Flax fibres. This indicates that the specimens manufactured in this study are representative of typical Flax fibre reinforced epoxy composites. Note that, in order to estimate Flax fibre properties, the epoxy modulus and strength from this study (3.03 GPa & 67.17 MPa, respectively) are assumed in the theoretical rule-of-mixtures prediction.

Compression In compression, onset of buckling possibly prevented the measurement of true compressive strength, so the failure strength observed should be considered only a lower bound estimate. Compressive response of both [0] and [0/90] shows a generally bilinear character, with an inflection region between 0.2-0.6% strain (Figure 5.2). Fibre direction strength and initial modulus are found to be 127 MPa and 30 GPa, respectively. Bos et al. [53] found the compressive strength and modulus to be 119-137 MPa and 30 GPa, respectively, which are in excellent agreement with the observations of this study. Note that the initial compressive modulus is nearly identical to that of the tensile case, and this holds true for both [0] and [0/90] tests. The Poisson's ratio is expected to be similar to the tensile case, so the observed compressive ratio 0.397 $\pm$0.046 is within the tested tensile range of 0.353 $\pm$0.011.

5.3.1.2 In-plane transverse

Tension In-plane properties perpendicular to the fibres (*22*) are measured from the $[90]_{16}$ specimens. The overall transverse response is generally bilinear (Figure 5.4(a)) – the first segment lasting up to the inflection point at $\sim$0.6% strain, followed by the second linear segment with a pronounced reduction of tangential modulus extending until specimen failure. Tensile failure strain is found to average 1.36%. As with the fibre direction case, the Poisson's ratio (ν_{21}) varies with loading and tends to 0.067. The strength and initial modulus averages 34 MPa and 5.6 GPa, respectively (see Table 5.6). Van de Weyenberg et al. [171] investigated 0.4 fibre volume fraction specimens (a lower fraction than specimens in this study) and found transverse strength and modulus to be 8 MPa $\pm$4 and 0.4 $\pm$0.2 GPa, respectively (failure strain is not reported) – which are much lower than those observed by our investigation. However, the same study succeeded in improving transverse properties by subjecting loose Flax technical fibres to a mild alkaline treatment (1% NaOH), resulting in strength and modulus of 20 MPa $\pm$4 and 2.3 $\pm$0.2 GPa, respectively – which are closer to our observations. The difference in measured properties may be explained by the (i) different fibre fractions involved, and (i) a better fibre-matrix interfacial bonding and load transfer in our study.

Compression In compression, the transverse response does not exhibit the distinctly bilinear nature of the tensile case. Compressive strength and initial modulus are 80 MPa and 5.7 GPa, respectively. As expected, the initial compressive modulus and the Poisson's ratio are identical to that of tensile response, and the compression failure strength is higher than that in tension. Failure occurs at $\sim$2.6% strain.

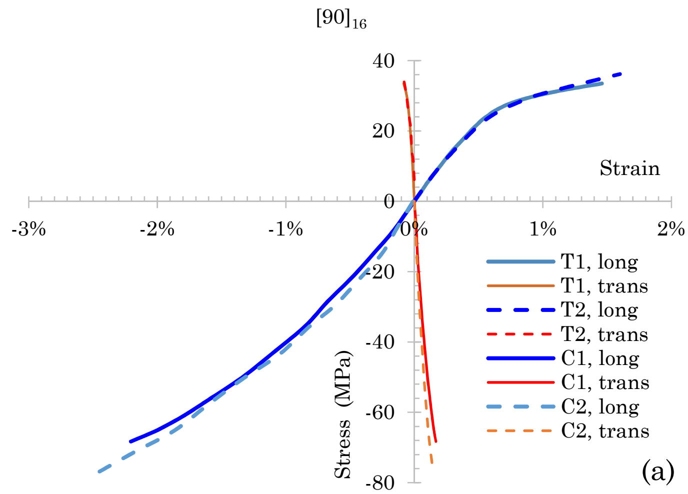

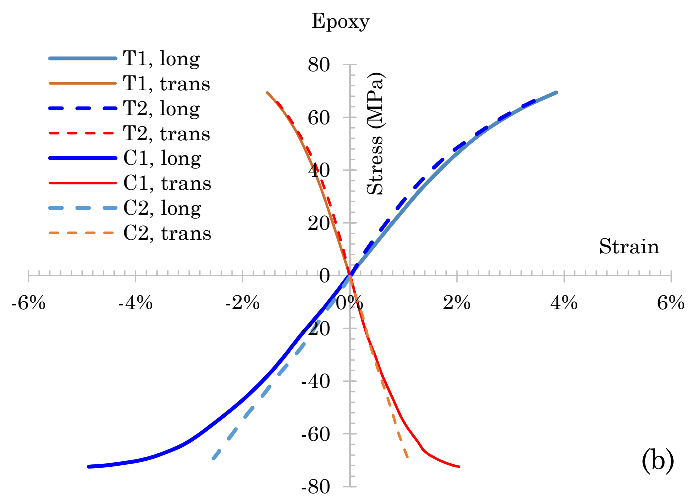

Figure 5.4: Response plots for specimens of (a) $[90]_{16}$, (b) Neat epoxy; T = tensile test, C = compressive test

5.3.1.3 Epoxy response

Contrasting the $[90]_{16}$ and neat epoxy tensile response, it is evident that the epoxy specimens are stronger (67 MPa ultimate strength, Figure 5.4(b)). This confirms that the presence of transverse fibres in epoxy introduces structural weaknesses, possibly in the form of lower-strength fibre-matrix interface, and weaker pectin adhesion within fibre bundles [55; 103]. In compression, both [90] and pure epoxy specimens have very similar strengths, indicating that the presence of fibres does not significantly alter the compressive strength of the epoxy material.

5.3.1.4 In-plane shear

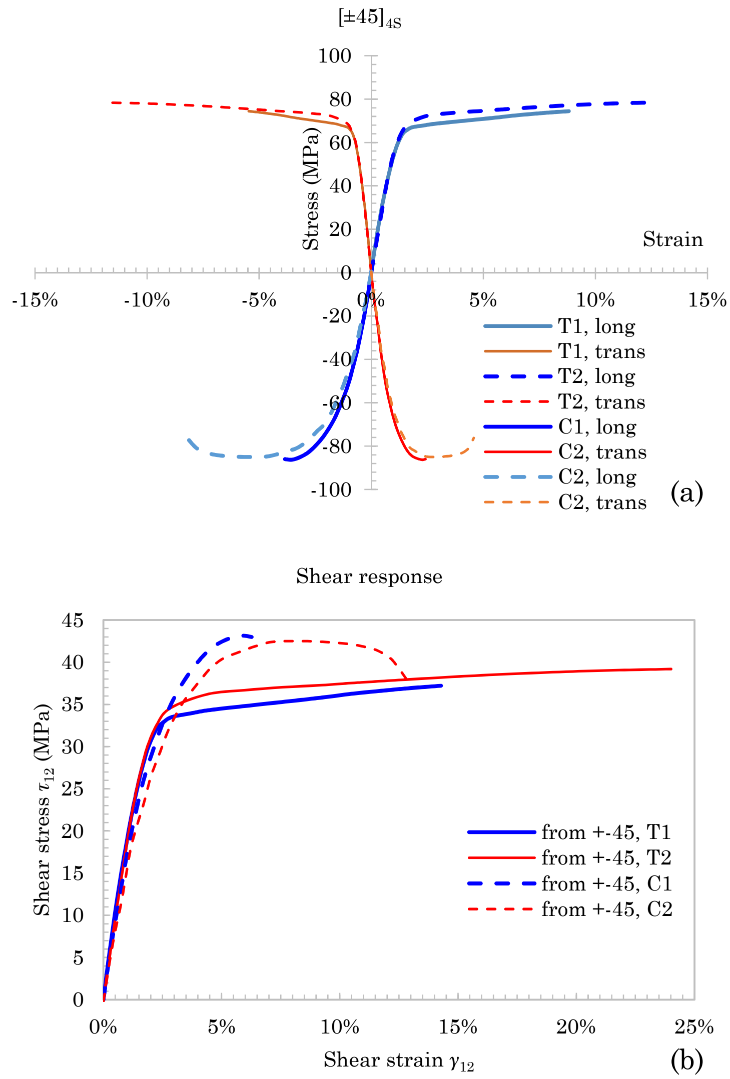

Figure 5.5: Response plots for specimens of (a) $[\pm 45]_{4S}$ laminate, and (b) derived in-plane shear response; T = tensile test, C = compressive test

The shear response is derived from the angle-crossply $[\pm 45]_{4S}$ tension specimens; however, the shear properties derived from compressive specimens also provide similar values (Table 5.6). The $[\pm 45]_{4S}$ laminate tensile strength and modulus are 74 MPa and 6.4 GPa, respectively, which is very consistent with reported data (see Table 5.4). The laminate Poisson's ratio averages 0.620 ±0.073, a range that also falls within reported data in Table 5.4. The derived shear strength and modulus are 37 MPa and 2.1 GPa, respectively. The laminate plot and the derived shear plot both exhibit a highly bilinear character (Figure 5.5). Most of the tested $[\pm 45]_{4S}$ specimens demonstrated varying degrees of ductile behaviour after 3% laminate strain (or ~5% shear strain), with very large laminate failure strains of 6-12% observed that exceed most existing reported data. It is observed that after the inflection point, the 45°-angled plies began to re-orient towards the loading axis, bringing the fibre angle down to ~35° before fracture (see Figure

5.6(a)). Based on this visual evidence, ply rotation is concluded to be the reason for the high-straining ductile behaviour. The fracture surface shows clear delamination and fibre breakage (Figure 5.6(b)).

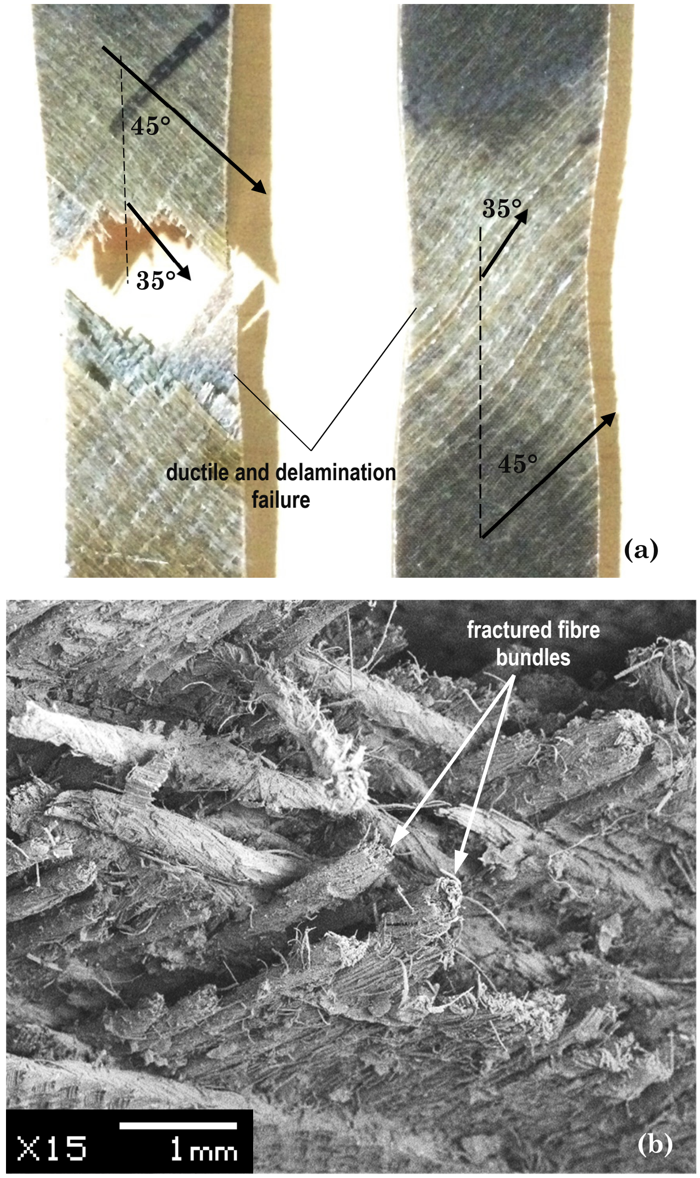

Figure 5.6: Tensile failure of $[\pm 45]_{4S}$: (a) specimen shows delamination, and ductile response due to ply rotation; (b) fracture surface at $\times 15$ shows delamination and fibre breakage

Compression response of the [±45] laminate is nearly identical to the tensile case, up to about 4-4.5% strain (Figure 5.5(a)). Laminate compression strength and modulus are 86 MPa and 6.0 GPa, respectively, which, as expected, are very similar to the tensile values. There is a considerable reduction in tangential modulus at 2-3% laminate strain. Critical buckling becomes evident at around 6.23% strain. The shear response derived from the compression laminates is also similar to that from the tensile case up to about 3% shear strain. The shear strength and modulus derived from the compression tests are found to be 43 MPa and 1.6 GPa, which are similar to the tensile shear modulus, as expected.

5.3.2 Damage and inelasticity evolution

5.3.2.1 Fibre direction

Tension Tensile damage in the fibre direction has a sigmoidal profile that can be described by a logistic function (Figure 5.7(a)).

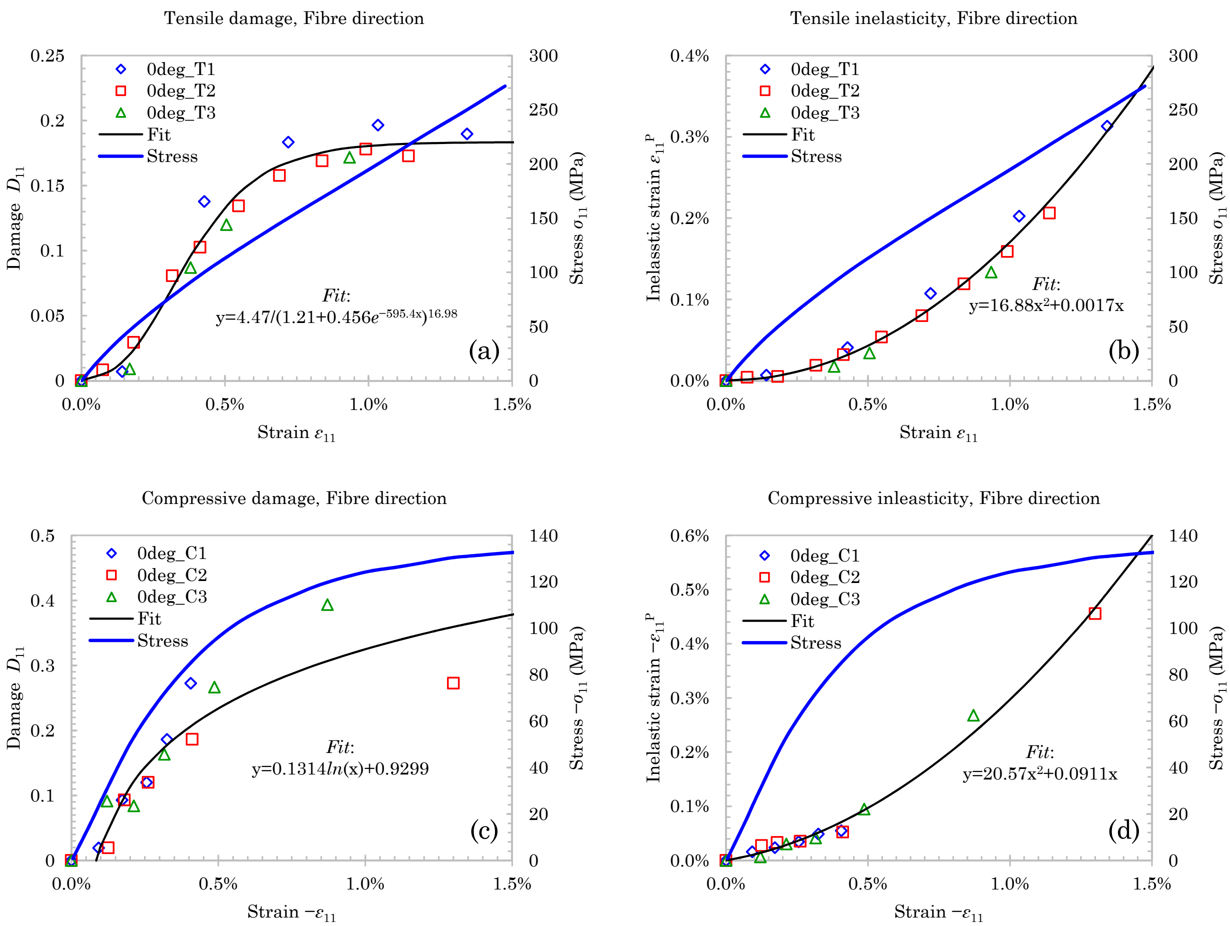

Figure 5.7: Fibre-direction damage and inelasticity; tensile (top) and compressive (bottom)

Initial evolution is relatively slow, increasing rapidly after about 0.15% strain at which stage damage is $D_{11} = 0.015$ (physically, this indicates that the modulus is degraded by 1.50%). This point at which the damage rate rapidly increases coincides with the inflection point in the stress response plot. Also, Figure 5.7(b) reveals that inelasticity is almost negligible until this 0.15% strain inflection point, after which the rate steadily increases – this matches a similar observation in Flax-polyester composites by Shah et al. [186] of an apparent 'threshold' strain before which fibre-direction permanent deformation is not detectable. Stiffness damage can be considered halted by 0.9% strain, until failure at ∼1.53% strain, at a constant $D_{11} = 0.183$ (in other words, specimen is reduced to about 80% of its original stiffness just before fracture). Inelastic strain accumulates at a steadily increasing rate throughout loading, and can be described by a quadratic fit. This irreversible strain reaches ∼0.4% just before failure, so at least a quarter of the failure strain is permanent.

SEM images of specimen transverse cross section (normal to loading) microstructure after 20% and 80% of tensile failure stress (corresponds to stress-strain of 60 MPa–0.25% and 240 MPa–1.27%, respectively) is shown in Figure 5.8. At $0.2{\cdot}\sigma_{11}^{tu}$, microcrack development is observed (i) along the fibre-matrix interface,

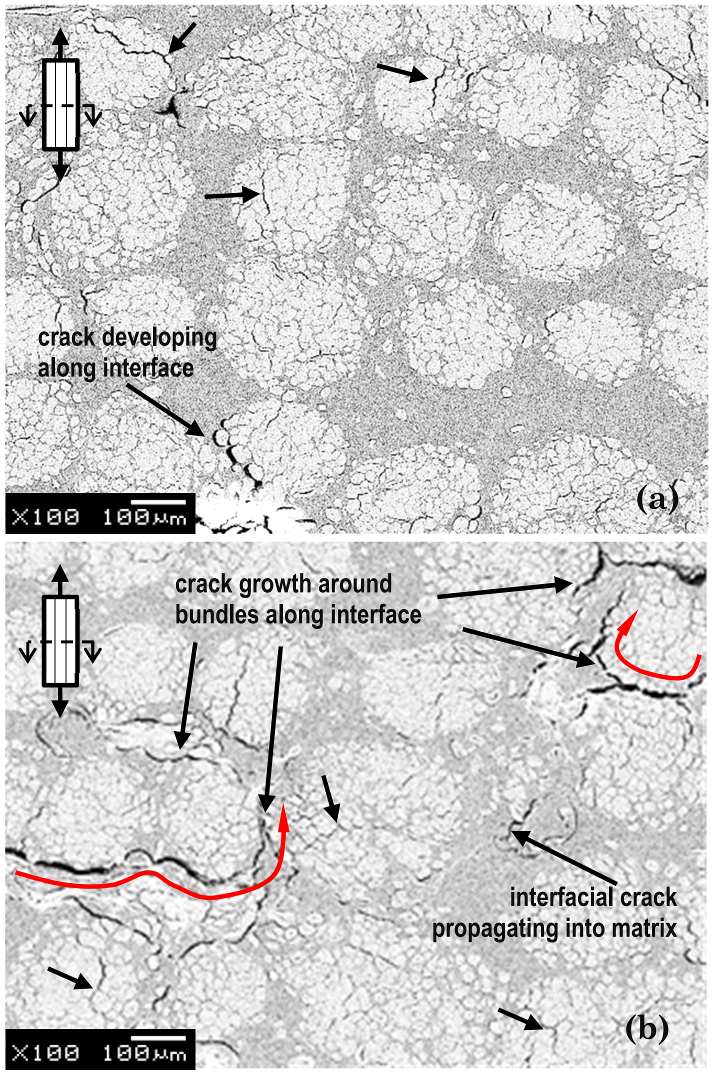

Figure 5.8: SEM observation of tensile damage in $[0]_{16}$ (a) at $0.2\sigma_{11}^{tu}$, and (b) at $0.8\sigma_{11}^{tu}$. Specimens are imaged at a transverse section cut. Small arrows point to intra-bundle cracks.

and (ii) within fibre bundles (intra-bundle) along elementary fibre boundaries. Intra-bundle cracking is a symptom of the 'splitting apart' of elementary fibres caused by a breakdown in the binding pectin-hemicellulose layers [55]. This *axial fibrillation* has been shown by Romhány et al. [55] to be the first stage in the sequence of progressive tensile fibre damage. After $0.8{\cdot}\sigma_{11}^{tu}$, (i) the majority of cracks appear to be those along the fibre-matrix interface, propagating around fibre bundles and merging with each other, (ii) the intra-bundle cracks have not propagated beyond the fibre bundle, and (iii) almost no cracks are observed in the matrix. The well-propagated circum-bundle cracks that debond fibre from the matrix are the most likely precursor to the fibre 'pull-out' evidenced at specimen fracture by Shah et al. [186]. Minimal cracking in the matrix even by $0.8{\cdot}\sigma_{11}^{tu}$ suggests that matrix contribution to the damaged state is not significant when compared with fibrous damage and interfacial debonding.

Compression Compressive damage in the fibre direction follows a logarithmic profile (Figure 5.7(c)). The damage plot initiates at non-zero strain, indicating that a strain threshold may exist at ∼0.09% before which stiffness degradation does not occur. Damage rate is rapid initially up to about 0.6% strain, thereafter decreasing steadily until failure. Damage just before failure is around $D_{11} = 0.38$, indicating that stiffness is reduced to about 60% of original before buckling. As with the tensile case, inelastic strain begins simultaneously with loading, and the accumulation rate increases with progressive loading. The total irreversible strain at specimen failure is 0.6%, which is about 40% of the failure strain.

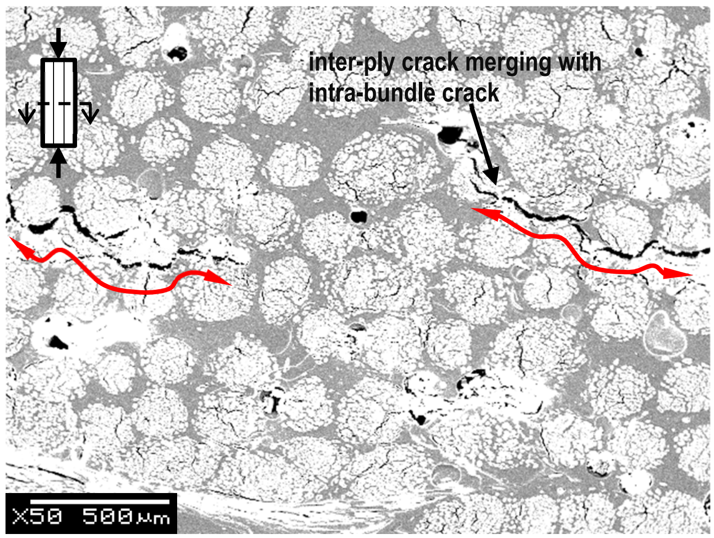

Figure 5.9: SEM observation of compressive damage at $0.8\sigma^{cu}$ in $[0]_{16}$, showing significant cracking between ply layers (delamination) and intra-bundle cracking. Specimens are imaged at a transverse section cut.

SEM micrograph of [0] transverse cross section after a loading of 80% compressive failure stress (stress-strain ∼102 MPa-0.66%) is given in Figure 5.9, which shows clear, deep fault lines developed between ply layers, indicating the debonding and delamination mechanisms that precede buckling. These inter-ply cracks are seen to weave around fibre bundles, merging with other cracks along the fibre-matrix interface. These extended cracks thus formed are the only cracks seen propagating across matrix-rich regions. Also, microracks were observed within nearly all fibre bundles, indicating a splitting or separation of elementary fibres – also evidenced in SEM observations by Bos et al. [53]. As in the tensile case, these intra-bundle cracks are typically arrested at the fibre-matrix interface, and do not propagate into the matrix. No evidence is seen of cracking damage initiating in the matrix even at this $0.8{\cdot}\sigma^{cu}$ load level, suggesting that the matrix polymer structural bonds are stronger than the fibre-matrix bonds and the intra-bundle adhesion.

5.3.2.2 In-plane Transverse

Tension In-plane transverse tensile damage is noticeably linear, and initiates at a non-zero threshold strain of 0.2% (Figure 5.10(a)) before which damage may be negligible. From the test data, damage

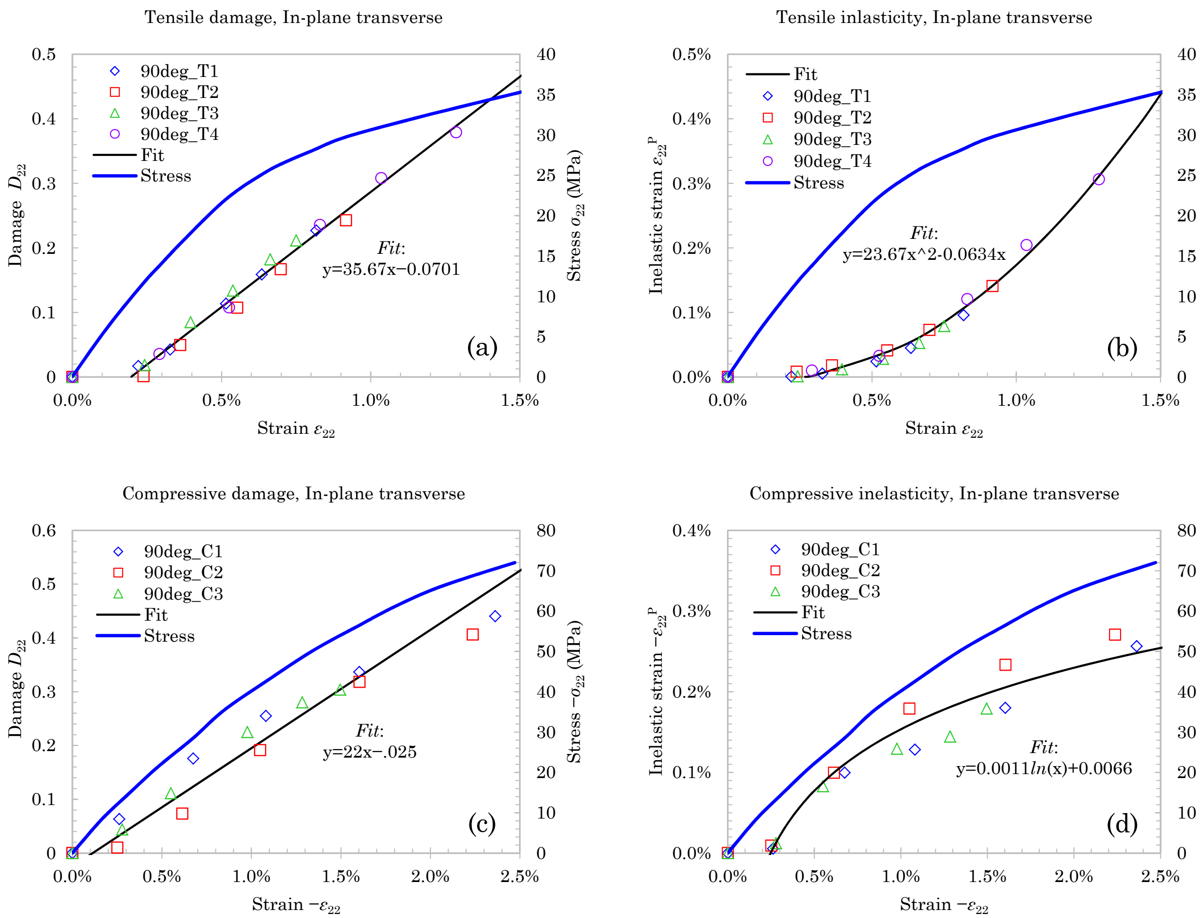

Figure 5.10: In-plane transverse damage and inelasticity; tensile (top) and compressive (bottom)

appears to be continuous, and the damage rate constant from initiation to failure, with stiffness being reduced by nearly half just before failure. The inelastic strain appears to initiate at a threshold applied strain of 0.27%, thereafter accumulating continuously at a progressively increasing rate (described by a simple quadratic function after initiation). The development of permanent strains appear to be the only reason behind the considerably bilinear in-plane transverse response (discussed earlier, see Figure 5.4(a)), since it is evident from comparing the stress and inelastic strain plots that the bilinearity develops only as the inelasticity rate increases. In contrast, there appears to be no correlation between the stiffness degradation damage and the response bilinearity. The total unrecoverable strain just before failure is predicted to be about 0.44%.

Figure 5.11 demonstrates physical damage observed in the [90] specimen microstructure after 20% and 80% tensile failure stress (stress-strain 7 MPa-0.12% and 27 MPa-0.74%, respectively). These images are of longitudinal sections cut from the midline along specimen axis. Intra-bundle microcracks (roughly

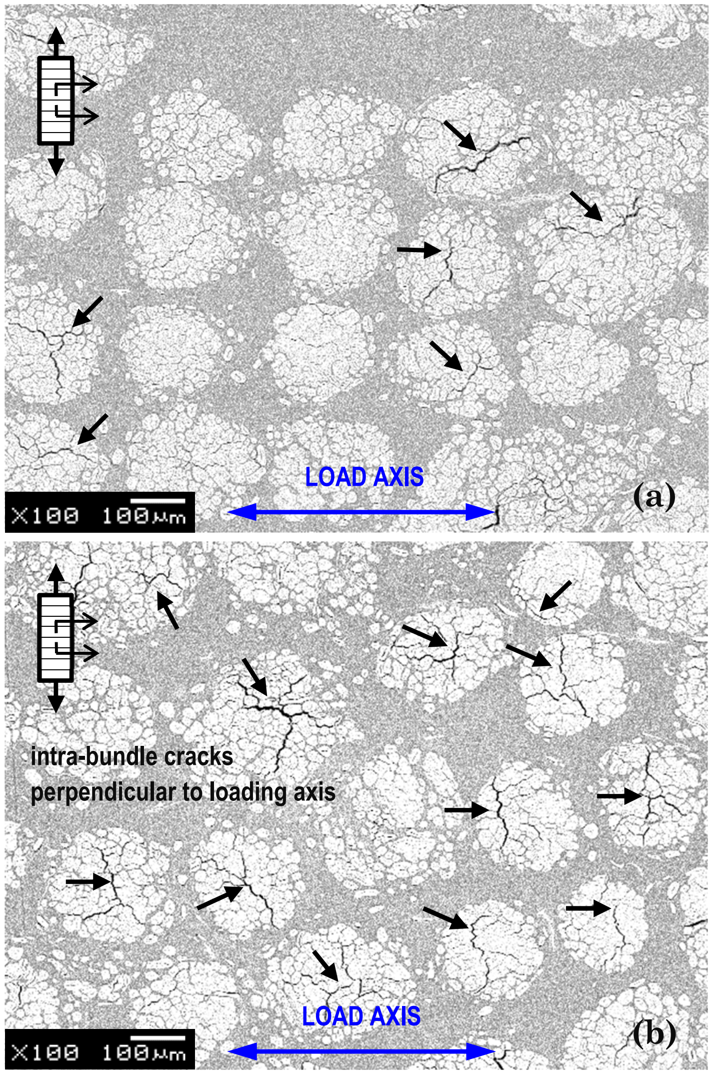

Figure 5.11: SEM observation of tensile damage in $[90]_{16}$ (a) at $0.2\sigma_{22}^{tu}$, and (b) at $0.8\sigma_{22}^{tu}$. Specimens are imaged at a longitudinal section cut. Small arrows point to intra-bundle cracks.

perpendicular to the loading axis) seem to be the typical damage mechanism at these load levels, and the prevalence of such cracking increases from 0.2 to $0.8{\cdot}\sigma_{22}^{tu}$. Interestingly, there is almost no evidence of interfacial cracks even at 80% loading – which is consistent with observations by Kersani et al [185]. It can be inferred that, at least up to $0.8{\cdot}\sigma_{22}^{tu}$, the linear stiffness degradation and increasing-rate inelasticity (evidenced in Figures 5.10(a) and (b)) is due to the increasing density of intra-bundle damage, rather than interfacial or matrix damage. Any other damage mechanisms, e.g. interfacial cracks due to fibre-matrix debonding, must occur after $0.8{\cdot}\sigma_{22}^{tu}$ applied load.

For further insight, the fracture surfaces of tensile [90] specimens were examined (Figure 5.12) and found to be characterised by bands of (i) exposed matrix with evident imprints of the removed fibre bundles, and (ii) exposed fibre surfaces with little or no matrix residue on it, where the bundles are largely intact (i.e. not split into inidividual elementary fibres). This shows that an almost clean separation of fibre-matrix does occur before failure, and the intact bundles suggest that the propagation of interfacial debonding cracks *around* fibre bundles is the dominant fracture-causing mechanism. It is worth noting that, though intra-bundle cracks are frequently evidenced in cross-section images, the fibre bundles along the fracture surface may yet appear intact because (i) splitting apart of elementary fibres may be localised and not span the length of the fibre, and (ii) the twist of the fibre bundle may contribute towards keeping the bundle together even under radial (transverse) forces.

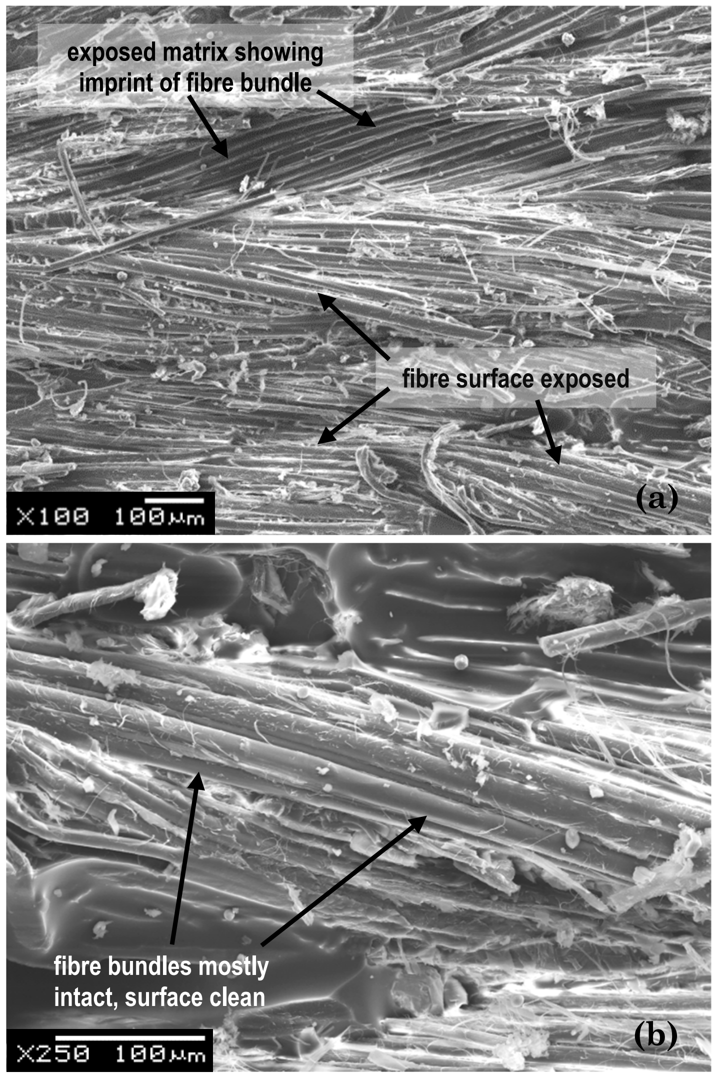

Figure 5.12: Fracture surface of [90] tension specimen: SEM images at (a) ×100 showing exposed fibre bundles and matrix with fibre imprint, and (b) ×250 showing intact bundles with minimal matrix residue on fibre surface

Compression Compressive transverse damage is found to be generally linear (Figure 5.10(c)), initiating at a low applied strain of 0.114%. Damage rises at a generally constant rate up to $D_{22} = 0.525$ (52.5% of original stiffness) just before failure. Inelastic straining is shown Figure 5.10(d), where it appears to initiate at 0.25% applied strain, and slows down by 0.7% applied strain, thereafter remaining at roughly a tenth of the applied strain, accumulating up to 0.26% permanent strain just before specimen buckling.

Micrographic observations of [90] longitudinal cross section after 80% compressive failure stress (stress-strain 57 MPa-1.7%) given in Figure 5.13 also indicate intra-bundle cracks, and clear delamination developing between plies. Just as in the [0] compression specimens, the delamination cracks seem to grow around fibre bundles, rather than through them – which suggests that damage initiates as fibre-matrix debonding, eventually propagating through the matrix and merging across several fibre bundles. As in the tensile case, no evidence is seen of cracks initiating in the matrix. The micrographs suggest that even cracks that arise at the fibre-matrix interface favour a propagation around the bundle, rather than into the matrix, unless it is in the vicinity of another circum-bundle crack.

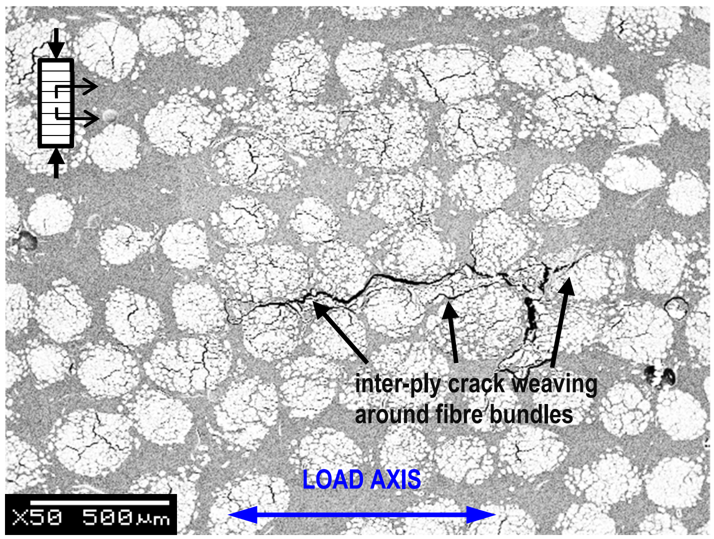

Figure 5.13: SEM observation of compressive damage at $0.8\sigma^{cu}$ in $[90]_{16}$, showing significant cracking between ply layers (delamination) and intra-bundle cracking. Specimens are imaged at a longitudinal section cut.

5.3.2.3 In-plane Shear

The shear damage evolution plot has a continuous logarithmic profile, initiating at a non-zero strain loading (Figure 5.14(a)). The loading threshold exists at 0.41% shear strain before which no degradation in shear modulus may be expected. Damage is rapid after initiation, but the rate slows down considerably around 3% shear strain – which coincides with the inflection point in the bilinear shear stress plot (ply re-orientation begins; discussed earlier). The damage is about $D_{12} = 0.63$ just before failure, indicating that stiffness is reduced to less than 40% of the original before fracture. Inelastic strain begins accumulating immediately with loading, with no initiation threshold detected. The accumulation rate increases progressively until failure. Note that, as expected, shear damage evolution and inelasticity accumulation trends are the same from tension or compression $[\pm 45]_{4S}$ specimens.

SEM images of $[\pm 45]_{4S}$ specimen cross sections show similar damage mechanisms at ~63 MPa (roughly 85%) under tension and compression (Figures 5.15(a) and (b)). Significant cracking is seen at ply boundaries (inter-ply cracking) progressing along fibre-matrix interface of adjacent bundles. This is expected,

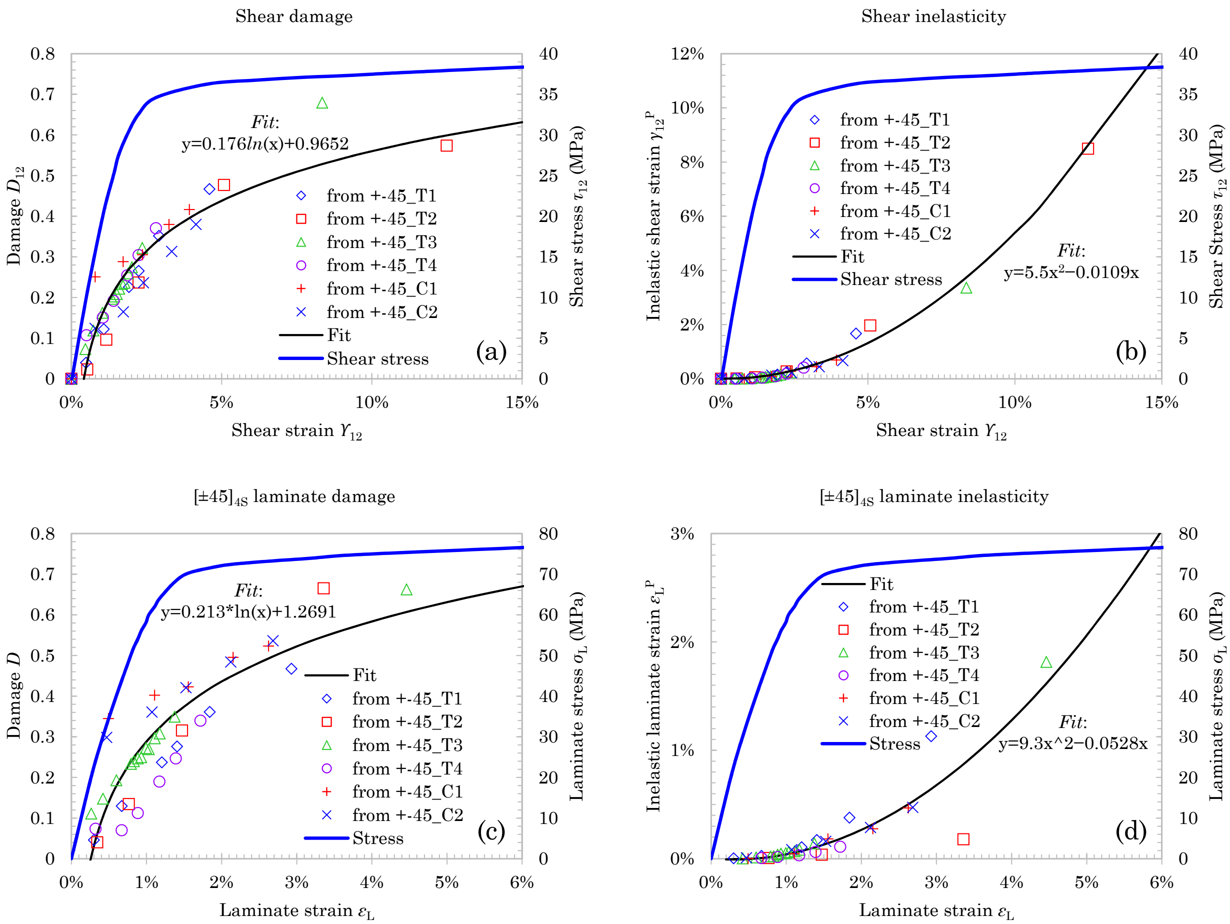

Figure 5.14: Damage and inelasticity (a-b) under in-plane shear, and (c-d) for $[\pm 45]_{4S}$ laminate ; T = tensile test, C = compressive test

since, under both tensile and compressive conditions, the angled plies tend to re-orient under loading and final fracture surfaces show evidence of delamination (tensile example shown in Figure 5.6). Interestingly, these inter-ply cracks are not seen to propagate through fibre bundles, but around them, suggesting that the cracking may have initiated as individual fibre-matrix debond cracks that later merged with each other along the inter-ply boundary. As in the cases discussed earlier, intra-bundle cracks do not extend out of the bundle past the fibre-matrix interface, and the matrix-rich regions appear almost entirely free of microcracks.

5.3.2.4 Neat epoxy

To serve as a comparable baseline for material response, load-unload tests are also conducted on specimens of the pure matrix material (cured epoxy) used for composite manufacture in this study. By comparing the stiffness damage and permanent strain evolution in epoxy specimens with those in Flax-reinforced specimens at similar strain loading, the contribution of epoxy matrix towards overall composite damaged state may be deduced. The epoxy specimens all fail in brittle fracture, with no evidence of ductile 'necking'. It is notable that, for epoxy specimens, an initiation threshold appears to always exist for both damage

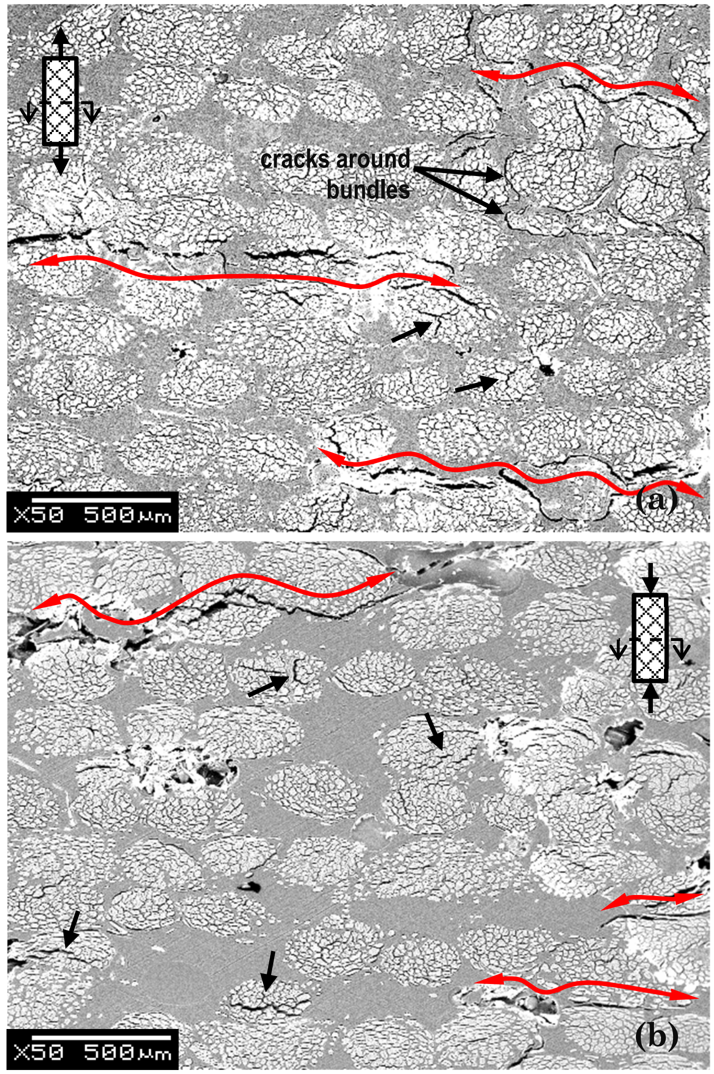

Figure 5.15: SEM micrograph of $[\pm 45]_{4S}$ sections (normal to loading axis) after 63 MPa laminate stress (i.e. $0.85\sigma^u$, or 32 MPa shear stress) in (a) tension and (b) compression, showing extended cracks between shearing plies (red wavy arrows) mostly around fibre bundles. Small arrows point to intra-bundle cracks.

and inelasticity evolution, under tensile and compressive loading (Figure 5.16). The damage initiation threshold is the same for tensile and compressive damage evolution: 0.29% loading strain; indicating that no modulus degradation may occur below this strain under either loading case. Note that this threshold is higher than those found for any of the in-plane directions in Flax-epoxy composite. The inelasticity initiation threshold is nearly the same in tension as in compression: 0.5-0.6%, which is also higher than those demonstrated by the composite specimens. Epoxy tensile damage rate is found to be constant, whereas the compressive damage shows an increasing rate. The reverse trend appears true for inelasticity evolution.

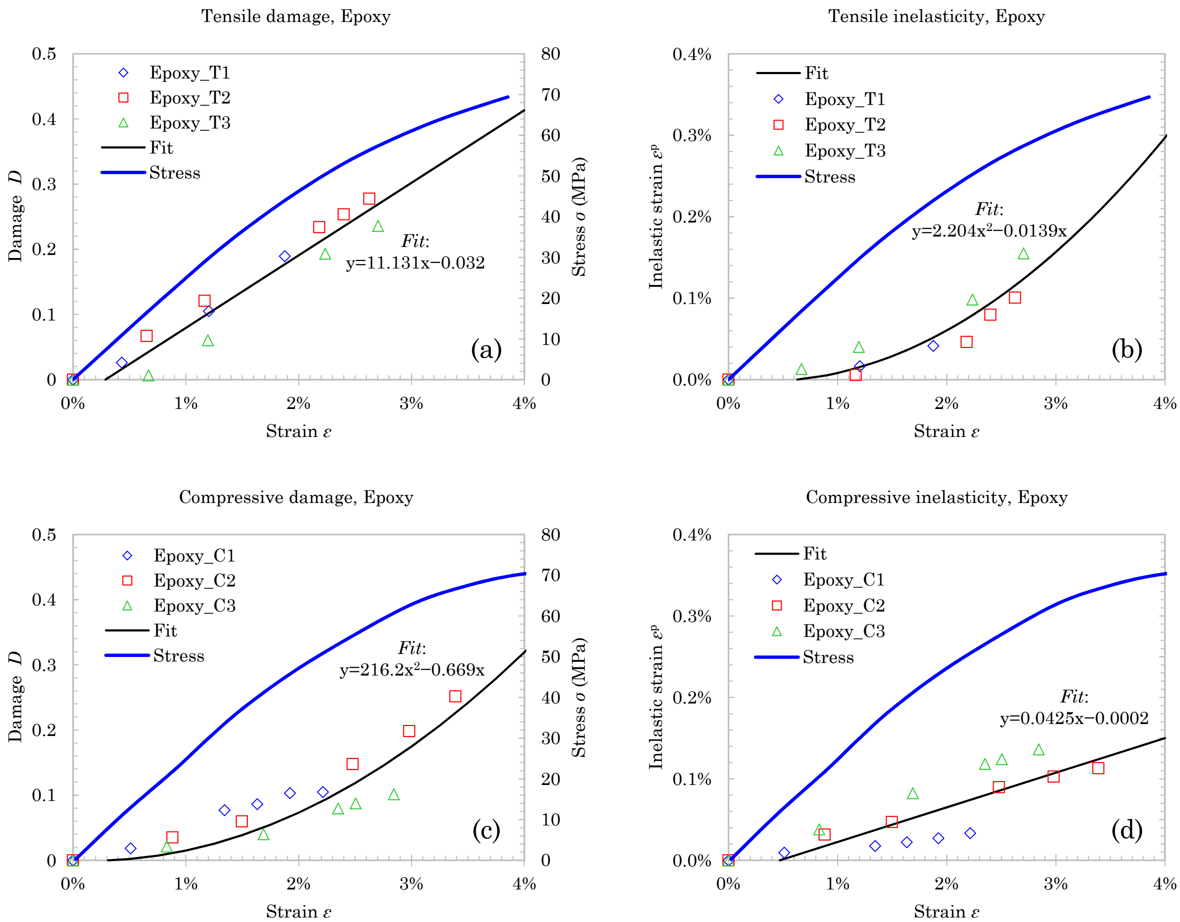

Figure 5.16: Epoxy damage and inelasticity; tensile (top) and compressive (bottom)

5.4 Further discussion

The hand-layup and compression moulding procedure provides composite plates with void content averaging 3.5%. Micrographic observation shows very good contact between Flax fibre bundles and epoxy matrix. Good agreement with published fibre-direction data and the classical rule-of-mixtures fit demonstrates that specimens manufactured in this study are well representative of most typical continuous Flax fibre-epoxy composites. Flax fibre modulus and tensile strength is estimated to be around 60 GPa and 585 MPa, respectively. Digital Image Correlation (DIC) methods proved a reliable and robust alternative to traditional strain transducers, particularly for high strain (>3%) deformation and compression testing. Load-unload tests are a straightforward method to obtain valuable insight on internal structural degradation until failure. All specimen layups demonstrate strain hardening behaviour, where the 'yield' stress point increases with progressively increased loading, accompanied by residual or permanent irreversible strains. All tested layup configurations demonstrate stiffness degradation and accumulation of irreversible strain, however:

1. damage is not necessarily proportional to loading,

2. not all loading levels result in identifiable damage, i.e. damage initiation thresholds exist, and

3. material stiffness may remain unchanged while still accumulating permanent strains, e.g. fibre-direction response after 0.9% strain

A summary of Flax-epoxy in-plane stiffness and inelasticity evolution behaviour is tabulated in Appendix A.4, Table A.2. In the case of the composite specimens, only in-plane transverse damage appears to be directly proportional to applied deformation. Of all composite in-plane directions, the fibre-direction response exhibits the least damage before failure, as well as the least amount of accumulated permanent deformation. Inelastic accumulation is always continuous for all cases. Stiffness degradation is continuous for all cases except fibre-direction tensile, where the degradation ceases by 0.9% strain loading (about $0.6{\cdot}\varepsilon_{11}^{tu}$). Note that, for pure epoxy specimens, stiffness damage initiates at 0.3% applied strain in tension and compression – which is a higher initiation threshold than observed in any of the composite specimens. The plasticity initiation thresholds for epoxy are 0.63% applied strain (tensile), and 0.47% applied strain (compressive), which are much higher than the thresholds for composite specimens. Furthermore, epoxy specimens accumulate the least amount of permanent deformation of all specimens under the same loading mode, even though their failure strain is considerably higher (tensile example shown in Appendix A.4, Figure A.4). These comparative observations suggest that the initiation and evolution of in-plane damage in our tested composites may not be matrix-related – a conclusion borne out by examining the damaged microstruture. SEM images of microstructure were studied post-loading for [0], [90], and [±45] specimens, and the implications of observed damage modes are discussed for each case in the previous section.

The following inferences on Flax-epoxy damage initiation, damage progression, and failure are summarised, based on damage/inelasticity plots and microstructure observations:

1. Since physical cracking is not evidenced in epoxy-rich regions, and as epoxy damage and inelasticity initiation thresholds are considerably higher than in the case of composite specimens, damage in Flax-composites does not appear to initiate in the matrix phase.

2. For similar reasons as above, and considering that total permanent strain accumulated in composite specimens is significantly higher than in epoxy specimens under the same loading strain, damage events must primarily accumulate in the non-matrix phases, i.e. within Flax fibre or at the fibre-matrix interface.

3. Critical failure modes in shear are delamination and fibre breakage, which initiate at the fibre-matrix interface and within Flax bundles, respectively.

4. Fibre-direction tensile failure modes are observed to be fibre bundle-matrix debonding and fibre cracking, which are precursors to the well-known fibre pull-out, defibrillation and fracture reported for Flax fibres and its composites.

5. Transverse stiffness degradation and permanent straining is primarily due to intra-bundle cracking, at least up to 80% failure stress. However, the fracture surface suggests that failure conditions develop due to fibre-matrix debonding after the 80% failure stress load level.

6. Compressive critical failure mechanism is similar for fibre-direction and transverse loading: inter-ply delamination that initiates as fibre-matrix debonding, before specimen buckling.

7. Matrix-related damage events (e.g. matrix cracking, polymer plasticity) are not a significant contributor to damage initiation, damage progression, or failure in the tested Flax-epoxy composites.

5.5 Conclusion

Fibre-direction (*11*), in-plane transverse (*22*), and in-plane shear (*12*) response derived from tensile and compressive tests are reported, along with mechanical data on some common layups (Tables 5.5 and 5.6). Load-unload tests show that the composite damaged state manifests as (i) degrading modulus and (ii) accumulating permanent strain. It is necessary to evaluate both modulus and inelastic strain to fully describe the composite damaged response at any stage of loading. A full description of in-plane stiffness degradation and permanent strain evolution is measured and plotted, complemented by a visual examination of microstructural damage mechanisms, which can be used to formulate and validate material models that predict damaged-condition response of Flax-epoxy composites, thereby aiding the reliable engineering design of components made from Flax-reinforced composites. Future tasks along similar lines of inquiry could involve a more detailed study of the damaging Flax-composite microstructure by following the crack propagation in the constituent phases from initiation to specimen failure, at shorter loading intervals, under in-plane loading conditions similar to this study. In addition, the tested data from this study may be utilised to develop a computational model of Flax-epoxy composite response.

Chapter 6

Modelling quasi-static response and progressive damage

This chapter proposes, identifies the parameters for, and discusses a continuum damage mechanics based progressive damage model to describe the in-plane tensile response of Flax-epoxy laminates. The literature survey and model described in this chapter are published in the following peer-reviewed article [189]:

Z. Mahboob, Y. Chemisky, F. Meraghni, and H. Bougherara. Mesoscale modelling of tensile response and damage evolution in natural fibre reinforced laminates, *Composites Part B: Engineering* 119 (2017) 168-183. doi: 10.1016/j.compositesb.2017.03.018.

6.1 Introduction

Successful innovation and adoption of high-performance NFCs depends on an accurate understanding of their physical damage mechanisms, supported by the development of predictive mechanical behaviour models that can emulate these mechanisms. Predicting damage initiation, damage progression, and development of failure conditions is essential to reliably design engineering components – and such capability remains relatively immature for NFCs when compared to traditional Carbon or Glass composites. This study develops a damage mechanics based model of in-plane tensile response in NFCs that accounts for their unique nonlinear *fibre-direction response* and internal damage progression. Considering Flax fibres have been shown to be the most promising natural fibre candidate for engineering applications, the model developed in this study is based on tensile test observations of a Flax fibre reinforced composite, thereby identifying Flax-specific model parameters.

6.1.1 Tensile damage mechanisms in NFCs

A discussion of Flax fibre and NFC damage mechanisms was summarised earlier in Chapter 2. As mentioned in previous chapters, damage may be thought of as surface or volume discontinuities (microcracks and microvoids) [124; 131]. Different types of damaging mechanisms encourage the development of such physical discontinuities, resulting in continuously evolving (typically degrading) material properties until the eventual failure of load-carrying capacity [131; 132; 155]. Flax fibres are known to exhibit varying stiffness and inelastic deformation under tension [23]. Tensile damage in composites of natural fibres share some similarity with well-known composite damage mechanisms. NFCs demonstrate a nonlinear response, with an initial rapid stiffness degradation rate that eventually decreases – unlike composites of synthetic fibres e.g. Glass where stiffness degradation tends to be constant and linear [90; 175]. As discussed in Chapter 2, this difference in response is attributed to the inherent non-homogeneous nature of natural fibres: hierarchical structure [23; 24; 190], defects in individual fibres [27; 69; 75], and variable fibre geometry [26; 81].

Depending on the matrix material used in the composite, some or all of the following distinct damage progression mechanisms have been identified through studies on NFC microstructure: (i) microfibril reorientation in the natural fibre secondary cell wall, (ii) 'intra-bundle' cracking, indicating splitting apart or separation of elementary fibres within a yarn bundle, (iii) transverse cracking in fibres, (iv) 'circum-bundle' interfacial cracks along the fibre-matrix boundary that indicate debonding or peeling, and (v) matrix shear cracks [22; 47; 95; 103; 170; 174; 178; 184–186; 191; 192]. Under tensile loading, the combined progress of fibre transverse cracking and axial splitting leads to fibre breakage [55; 95]. The circum-bundle propagation of fibre-matrix debonding is understood to be the precursor to fibre 'pull-out' evidenced on tensile fracture surfaces of NFC composites [170; 178; 191]. Interestingly, matrix cracks are not significantly reported [178; 184; 185] or considered critical to composite failure [192] in Flax-reinforced composites. Under both tensile and compressive loading, similar fibre-matrix interfacial cracks of adjacent fibre bundles merge and propagate along inter-laminar boundaries (between plies) to cause eventual delamination before fracture [174; 178].

6.1.2 Modelling damaged response in NFCs

A summary of failure and damage modelling techniques for fibre-composites was given earlier in Section 3.1. Well-known semi-empirical models and polynomial-based failure criteria (e.g. rule-of-mixtures, *Halpin-Tsai* equation, shear lag models, Maximum Stress criterion, *Tsai-Hill* criterion etc.) have been shown to reliably predict NFC tensile modulus and strength, as shown in the works of Facca et al. [193; 194], Hughes et al. [90], and Shah et al. [186]. Andersons et al. [195] proposed a semi-empirical model whereby tensor-based orthotropic stress-strain relationships were made to fit experimental observations of single ply Flax-composites, and classical laminate theory was employed to simulate laminate tensile response. The authors showed that a purely macroscale analytical approach can offer reasonable reproductions of nonlinear behaviour in NFC UD-laminates – except for $[\pm 45]_{\mathrm{nS}}$ layups, where the simulated response diverges from the experimental after $\sim$0.8-1.0% strain. This, the authors note, is because the 'rotation' of the angled plies (changing of ply orientation) in the test specimens is not accounted for in the model [195].

Recently, Panamoottil et al. [196] demonstrated a 'hierarchical' approach to simulate tensile response of a single resin-impregnated Flax yarn. Analytical microscale models (experimentally validated) are developed separately for elementary Flax fibre, matrix resin, and the fibre-matrix interphase layer, which are then combined in a finite element based 'unit model' of a Flax yarn (bundle of elementary fibres) impregnated and surrounded by matrix. A salient feature of this work is that the elementary fibres are treated as composites themselves, idealised as cylindrical tubes of varying diameters, reinforced by microfibrils at variable orientations, governed by classical laminate theory. Plastic yield and failure in all material phases are predicted by polynomial criteria. The authors intend to eventually simulate a full NFC laminate in the future by building a macromodel of repeated unit micromodels [196].

NFCs are known to accumulate progressive damage and permanent deformation well before final failure [22; 178; 186]. Analytical models, as discussed above, can be calibrated to capture initial undamaged mechanical properties, overall laminate nonlinear response, and final failure in composites of different natural fibres at varying fibre volume fractions and ply orientations. However, these models do not typically offer the means to predict the initiation and evolution of internal damage or permanent strains – as can be done when taking a damage mechanics approach to modelling. In contrast, Continuum Damage Mechanics (CDM) techniques apply continuum constitutive models wherein damage and inelasticity are quantified by evolving internal state variables and associated thermodynamic forces that represent, directly or indirectly, the distribution of microdefects in the material – as discussed in broader detail earlier in Chapter 3.

Panamoottil et al. [184] proposed another semi-empirical approach to model UD Flax/ polypropylene tensile response that does incorporate progressive degradation of stiffness. The authors implement a tensorial anisotropic elasticity relationship where a *damage effect tensor* degrades the laminate compliance. This damage effect tensor is defined in terms of crack densities measured from direct microscropic observation of physical cracking in tested specimens (microstructure imaged at the three orthotropic planes), following the work of Voyiadjis and Venson [197]. Note that only cracks within and around Flax bundles were measured, since matrix cracks were not detected. Measurements were taken from specimens tested at various load levels up to failure, in order to quantify damage tensor entries for those load levels. When executed, the model produces a poor reproduction of experimental monotonic response for single plies, however, the simulation improves for a five-layer UD laminate [184]. No simulation results are reported for transverse or shear response. While this approach offers a direct means to estimate progressive stiffness degradation damage in terms of physical crack density, it is perhaps better suited for UD plies, not multi-orientation laminates where crack identification and measurement will prove a cumbersome exercise. Furthermore, this approach is not developed within a framework of thermodynamics, so it is unable follow inelasticity evolution or predict permanent strains.

Poilâne et al. [198] developed a thermodynamics and CDM-based viscoelastoplastic model for fibre-direction-only tensile response in a single-ply Flax/epoxy composite. The strain response was considered split into pure elastic, viscoelastic, and viscoplastic components. Based on observations from creep and repeated load-unload tests, the authors propose free energy and dissipation potentials that capture plastic yielding, temperature dependence and strain rate effects in the fibre-direction. Notably, the proposed model (i) does not incorporate or define any damage state variable (i.e. no degradation of mechanical properties is allowed for), and (ii) viscoplastic behaviour is modelled as a combination of classical linear kinematic hardening (pure translation of fibre-direction elastic domain) and a nonlinear kinematic hardening (translation coupled with contraction of elastic domain). As such, while material modulus is assumed constant, the irreversible effects of damaging phenomena was considered captured in the plasticity laws. Note that this assumption of constant fibre-direction stiffness is an approximation of Flax/epoxy response, which has been shown to have a clear stiffness degradation at room temperature in the preceding Chapter

5. The authors concluded that fibre-direction (i) viscous deformation exists at any temperature, (ii) viscoelastic effects are not significant at room temperature, so (iii) Flax/epoxy nonlinear behaviour can be attributed to plastic (or viscoplastic) effects, (iv) that are well captured by a combined linear and nonlinear kinematic hardening model [198].

Recently, Sliseris et al. [199] proposed two CDM-based micromechanical models within a thermodynamic framework: one for a random distribution short-fibre Flax/polypropylene, and another for a single-ply woven fabric Flax/epoxy composite, both under tension. For the short-fibre Flax/polypropylene model, fibre length and diameter were randomly distributed, and separate constitutive laws were defined for (i) elementary Flax fibre, (ii) 'defected' regions of elementary fibre, (iii) regions between elementary fibres but within overall yarn bundle (intra-bundle), and (iv) matrix resin. An interesting feature is that the authors chose to separately distinguish material behaviour in fibre defect regions and in intra-bundle regions to better reflect reported observations of kink-bands and weak pectin-hemicellulose adhesion between elementary Flax fibres in a bundle, respectively. The fibres were modelled simply as linear elastic (constant stiffness), but the defected fibre and intra-bundle regions were modelled as brittle materials with linearly degrading stiffness (damage variable defined) after a specified threshold. The matrix is modelled with constant stiffness and von Mises plasticity with isotropic hardening. For the woven fabric Flax/epoxy model, both Flax fibre and matrix were governed by nonlinear, isotropic hardening plasticity laws, but with no state variable laws that would permit any degradation of material properties. Both models were exercised via a finite element based RVE (representative volume element) loaded in tension. The models captured the initiation and progressive evolution of 'damaged zones' (locations that develop plasticity or fibre damage), and the RVE response closely reproduced experimentally observed nonlinear stress-strain response [199] .

Recall from Section 3.1.4 that, since thermodynamics-based CDM techniques are able to (i) make predictions of damage initiation within plies from an undamaged state (unlike fracture mechanics methods that require a pre-existing crack) and (ii) capture the evolution of interim diffuse damage within each ply until rupture (unlike the failure-criteria-based analytical approaches that can only track ply failures), this study models damaged mechanical response in Flax-laminates by modifying an existing mesoscale CDM framework developed at LMT-Cachan (*Laboratoire de Mécanique et Technologie*[11], Cachan, France), described by Ladevèze and others [122; 124; 140]. Herakovich [124] named it the the *Mesoscale Damage Theory* (MDT), since the scale modelling is between that of micromechanics (composite constituents) and the macroscale (laminate) – thus the term *meso*-scale. As noted earlier in Section 3.1.4.1, this framework assumes that laminate response under any loading until fracture can be predicted by modelling two elementary mesoscale entities – the *ply* and the *interface* – and damage-coupled elasto-plastic constitutive laws can be developed for each. The interface layer is usually idealised as a mechanical surface that connects two plies, and only included in the model when delamination or out-of-plane deformation is of interest [141; 142; 144]. Applying the concept of mean *effective stress*, the hypothesis of *strain equivalence*, and based on the *thermodynamics of irreversible processes* (see Chapter 3), the standard MDT model predicts in-plane damage growth in a single ply due to damage mechanisms that change material properties along transverse (perpendicular to fibre-direction) and shear planes – each represented by a unique damage variable [122; 140]. It is the basis for a large number of CDM models in literature, and has been shown to be robust in predicting damaged response of composite structures under a variety of conditions

[11] `http://lmt.ens-paris-saclay.fr/`

[123; 124; 136; 141–154]. The MDT is adapted in this study to also include original fibre-direction nonlinear evolution laws for NFCs, and will be further described in the following sections.

While the approach of Andersons et al. [195] offers a convenient macroscale method to simulate overall stress-strain response of multi-orientation Flax-laminates, capturing internal damage and residual inelasticity is out of its scope. The microscale models proposed by Sliseris et al. [199], while demonstrating that individual damaging mechanisms may be modelled separately, (i) assumes fibre modulus degradation only in the kink-bands and intra-bundle regions (ignores other fibre damage effects, e.g. cell wall reorganisation or cracking), which are (ii) modelled as brittle, simple linear function degradations (may not reflect reported nonlinear, continuous damage evolution [22; 178]), and (iii) are not validated for UD off-axis loading. Poilâne et al. [198] showed a well-validated means of incorporating rate effects (viscoelasticity and viscoplasticity) at the mesoscale ply-level, but assumes the nonlinear response to be completely due to viscous or plastic deformation, and therefore does not allow for material damage effects in their model formulation. Considering that Flax/epoxy fibre-direction modulus reduces by $\sim$20% at room temperature [178], ignoring this loss of stiffness (or any other degradation effect of damage) is an inaccurate assumption that unduly magnifies the role of plastic effects. While the assumption may yet allow a reasonable simulation of fibre-direction response, the model needs further expansion by incorporating damage kinematics in order to capture tensile response in transverse and shear planes, or even compressive response – all of which exhibit up to to 50% stiffness degradation [178].

As such, this chapter develops a mesoscale alternative to aforementioned recent models, that quantifies and couples material damage and inelasticity, proposing nonlinear evolutions for both based on experimental observations, thereby allowing a ply-level scrutiny of initiation and progression along the principal orthotropic directions, within a multi-directionally reinforced NFC laminate – with model parameters identified specifically for Flax/epoxy composites.

6.2 Experimental methods

6.2.1 Manufacturing

The details of manufacturing composite plates for this study were elaborated earlier in Chapter 4. The epoxy matrix material and reinforcing UD Flax fabric used are described in Sections 4.2.1–4.2.2. The Flax-epoxy composite plates were fabricated as described in Section 4.3. Composite specimens preparation and final dimensions are as described in Section 4.5. Note that, while the Flax fabric is not perfectly unidirectional (due to the presence of cross-weave strands), results from the preceding Chapter 5 showed that the tested mechanical properties compare very well with existing published data on unidirectional continuous-fibre Flax composites – thus indicating that the cross-weaves do not have a significant influence on the bulk composite response, and that the fabric may be considered practically unidirectional in nature.

6.2.2 Testing

All tensile tests were conducted at room temperature and pressure conditions in a servo-hydraulic MTS 322 (Eden Prairie, MN, USA) test frame at a displacement rate of 2 mm/min. Longitudinal strain was measured using a uniaxial extensometer (gauge length 0.5 in, or 12.7 mm), and transverse strain was measured by a 350Ω strain gauge. For $[\pm 45]_{4S}$ specimens, in addition to the extensometer for longitudinal strain, measurements were also taken using a Digital Image Correlation (DIC) setup and software VIC-2D™ [183] supplied by Correlated Solutions (Irmo, SC, USA). To observe the evolving stiffness of specimens and thereby measure damage progression, repeated cycles of loading and unloading are imposed on specimens at progressively increasing maximum loads until specimen fracture. Figure 5.1 shows the evolving stiffness and the inelastic strain measured from a typical cycled load-unload response plot. As noted in the preceding Chapter 5, damage is experimentally measured as stiffness degradation, and described as a function of original undamaged modulus E_0 and damaged-condition modulus E:

$$d = 1 - \frac{E}{E_0} \tag{6.1}$$

6.3 Model

The Mesoscale Damage Theory (MDT) is developed within the framework of irreversible thermodynamics, as explained earlier in Section 3.2.5. The MDT essentially allows prediction of damage and permanent strain development in an elementary ply in a fibre reinforced composite. The ply is considered as an orthotropic elastic-plastic material that demonstrates deteriorating mechanical properties (reflected in stiffness tensor) due to internal damage under applied loading. It is assumed that the damage events are uniformly distributed through the thickness of a ply, and that the damage state can vary from ply to ply. As will be outlined in the following sections, the damage model is applied for each ply in the laminate being loaded and the resulting global laminate response is determined. A full description of the standard model, including validated examples, can be found in [122–124]. Since the standard MDT model assumes a simple linear elastic brittle response in the fibre-direction, and is therefore unsuitable for modelling NFCs, this study improves the model further by introducing formulations for fibre-direction damage and plasticity, so as to effectively describe the nonlinear NFC response. Based on the earlier discussion in Section 3.2, the modified MDT model for NFC tensile applications is developed in the following sections.

6.3.1 Damage state variables and thermodynamic potential

The damaged stiffness tensor $\tilde{\mathcal{L}}$ is expressed in terms of a set of internal damage variables $\boldsymbol{d} = \left\{ d_{11} \quad d_{22} \quad d_{12} \right\}$. Analogous to the uniaxial case in Section 3.2, the *damaged ply* elastic constants in $\tilde{\mathcal{L}}$ are:

$$E_1 = (1 - d_{11})\, E_1^0 \qquad \text{if} \quad \sigma_{11} \geq 0; \quad \text{else } E_1 = E_1^0 \tag{6.2a}$$

$$E_2 = (1 - d_{22})\, E_2^0 \qquad \text{if} \quad \sigma_{22} \geq 0; \quad \text{else } E_2 = E_2^0 \tag{6.2b}$$

$$G_{12} = (1 - d_{12})\, G_{12}^0 \tag{6.2c}$$

where E_1, E_2 and G_{12} are the fibre-direction, in-plane transverse, and in-plane shear moduli, respectively[12]; d_{11} quantifies fibre-direction stiffness degradation damage, d_{22} represents in-plane transverse damage, and

[12] The superscript notation ^{0} indicates initial undamaged condition, to be determined experimentally

d_{12} represents in-plane shear damage. Note that stiffness degradation in fibre and transverse directions are only modelled for tensile conditions ($\sigma_{ij} \geq 0$).

The mean stress $\boldsymbol{\sigma}$ is defined in terms of damaged stiffness tensor in (6.3). Applying the hypothesis of *strain equivalence* discussed in Section 3.2.3, the *effective stress* state $\tilde{\boldsymbol{\sigma}}$ of the material can be defined at the *same* strain state ε, as given in (6.4). Therefore, ply effective stress $\tilde{\boldsymbol{\sigma}}$ and mean stress $\boldsymbol{\sigma}$ are related per (6.5) (see Figure 6.1 for physical interpretation of both stress spaces).

$$\boldsymbol{\sigma} = \tilde{\mathcal{L}} : \boldsymbol{\varepsilon} \tag{6.3}$$

$$\tilde{\boldsymbol{\sigma}} = \mathcal{L} : \boldsymbol{\varepsilon} \tag{6.4}$$

$$\tilde{\boldsymbol{\sigma}} = \mathcal{L}\tilde{\mathcal{L}}^{-1} : \boldsymbol{\sigma} \tag{6.5}$$

Note that operator ':' implies tensor product, where if $\boldsymbol{A}$ and $\boldsymbol{x}$ are higher- and lower-order tensors, respectively, then $\boldsymbol{A} : \boldsymbol{x} \equiv [A]\{x\}$, and $\boldsymbol{x} : \boldsymbol{x} \equiv \{x\}^\top\{x\}$.[13]

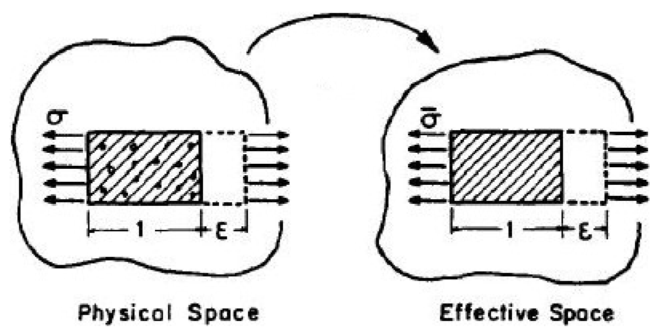

Figure 6.1: Schematic illustration of transformation between engineering stress σ and effective stress $\tilde{\sigma}$ space based on hypothesis of *strain equivalence*. Reproduced with permission from [200].

From earlier in Section 3.2.6, the measure of 'useful' or process-initiating work that can be obtained from a purely mechanical system under isothermal and isobaric quasi-static mechanical deformation can be expressed by the Elastic Strain Energy Density function W_D in (3.9). For a damaging orthotropic ply under in-plane loading conditions, the function can incorporate damage variables and be reduced to (3.10). For the computational implementation in this study, (3.9)–(3.10) is rewritten here in a 3D formulation that incorporates ply in-plane damage only, and is able to distinguish between tensile and compressive loading:

$$\begin{aligned} 2W_D =& \boldsymbol{\sigma} : \tilde{\mathcal{L}}^{-1} : \boldsymbol{\sigma} \\ =& \frac{\langle\sigma_{11}\rangle_+^2}{E_1^0(1-d_{11})} + \frac{\langle\sigma_{11}\rangle_-^2}{E_1^0} + \frac{\langle\sigma_{22}\rangle_+^2}{E_2^0(1-d_{22})} + \frac{\langle\sigma_{22}\rangle_-^2}{E_2^0} + \frac{\sigma_{33}^2}{E_3} \\ &+ \frac{\sigma_{12}^2}{G_{12}^0(1-d_{12})} + \frac{\sigma_{13}^2}{G_{13}} + \frac{\sigma_{23}^2}{G_{23}} \\ &- \left(2\frac{\nu_{12}}{E_1}\right)\sigma_{11}\sigma_{22} - \left(2\frac{\nu_{13}}{E_1}\right)\sigma_{11}\sigma_{33} - \left(2\frac{\nu_{32}}{E_3}\right)\sigma_{22}\sigma_{33} \end{aligned} \tag{6.6}$$

[13] For example, operation $\boldsymbol{\sigma} : \tilde{\mathcal{L}}^{-1} : \boldsymbol{\sigma}$ is equivalent to matrix multiplication $\{\sigma\}^\top[\tilde{\mathcal{L}}]^{-1}\{\sigma\}$.

where the Macaulay brackets notation $\langle..\rangle$ implies:

$$\begin{aligned} \langle a \rangle_+ = a \quad \text{if} \quad a \geq 0; \quad \text{else} \quad \langle a \rangle_+ = 0 \\ \langle a \rangle_- = a \quad \text{if} \quad a \leq 0; \quad \text{else} \quad \langle a \rangle_- = 0 \end{aligned} \tag{6.7}$$

This allows defining different potentials for tension (includes stiffness degradation damage) and compression (no stiffness degradation allowed), per standard MDT model [122; 124]. Note that this formulation assumes compressive modulus to remain constant, which does not reflect actual NFC response (as was shown in preceding Chapter 5), however it is an approximation made here in order to develop a tension-specific damage model. An extended model may be developed to simulate realistic NFC compressive response by defining separate compression-specific evolution laws and model parameters, as possible future work.

Unlike the fully linear-elastic, brittle fibre material assumed in typical MDT models, experimental tests described in Chapter 5 confirm that Flax-composites exhibit progressive damaging behaviour (modulus degradation) in the fibre-direction. The *thermodynamic force* Y (conjugates of damage variables, see 3.2.7.1) for all in-plane internal damage variables in a single ply are therefore derived:

$$Y_{11} = \frac{\partial W_D}{\partial d_{11}} = \frac{1}{2} \frac{\langle \sigma_{11} \rangle_+^2}{E_1^0 (1 - d_{11})^2} \tag{6.8a}$$

$$Y_{22} = \frac{\partial W_D}{\partial d_{22}} = \frac{1}{2} \frac{\langle \sigma_{22} \rangle_+^2}{E_2^0 (1 - d_{22})^2} \tag{6.8b}$$

$$Y_{12} = \frac{\partial W_D}{\partial d_{12}} = \frac{1}{2} \frac{\sigma_{12}^2}{G_{12}^0 (1 - d_{12})^2} \tag{6.8c}$$

The damage force Y, also called *damage energy release rate*, governs damage development the same way that the energy release rate K governs crack propagation in fracture mechanics. A previous maximum value of some function of the damage forces Y_{ij} (defined in the following section) has to be exceeded if new damage is to occur.

6.3.2 Damage evolution

Since the ply material is considered 'non-healing', damage values do not decrease upon unloading, and must remain at the previous peak value until a higher damaging load is applied. The damage evolution along transverse and shear planes is considered to be coupled, i.e. they influence one another (see Section 3.2.7.2), however the fibre-direction is considered decoupled from transverse-shear damage. The governing forces for in-plane damage evolution are therefore:

$$Y_f = \sqrt{Y_{11}}, \qquad \text{fibre damage, fibre fracture} \tag{6.9a}$$

$$Y_{ts} = \sqrt{Y_{12} + b \cdot Y_{22}}, \qquad \text{transverse cracking, fibre-matrix debonding} \tag{6.9b}$$

where b is a transverse-shear damage coupling parameter (to be determined) to express the relative effect of shear and transverse stresses on the fibre-matrix debonding mechanism; and subscripts f, t & s denote fibre-direction, transverse, and shear, respectively.

For transverse and shear damage, the standard MDT linear evolution functions from (3.13) were found to adequately describe Flax/epoxy damaged response. However, from tensile tests on $[0]_{16}$ Flax/epoxy specimens, the fibre-direction damage evolution $Y_f\left(d_{11}\right)$ was observed to follow an *exponential* profile, approaching a limiting value before specimen fracture, as shown in Figure 6.3. A set of damage evolution functions $\boldsymbol{\Phi}_d = \left\{\Phi_{d_{11}} \quad \Phi_{d_{22}} \quad \Phi_{d_{12}}\right\}$ is defined where:

$$\Phi_{d_{11}} = d_{\lim}\left[1 - \exp\left(\frac{Y_f^0 - Y_f}{m}\right)\right] - d_{11} \quad \text{while} \quad \varepsilon_{11} < \varepsilon_{11}^{\max}; \qquad \text{else} \quad d_{11} = 1 \tag{6.10a}$$

$$\Phi_{d_{22}} = \frac{\left\langle Y_{ts} - Y_t^0\right\rangle_+}{Y_t^c} - d_{22} \quad \text{while} \quad d_{22} < 1, \quad Y_{22} < Y_{22}^{\max}, \quad Y_{12} < Y_{12}^{\max}; \qquad \text{else} \quad d_{22} = 1 \tag{6.10b}$$

$$\Phi_{d_{12}} = \frac{\left\langle Y_{ts} - Y_s^0\right\rangle_+}{Y_s^c} - d_{12} \quad \text{while} \quad d_{12} < 1, \quad Y_{22} < Y_{22}^{\max}, \quad Y_{12} < Y_{12}^{\max}; \qquad \text{else} \quad d_{12} = 1 \tag{6.10c}$$

with the following Kuhn-Tucker conditions[14]:

$$\Phi_{d_{ij}} = 0, \quad \dot{d_{ij}} \geq 0, \quad \dot{d_{ij}}\Phi_{d_{ij}} = 0; \quad \text{for} \quad i,j \in \{1,2\} \tag{6.11}$$

where $\Phi_{d_{ij}}$ is the damage function for the corresponding damage variable d_{ij}, $\varepsilon_{11}^{\max}$ is the fibre-direction ultimate strain, while m, $d_{\lim}$, Y_f^0, Y_t^0, Y_t^c, Y_s^0, Y_s^c, $Y_{22}^{\max}$, and $Y_{12}^{\max}$ are parameters to be determined; and notation $\langle..\rangle_+$ is defined earlier in (6.7). A damage value of $d_{ij} = 1$ indicates a complete loss of stiffness in plane ij. Note that both transverse and shear damage evolutions as defined in (6.10) are not influenced by fibre-direction parameters – i.e. the fibre-direction damage remains fully decoupled from transverse-shear in the model proposed here.

Once the damage state or the damaged stiffness matrix is known, the elastic component of strain is given by:

$$\boldsymbol{\varepsilon}^e = \tilde{\boldsymbol{\mathcal{L}}}^{-1} : \boldsymbol{\sigma} \tag{6.12}$$

6.3.3 Inelasticity evolution

As shown in Chapter 5, Flax-composites develop permanent strains when loaded beyond a threshold limit. The standard MDT formulation [123; 124] based on *classical plasticity* of generalised standard materials [158; 160] is adapted here to numerically simulate inelasticity in NFCs, wherein the total strain $\boldsymbol{\varepsilon}$ (or total strain *increment* $\dot{\boldsymbol{\varepsilon}}$[15]) in any orthotropic direction is decomposed into elastic and inelastic components:

$$\boldsymbol{\varepsilon} = \boldsymbol{\varepsilon}^e + \boldsymbol{\varepsilon}^p; \quad \dot{\boldsymbol{\varepsilon}} = \dot{\boldsymbol{\varepsilon}}^e + \dot{\boldsymbol{\varepsilon}}^p \tag{6.13}$$

where e and p represent elastic and inelastic components, respectively. Based on this additive decomposition of total strain, the elastic relationship (6.12) may be rewritten as:

$$\boldsymbol{\varepsilon} - \boldsymbol{\varepsilon}^p = \tilde{\boldsymbol{\mathcal{L}}}^{-1} : \boldsymbol{\sigma} \tag{6.14}$$

[14] Kuhn-Tucker complimentarity conditions are classical in the convex mathematical programming literature; see [201; 202].
[15] In computational plasticity literature, alternative notations for strain increment include $\Delta\varepsilon$ and $d\varepsilon$.

Effective inelastic strain increments are defined in terms of damage:

$$\dot{\tilde{\varepsilon}}_{ij}^{p} = \dot{\varepsilon}_{ij}^{p} \left(1 - d_{ij}\right), \quad \text{for} \quad i, j \in \{1, 2\} \tag{6.15}$$

A set of yield surfaces (or elastic domain functions) $\mathbf{\Phi}^p = \left\{ \Phi_f^p \quad \Phi_{ts}^p \right\}$ is defined for fibre-direction and coupled transverse-shear plasticity evolutions, respectively. To formulate the transverse-shear yield surface Φ_{ts}^p, the standard MDT [122; 124] assumes a Mises-type coupling between the transverse and shear effective stresses, as given in (3.18), with the hardening assumed to be isotropic and governed by a power law (3.19). Unlike in typical MDT-based models, a fibre-direction plasticity evolution Φ_f^p is also introduced here since natural fibres demonstrate considerable inelastic behaviour. The fibre-direction response is still assumed decoupled from the other in-plane deformations similar to the standard model, and the fibre-direction hardening also appears to follow a power law based on experimental observations, shown in Figure 6.4.

Fibre-direction and coupled transverse-shear hardening are described by the following power law functions:

$$h_f = \beta_f (\tilde{p}_f)^{\alpha_f} \tag{6.16a}$$

$$h_{ts} = \beta_{ts} (\tilde{p}_{ts})^{\alpha_{ts}} \tag{6.16b}$$

where h_f and h_{ts} are hardening functions (analogous to R_H in (3.19)) that are dependent on *accumulated effective inelastic strains* (analogous to $\tilde{p}$ in (3.19)): fibre-direction represented by $\tilde{p}_f$, and $\tilde{p}_{ts}$ represents transverse-shear coupled plasticity similar to that defined in standard MDT model [122–124]; while β_f, α_f, β_{ts}, and α_{ts} are all parameters to be identified.

We consider $\mathbf{\Phi}^p$ having the following form, along with the loading/unloading Kuhn-Tucker conditions:

$$\Phi_f^p = \tilde{\sigma}_f^{eq} - h_f - \sigma_f^0 \leq 0; \qquad \dot{\tilde{p}}_f \geq 0, \qquad \dot{\tilde{p}}_f \Phi_f^p = 0 \tag{6.17a}$$

$$\Phi_{ts}^p = \tilde{\sigma}_{ts}^{eq} - h_{ts} - \sigma_{ts}^0 \leq 0; \qquad \dot{\tilde{p}}_{ts} \geq 0, \qquad \dot{\tilde{p}}_{ts} \Phi_{ts}^p = 0 \tag{6.17b}$$

where function Φ_f^p represents the inelastic behaviour in the fibre-direction, Φ_{ts}^p represents coupled in-plane transverse-shear response; σ_f^0 and σ_{ts}^0 are plasticity initiation parameters to be determined (analogous to R_0 in (3.19)); h_f and h_{ts} are hardening functions defined earlier in (6.16) that are dependent on $\tilde{p}_f$ and $\tilde{p}_{ts}$, respectively. *Equivalent stresses* $\tilde{\sigma}_f^{eq}$ and $\tilde{\sigma}_{ts}^{eq}$ are scalars that influence plasticity in the fibre-direction and transverse-shear, respectively, defined similar to that in standard MDT [122–124]:

$$\tilde{\sigma}_f^{eq} = \frac{\sigma_{11}}{(1 - d_{11})} = \tilde{\sigma}_{11} \tag{6.18a}$$

$$\tilde{\sigma}_{ts}^{eq} = \sqrt{\frac{\sigma_{12}^2}{(1 - d_{12})^2} + A_{ts} \frac{\sigma_{22}^2}{(1 - d_{22})^2}} = \sqrt{\tilde{\sigma}_{12}^2 + A_{ts} \cdot \tilde{\sigma}_{22}^2} \tag{6.18b}$$

where A_{ts} is the transverse-shear coupling parameter (similar to a^2 in (3.18)) to be identified. Note that, at a given applied stress σ_{ij}, any increase in damage values d_{ij} has the effect of increasing the effective stress $\tilde{\sigma}_{ij}$, thus increasing equivalent stress $\tilde{\sigma}^{eq}$.

Following the normality condition requirement of classical plasticity associated with instantaneous dissipative phenomena, the accumulated plastic strain rate $\dot{\tilde{p}}$ is normal to the elastic domain surface, i.e. it follows the direction of the gradient of the respective yield function Φ^p. Therefore, similar to standard MDT [122; 124]:

$$\dot{\tilde{p}} = \dot{\lambda}, \quad \Lambda = \frac{\partial \Phi^p}{\partial \tilde{\sigma}_{ij}}, \quad \dot{\tilde{\varepsilon}}^p_{ij} = \dot{\tilde{p}}\Lambda; \quad \text{for} \quad i,j \in \{1,2\} \tag{6.19}$$

where $\dot{\lambda}$ is the plastic multiplier, and Λ is the plasticity direction tensor. It follows that the effective strain increments $\dot{\tilde{\varepsilon}}^p$ are computed from:

$$\dot{\tilde{\varepsilon}}^p_{11} = \dot{\lambda}_f \frac{\partial \Phi^p_f}{\partial \tilde{\sigma}_{11}} = \dot{\tilde{p}}_f \frac{\tilde{\sigma}_{11}}{(h_f + \sigma^0_f)} = \dot{\tilde{p}}_f \tag{6.20a}$$

$$\dot{\tilde{\varepsilon}}^p_{22} = \dot{\lambda}_{ts} \frac{\partial \Phi^p_{ts}}{\partial \tilde{\sigma}_{22}} = \dot{\tilde{p}}_{ts} \frac{A_{ts} \cdot \tilde{\sigma}_{22}}{(h_{ts} + \sigma^0_{ts})} \tag{6.20b}$$

$$2\dot{\tilde{\varepsilon}}^p_{12} = \dot{\lambda}_{ts} \frac{\partial \Phi^p_{ts}}{\partial \tilde{\sigma}_{12}} = \dot{\tilde{p}}_{ts} \frac{\tilde{\sigma}_{12}}{(h_{ts} + \sigma^0_{ts})} \tag{6.20c}$$

6.3.4 Implementation

6.3.4.1 Ply damage model

The numerical implementation of the mesoscale model is similar to the *convex cutting plane algorithm* proposed by Simo and Hughes [202]. The system of non-linear equations that arises from the multiple damaging phenomena (damage evolution functions $\boldsymbol{\Phi}_d$ and plasticity yield functions $\boldsymbol{\Phi}^p$) are treated using generic numerical schemes presented in [203].

The damage mesomodel for a single ply is schematically described in Figure 6.2, executed in incremental steps. In general, for each ply in the laminate, an array of current total strain increments $\dot{\boldsymbol{\varepsilon}}$ is passed to the subroutine, along with stress, strain, and other state variables from the 'previous' step $(n-1)$, which are then used to compute the new 'updated' state variables according to the damaged-elastoplastic constitutive laws described in the previous sections.

The algorithm initiates assuming that deformation is fully elastic, i.e. the strains in the current strain increment tensor are all elastic ($\dot{\boldsymbol{\varepsilon}}^e = \dot{\boldsymbol{\varepsilon}}$), and there is no change in plasticity ($\dot{\tilde{p}} = 0$). A trial stress increment tensor $\dot{\boldsymbol{\sigma}}^{\text{try}}$ is computed based on this assumption of elastic deformation, using the differential form of the elastic relation:

$$\dot{\boldsymbol{\sigma}}^{\text{try}} = \tilde{\mathcal{L}}_{(n-1)} : \dot{\boldsymbol{\varepsilon}}^e + \dot{\tilde{\mathcal{L}}} : \boldsymbol{\varepsilon}^e_{(n-1)} = \tilde{\mathcal{L}}_{(n-1)} : \dot{\boldsymbol{\varepsilon}}^e \tag{6.21}$$

where $\dot{\tilde{\mathcal{L}}} = 0$ is assumed, i.e. previous stiffness is still considered valid until higher damage values are computed in the next step. A system of equations consisting of damage force equations (6.8)–(6.9), damage evolution functions (6.11), stiffness components update (6.2), and damaged-elastic relationship (6.12) are solved together iteratively, using repeated revised guesses of $\dot{\boldsymbol{\sigma}}^{\text{try}}$), to compute damage variables $\boldsymbol{d}$ such that all three sub-functions in $\boldsymbol{\Phi}_d = 0$. During this iterative solving process, the stiffness tensor is continually updated. Next, the effective stresses $\tilde{\boldsymbol{\sigma}}$ are computed from (6.5) and, along with the current plastic assumption $\tilde{p}^{\text{try}}$, is inserted into the yield functions in $\boldsymbol{\Phi}_p$ from (6.17) to check for plasticity. If the

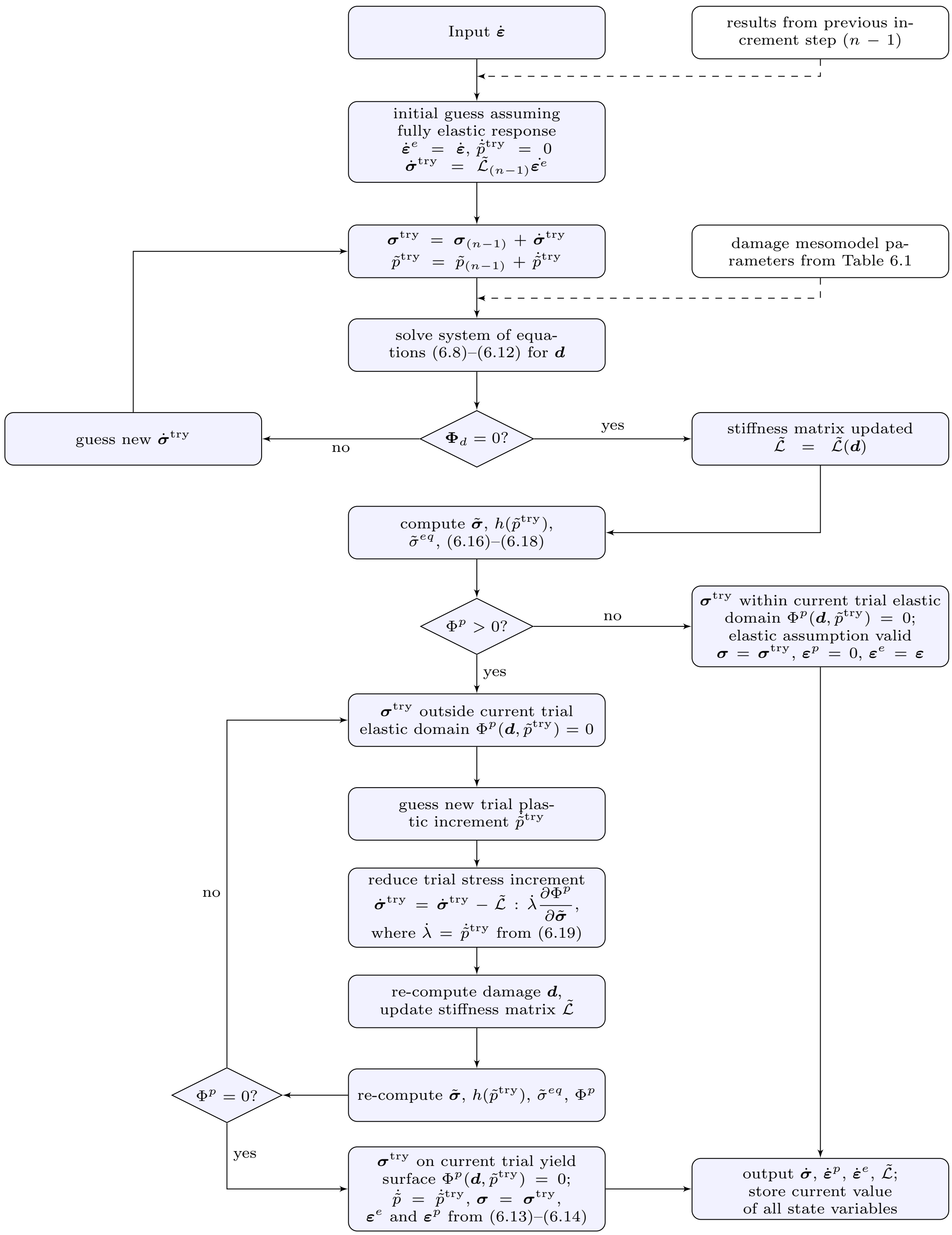

Figure 6.2: Flowchart of ply damage mesomodel algorithm

current stress state is found to exceed the elastic domain, i.e. if $\mathbf{\Phi}_p > 0$ is detected, then the plasticity subroutine is initiated; otherwise the elastic assumption is found valid and the current trial stress is considered the actual stress state.

As noted earlier, damage and plasticity is coupled by use of (i) the effective stresses in the yield functions, and (ii) the damaged stiffness tensor to compute the relationship (6.14). When the plasticity subroutine is initiated, new non-zero, non-negative values of $\dot{\tilde{p}}^{\text{try}}$ have to be guessed, since original elastic assumption was found invalid. A larger system of nonlinear equations consisting of the damage evolution relations (6.8)–(6.11), additive strain decomposition (6.13), damaged elastoplastic relation (6.14), strain increment relations (6.15), (6.19)–(6.20), hardening-yield evolution functions (6.16)–(6.18), are solved together iteratively for $\tilde{p}^{\text{try}}$ (and corresponding $\boldsymbol{\sigma}^{\text{try}}$), until both sub-functions in $\mathbf{\Phi}^p = 0$. This iterative solving to find the stress state $\tilde{\boldsymbol{\sigma}}$ that falls on the new hardened yield surfaces $\mathbf{\Phi}^p$ can be understood as the well-known *return-mapping algorithm* from classical computational plasticity [161; 202; 204], where the trial stress state $\boldsymbol{\sigma}^{\text{try}}$ is 'corrected' by downscaling it back along the plastic flow direction vector $\dfrac{\partial \Phi^p}{\partial \tilde{\boldsymbol{\sigma}}}$ to 'return' it on to the current yield surface. The trial-prediction/correction iteration step can be derived from the damaged-elastoplastic relation (6.14) and expressed as:

$$\dot{\boldsymbol{\sigma}}^{\text{try}} = \overbrace{\tilde{\mathcal{L}}_{(k-1)} : \dot{\boldsymbol{\varepsilon}}}^{\dot{\boldsymbol{\sigma}}^{\text{try}}_{(k-1)}} - \tilde{\mathcal{L}} : \dot{\boldsymbol{\varepsilon}}^p = \dot{\boldsymbol{\sigma}}^{\text{try}}_{(k-1)} \underbrace{- \tilde{\mathcal{L}} : \dot{\lambda} \frac{\partial \Phi^p}{\partial \tilde{\boldsymbol{\sigma}}}}_{\text{plastic corrector}} \tag{6.22}$$

where k is the iteration counter, $\dot{\boldsymbol{\sigma}}^{\text{try}}$ is the current iteration guess, $\dot{\boldsymbol{\sigma}}^{\text{try}}_{(k-1)}$ is the previous iteration guess, which in this case is the *elastic predictor* $\left(\tilde{\mathcal{L}}_{(k-1)} : \dot{\boldsymbol{\varepsilon}}\right)$, and $\dot{\lambda}$ is the plastic multiplier (may be understood as a 'scaling factor' for the flow direction vector that determines the magnitude of plastic increment, see Section 3.2.8.2), and $\left(-\tilde{\mathcal{L}} : \dot{\lambda} \dfrac{\partial \Phi^p}{\partial \tilde{\boldsymbol{\sigma}}}\right)$ is the backtracking *plastic corrector* term that is used to reduce the previous trial stress.

After solution convergence, i.e. when $\mathbf{\Phi}^p = 0$, all state variables from the last iteration are returned by the subroutine.

6.3.4.2 Implementation within a multi-ply framework

The above in-plane single-ply damage mesomodel for NFCs was implemented by incorporating it into an existing open-source code for multi-ply laminate response, available from the 'SMARTplus' package (Smart Materials Algorithms and Research Tools) [205]. This is a collection of C++ libraries developed by several collaborating institutions, primarily the *Laboratoire d'étude des microstructures et de mécanique des matériaux*[16] (LEM3) in Metz, France, which is jointly operated by Arts et Métiers ParisTech[17], the University of Lorraine, and CNRS[18]. The coding and incorporation of the single-ply damage algorithm into a broader multi-ply laminate simulation was accomplished in collaboration with Dr. Yves Chemisky of LEM3/Arts et Métiers ParisTech, who is a co-author of the paper [189] that is based on this chapter.

[16] Laboratory for the Study of Microstructures and Mechanics of Materials; `http://www.lem3.univ-lorraine.fr/`

[17] formerly *École nationale supérieure d'arts et métiers* (ENSAM)

[18] *Centre national de la recherche scientifique*; The National Centre for Scientific Research is a public organisation overseen by the Ministry of Education and Research, France; `http://www.cnrs.fr/en/aboutcnrs/overview.htm`

Since the laminate model itself is not a contribution of the present study, only a brief overview of its features, along with relevant references for further reading, is given here. The SMARTplus solver uses the *material point method* to simulate specimen behaviour. The global laminate response is determined from individual ply behaviour by applying a multi-scale homogenisation procedure based on *periodic homogenisation theory*, which follows the principles introduced in the pioneering works of Bensoussan et al. [206] and Sanchez-Palencia [207]. This approach has been successfully implemented for composite materials with plies exhibiting a strong non-linear response, such as shape-memory alloy composites [208]. A fully coupled thermomechanical approach has also been recently developed [203], which may allow further work on coupling between damage and other dissipative processes.

6.3.5 Identification of model parameters

The Flax/epoxy material properties were already investigated from mechanical tests, and are given in the previous Chapter 5. All other parameters related to damage and plasticity of the proposed model are mainly identified by applying a cost-function minimising optimisation method. The optimisation algorithm *searches* for parameters that result in predictions that best match experimental observations. Note that, to determine evolution functions for fibre-direction damage and inelasticity (equations (6.10) and (6.16)), an important contribution of this study on NFCs), it was necessary to also conduct experimental methods of identification (shown in Figures 6.3–6.4), similar to those recommended by publications on standard MDT [122–124].

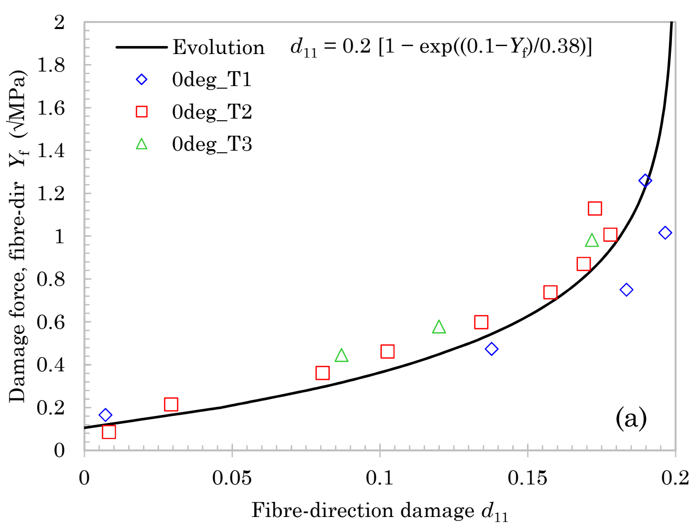

Figure 6.3: Fibre-direction tensile damage evolution function $Y_f(d_{11})$ has an exponential profile, as identified from tests on Flax-epoxy $[0]_{16}$ specimens.

A computational identification approach necessitates running the numerical damage model, since no analytical closed-form solution is available for such nonlinear ply response – or, if one exists, it has not been explored yet due to the dependence of such relations on the constitutive model adopted and composite configurations. The proposed scheme is an inverse identification procedure based on a hybrid genetic/gradient method [209] that combines an evolutionary-genetic algorithm with the Levenberg-Marquardt algorithm

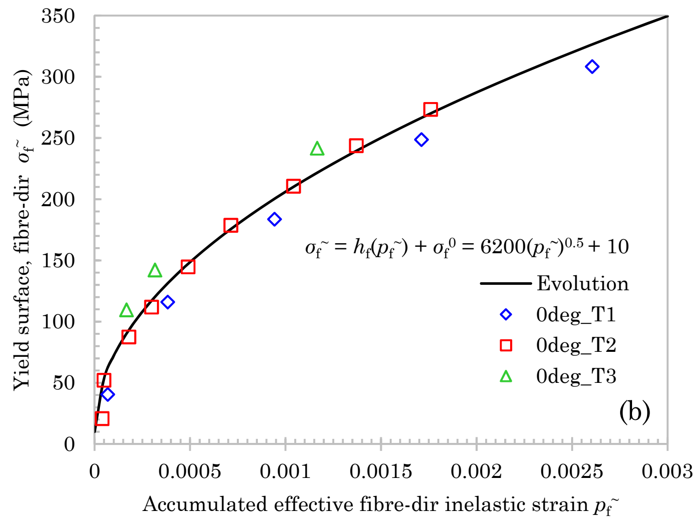

Figure 6.4: Fibre-direction tensile inelasticity evolution and plastic hardening function $\sigma_f^0 + h_f(\tilde{p}_f)$ identified from tests on Flax-epoxy $[0]_{16}$ specimens. Hardening follows a power law.

to minimise the cost function. Such a procedure is able to identify material parameters directly from the modelled structure, e.g. a multi-ply composite, involving different stacking sequences and loading configurations.

The identification problem is determining parameters that minimise the difference between computed and experimental data. An applied stress loading path is used to define the boundary value problem of the multi-ply numerical simulation, so the resulting strains (specimen longitudinal and transverse) are used to define the cost function:

$$C(\mathbf{p}) = \frac{1}{2}\left(\frac{\sum_t \sum_{stackseq}\left(\varepsilon_{xx}^{\mathrm{num}}(\mathbf{p}) - \varepsilon_{xx}^{\mathrm{exp}}\right)^2}{\sum_t \sum_{stackseq}\left(\varepsilon_{xx}^{\mathrm{exp}}\right)^2} + \frac{\sum_t \sum_{stackseq}\left(\varepsilon_{yy}^{\mathrm{num}}(\mathbf{p}) - \varepsilon_{yy}^{\mathrm{exp}}\right)^2}{\sum_t \sum_{stackseq}\left(\varepsilon_{yy}^{\mathrm{exp}}\right)^2}\right) \tag{6.23}$$

where $C(\mathbf{p})$ is the cost function, $\varepsilon_{xx}^{\mathrm{exp}}$ and $\varepsilon_{yy}^{\mathrm{exp}}$ represent the longitudinal and transverse strains, respectively, from a test performed with ply stacking sequence *stackseq*; $\varepsilon_{xx}^{\mathrm{num}}$ and $\varepsilon_{yy}^{\mathrm{num}}$ represent the corresponding values computed using the multiscale model; and $\mathbf{p}$ denotes the set of guessed parameters. Since the experimental data include repeated tests of various laminate architectures, an equal weighting of all stacking sequences was considered.

Optimisation algorithms must account for local minima, which are expected here considering the presence of multiple nonlinear phenomena. Since gradient-based techniques ensure convergence to a local minima, an heuristic such as genetic algorithm is utilised simultaneously with a gradient-based one, to determine preferential sets of parameters and avoid, as much as possible, convergences to local minima. The identified parameters are all listed in Table 6.1.

Table 6.1: Identified model parameters for Flax/epoxy laminate in-plane damaged response

Material properties			Shear damage		
E_1^0	31	GPa	$Y_{12}^{\max}$	2.96	MPa
$\varepsilon_{11}^{\max}$	1.6	%	Y_s^0	0.01	$\sqrt{\text{MPa}}$
ν_{12}^0	0.353		Y_s^c	2.5	$\sqrt{\text{MPa}}$
E_2^0	4.6	GPa	**Transverse coupled damage**		
ν_{21}^0	0.063		b	14	
G_{12}^0	2.0	GPa	$Y_{22}^{\max}$	1.237	MPa
Fibre-direction damage			Y_t^0	0.51	$\sqrt{\text{MPa}}$
Y_f^0	0.1	$\sqrt{\text{MPa}}$	Y_t^c	6.8	$\sqrt{\text{MPa}}$
$d_{\lim}$	0.2		**Transverse-Shear yield & inelasticity**		
m	0.38	$\sqrt{\text{MPa}}$	A_{ts}	2.195	
Fibre-direction yield & inelasticity			σ_{ts}^0	16	MPa
σ_f^0	10	MPa	α_{ts}	0.16009	
α_f	0.54		β_{ts}	180	
β_f	6200				

6.4 Results, Validation and Discussion

The model proposed in this study was executed and the results were validated for both synthetic laminates (T300/914 Carbon/epoxy) and natural fibre-based laminates (Flax/epoxy).

6.4.1 Carbon/epoxy (T300/914)

To validate the incremental periodic homogenisation scheme integrated in this multi-ply damage model, simulations of stress-strain response for T300/914 Carbon/epoxy laminates with various fibres orientation were compared with standard MDT model predictions and experimental data published by Le Dantec [123] and Ladevèze and Le Dantec [122]. As can be seen in Figure 6.5, predictions by this model and those by Ladevèze and Le Dantec are very similar, confirming that the periodic homogenisation-based multi-ply response adopted in this study is robust, in a sense that it can simulate laminates with a variety of fibre orientations and is also capable of producing reliable damaged response predictions.

Note that such results were obtained using parameters identified using the optimisation algorithm, which thus incorporates the inherent non-linear response of the plies and not the linear elastic approximation present in Ladevèze and Le Dantec [122]. The determination of plies parameters based on the

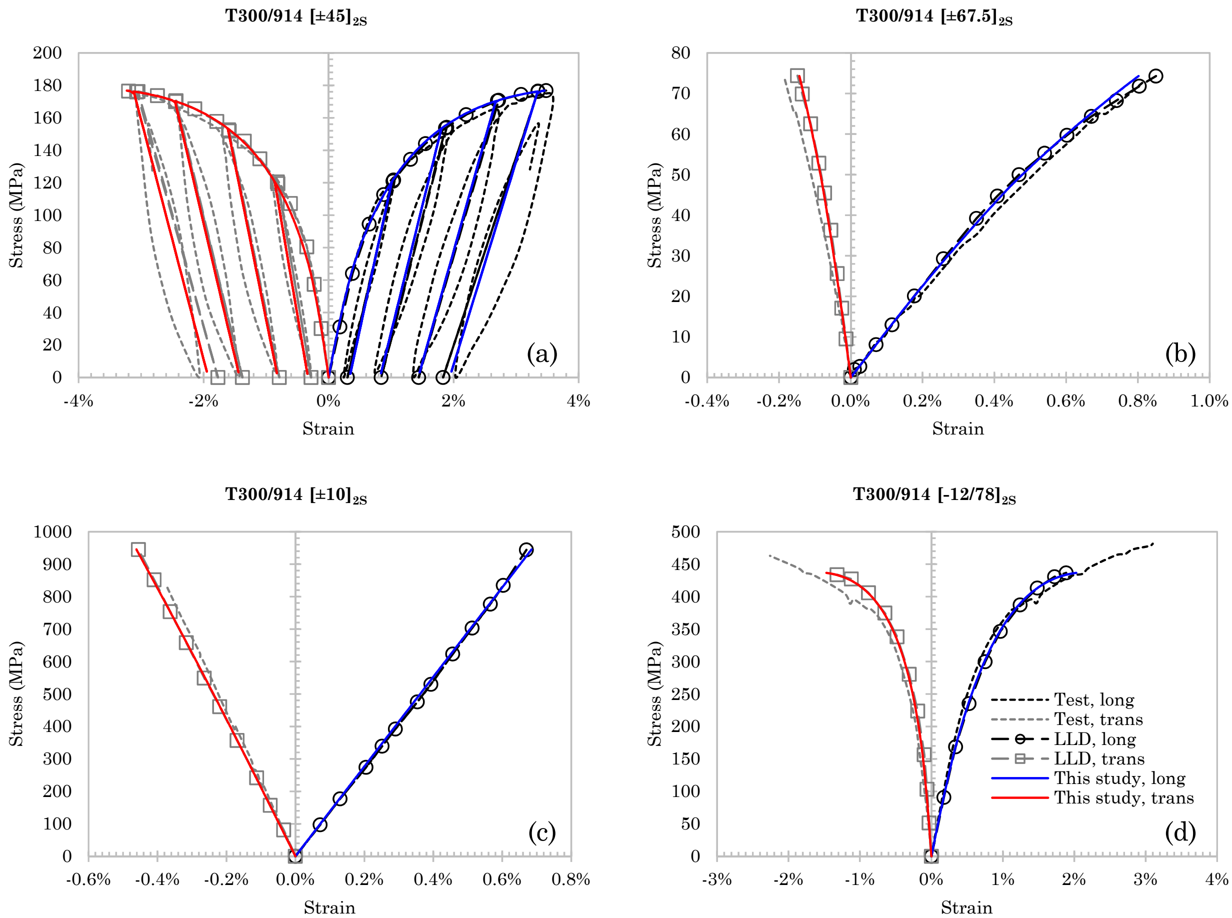

Figure 6.5: Comparing simulations by model proposed in this study with published Ladevèze-Le Dantec (LLD) model predictions [122–124], for T300/914 Carbon/epoxy laminates. Corresponding test data adapted from [123].

non-linear behaviour of the plies is essential to properly consider the local stress state, which strongly depends on the development of permanent strains and thus the strain mismatch between the plies.

6.4.2 Flax/epoxy

Publications on the standard MDT model recommend cycled load-unload tests on [0], [90], $[\pm 45]_S$, and $[\pm 67.5]_S$ laminates to determine the material properties and parameter set [122; 124]. Using the cost-function minimising optimisation method discussed earlier, this study identified parameters for Flax/epoxy laminates based on the tested response of these 'standard' laminates. Cycled progressive loading tests on $[0]_{16}$ provide fibre-direction material properties (E_1^0, ε_{11}^u, ν_{12}^0) and evolution parameters for damage (Y_f^0, d_{lim}, m) and inelasticity (σ_f^0, α_f, β_f). Tests on $[90]_{16}$, $[\pm 45]_{4S}$, and $[\pm 67.5]_{4S}$ allow identification of in-plane transverse and shear material properties (E_2^0, ν_{12}^0, G_{12}^0), evolution parameters for shear-transverse coupled damage (Y_s^0, Y_s^c, Y_t^0, Y_t^c, b, $Y_{22}^{\max}$, $Y_{12}^{\max}$) and inelasticity (σ_{ts}^0, α_{ts}, β_{ts}, A_{ts}).

At least four cycled progressive loading tests were conducted per laminate. The parameters thus identified are listed in Table 6.1, and the simulation results for these laminates are plotted along with experimental response in Figures 6.6 and 6.7. Note that, to maintain clarity of demonstration, only one cycled test is shown for each laminate. A very good agreement is observed between experimental and simulated response for most laminates, including predictions of damaged-condition modulus and residual strain (refer back to Figure 5.1 for definitions). Figures 6.6(a) and (c) compare simulation with tested monotonic response of three specimens each along fibre- and transverse directions, respectively; whereas Figures 6.6(b) and (d) make similar comparisons to demonstrate the close agreement of predicted damaged-state modulus E and inelastic strain ε^p at each unload-reload cycle.

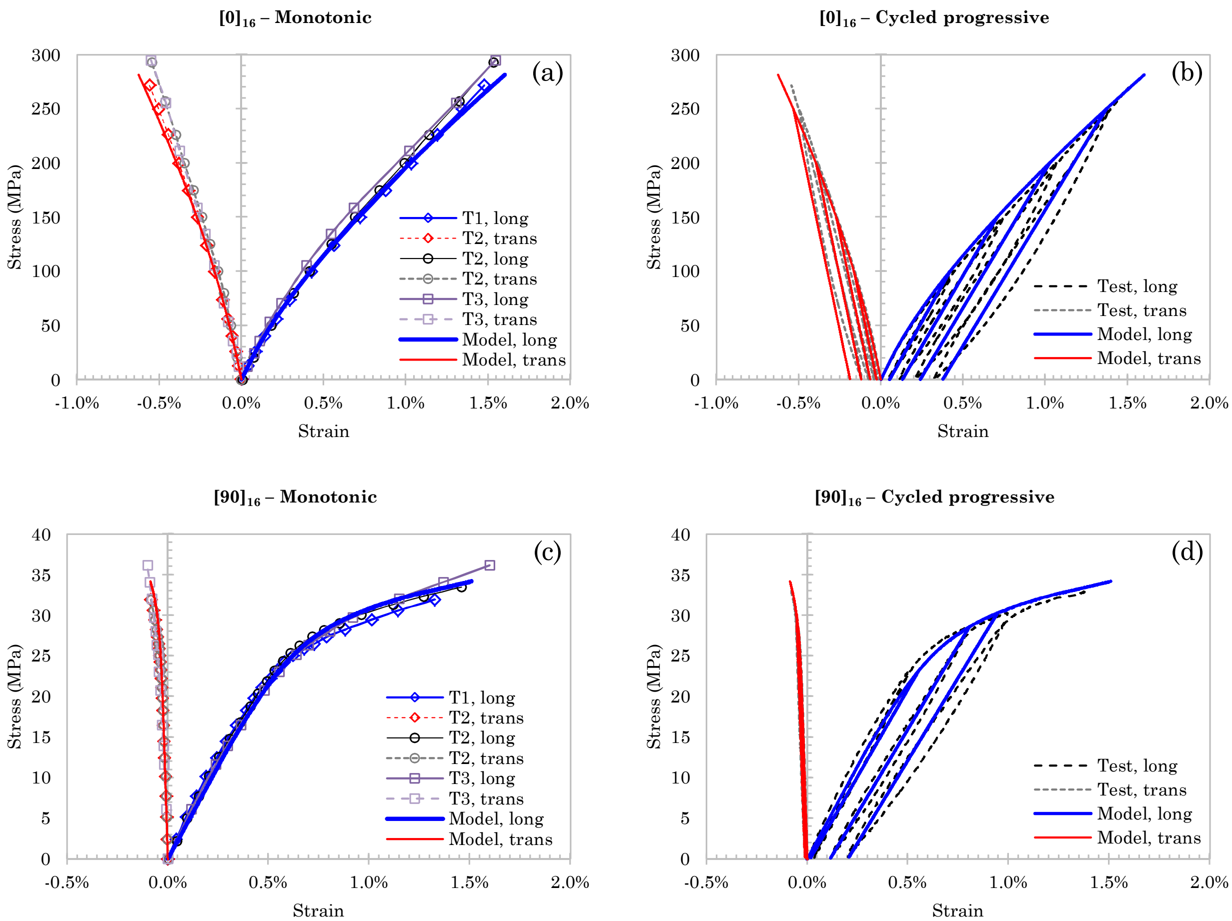

Figure 6.6: Comparison of model simulation with experimental tests for $[0]_{16}$ and $[90]_{16}$ Flax-epoxy specimens. Monotonic tests (left) compare overall laminate response; cycled progressive loading tests (right) compare evolving modulus and permanent strain.

Figure 6.7 provides similar comparative demonstration for $[\pm 45]_{4S}$ and $[\pm 67.5]_{4S}$ specimens. Of note is the model prediction for $[\pm 45]_{4S}$: while accurately predicting overall laminate response for most of the loading (see Figure 6.7(b)), this model predicts failure at a much lower strain ($\sim$2.5%) than observed in experimental specimens (9-12%, see Figure 6.7(a)) – but, at a failure stress that matches experiments (75-78 MPa). The simulated response diverges from the experimental after $\sim$1.7% laminate strain, as seen when comparing plots in Figure 6.7(a). The apparent ductile response and large strains observed in tested

$[\pm 45]_S$ specimens is well-documented for Flax-epoxy [22; 178; 185], and is attributed to the rotation of plies towards the loading axis [178; 195]. The model prediction begins to diverge at around the same loading point at which ply-rotation is found to initiate, which is expected since the model continues to enforce a ±45 fibre angle and does not account for any reorientation before failure. The similar discrepancy between experimental and simulated Flax-epoxy $[\pm 45]_S$ response was also observed and discussed by Andersons et al. [195].

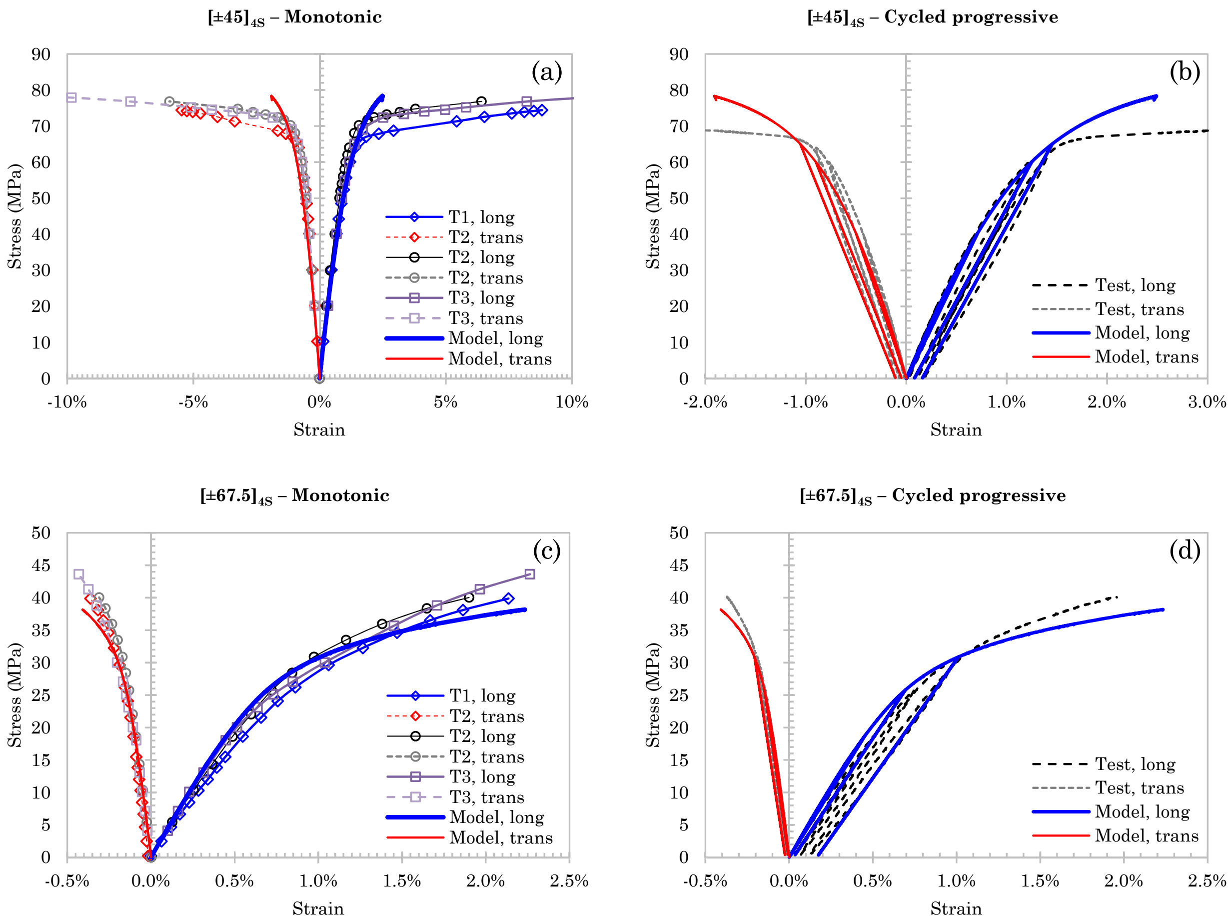

Figure 6.7: Comparison of model simulation with experimental tests for $[\pm 45]_{4S}$ and $[\pm 67.5]_{4S}$ Flax-epoxy specimens. Monotonic tests (left) compare overall laminate response; cycled progressive loading tests (right) compare evolving modulus and permanent strain.

The good agreement between tested and simulated response confirms that the damage and inelasticity evolution laws developed for this modified-MDT model (Φ_d and Φ^p), including those proposed for the decoupled fibre-direction (Figures 6.3–6.4), are appropriately formulated to simulate NFC in-plane tensile response. To further demonstrate the predictive power of the proposed modified-MDT model, numerical simulation is executed for other commonly-studied laminates: angle-ply $[45]_{16}$, cross-ply $[0/90]_{4S}$, and quasi-isotropic $[0/-45/90/+45]_{2S}$; shown in Figure 6.8. As can be seen, the numerical simulations continue to be in close agreement with tested observations, thus indicating that the multi-ply damaged response model developed in this study is flexible and predictive.

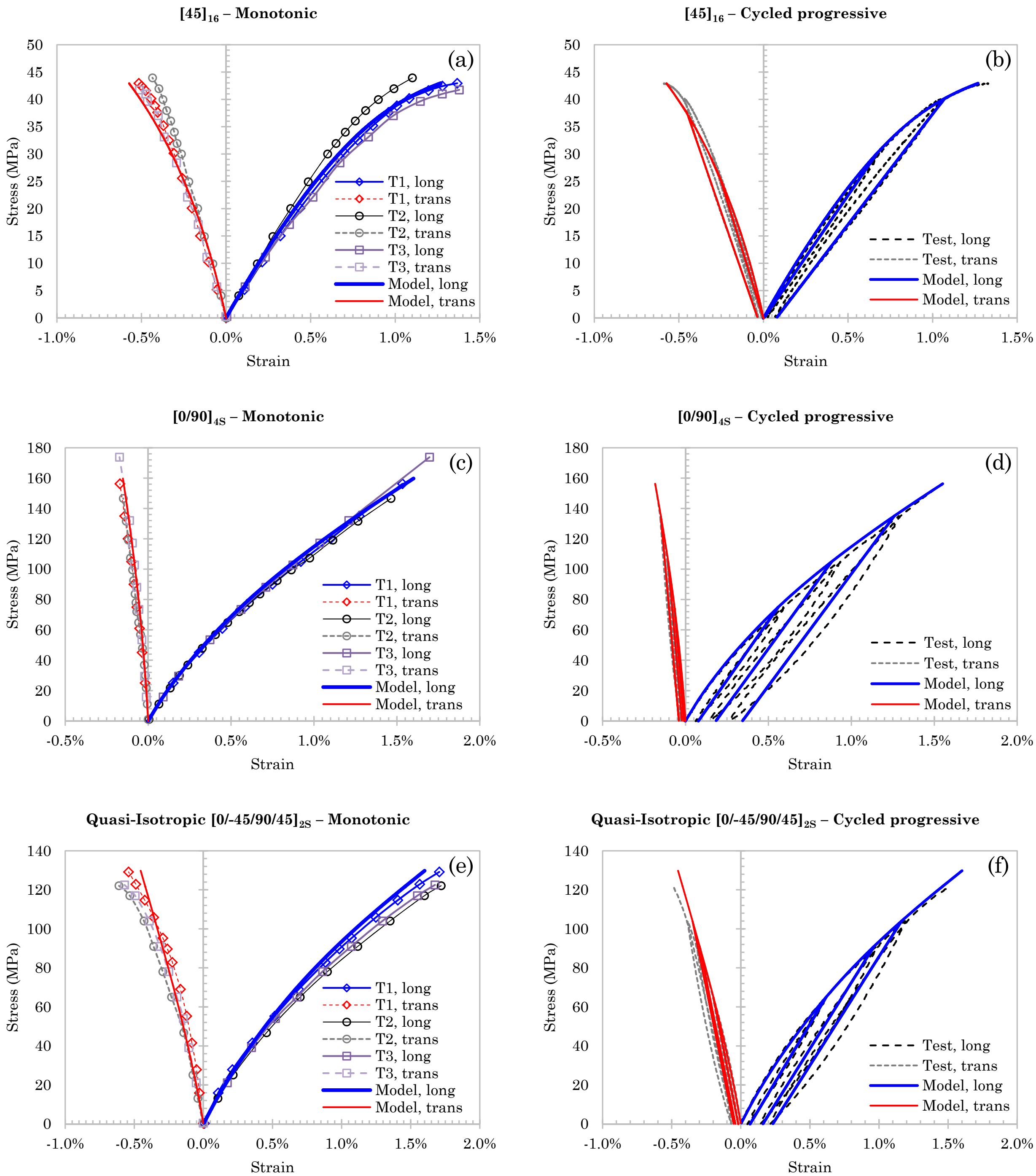

Figure 6.8: Model prediction compared with experimental tests for angle-ply $[45]_{16}$, cross-ply $[0/90]_{4S}$, and quasi-isotropic $[0/-45/90/45]_{2S}$ Flax-epoxy laminates. Monotonic tests (left) compare overall laminate response; cycled progressive loading tests (right) compare evolving modulus and permanent strain.

6.4.3 Further discussion

The ply-level, or mesoscale, is chosen to be the basic scale of modelling, since quantification of the internal damaged state is still possible at this scale (via mean ply damage and plasticity state variables), unlike at the laminate scale (macroscale), without sacrificing computational simplicity as in the case with micromechanical modelling. The modification to the standard MDT proposes nonlinear stiffness degradation and permanent strain accumulation for both fibre-direction and coupled transverse-shear response, where the evolution laws for each are formulated based on experimental observations of NFCs – particularly Flax/epoxy laminates. The unique damage and inelasticity parameters assigned for each in-plane principal direction allows the orthotropic damage effects within each ply to be followed separately. Insight can thus be obtained on the contribution of each variable to the ply response, and subsequently, the contribution of each ply to the mechanical health of the overall laminate under loading.

As the global laminate mechanical response is a function of the plies within, a multi-scale periodic homogenisation scheme (presented in [203; 208]) is adopted to derive the laminate mechanical properties from the individual ply damaged response. An inverse method (cost-function minimisation approach) is applied to identify model parameters specifically for a continuous Flax fibre reinforced epoxy composite. As can be clearly observed from the numerical simulation plots in Figures 6.5–6.8, the modified-MDT model is able to well simulate the damaged modulus and inelastic strain, and thereby predict the complex nonlinear NFC laminate response. In addition, the identified Flax-specific parameters result in predictions that closely match experimental observations (Figures 6.6, 6.7 and 6.8).

6.5 Future work and scope for model expansion

A notable feature of the proposed model is that it does not employ a separate 'interface' layer, as is considered by many MDT-based laminate damage models [136; 141; 152], since a ply-layer-only model is able to well capture the tensile response of Flax/epoxy NFCs considered in this study (see Figures 6.5, 6.6, 6.7 and 6.8) without the additional complexity of an interface model. If inter-ply delamination mechanisms are of interest, an interface layer may be incorporated by following the approach shown in [91; 141; 152; 210]. A limitation of this mesoscale model is that, while multiple damage mechanisms may contribute towards stiffness degradation along a particular direction, all such mechanisms are expressed by only a single damage variable, so the model does not distinguish each distinct damage type at the constituent level. For instance, as discussed earlier in Chapter 2, fibre-direction damage involves both cracking in the Flax fibre cell walls, reorganisation of microfibrils, and separation of elementary fibres due to breakdown in the pectin adhesion [55; 95]; however, both are represented by only the single variable d_{11} in this model. If separate quantification of individual damage mechanisms is desired, a micromechanical model may be necessary where each contributing damage mode is assigned a unique damage variable and evolution law, similar in approach to that in [199].

Reported creep tests have confirmed the viscous nature of NFC response [198]. If isolating viscoelastic or viscoplastic response is of interest, the inelastic dissipation in this proposed model may be re-formulated similar to that proposed by Poilâne et al. [198], where the total strain is split into elastic, viscoelastic and viscoplastic components, with experimentally-vetted platicity evolution laws defined to allow kinematic hardening. The same study also demonstrated a marked dependence of NFC fibre-direction response on operating temperature and rate of applied strain. Figure 6.9, adapted from the work of Poilâne et al. [198], reveals an *inverse relationship* between fibre-direction material properties (modulus, strength) and rate of applied strain, as well as operating temperature; however, with insignificant (or inconclusive) effect of either factor on failure strain. Such dependence on strain rate or temperature is also probable for transverse or shear response.

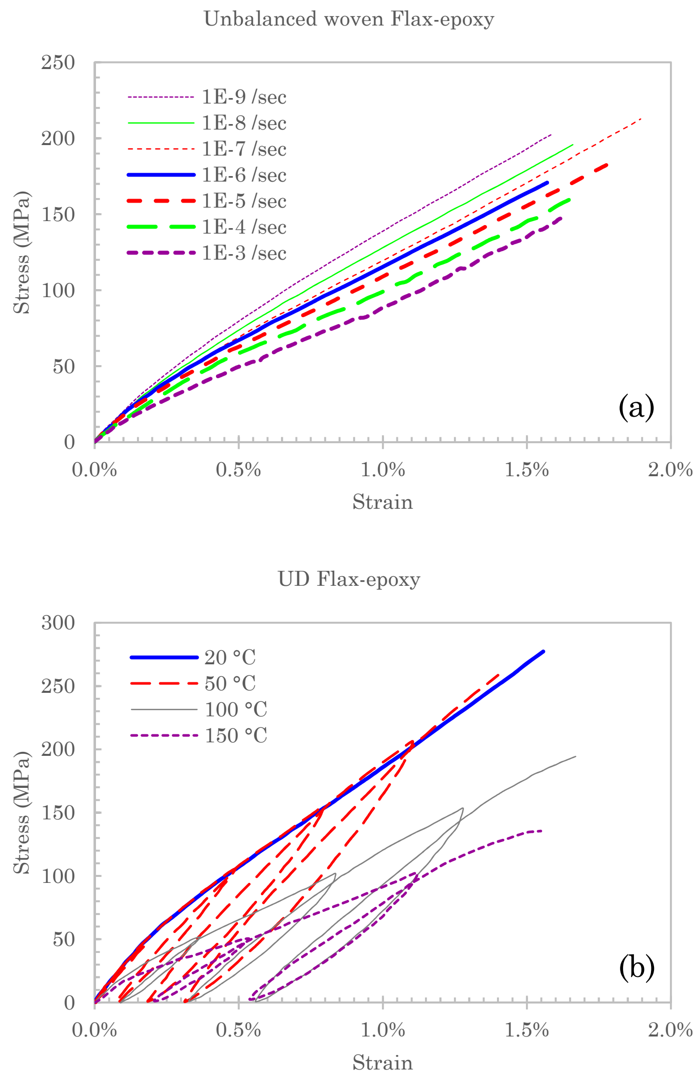

Figure 6.9: (a) Unbalanced-fabric Flax-epoxy response in fibre-dominant direction at different applied strain rates, and (b) UD Flax-epoxy fibre-direction response at different ambient temperatures; both figures adapted from [198]

As far as fibre-direction response is concerned, correlation with strain rate appears to be roughly proportional on a logarithmic scale (Figure 6.9(a)), i.e. the reduction in modulus or failure stress is about the same for each strain rate increase of one order of magnitude. The temperature relationship does not appear to be proportional from the data available (Figure 6.9(b)), but it must be noted that, since the source authors Poilâne et al. [198] reported only one test per operating temperature, the data

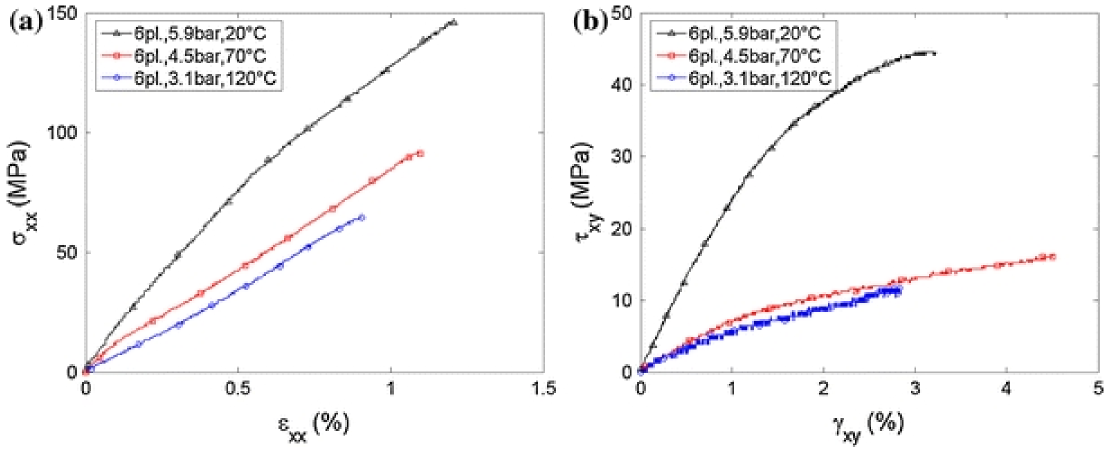

Figure 6.10: Flax-epoxy monotonic behaviour under different ambient temperatures: (a) $[0/90]_{nS}$ longitudinal response, and (b) $[\pm 45]_{nS}$ shear response. Reproduced with permission from [176].

is insufficient to conclusively determine a trend. However, it may be safe to accept that there is no apparent effect on material response between 20-50 °C, after which there is *significant* reduction in both strength and modulus. This reduction in fibre-direction properties may be due to a possible 'softening' in fibre structure, and due to transition of the epoxy matrix from a hard, glassy state to a rubbery state (the epoxy-hardener combination reported in [198] has a glass transition temperature T_g = ~140 °C, per manufacturer datasheet).

In this study, the parameter set identified for Flax/epoxy is for response under a 2 mm/min strain rate, at laboratory room temperature ~20 °C. To apply this model for different loading rates or temperature conditions (at least for >50 °C), the fibre-direction damage parameters *may* need to be re-identified. Alternatively, if identifying new parameter sets is inconvenient: considering failure strain remains uninfluenced while modulus and failure stress is affected, and assuming that the identified damage evolution laws in Equation (6.10) still hold true, dependence on strain rate or temperature may be modelled by applying appropriate 'scale factors' to scale up or down the simulated modulus E (Equation (6.2)) – similar to the approach used in [210]. To expand the model further for in-plane transverse and shear response at different strain rates or temperatures, the relevant damage and inelastic evolution laws can be re-examined and, if necessary, re-formulated based on experimental observation.

6.6 Conclusion

In summary, this study adopts a thermodynamically consistent Continuum Damage Mechanics (CDM) based approach to develop a predictive model for tensile response in natural fibre reinforced composites (NFC). On account of fibre-specific damage mechanisms unique to hierarchical fibrous structures like plant fibres, NFCs tend to exhibit considerable nonlinearity in their fibre-direction response (unlike traditional Glass or Carbon fibre composites) – which is accounted for in the damage model developed in this study in the form of nonlinear evolutions of stiffness and inelasticity. The effect of well-known NFC damage mechanisms (fibre cell-wall cracking, axial splitting of fibre bundles, fibre-matrix debonding, matrix damage, and inelasticity) are captured through the state variables for damage and inelastic dissipation, defined along the lines of standard Mesoscale Damage Theory (MDT) first introduced by Ladevèze and Le Dantec [122; 123], and elaborated by Herakovich [124]. Experimental observations of continuous Flax fibre reinforced epoxy material are used to develop the model and identify Flax-specific model parameters. The model is found to offer very good predictions of room-temperature tensile response for various Flax/epoxy laminate configurations. Limitations of the model (discussed in the previous section) notwithstanding, this modified-MDT damage model offers a powerful means of capturing damaged mechanical response in multi-ply NFC laminates, and a viable mesoscale alternative to the few macroscale or micromechanical approaches proposed for NFCs to date (reviewed earlier). The damage model and Flax-specific parameters can be incorporated in a user-defined material properties subroutine, e.g. as part of a finite element structural model, thereby enabling the convenient design and development of Flax fibre reinforced load-bearing structures.

Chapter 7

Fatigue response, constant stress amplitude

This chapter reviews most existing fatigue studies on natural fibre composite (NFC) fatigue. The reported fatigue endurance of, and damage mechanisms in, composites reinforced by different natural fibres (including flax, sisal, jute, and hemp), arranged in different laminate architectures, are collated and analysed. Stress-life relationships for most common NFC configurations are quantified, and compared with those of equivalent Glass-composites. The progressive stiffness increase in the fibre-direction reported for fatiguing Flax-epoxy composites is critically studied. Limitations and ambiguity of current knowledge of NFC fatigue behaviour are identified.

The work detailed in this chapter is published in the following peer-reviewed article [211]:

Z. Mahboob and H. Bougherara. Fatigue of flax-epoxy and other plant fibre composites: Critical review and analysis, *Composites Part A: Applied Science and Manufacturing* 109 (2018) 440-462. doi: 10.1016/j.compositesa.2018.03.034.

7.1 Introduction

It is well documented that fatigue-related mechanisms are responsible for many, if not most, failures in engineering structures where dynamic repetitive loading (vibration, rotation, wind and wave action, turbulence, pressurisation, etc) at levels much lower than ultimate strengths still result in sudden and catastrophic failure due to internal damage accumulation over a period of time [212–214]. It follows that determining the fatigue life and observing fatiguing mechanical properties (damaged response) is an essential aspect of characterising a fibre-composite.

Fatigue performance investigations usually begin with an intensive experimentation program to observe the macroscopic changes in composite properties (e.g. as a function of fatigue cycles), and to determine 'time to failure' under cyclic loading (i.e. generating stress-life or strain-life plots, constant life diagrams, etc). The subject specimens in such experiments may vary in form and size, from standardised specimens (small scale, regular geometry), to prototype components (intermediate scale, complex geometry), and structures (full-scale design verification) [213]. Depending on the purpose of the investigation, the cyclic loading test may vary several features: loading direction (uniaxial, biaxial, multiaxial), loading amplitude (constant or varying), loading control mode (stress-controlled or displacement-controlled), min-max loading ratio (tension-tension, tension-compression, compression-compression), frequency (constant or varying), ambient environmental conditions (temperature, moisture), presence of defects (notches, holes), etc [213; 214]. Characterisation studies on novel materials, however, tend to focus on small-scale specimens under constant amplitude uniaxial loading, the results of which can be conveniently reproduced and compared with similar data for other materials. Such tests of basic layup architectures reveal fundamental damage mechanisms, thereby allowing the development of theoretical models to predict macroscopic damaged response and failure.

As discussed in the introductory chapters, natural fibre reinforced materials are a relatively new class of fibre-composites. Being given serious academic attention for engineering applications only recently, research on their fatigue behaviour is still limited. Only in the last decade has there been a steady rise in available fatigue test data for natural fibre composites (NFCs) [25; 31; 50; 94; 103; 108–110; 112–116; 119; 175; 215–218], of which only a handful of publications have studied Flax-composite fatigue response [25; 50; 103; 108–110; 112; 115; 175] – all in the last five years.

This chapter reviews and analyses the literature on all openly-available original fatigue-related NFC studies (to the best of the author's knowledge), excluding those on composites of hybrid natural-and-synthetic reinforcement. The subsequent analysis collates disparate data on NFC fatigue performance in order to investigate and, where possible, quantify trends in endurance (S-N curves), effects of varying testing parameters or laminate architecture, damage accumulation behaviour, and the suitability of potential damage indicators.

7.1.1 Review of NFC fatigue studies

Reported fatigue studies on NFCs were reviewed earlier in Chapter 2, section 2.3. These studies are all conducted under stress-amplitude control. Data from these studies are used in an original analysis of fatigue endurance and damage accumulation detailed in the following sections.

7.1.2 On general NFC fatigue characteristics

In summary, the following damaged response and failure characteristics of NFCs have been evidenced in constant stress amplitude fatigue studies published to date:

1. Fatigue damage mechanisms causing strength and stiffness degradation in cellulosic NFCs seem to be independent of plant type, at least when comparing composites of Flax, Hemp, and Jute [115].

2. NFC laminates with higher static tensile strengths demonstrate longer fatigue lives (number of cycles to failure), delayed damage initiation, and slower damage progression [50; 109; 110; 115].

3. Strain amplitude is continually increasing for all laminate architectures under constant stress amplitude cycling, typically following a 3-stage evolution trend where the first and last stages show a more rapid increase than that in the middle stage. This is evidenced by measurements of total strain [25; 112], permanent (residual) strain [50; 106; 109; 110], mean strain [103], and minimum cycle strain [25; 112]. Most permanent strain accumulation occurs early in the fatigue life, during the first stage [109].

4. Monotonic static tensile properties (stress-strain response, modulus, ultimate strength, failure strain) of all Flax-epoxy laminate architectures tested by Bensadoun et al. [109; 110], appear to be statistically *unchanged* even after fatiguing for 500,000 cycles at 0.3UTS – with the exception of low-twist twill fabric reinforced specimens (see Figure 2.29).

5. Damage and failure modes in NFCs under fatigue conditions appear identical to those identified for quasi-static loading: fibre wall cracking, intra-bundle cracking (separation of elementary fibres), fibre-matrix debonding, fibre pull-out, brittle fibre-fracture, and delamination [50; 103; 108]. Cracking in matrix-rich regions are not typically observed [50].

6. Microscopic crack density or count correlates very well with the increase in inelastic and mean strain [50; 103], thereby directly linking internal damage with an externally observable material property.

7. Water-ageing reduces fatigue life, and increases dissipated strain energy, suggesting that moisture ingress encourages damage activity in NFCs [94; 112; 118]. Evidence from acoustic emission studies [112] and post-mortem micrography [94; 118] indicates that moisture degrades fibre-matrix adhesion, thereby intensifying damage progression and hastening fatigue failure .

8. Fibre-matrix adhesion in NFCs may be improved by alkali treatment of the fibres, which enhances load transfer between fibre and matrix, resulting in longer fatigue life of treated specimens – however significant improvement is only observed in polyester-based composites, and not in those of epoxy matrix [113; 114].

The influence of structural variation within NFCs are summarised:

1. For the case of laminates with [0] plies, higher fibre volume fractions result in increased fatigue lives, evidenced for at least up to v_f=0.4 [94; 115; 118].

2. Ply orientation stacking sequence in UD-ply laminates, and type of weave in woven-fabric laminates, have an impact on fatigue life [25; 50; 103; 109; 115] – though the effect is not significant at loading levels below 0.3UTS [109]. Angled cross-ply [±45] specimens typically endure longer than [0/90] [25; 50; 116].

3. UD [0] specimens accumulate significantly less permanent strain than cross-ply or woven-textile specimens, suggesting that intra-fibre damage mechanisms are not as intensive as fibre-matrix debonding or delamination [109; 110]. In general, UD-based laminates with more off-axis plies accumulate higher permanent strain than those with more [0] plies [25; 50; 103].

- For an angled cross-ply configuration like $[\pm 45]_{nS}$, Flax-reinforced specimens accumulate considerably *less* residual strain over their fatigue lives than Glass-reinforced specimens, when loaded at the same stress-amplitude [25; 50].
- In contrast, for layups where at least half the plies are at 0°, Flax-reinforced specimens accumulate *higher* residual strain than Glass-composites [25; 50].

4. When under the same fatigue testing parameters, stiffness evolution trend is different in NFC laminates with off-axis plies than in those with 0° reinforcement.
   - Off-axis-ply laminates exhibit a continual stiffness *decrease* over fatigue life, but laminates where at least half the reinforcement is at 0° [25; 50; 103; 106] (including in randomly-oriented short-fibre specimens [109]) tend to show a stiffness *increase* over fatigue life (2–8% increase in [0] specimens, 1–4% in [0/90] [50]).
   - Quasi-isotropic specimens are reported to show a cosntant stiffness over fatigue life [112].
   - In contrast, comparable Glass-composites of all reported architectures only exhibit degrading stiffness under fatigue [25; 38; 119].
5. Dissipated strain energy (area within hysteresis loop) *decreases* over fatigue life for NFC laminates with 0° plies [50; 113; 114] (including quasi-isotropic layups [112]), but *increases* for laminates with only off-axis plies [50]. The change in hysteresis energy from the beginning of fatigue life to the end appears to be proportional to the loading amplitude. The magnitude of dissipated energy (size of hysteresis loop) is an indicator of internal damage activity [112]. In general, [0] specimens show the smallest energy dissipation, when compared with cross-ply or woven-fabric specimens [109; 110].
6. Reports on the effect of fibre *crimp* are contradictory. Bensadoun et al. [109] did not find any influence of crimp on fatigue response. In contrast, Asgarinia et al. [108] observe that higher degrees of crimp in woven fabrics tend to result in shorter fatigue lives, since more out-of-plane fibre weaves increase sites of crack initiation, thus concluding that 'flatter' natural fibre fabrics or high-twist yarns are preferable for optimal fatigue endurance.

The influence of fatigue testing parameters are summarised:

1. Loading frequency f may influence fatigue life and observed stiffness evolution in NFCs, depending on the frequency and fibre architecture:
   - For [0] specimens, loading frequency is shown to have a significant effect on fatigue life and the degree of stiffening – but only for frequencies below 2 Hz, as shown earlier in Figure 2.28 [106]. Increasing frequency between 0.25–2 Hz results in extended fatigue lives, but reduces the relative stiffness increase. For frequencies between 2–5 Hz, no noticeable influence on fatigue life of [0] is reported [106].
   - For textile or woven-fabric laminates where the reinforcement is balanced biaxial, no significant influence of varying loading frequency (1–3 Hz) is found on fatigue life [108].
2. Loading ratio R has a clear influence on fatigue life (see Figure 2.31(a)). Higher ratios result in longer fatigue lives and less steep stress-life curves (see Figure 2.30(a)) [38; 115]. It is reasoned that

since higher ratios imply smaller stress amplitudes, test specimens experience lower stress gradients between fibre and matrix phases, thereby delaying interfacial crack initiation and progression [115].

7.2 Analysing fatigue endurance of NFCs

Literature review in section 2.3, and the preceding section summarily reviewed fatiguing mechanical behaviour of several Flax-composites and the effect of test parameters on the response of NFCs, as reported by studies to date. Considering that these studies tend to have some overlap in the composites of interest, a holistic analysis of compiled data should provide clearer insight on general NFC fatigue performance, and its comparison with equivalent Glass-composites. To that end, the constant stress amplitude *S*-*N* data from these reviewed studies [25; 38; 50; 94; 103; 108; 110; 112–116; 118; 119] are compiled in Figures 7.1–7.10.

As will be seen, different plant fibres or laminate architectures may produce the same fatigue life performance, suggesting that the initial strength of reinforcement, and the eventual strength-degrading damage mechanisms, may be similar. When such similarities are identified, these laminate groups are treated as a collective, and the combined fatigue endurance is quantified by applying a linear *S*-*N* model relationship. First, data specifically of FE laminates are studied separately to identify Flax-specific baseline performance, followed by an analysis of other NFCs that are based on different matrix material like polyester or polyethylene, or reinforced by other plant fibres like Hemp, Sisal, or Jute.

7.2.1 Flax-epoxy composites

Table 7.1 lists the source studies of the Flax-epoxy (FE) fatigue data, and other relevant data that will aid interpretation of the developed *S*-*N* plots. In the Figures 7.1-7.5, linearised median *S*-*N* trends are estimated for each FE laminate group (UD, crossply, angled-crossply, woven, random-oriented short-fibre mat, etc) following the procedure detailed in ASTM E739 [219], assuming a (i) normal distribution for $\log(N_\mathrm{f})$ and (ii) constant standard deviation at all load levels:

$$\log\left(N_\mathrm{f}\right) = A + B \cdot \sigma_\mathrm{max} \tag{7.1}$$

where N_f is fatigue life, i.e. number of cycles until failure (dependent variable), σ_max is the commanded *peak stress* (independent variable), A and B are material-specific parameters to be determined by fitting σ-N test data[19]. Note that the static strengths of the tested laminates are plotted at $N_\mathrm{f} = 1$, but the run-outs (specimens that did not fail) are not plotted; however, neither static strength nor run-out data are considered when estimating the medians. To be conservative, the median trend for a laminate-group is drawn only after $N_\mathrm{f} = 500$ (this covers the bulk of the reported test data). For the preceding period $1 \leq N_\mathrm{f} \leq 500$, the *S*-*N* trend is approximated by a straight line from the averaged tensile static strength σ^{tu} of the laminate-group.

Figure 7.1 plots data for generally biaxial (plain weave, $[0/90]_\mathrm{nS}$, and twill-woven layups that have fibres oriented along loading axis) specimens. It is by now well-known that higher fibre content tend to result in higher ultimate tensile strengths (to an extent), which in turn predicts longer fatigue endurance, as concluded by studies reviewed in previous section. Since the data considered here are from composites of differing fibre volume fractions, a fairer comparison of their fatigue endurance is needed that makes

[19] Though the Greek notation σ is used here to denote engineering stress, in the following discussion these σ-N plots will be referred interchangeably as *S*-*N* curves, as is the convention in fatigue literature.

Table 7.1: Reported material data of Flax-epoxy (FE) composites from studies considered in Figures 7.1–7.5. Glass-epoxy (GE) data from comparative studies are also listed.

Author code	Reference	Year	Laminate	Mean tensile strength σ^{tu} (MPa)	Composite density ρ_c (g/cm^3)	Fibre volume fraction v_f (%)	Porosity v_p (%)	Test frequency f (Hz)	Loading ratio R
Lng	Liang et al. [25; 50]	2012, 2014	FE [0]	318	1.31 ±0.01	43.1 ±1.5	1-3	5	0.1
			FE [90]	26.1					
			FE $[0/90]_{nS}$	170	1.28 ±0.01	43.7 ±1.5	1.3 ±0.8	5	0.1
			FE $[\pm45]_{nS}$	79					
			GE [0/90]	380	1.79 ±0.03	42.5 ±1	3.8 ±2	5	
			GE $[\pm45]_{nS}$	103					
Els	El Sawi et al. [103]	2014	FE [0]	304	∼1.26	∼48-49	–	5	0.1
			FE $[\pm45]_{nS}$	68.4					
Asg	Asgarinia et al. [108]	2015	FE twill 200 g/m^2	106	1.05	34.3 ±0.4	3.7 ±1.1	5	0.1
			FE twill 550 g/m^2	105.9	1.13	42.3 ±0.3	0.2 ±0.1	5	
			FE twill 224 g/m^2	112.2	1.07	31.1 ±0.7	0.2 ±0.1	1, 1.5, 3	
Uki	Ueki et al. [106]	2015	FE [0]	282	1.28	31.4 ±0.2	0.3 ±0.3	5, 2	0.1
Bns	Bensadoun et al. [109; 110]	2016	FE Mat	83	1.262[a]	30	<0.5	5	0.1
			FE Plain weave	133	1.289[a]	38			
			FE Twill lo-twist	133	1.296[a]	40			
			FE Twill med-twist	129	1.299[a]	41			
			FE Twill hi-twist	139	1.296[a]	40			
			FE [0]	264	1.310[a]	44	<0.5	5	0.1
			FE $[0/90]_{nS}$	124	1.293[a]	39			
			FE quasi-UD[b] [0]	236	1.306[a]	43			
			FE quasi-UD[b] $[0/90]_{nS}$	155	1.303[a]	42			
			GE Mat	207	1.58	29	<0.5	5	0.1
			GE Twill	238	1.72	35			
			GE quasi-UD[b] $[0/90]_{nS}$	312	1.72	38			
			GE $[0/90]_{nS}$	325	1.72	41			
Sdk	Sodoke et al. [112]	2016	FE $[0_2/90_2/\pm45]_S$	145.55	1.388 (dry), 1.740 (wet)[c]	68.07	–	5	0.1

[a] estimated from reported constituent densities and volume fractions
[b] individual plies are not perfectly UD; a small fraction of fibres (≤10%) cross-weave the UD fibres
[c] estimated from reported weight gain of 25.68% after water-ageing

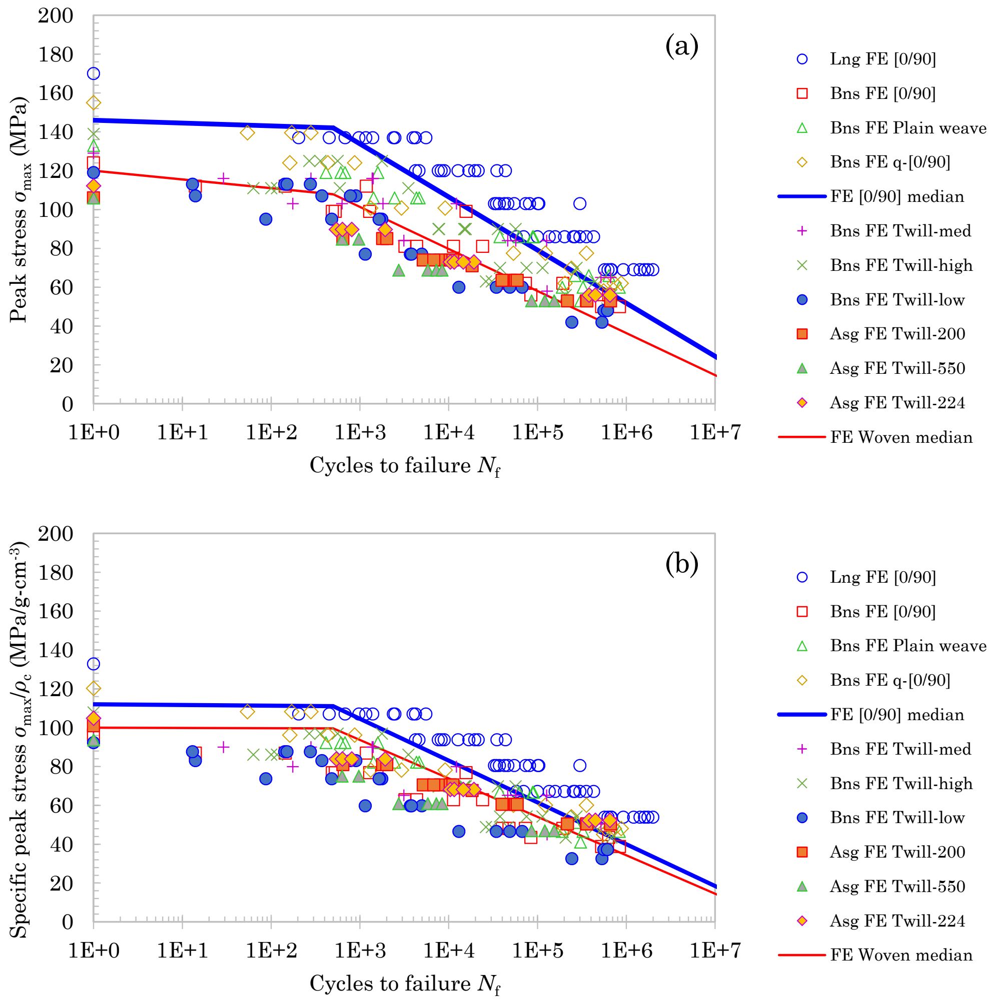

Figure 7.1: Reported fatigue life data for Flax-epoxy (FE) $[0/90]_{nS}$ and woven laminates, presented as: (a) stress-life plot, and (b) same plot normalised by composite density ρ_c. Data adapted from from El Sawi et al. [103] (Els), Liang et al. [25; 50] (Lng), Ueki et al. [106] (Uki), Bensadoun et al. [109; 110] (Bns), and Asgarinia et al. [108] (Asg).

allowance for the influence of fibre content. This can be possible if the data is *normalised for specimen density* (i.e. dividing peak stress $\sigma_{\max}$ by composite density ρ_c) – since the composite density accounts for fibre volume fraction (v_f) *by definition*[20]. The density-normalised, or *specific*, linear trend is therefore a modified form of (7.1):

$$\log\left(N_f\right) = \bar{A} + \bar{B} \cdot \left(\frac{\sigma_{\max}}{\rho_c}\right) \tag{7.2}$$

where $\bar{A}$ and $\bar{B}$ are the material-specific parameters to be determined by fitting specific-stress-life $\frac{\sigma_{\max}}{\rho_c}$–$N_f$ test data. The fatigue life relation parameters of (7.1) and (7.2) for all considered FE composite groups are thus identified (from source *S*-*N* data and composite material properties noted in Table 7.1), and listed in Table 7.2.

Once normalised for density and fibre-fraction, the biaxial and twill-woven curves are much closer

[20] Density of ideal composite in terms of constituent volume fractions and densities: $\rho_c = v_f\rho_f + v_m\rho_m$

Table 7.2: Identified parameters of stress-life and *specific* stress-life (density-normalised) relationships (7.1)–(7.2) for various Flax-epoxy (FE) and Glass-epoxy (GE) laminate architectures under tension-tension fatigue, derived from data in sources listed in Table 7.1.

			Stress–Life (S-N or σ-N) parameters						Specific Stress–Life (σ/ρ-N) parameters					
Laminate	n	Var[a]	A		$\mathrm{CI}_{0.95}$[b]	B		$\mathrm{CI}_{0.95}$[b]	$\bar{A}$		$\mathrm{CI}_{0.95}$[b]	$\bar{B}$		$\mathrm{CI}_{0.95}$[b]
FE [0]	86	0.669	8.881	±	0.810	-0.025	±	0.004	8.745	±	0.835	-0.031	±	0.006
FE [0/90]	110	0.528	7.895	±	0.521	-0.037	±	0.005	7.856	±	0.527	-0.046	±	0.007
FE Woven	105	0.413	7.681	±	0.481	-0.046	±	0.006	7.732	±	0.724	-0.051	±	0.011
FE [±45]	48	0.244	10.19	±	1.053	-0.102	±	0.019	8.642	±	1.536	-0.116	±	0.044
FE Mat	31	0.146	9.338	±	0.623	-0.114	±	0.012	9.338	±	0.623	-0.144	±	0.016
FE [90]	20	0.140	10.69	±	1.061	-0.390	±	0.061	10.69	±	1.061	-0.511	±	0.080
FE QIso	14	0.087	9.150	±	1.498	-0.044	±	0.015	9.150	±	1.498	-0.061	±	0.020
water-aged	20	0.059	7.239	±	0.520	-0.027	±	0.006	7.239	±	0.520	-0.047	±	0.010
GE [0/90]	43	0.377	8.008	±	0.795	-0.018	±	0.004	8.169	±	0.764	-0.033	±	0.006
GE Woven	9	0.325	9.450	±	2.281	-0.036	±	0.015	9.450	±	2.281	-0.062	±	0.025
GE [±45]	15	0.230	9.851	±	1.711	-0.090	±	0.025	9.851	±	1.711	-0.161	±	0.045
GE Mat	13	0.111	8.272	±	0.884	-0.034	±	0.007	8.272	±	0.884	-0.054	±	0.011

[a] Var = variance s^2 of the normal distribution of $\log(N_\mathrm{f})$, where s is standard deviation
[b] 95% confidence interval

together (Figure 7.1(b)) – indicating that the woven laminates are not as inferior to [0/90] as the usual S-N curve in Figure 7.1(a) suggests. For instance, to survive 500 cycles, biaxial [0/90] specimens can endure a normalised loading of up to 111 MPa/g-cm^{-3},[21] whereas woven specimens manage 100 MPa/g-cm^{-3} – a difference of ~10% (see Figure 7.1(b)). Still, the UD-ply based [0/90] laminates consistently exceed the twill-woven laminates in performance despite their similar biaxial reinforcement (slope $\bar{B} = -0.046$ for [0/90] vs $\bar{B} = -0.051$ for woven, from Table 7.2), suggesting that fatigue damage and failure mechanisms are more intensive, or progress quicker, in twill-woven specimens. This reasoning is in agreement with the findings of Asgarinia et al. [108], who had concluded that reinforcement by woven fabrics or high-crimp/low-twist yarns are more likely to develop fibre-matrix debonding earlier in fatigue life, due to the higher proportion of out-of-plane fibre arrangement.

Figure 7.2 plots the specific stress-life data (i.e. density normalised) for FE [0], [90], and angled-biaxial ($[\pm45]_{\mathrm{nS}}$ layups where fibres are not aligned with loading axis) specimens[22]. To aid comparison, the median trends for biaxial specimens from Figure 7.1(b) are also re-plotted. It can be seen that [0] specimens clearly exceed others in specific fatigue endurance at all tested peak-stress levels, followed by biaxial specimens, then the [90] demonstrating the weakest resistance to fatigue. To last a lifetime (N_f) of 500 cycles, [0] specimens can endure an estimated 196 MPa/g-cm^{-3} peak-stress cyclic loading, while the same estimate for [0/90] specimens is 111 MPa/g-cm^{-3}, twill-woven specimens is 100 MPa/g-cm^{-3}, [±45] is 51 MPa/g-cm^{-3}, and for [90] is a significantly lower 21 MPa/g-cm^{-3}. However, it is observed that the difference in fatigue life between [0/90], woven, and [±45] specimens is considerably reduced at low stress levels (<45 MPa/g-cm^{-3}) – e.g. for a fatigue life of 2 million cycles, the estimated constant-amplitude peak

[21] MPa/g-cm^{-3} is chosen as the working unit of density-normalised peak-stress values, though g-cm^3 is not the SI convention for density, to aid convenience of comparison with regular S-N plots.
[22] For reference, the non-normalised S-N plot is provided in Appendix A.5.

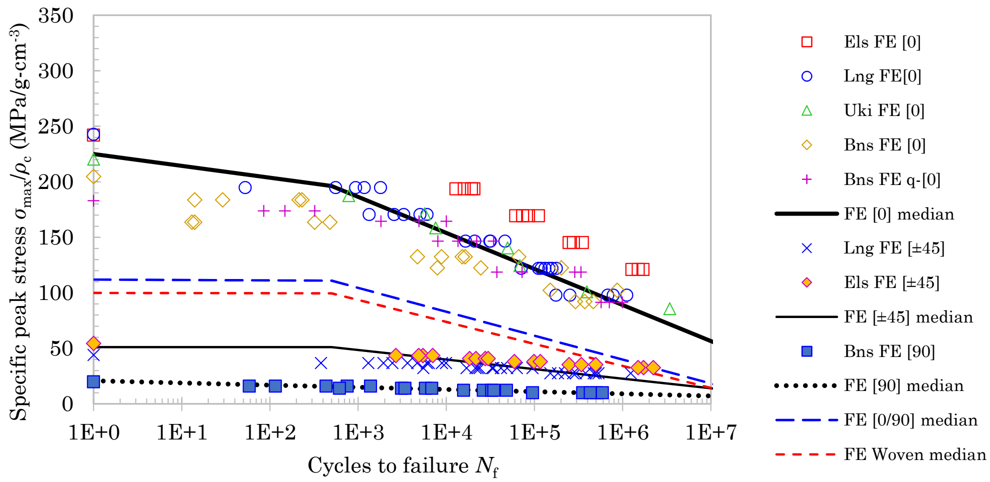

Figure 7.2: Specific fatigue life plots for Flax-epoxy (FE) [0], $[\pm 45]_{nS}$, and [90] laminates. Data adapted from from El Sawi et al. [103] (Els), Liang et al. [25; 50] (Lng), Ueki et al. [106] (Uki), Bensadoun et al. [109; 110] (Bns), and Asgarinia et al. [108] (Asg).

stress capability is 33.5 MPa/g-cm^{-3} for [0/90], 28 MPa/g-cm^{-3} for woven specimens, and 20 MPa/g-cm^{-3} for [±45]. The observed trends corroborate an earlier study on Jute-composites by Munikenche Gowda et al. [220] that suggested a steeply decreasing slope reflects a strong influence of fibre damage, while a gradually decreasing slope reflects matrix dominated damage mechanisms.

Figure 7.3 compares the density-normalised fatigue endurance of short-fibre reinforced and quasi-isotropic FE laminates. Interestingly, randomly-oriented short-fibre 'mat' reinforcement produces a similar fatigue resistance to that identified for [±45] layups (see Figure 7.3(a)). The estimated stress-life median slope is lower for the mat specimens ($\bar{B} = -0.144$ for mat vs $\bar{B} = -0.116$ for [±45], from Table 7.2), so their fatigue endurance is marginally shorter-lived at loading levels above 30 MPa/g-cm^{-3}. However, the difference is negligible below 30 MPa/g-cm^{-3}, where both laminate architectures survive 250,000+ cycles. Similarly, Figure 7.3(b) shows that quasi-isotropic (QIso) FE specimens have a very similar fatigue life trend to that of [0/90] and twill-woven specimens. For example, to survive until $N_f = 500$, QIso specimens can endure 105 MPa/g-cm^{-3}, compared to 142 MPa/g-cm^{-3} for [0/90] and 108 MPa/g-cm^{-3} for twill-woven. Water-aged QIso specimens show marginally reduced fatigue performance (97 MPa/g-cm^{-3} at $N_f = 500$), but still remain within the same range as biaxial/woven composites (compare their density-normalised median parameters in Table 7.2).

The above suggests that, for engineering applications where fatigue longevity is of importance, short-fibre mat and quasi-isotropic laminates may be interchangeable with [±45] and biaxial/twill-woven, respectively. However, it must be noted that the quasi-isotropic data was sourced from the work of Sodoke et al. [112], where the tested $[0_2/90_2/\pm 45]_S$ laminates were not strictly quasi-isotropic – since they have twice as much reinforcement along 0° and 90° than along +45° or −45°. As such, these laminates may be expected to have similar fatigue lives to [0/90] or twill-woven specimens anyway, on account of their 0-90° bias. Fatigue data for a truly balanced quasi-isotropic FE laminate is not yet available.

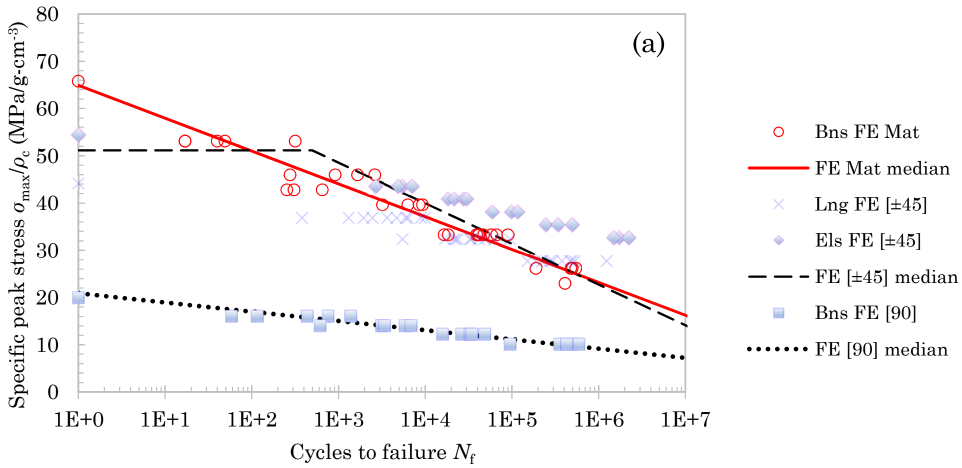

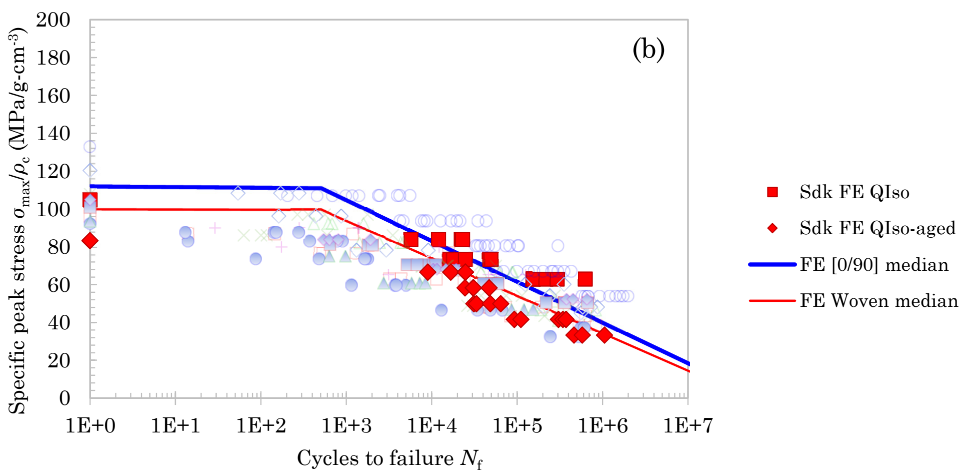

Figure 7.3: Specific stress-life plots for: (a) Short-fibre random mat FE laminate, superimposed on data for FE [±45] laminates; and (b) Quasi-istotropic FE laminate $[0_2/90_2/\pm45]_S$, superimposed on data for biaxial FE laminates. Data adapted from Sodoke et al. [112] (Sdk), Liang et al. [25; 50] (Lng), El Sawi et al. [103] (Els), and Bensadoun et al. [109; 110] (Bns).

7.2.2 Comparison with Glass-epoxy composites

Studies by Liang et al. [25] and Bensadoun et al. [109; 110] also examined equivalent Glass-epoxy (GE) composites as controls for their Flax-epoxy (FE) studies (Figures 7.4–7.5). Their data enables studying the comparative fatigue performance of several FE architectures, and their suitability of replacing equivalent Glass-composites in fatigue applications. Figure 7.4 shows the fatigue lives of [0/90] and twill-woven GE specimens, superimposed on the same for their FE counterparts. Biaxial GE [0/90] fatigue performance proves to generally exceed that of uniaxial FE [0] specimens for loading levels above 150 MPa, as shown in Figure 7.4(a). This is expected, since GE [0/90] has a higher static tensile strength (averaging ~325 MPa; see Table 7.2) than FE [0] (~290 MPa). Twill-woven GE specimens also demonstrate higher absolute fatigue resistance than FE biaxial/woven specimens. However, when accounting for composite density and fibre content, these differences are significantly narrowed or even eliminated, as shown by the density-normalised trends in Figure 7.4(b). Density-normalised performance of FE [0] consistently exceeds that of

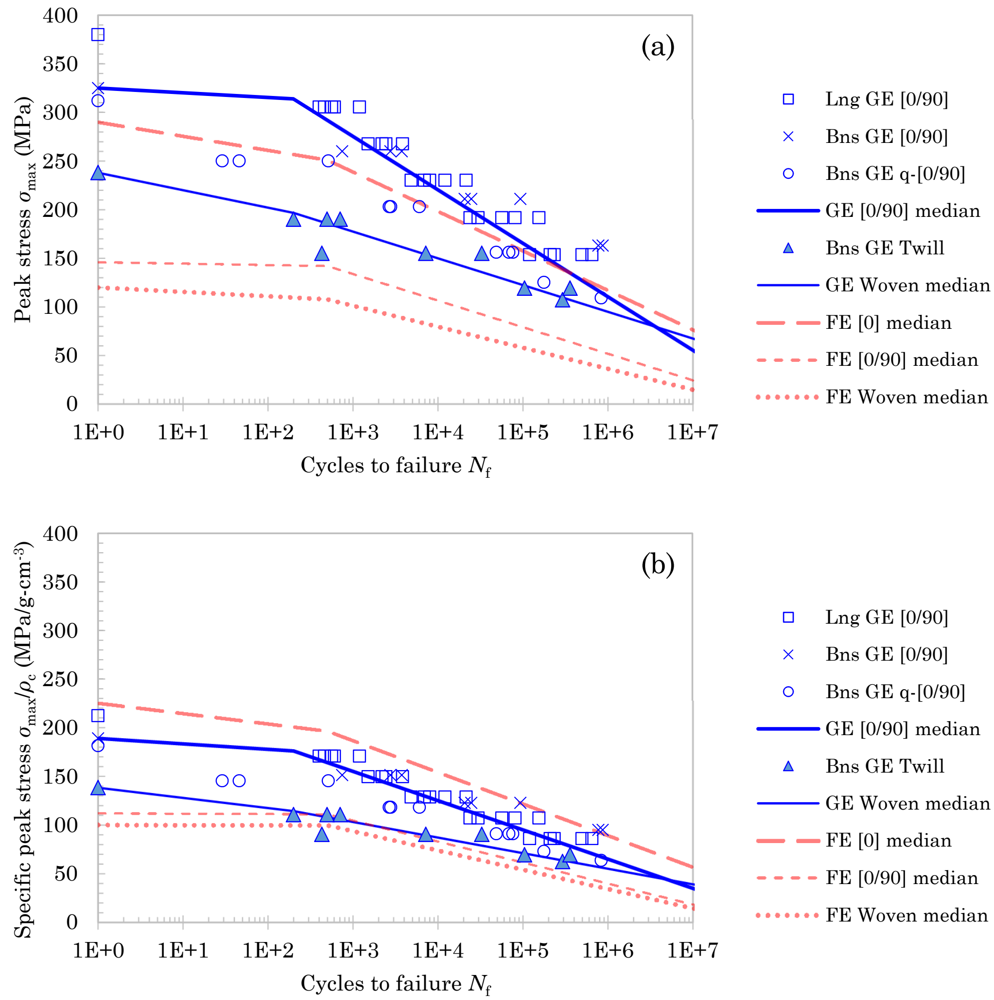

Figure 7.4: Comparison of reported fatigue lives of Flax-epoxy (FE) and Glass-epoxy (GE) biaxial laminates ($[0/90]_{nS}$ and twill-woven) showing (a) stress-life plot, and (b) same plot normalised by composite density ρ_c. For clarity, only median trendlines for FE are shown from Figures 7.1 and 7.2. GE data adapted from Liang et al. [25; 50] (Lng), and Bensadoun et al. [109; 110] (Bns).

biaxial GE (median slope is $\bar{B} = -0.031$ for FE [0] vs $\bar{B} = -0.033$ for GE [0/90], from Table 7.2). For an example longevity of $N_f = 500$, GE [0/90] can withstand cycling at 189 MPa/g-cm^{-3} peak load, compared to the higher 225 MPa/g-cm^{-3} for FE [0] – a difference of ~20%.

In the case of woven laminates, density-normalised performance of FE and GE are comparable, as seen in Figure 7.4(b). For a low-cycle fatigue life of $N_f = 500$, GE woven specimens endure 138 MPa/g-cm^{-3} peak load, compared to 112 MPa/g-cm^{-3} for FE [0/90] and 100 MPa/g-cm^{-3} peak load for FE woven specimens. For a high-cycle fatigue life of $N_f = 2,000,000$, GE woven specimens can take up to 50 MPa/g-cm^{-3}, while FE [0/90] and woven can be expected to endure an estimated 34 and 28 MPa/g-cm^{-3} peak load, respectively.

Similar comparable fatigue performance is also evidenced for angled cross-ply [±45] specimens of FE and GE, as seen in Figure 7.5. Though GE [±45] laminates have a higher static tensile strength (~103 MPa, from Table 7.2) than FE [±45] (~73 MPa), their absolute fatigue performance appears comparable

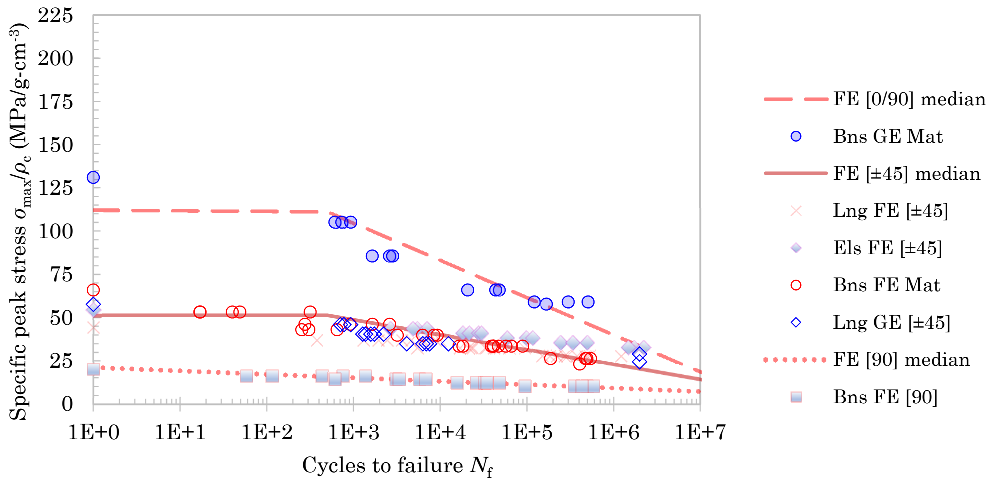

Figure 7.5: Comparison of specific fatigue lives of $[\pm45]_{nS}$ and short-fibre-mat Flax-epoxy (FE) and Glass-epoxy (GE) laminates. For clarity, only median trendlines for FE are shown from Figures 7.2 and 7.1(b). GE data adapted from Liang et al. [25; 50] (Lng and Bensadoun et al. [109; 110] (Bns).

at all load levels. Accounting for density shows further similarity in their fatigue endurance, with FE specimens even marginally exceeding GE for peak loads above 24 MPa/g-cm^{-3}. For a randomly-oriented short-fibre architecture, GE laminates demonstrate higher fatigue resistance and longer lives than FE, even when the stress-life data is normalised for density and fibre fraction. The closest-matching FE layup that delivers a similar fatigue performance as GE Mat per unit density is FE [0/90], as seen in Figure 7.5. This may be because the high stiffness of individual Glass fibres compensates for the higher damage (cracking) activity one may expect in a short-fibre reinforced laminate, thereby producing a performance nearly identical to the lower-stiffness Flax fibre reinforced [0/90] layup. For an example fatigue life of 500 cycles, GE Mat can endure cyclic peak loads of 104 MPa/g-cm^{-3}, compared to 111 MPa/g-cm^{-3} for FE [0/90]. This suggests that FE [0/90] (or even FE twill-woven) composites have the mechanical potential to replace short-fibre reinforced GE Mat in applications where fatigue longevity is of interest. Of course, such comparisons of fatigue life do not imply that the *evolution* of density-normalised mechanical properties or internal damage kinetics will also be similar, but this finding may encourage further study of GE Mat and FE [0/90] interchangeability for fatigue-critical applications.

7.2.3 Comparison with other NFCs

Considering the limited number of available studies on Flax-epoxy (FE) fatigue (6 sources listed in Table 7.1), it seems necessary to examine publications on composites of *other* natural fibres for further insight on NFC fatigue. Available publications on the fatigue of other NFCs are listed in Table 7.3, all published within the last 7 years. The reinforcement in these reported composites include fibre of Flax (F), Sisal (S), Hemp (H), and Jute (J) plant, while the matrix materials include epoxy (E), polyester (Pe), and high-density polyethylene (HDPE). Laminate architectures studied include UD ([0], [90]), crossply ([0/90], [±45]), and random-oriented short-fibre *mat*-reinforced laminates.

Unfortunately, these studies are still few in number (7 sources listed in Table 7.3), and they all have been conducted under different fatigue-testing parameters (i.e. cycling frequency f, loading rate R) than those employed for the aforementioned FE studies – thereby limiting a direct comparison of fatigue behaviour. For instance, all but one of reported FE tension-tension fatigue studies were conducted at 5 Hz (see Table 7.1), but all available fatigue studies on other NFCs were conducted at different cycling frequencies (see Table 7.3). Nevertheless, this section will still evaluate the fatigue performance of these non-Flax/epoxy NFCs, and attempt to draw meaningful conclusions of comparative behaviour, with the caveat that the possible influence of differing test parameters be accounted for.

Similar to the methodology in the preceding two sections, fatigue endurance of other NFCs for which data are available is analysed by constructing *S*-*N* charts. As before, linearised median *S*-*N* trends are estimated following ASTM E739 [219] procedure, which assumes a log-normal distribution and constant standard deviation for fatigue life N_f, per relation (7.1). The static tensile strengths are plotted at $N_\mathrm{f} = 1$, but are not considered when estimating the linear parameters A and B per relation (7.1). Conservatively, the computed median plot is considered applicable only for $N_\mathrm{f} \geq 500$ (covers reported test data); while for the preceding period $1 \leq N_\mathrm{f} \leq 500$, the *S*-*N* trend is approximated by a straight line from the mean tensile strength σ^{tu} datapoint at $N_\mathrm{f} = 1$.

As understood in the preceding sections, density-normalised *specific* stress-life plots (where the vertical-axis stress level σ_max is divided by composite density ρ_c) prove a more useful means of comparing specimens of different fibre-fractions and fibre-densities. Density-normalised fatigue life data for the considered NFCs are presented in Figures 7.6–7.10, and discussed concurrently. To aid comparison, the plots also show trends for similar FE laminates as estimated previously.

Table 7.3 lists the source studies of the NFC fatigue data, and other relevant data that will aid interpretation of the developed *S*-*N* plots.

7.2.3.1 NFCs of epoxy and polyethylene

Composites based on *epoxy* and *polyethylene* matrix material are examined separately for comparison with Flax-epoxy fatigue lives estimated in the previous sections, as shown in Figures 7.6–7.7. The fatigue life relation parameters from relations (7.1) and (7.2) are identified for all considered NFC composites using source *S*-*N* data and composite material properties, and are listed in Table 7.4.

It is found that the performance of Sisal-epoxy (SE) [0] laminates is practically identical to that of FE [0], evidenced in the specific-stress-life plot in Figure 7.6, and from the stress-life parameters listed in Table 7.4. SE [0] laminates are reported to have a static tensile strength of ~322 MPa for fibre volume fractions of $v_f = 0.7$ (from Table 7.3), but when normalising for composite density and fibre content, the static tensile strength is ~252 MPa/g-cm^{-3} – which is very close to ~225 MPa/g-cm^{-3} for FE [0] (computed from data in Tables 7.1–7.3). It is therefore not surprising that the SE [0] stress-life data superimpose neatly around FE [0] median line. Note that these SE fatigue tests reported by Towo et al. [113; 114] were conducted at 1.5-3.9 Hz frequency and loading ratio $R = 0.1$ (see Table 7.3), which are close to the 5 Hz and $R = 0.1$ applied for the coutnerpart FE tests (see Table 7.1), so a comparison of fatigue performance here is reasonable. Considering that both composites are of epoxy reinforced by plant/bast fibres of similar hierarchical microstructure, the identical fatigue performance suggests that the damage mechanisms in both composites may have similar intensities and progressive evolution over the fatigue life.

Table 7.3: Reported material data of other NFCs: Hemp-epoxy (HE), Hemp-polyester (HPe), Sisal-polyester (SPe), Jute-polyester (JPe), Flax-polyester (FPe), and Hemp-High density polyethylene (H-HDPE) from studies considered in Figures 7.6–7.10. Glass-polyester (GPe) data from comparative studies are also listed.

Author code	Reference	Year	Laminate	Tensile strength σ^{tu} (MPa)	Composite density ρ_c [a] (g/cm^3)	Fibre volume fraction v_f (%)	Porosity v_p (%)	Test frequency f (Hz)	Loading ratio R
Ynj	Yuanjian & Isaac [119]	2007	HPe Mat	20.1	1.254	14.34 [b]	–	1	0.1
				53	1.299	40.84 [b]	–		
			GPe [±45]	43	1.581	25.37 [b]	–		
Tw1	Towo & Ansell [114]	2008	SPe [0]	222.6 ±21.2	1.289	68.2 ±3.2	–	*variable* 1.5–3.9; 200 MPa/s [c]	0.1, -1
			SE [0]	329.8 ±20.9	1.282	71.5 ±2.5	–		
Tw2	Towo & Ansell [113]	2008	SPe [0]	222.6 ±21.2	1.291	∼70	–	*variable* 1.5–3.9; 400 MPa/s [c]	0.1
			SE [0]	329.8 ±20.9	1.279	∼70	–		
Sha	Shah et al. [115]	2013	HPe [0]	171.3 ±6.5	1.303 ±0.006	35.6 ±0.8	1.3 ±0.4	10	0.1, 0.3, 0.5, 2.5, -1
			JPe [0]	175.1 ±10.3	1.225 ±0.002	31.7 ±0.1	4.2 ±0.8	10	0.1
				224.7 ±26.5	1.276 ±0.002	37.8 ±0.1	1.1 ±0.2		
			FPe [0]	143 ±6.8	1.282 ±0.004	27.7 ±0.3	0.9 ±0.3	10	0.1
			FPe $[\pm45]_4$	51.4 ±2.8	1.293 ±0.005	28.9 ±0.1	0.3 ±0.2		
			FPe [90]	13.2 ±0.4	1.278 ±0.004	25.8 ±0.3	0.7 ±0.2		
Szd	Shahzad & Isaac [38]	2014	HPe Mat	46.4 ±4.6	1.318	51.78	–	1	0.1, -1
			GPe Mat	200.9 ±6.3	1.737	36.46	–		0.1
Vas	de Vasconcellos et al. [116]	2014	HE $[0/90]_7$	113 ±9	1.240 ±0.010	36 ±2	4	1	0.01
			HE $[\pm45]_7$	66 ±7					
Fth	Fotough et al. [94; 118]	2014	H-HDPE [0]	29.54 ±0.18	1.015	13.5 [b]	–	3	0.1
				30.18 ±0.173	1.103	30.1 [b]	–		
			water-aged	26.45 ±0.117	1.039 [d]	13.5 [b]	–		

[a] if not stated in source, then estimated from reported constituent densities and volume fractions
[b] estimated from reported constituent densities and fibre weight fraction
[c] constant stress rate enforced, so frequency varied
[d] estimated from reported weight gain of 2.4% after water-ageing

Specimens of Hemp-reinforced High-density Polyethylene (H-HDPE) [0] laminate demonstrate very poor fatigue performance when compared to FE [0], but offer a marginal improvement on FE [90] specimens, as seen in Figure 7.6. It will be seen later in Figure 7.8 that even Hemp-*polyester* [0] specimens provide fatigue resistance superior to H-HDPE [0]. It may be that HDPE material simply does not bond as well with natural fibres as epoxy matrix. Their significantly poor performance indicates that natural fibre

Table 7.4: Identified parameters of stress-life and *density-normalised* stress-life relationships (7.1)–(7.2) for various laminates of Sisal-epoxy (SE), Hemp-epoxy (HE), Flax-polyester (FPe), Jute-polyester (JPe), Sisal-polyester (SPe), Hemp-polyester (HPe), Hemp-High-density polyethylene (H-HDPE), and Glass-polyester (GPe) under tension-tension fatigue, derived from data in sources listed in Table 7.3.

			Stress–Life (S-N or σ-N) parameters						Stress/Density–Life (σ/ρ-N) parameters					
Laminate	n	Var[a]	A		$\mathrm{CI}_{0.95}$[b]	B		$\mathrm{CI}_{0.95}$[b]	$\bar{A}$		$\mathrm{CI}_{0.95}$[b]	$\bar{B}$		$\mathrm{CI}_{0.95}$[b]
SE [0]	26	0.327	9.724	±	0.945	-0.029	±	0.005	9.719	±	0.950	-0.037	±	0.006
HE [0/90]	10	0.218	8.024	±	1.355	-0.052	±	0.019	8.024	±	1.355	-0.065	±	0.024
HE [±45]	10	0.212	9.496	±	1.826	-0.116	±	0.039	9.496	±	1.826	-0.143	±	0.048
F/J/S-Pe [0][c]	34	0.473	9.470	±	0.914	-0.037	±	0.007	9.672	±	0.846	-0.049	±	0.008
HPe [0]	7	0.095	10.98	±	1.379	-0.062	±	0.012	10.98	±	1.379	-0.080	±	0.015
HPe Mat	28	0.308	9.190	±	1.086	-0.170	±	0.036	9.066	±	1.119	-0.217	±	0.048
H-HDPE [0]	48	0.085	9.224	±	0.447	-0.268	±	0.023	9.331	±	0.214	-0.288	±	0.012
GPe [±45]	11	0.377	11.94	±	2.663	-0.266	±	0.092	11.94	±	2.663	-0.421	±	0.145
GPe Mat	14	0.164	7.631	±	0.725	-0.036	±	0.007	7.631	±	0.725	-0.062	±	0.013
FE [0][d]	86	0.669	8.881	±	0.810	-0.025	±	0.004	8.745	±	0.835	-0.031	±	0.006
FE Woven[d]	105	0.413	7.681	±	0.481	-0.046	±	0.006	7.732	±	0.724	-0.051	±	0.011
FE [±45][d]	48	0.244	10.19	±	1.053	-0.102	±	0.019	8.642	±	1.536	-0.116	±	0.044

[a] Var = variance s^2 of the normal distribution of $\log(N_\mathrm{f})$, where s is standard deviation
[b] 95% confidence interval
[c] FPe [0], JPe [0], and SPe [0] laminate data are considered collectively since they are found to overlap
[d] Repeated here from Table 7.2 for ease of comparison

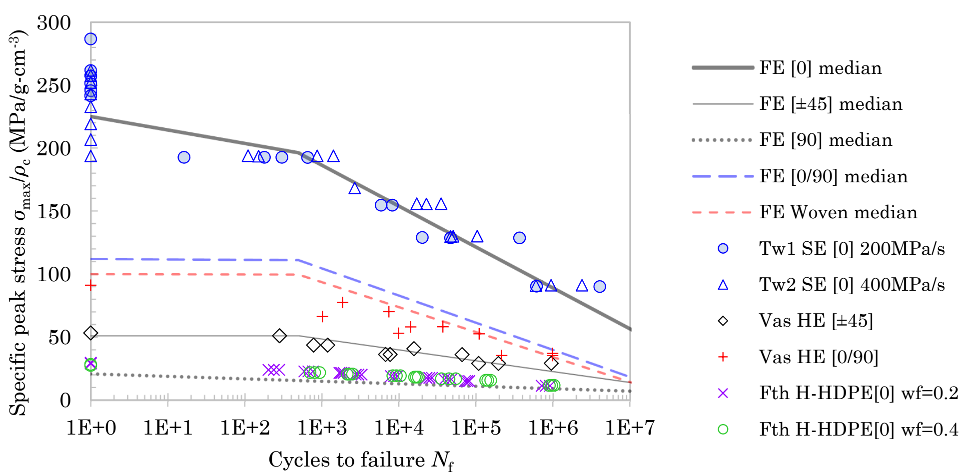

Figure 7.6: Specific fatigue lives of Sisal-epoxy (SE), Hemp-epoxy (HE), and Hemp-High Density Polyethylene (H-HDPE), compared with median Flax-epoxy (FE) trends. SE, HE, and H-HDPE data adapted from Towo et al. [113; 114] (Tw1 & Tw2), de Vasconcellos et al. [116] (Vas), and Fotouh et al. [94; 118] (Fth), respectively.

composites of HDPE do not offer any meaningful fatigue capability when compared to epoxy-based, or even polyester-based composites, in the pursuit of replacing Glass-composites.

Figure 7.6 also shows that Hemp-epoxy (HE) [±45] fatigue life data coincide with the FE [±45] median line, which is now expected since their density-normalised tensile strengths are practically identical at 53 and 51 MPa/g-cm^{-3}, respectively (computed from data in Tables 7.1–7.3). In the case of [0/90] laminates, however, HE is found to somewhat underperform when compared to FE, as seen in Figure 7.6. It must be stressed that the source data for these HE laminates are from fatigue tests conducted at 1 Hz and loading ratio $R = 0.01$ by de Vasconcellos et al. [116] – which are considerably lower than the 5 Hz and $R = 0.1$ applied in the source FE laminate tests (see Table 7.1). It was discussed earlier that both test frequency (if below 2 Hz) and loading ratio have an effect on NFC fatigue life: Shah et al. [115], and Shahzad and Isaac [38] both found that lower loading ratios result in shorter fatigue lives, reasoning that lower ratios imply higher stress gradients across the fibre-matrix interface, thereby encouraging higher-intensity crack initiation and progression at the interface. This relationship between loading ratio and fatigue life is clearly seen for SE [0] specimens in Figure 7.7, where fatigue performance under tension-compression tests ($R = -1$) is significantly poorer than for tension-tension tests ($R = 0.1$). As discussed at length in the

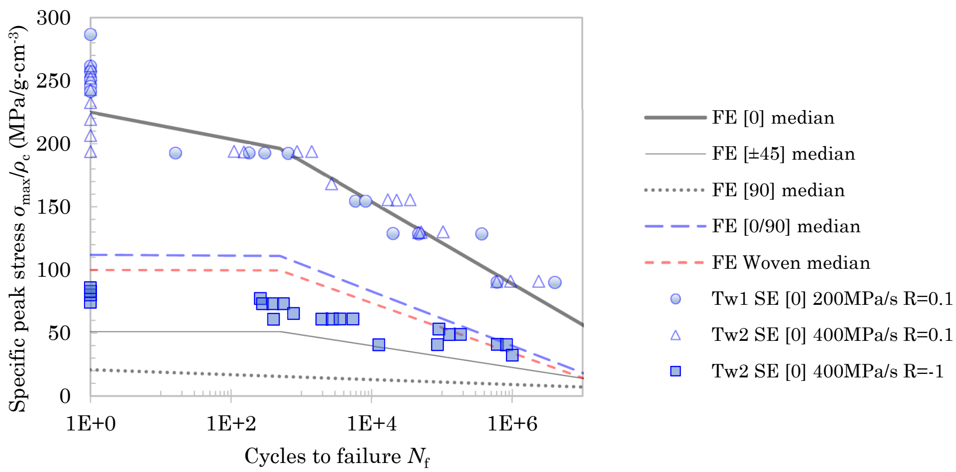

Figure 7.7: Specific fatigue lives of Sisal-epoxy [0] specimens under tension-tension ($R = 0.1$) and tension-compression ($R = -1$) cycling, compared with median Flax-epoxy (FE) trends. SE data adapted from Towo et al. [113; 114] (Tw1 & Tw2).

introductory Chapter 2, Hemp fibres are very similar to Flax in microstructural arrangement, constitution, and damaging mechanisms. Therefore, the very low loading ratio $R = 0.01$ may explain the shorter fatigue lives of HE [0/90] specimens in Figure 7.6 despite their structural similarity to FE [0/90], so an equivalence may be yet made between FE and HE performance.

7.2.3.2 NFCs of polyester matrix

Reported fatigue endurance of natural fibre reinforced *polyester* specimens are shown in Figures 7.8–7.10. Of note, the specific static strengths (density-normalised) of Flax-polyester (FPe, 183 MPa/g-cm^{-3}), Jute-polyester (JPe, 159 MPa/g-cm^{-3}), and Sisal-polyester (SPe, 173 MPa/g-cm^{-3}) are similar, and their fatigue lives appear to coincide along a common trend. Considering their similarity in fatigue performance, the datasets of FPe, JPe, and SPe [0] specimens are considered collectively when estimating parameters for linear stress-life functions (7.1)–(7.2) (listed in Table 7.4 as F/J/S-Pe). It must be noted with caution that the FPe and JPe specimens were cycled at 10 Hz [115], the SPe specimens were cycled at a constant stress-rate that resulted in frequencies that varied between 1.5–3.9 Hz from specimen to specimen (but was

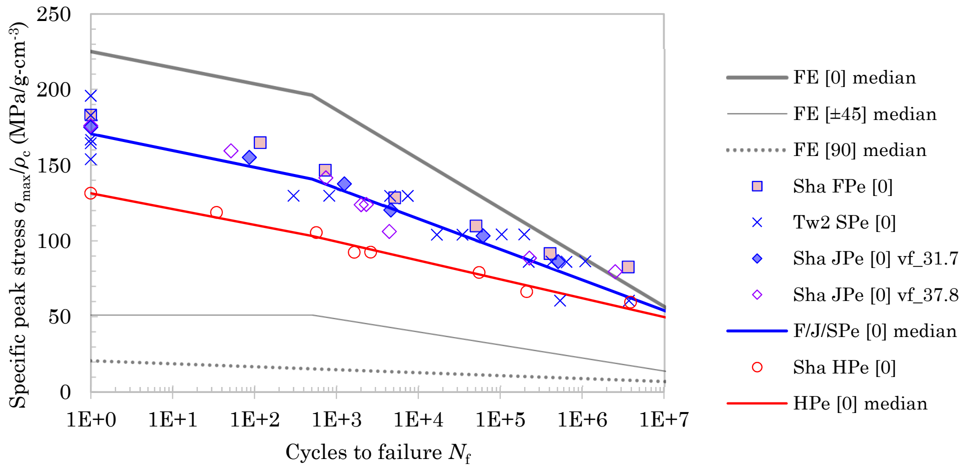

Figure 7.8: Specific fatigue lives of Flax-polyester (FPe), Sisal-polyester (SPe), Jute-polyester (JPe), Hemp-polyester (HPe), and Glass-polyester (GPe) laminates, compared with median Flax-epoxy (FE) trends from Figure 7.2. Data adapted from Shah et al. [115] (Sha), Towo et al. [113; 114] (Tw1 & Tw2), and Yuanjian et al. [119] (Ynj).

constant for each test), whereas the baseline FE [0] composites were tested at 5 Hz (see Tables 7.1–7.3). Recall that, as reported by Ueki et al. [106], varying test frequencies from 0.25 to 2 Hz has an *increasing* influence on NFC [0] fatigue lives, but no significant effect is observed between 2–5 Hz. As such, it may be acceptable to compare SPe data with those available for FE, but unfortunately there is simply no evidence yet to accept or reject a comparison between the 10 Hz fatigue data for FPe and JPe with those obtained at 5 Hz for FE.

Assuming that the available polyester-NFC data are indeed comparable to those for FE, it is interesting to find that all polyester-NFC [0] specimens exhibit significantly shorter fatigue lives than FE [0], as seen in Figure 7.8. This suggests that composites of polyester are less durable that those of epoxy under fatigue loading. There is support for this conclusion in the work of Towo and Ansell [114], where the authors found that while alkali treatment improved fibre-matrix adhesion in SPe, it had little influence on already-stronger SE laminates. It can subsequently be reasoned that natural fibres have lower bonding strength with polyester matrix than with epoxy, so cracking initiation and progression occurs sooner in polyester-NFCs than in the case of epoxy-NFCs – thus explaining the collective shorter fatigue endurance of polyester-based NFCs.

This poorer fatigue performance of polyester-composites vis-a-vis epoxy-composites also extends to short-fibre mat NFCs (see Figure 7.9) and Glass-reinforced laminates (see Figures 7.10–7.9). Short-fibre mat HPe specimens have a lower specific static strength (~38 MPa/g-cm^{-3}) than FE specimens of the same architecture (~65 MPa/g-cm^{-3}), and this is reflected in their lower fatigue resistance, as shown in Figure 7.9. As further indication that polyester-composites are inferior to epoxy-composites under fatigue conditions, GPe Mat and $[\pm45]_{nS}$ specimens also exhibit shorter fatigue lives than their GE counterparts, as shown in Figures 7.9 and 7.10. In fact, Flax-epoxy $[\pm45]_{nS}$ specimens exceed Glass-polyester $[\pm45]_{nS}$ in fatigue performance (Figure 7.10), so it appears the presence of polyester matrix cannot be compensated for by a higher-strength reinforcement.

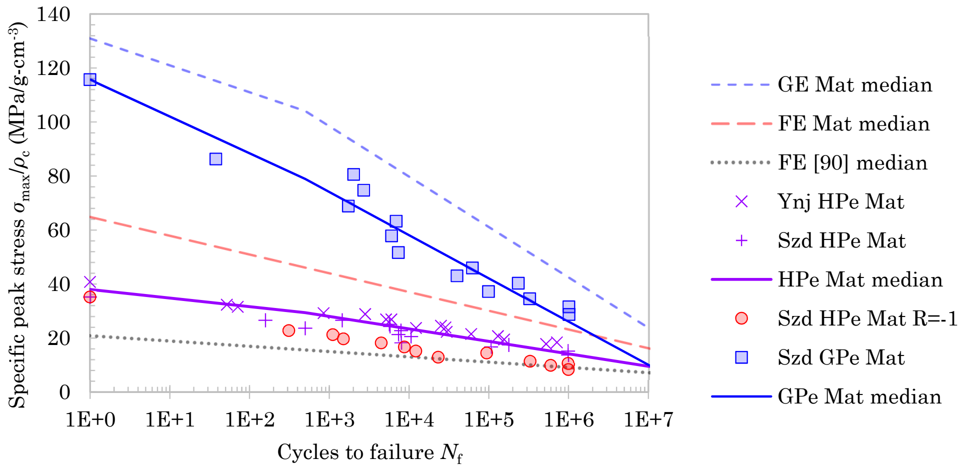

Figure 7.9: Specific fatigue lives of short-fibre *mat* Hemp-polyester (HPe) and Glass-polyester (GPe) laminates, compared with median Flax-epoxy (FE) trends. A tension-compression dataset ($R = -1$) for HPe is also shown. Data adapted from Shahzad et al. [38] (Szd) and Yuanjian et al. [119] (Ynj).

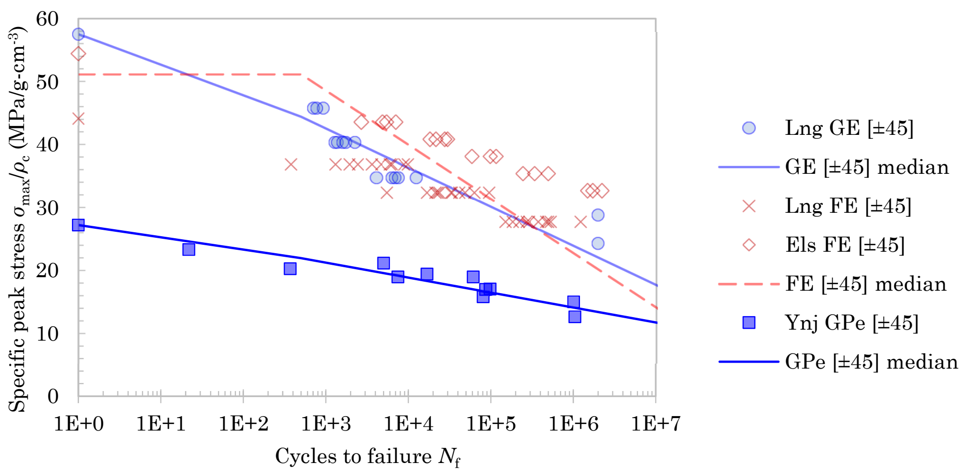

Figure 7.10: Specific fatigue lives of Glass-polyester (GPe) $[\pm 45]_{nS}$ laminates, compared with median Flax-epoxy (FE) and Glass-epoxy (GE) trends from Figure 7.5. Data adapted from Yuanjian et al. [119] (Ynj).

7.3 Analysing stiffness degradation of NFCs

Determining fatigue longevity (in terms of cycles to failure) alone is not sufficient to characterise the performance, since the interim material degradation behaviour may be different even for NFCs with similar fatigue lives. For instance, Hemp-polyester (HPe) mat laminates have a similar fatigue endurance to Glass-polyester (GPe) [±45] laminates (compare plots in Figures 7.10 and 7.9), however, their modulus evolution behaviour is very different – as seen in Figure 7.11(a). Most engineering fibre-composites to date demonstrate a progressive *degradation* of stiffness under stress-controlled fatigue loading [213; 222]. This degradation typically follows a 3-stage 'rotated sigmoidal' trend, as in Figure 7.11(b). The first and last stages are characterised by rapid decrease, whereas the interim stage (typically of longer duration) may show slower-degrading or even stable stiffness [214; 221].

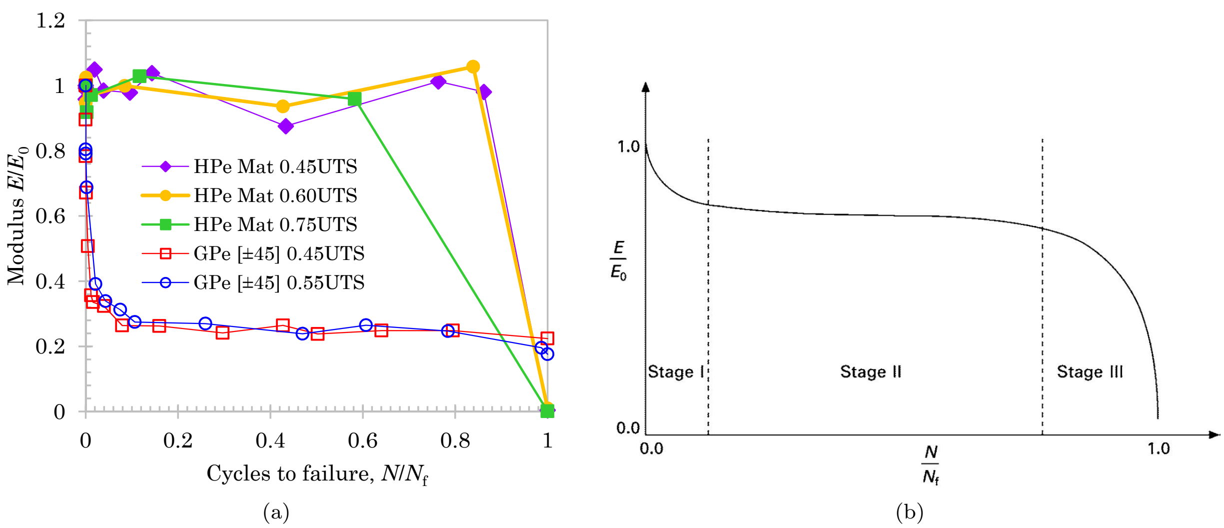

Figure 7.11: (a) Residual modulus evolution over fatigue life for short-fibre Hemp-polyester (HPe) and $[\pm 45]_4$ Glass-polyester (GPe), data adapted from [119]; (b) Typical stiffness (modulus) degradation curve for fibre-reinforced composite materials. Reproduced with permission from [221].

From the fatigue studies of Liang et al. [25; 50] and El Sawi et al. [103], however, it appears that some Flax-epoxy (FE) configurations exhibit an *increasing* stiffness evolution – which clearly does not conform to the typical fibre-composite degradation trend in Figure 7.11(b). It was found that FE specimens wherein fibre orientation coincides with the loading axis tend to demonstrate a stiffening behaviour, a phenomenon not evidenced in laminates where fibre orientation is off-axis. This suggests that damage behaviour in the former is more influenced by fibre characteristics, i.e., shows *fibre-dominant* response, while the latter shows *matrix-dominant* response.

7.3.1 Fibre-dominant response

All FE fatigue studies to date have consistently noted an unusual characteristic of symmetric laminates that contain 0° plies: stiffness appears to progressively *increase* until about 80% of its fatigue life (see Figures 7.12 and 7.13), after which it returns to its original stiffness just before specimen failure. This apparent stiffening is at odds with the typical degrading stiffness evolution identified for fibre-composites to date.

The fatigue tests reported by Liang et al. [50] and El Sawi et al. [103] were all conducted under constant stress amplitude, at the same cycling parameters of 5 Hz and loading ratio $R = 0.1$, so it is acceptable to compare their secant modulus data. To mitigate the influence of differing fibre content in the test specimens, modulus comparisons are only made after normalising by initial undamaged modulus E_0. An analysis of stiffness evolution characteristics is possible by examining the relationship between stiffening and loading level at various points during specimen fatigue life, as is conveniently accomplished by Figure 7.14. Unfortunately, the identified mean trends of stiffness evolution from both sources suggest contradictory conclusions. FE [0] data reported by Liang et al. [50] reveals that the extent of stiffening *reduces* with increasing loading levels (see Figure 7.14(a)); however, data from El Sawi et al. [103] suggests

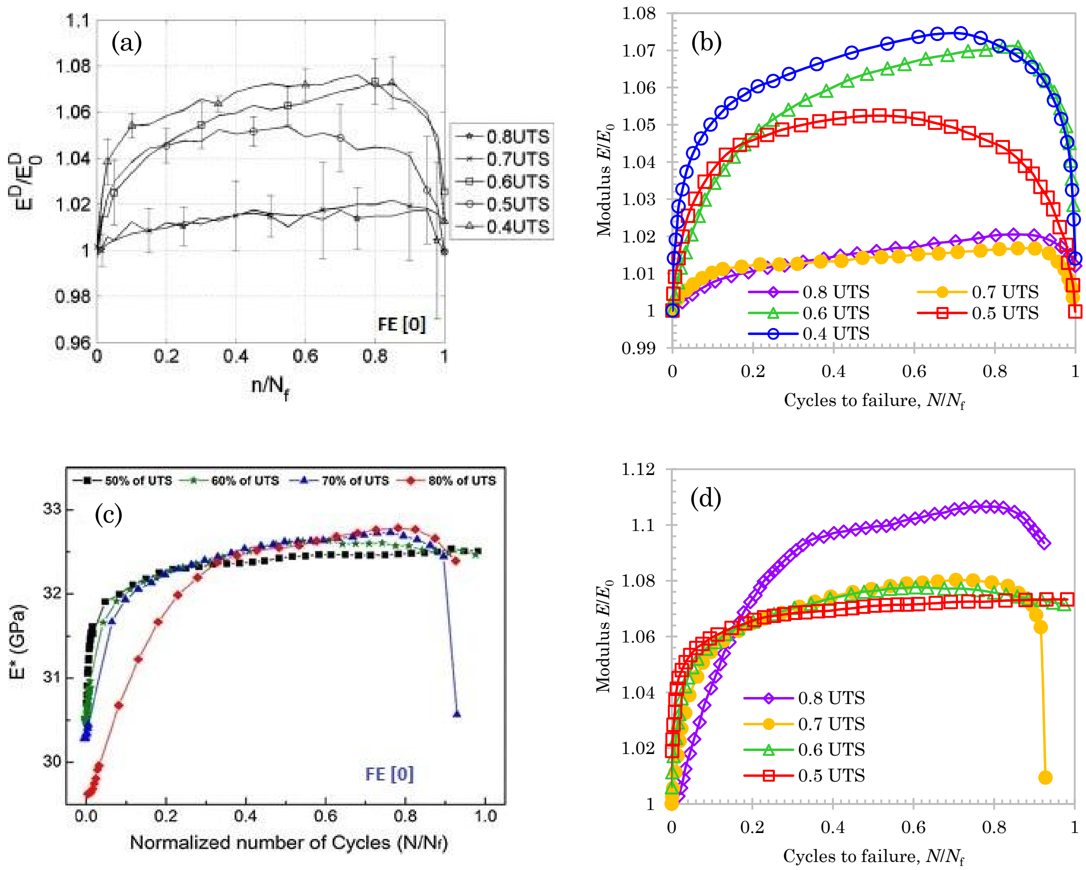

Figure 7.12: Reported secant modulus evolution of Flax-epoxy [0] laminates under constant stress amplitude fatigue (5 Hz, $R = 0.1$), from two different sources: (a) $[0]_{12}$ reproduced with permission from [50]; (b) shows same dataset as (a) but with noise-filtered/smoothed median trends; (c) $[0]_{16}$ reproduced with permission from [103]; (d) shows same dataset as (c) but plotted with normalised modulus.

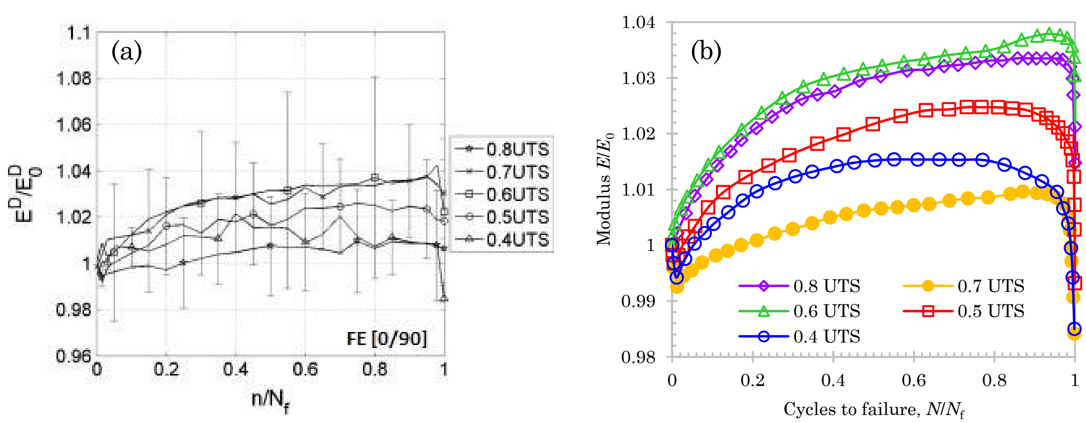

Figure 7.13: Reported secant modulus evolution for Flax-epoxy $[0/90]_{3S}$ under constant stress amplitude fatigue (5 Hz, $R = 0.1$): (a) chart reproduced with permission from [50]; (b) shows same dataset as (a) but with noise-filtered/smoothed median trends.

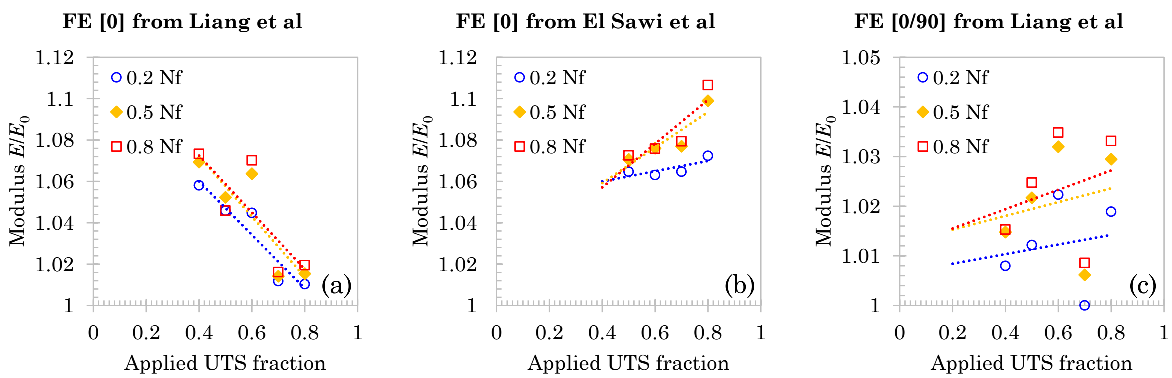

Figure 7.14: Mean trend of modulus evolution over applied loading levels for Flax-epoxy [0] and [0/90] specimens at early (0.2 N_f), mid (0.5 N_f), and late (0.8 N_f) fatigue life. Derived from data reported by Liang et al. [50] and El Sawi et al. [103].

that the stiffening *increases* at higher loading levels (see Figure 7.14(b)). In the case of FE [0/90] (see Figure 7.14(c)), the reported data produces an erratic curve, but a weak increasing relationship can be inferred between loading level and stiffening. In all cases, though, a proportional relationship appears to exist between stiffening percentage and applied peak stress (or stress amplitude). Also, note that all three fibre-dominant laminates exhibit stiffness increase, at least until $0.8N_\mathrm{f}$, under *all* tested load levels.

It must be noted that the progressive stiffness data from Liang et al. [50] appears to involve considerable signal noise, producing large standard deviations and error bars, as can be seen in Figures 7.12(a) and 7.13(a). This may have resulted from the strain calculation method adopted in their study. Strain was not measured by a dedicated transducer, but estimated from actuator crosshead displacement – which is a less-precise method of recording specimen deformation. In contrast, the tests of El Sawi et al. [103] employed a 25-mm-gauge extensometer to measure specimen strain directly, possibly resulting in the smoother, relatively noise-free evolution curves seen in Figure 7.12(c). Since El Sawi et al. [103] did not disclose standard deviations of their modulus data, it is not possible to to compare data precision between the two sources. However, as their strain was obtained via extensometer, the resulting modulus values and stiffening trends may be considered more reliable.

Most studies popularly attribute this apparent fatigue-stiffening in fibre-dominant specimens to microstructural reorganisation in the Flax fibres, such as reorientation of microfibrils and strain-induced crystallisation of amorphous cellulose (these mechanisms are discussed at length in the introductory Chapter 2), which are thought to enhance the stiffness of the fibre structure [25; 50; 109; 110; 115]. These mechanisms of irreversible microstructural changes are also popularly cited as the cause for fibre-direction permanent deformation, as discussed earlier in Section 2.2.3.2. However, though plausible and supported by indirect experimental evidence, these conclusions are still speculative. No *in-situ* observation methods have yet been reported that directly correlate these processes to apparent mechanical stiffening under stress-controlled fatigue, perhaps because examining material microstructure under such dynamic loading remains a technical challenge even in laboratory conditions.

7.3.2 Matrix-dominant response

Unlike fibre-dominant behaviour in the preceding section, specimens of off-axis laminates such as FE [±45] and [90] demonstrate *degrading* stiffness evolution that matches the typical 3-stage trend expected of fibre-composites. Figures 7.15 and 7.16 show reported evolution for FE [±45] and FE [90], respectively, from two independent sources.

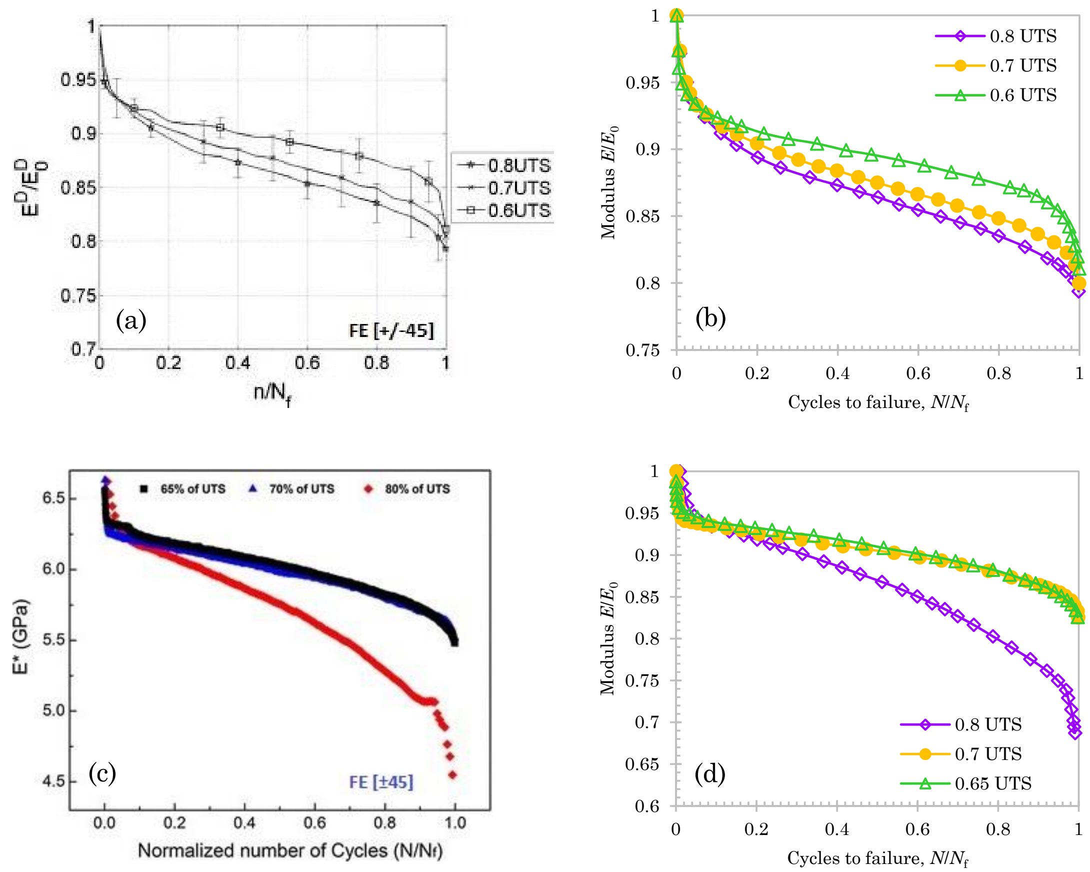

Figure 7.15: Reported secant modulus evolution of Flax-epoxy laminates under constant stress amplitude fatigue (5 Hz, $R = 0.1$): (a) $[\pm45]_{3S}$ reproduced with permission from [50]; (b) same dataset as (a) but with noise-filtered/smoothed median trends; (c) $[\pm45]_{4S}$ reproduced with permission from [103]; (d) shows same dataset as (c) but plotted with normalised modulus.

It is seen that degradation is rapid during the early stages (first 10% of fatigue life), where stiffness reduces to ∼0.95 of original modulus E_0 in FE [±45] (Figure 7.15), and to $\sim0.98E_0$ in FE [90] specimens (Figure 7.16). This is followed by an interval of less-intense degradation (0.1–$0.9N_f$), wherein reported data suggests that the extent of stiffness degradation is directly proportional to the fatigue load level. This direct relationship between loading level and stiffness reduction over fatigue life becomes evident when data is viewed as done in Figure 7.17. The final stage (last 10% of fatigue life) is also of rapid degradation, just before failure. Total stiffness loss in the [±45] specimens ranges between 15-30%, depending on the source and fatigue loading level (compare Figures 7.15(b) and (d)). In the [0/90] specimens, relative stiffness loss is more modest 10-15%.

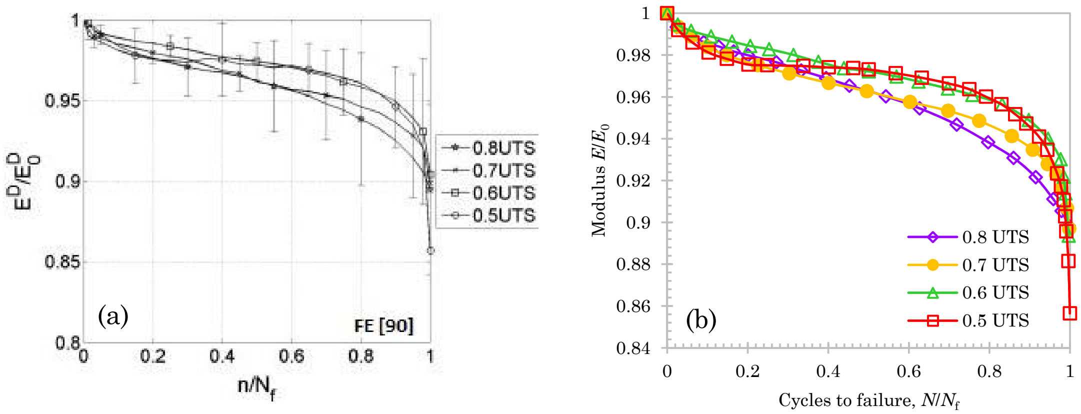

Figure 7.16: Reported secant modulus evolutions of Flax-epoxy $[90]_{12}$ laminate under constant stress amplitude fatigue (5 Hz, $R = 0.1$): (a) reproduced with permission from [50]; (b) same dataset as (a) but with noise-filtered/smoothed median trends.

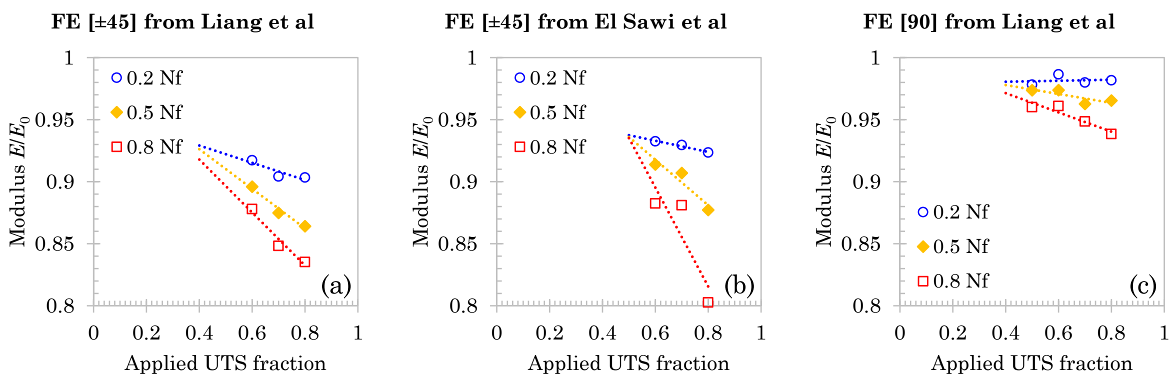

Figure 7.17: Mean trend of modulus evolution over applied loading levels for Flax-epoxy [±45] and [90] specimens at early (0.2 N_f), mid (0.5 N_f), and late (0.8 N_f) fatigue life. Derived from data reported by Liang et al. [50] and El Sawi et al. [103].

7.3.3 Comparison with other NFCs

Comparable progressive fatigue damage studies of other NFCs, i.e. tests conducted under the same parameters as those reported for Flax-epoxy (Table 7.1), are not yet available. So, a comparison of stiffness degradation or permanent strain accumulation cannot be directly made without accounting for the influence of differing fatigue parameters. However, some interesting observations can still be made from the reported study on Hemp-epoxy (HE) fatigue. Figure 7.18 shows the stiffness evolution in HE cross-ply specimens of [0/90] and [±45], which were tested at 1 Hz and a very low loading ratio of $R = 0.01$ by de Vasconcellos et al. [116].

Considering that Hemp fibre is very similar to Flax fibre in microstructure and mechanical properties (as discussed earlier in this chapter and in Chapter 2), HE specimens can be expected to demonstrate similar fatigue damage progression behaviour as FE. However, Figure 7.18(a) shows that HE [0/90] specimens exhibit *degrading* stiffness, which is unlike reported FE [0/90] behaviour shown in Figure 7.13. Furthermore, there is a clear relationship between loading stress level and stiffness degradation – higher loading

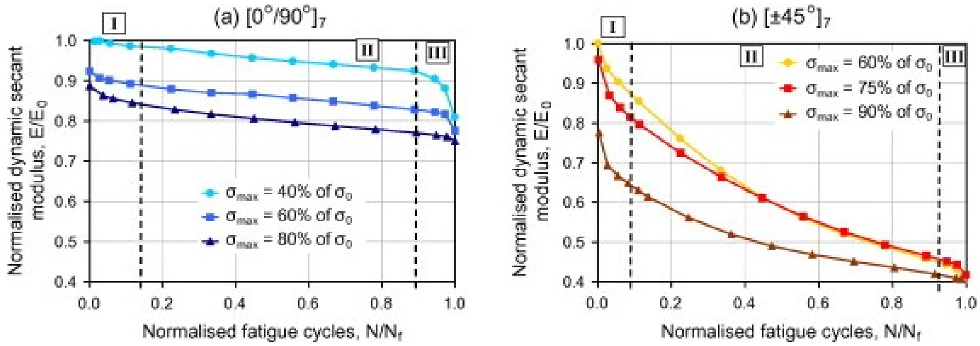

Figure 7.18: Reported secant modulus evolution of asymmetric Hemp-epoxy crossply laminates under constant stress amplitude fatigue at 1 Hz and $R = \frac{\sigma_{\min}}{\sigma_{\max}} = 0.01$: (a) $[0/90]_7$, and (b) $[\pm 45]_7$. Reproduced with permission from [116].

amplitude corresponds directly with deeper stiffness loss.

For HE [±45], the modulus evolution seen in Figure 7.18(b) is similar to the degrading behaviour of FE [±45] in Figure 7.15, following the typical trend of engineering fibre-composites. Again, the stiffness loss is proportional to the loading level. Interestingly, most of the stiffness decrease occurs during the early half of fatigue life, and the total percentage decrease before failure is almost identical (60% loss) for all specimens tested at 0.6–0.9UTS. In contrast, FE [±45] specimens tested under similar stress amplitude reported by Liang et al. [50] lose only 20% of original stiffness (see Figure 7.15(b)).

The reverse stiffness evolution behaviour of HE [0/90] when compared to FE [0/90] is concerning, as this contradiction introduces additional confusion in predicting progressive damage in fibre-dominant NFCs.

7.4 Further discussion

7.4.1 On fatigue endurance of all NFCs

The general findings on the fatigue life characteristics of all NFCs under constant stress-amplitude fatigue are summarised and discussed:

1. All NFC fatigue life data reported to date can be modelled by linear relationships between cyclic peak stress $\sigma_{\max}$ and logarithm of cycles-to-failure $\log(N_{\mathrm{f}})$, per (7.1) adopted from ASTM E739 [219].

2. NFCs of higher static tensile strengths tend to have longer fatigue lives. The most durable FE laminate under constant stress amplitude fatigue is [0], followed by [0/90], quasi-isotropic, twill-woven reinforced, [±45], random-oriented short-fibre reinforced, and [90] – in decreasing order of fatigue endurance (Figures 7.1–7.3).

3. A natural high-cycle fatigue strength or limit is not identifiable for NFCs from the available studies, as all stress-life data follow linear trends of constant slope. As such, an arbitrary definition of fatigue

limit must be resorted to – e.g. stress at which specimens life exceeds 2 million cycles. This fatigue strength may be easily calculated by applying relations (7.1)–(7.2).

- Recall that Bensadoun et al. [109; 110] found monotonic static properties to be statistically unchanged after 500,000 fatigue cycles under 0.3UTS for nearly all Flax-epoxy laminates considered in their study. Such *post-fatigue* static tests may be a means to confirm an arbitrarily-defined fatigue limit. For example, if a specimen demonstrates insignificant reduction of material properties even after, say, 2 million cycles at a certain stress amplitude, then that peak stress level may reasonably be considered as the fatigue or endurance limit.

4. A common complication in comparing data from disparate fatigue studies is the inconsistent fibre content in tested specimens, which not only varies from study to study, but also from laminate to laminate within a given study. A convenient way to mitigate the influence of varying fibre content is to normalise peak stress by composite density, since composite density accounts for fibre content by definition. Fatigue life performance is compared after essentially converting stress-life (σ-log(N)) data to *specific*-stress-life (σ/ρ-log(N)).

5. Parameters of the linear stress-life relationships (7.1) and (7.2) are identified for all considered NFC laminates and some equivalent Glass-composites, and listed in Tables 7.4 and 7.4.

7.4.2 On fatigue endurance of Flax-epoxy

When normalised for composite density, the following becomes evident about the fatigue performance and potential of Flax-epoxy composites:

1. Flax-epoxy [0] specimens are found to exceed Glass-epoxy [0/90] in fatigue longevity. Therefore, FE [0] laminates may be potential replacements for GE [0/90] in fatigue-life critical applications. Note, however, that GE [0/90] specimens survive significantly longer than equivalent [0/90] stacking sequence of FE (Figure 7.4(b)).

2. Interestingly, *short-fibre* Glass-epoxy specimens have similar fatigue performance to Flax-epoxy [0/90], suggesting that they may be interchangeable for fatigue-critical applications.

3. FE [±45] laminates have similar specific strengths and fatigue lives as their GE counterparts (Figure 7.5), suggesting a potential for replacing these angled-crossply Glass-composites with those of Flax.

4. Furthermore, *short-fibre* FE specimens appear to have similar fatigue lives to FE [±45] (Figure 7.3(a)) which are, as noted above, similar to GE [±45] in endurance. This suggests that short-fibre and [±45] Flax-epoxy may *both* be potential replacements for Glass-epoxy [±45].

5. FE Twill fabric laminates have marginally shorter fatigue lives than FE [0/90] (Figure 7.1(b)), but may be considered comparable. Also, FE quasi-isotropic specimens have identical fatigue lives as [0/90] and twill-woven specimens (Figure 7.3(b)). This suggests that both biaxial and quasi-isotropic configurations of Flax-epoxy may be interchangeable amongst each other, for fatigue-life critical applications.

6. The shorter fatigue lives of above balanced *textile* FE laminates compared to [0/90], despite their identical biaxial reinforcement, suggests that woven laminates experience earlier damage initiation and/or quicker internal damage progression, resulting in expedited specimen fracture. This conclusion is supported by the observations of Asgarinia et al. [108], who propose that that presence of crimp or out-of-plane weaves result in poorer matrix impregnation between woven fibre bundles, and are therefore more likely to develop interfacial cracks.

7.4.3 On fatigue endurance of other NFCs

When normalised for composite density, the following is observed about the fatigue performance of other NFCs when compared to Flax-epoxy:

1. Sisal-epoxy (SE) specimens offer comparable fatigue performance to Flax-epoxy composites, particularly when loaded in the fibre-direction (Figure 7.6). It follows that these SE [0] laminates are candidates to replace the same Glass-composites that were found to be interchangebale with Flax-epoxy.

2. Hemp-epoxy (HE) [0/90] specimens show comparable, but marginally shorter fatigue lives than FE [0/90] and twill-woven specimens. However, in the angled-crossply configuration [$\pm$45], HE fatigue performance appears identical to those of FE (Figure 7.6). It may be concluded that, when loaded in the fibre-direction, Hemp-composites suffer quicker damage initiation and progression than Flax-composites. But, when loaded off-axis as in [$\pm$45], damage mechanisms and progression are similar.

3. Natural fibre composites of High-density Polyethylene (HDPE) are significantly inferior in fatigue endurance to composites based on epoxy or polyester matrix material (Figure 7.6). A possible reason may be that HDPE offers poor adhesion with natural fibres, which manifests in low fatigue resistance.

4. Polyester-based composites reinforced by Flax, Sisal, or Jute fibres demonstrate identical fatigue longevity, at least when loaded in fibre-direction (Figure 7.8). This is in agreement with the previously-stated finding that Sisal-epoxy specimens showed similar fatigue endurance as Flax-epoxy. Based on these polyester-based specimens' performance, it appears Jute fibre reinforcement may also offer similar density-normalised fatigue performance as Flax.

5. Polyester composites reinforced by Hemp, however, underperform when loaded in the fibre-direction, compared to the Flax, Sisal, and Jute specimens (Figure 7.8). This observation is in agreement with the behaviour of epoxy-based specimens noted earlier, where Hemp-epoxy [0/90] also had shorter lives than Flax-epoxy [0/90] (Figure 7.6).

6. The above findings strongly suggest that Hemp fibres offer poorer fibre-direction fatigue endurance than Flax, Sisal, and Jute – which is unexpected, since Hemp fibres have comparable cellulose content, cellulose crystallinity, and mechanical properties as Flax and Jute [115]. Hemp does appear to have smaller microfibre orientation angle (2–6°) compared to Flax or Jute (5–10°) [115], so it can be reasoned that microfibrils in Hemp become taut and fully engaged in fibre-direction load resistance *earlier* during fatigue cycling, thus accumulating damage *sooner*. As such, Hemp-composite behaviour may be attributed to higher damage incurred within its fibre structure, or even poorer

adhesion of Hemp fibres with surrounding matrix (unlikely). Further controlled experimentation is required to conclusively identify a plausible root cause.

7. In short, Flax fibre offers better fatigue resistance than Hemp, but comparable performance to Sisal and Jute.

8. Epoxy composites of natural fibres, regardless of stacking sequence or fibre architecture, consistently show superior fatigue endurance when compared to composites of polyester and polyethylene matrix material (Figures 7.8–7.9). This is further corroborated when comparing Glass-epoxy (GE) with Glass-polyester (GPe) fatigue performance: GE [±45] and short-fibre mat specimens outperform GPe specimens of the same architectures (Figures 7.9–7.10).

7.4.4 On progressive damage accumulation

The stiffness degradation characteristics of Flax-epoxy and other NFC specimens under constant stress-amplitude fatigue are summarised and discussed:

1. Evolving material stiffness can be considered a measure of internal damage accumulation.

2. Under stress-amplitude-controlled loading ratio of R=0.1, Flax-epoxy (FE) specimens reinforced along loading-axis ('fibre-dominant', e.g. [0], [0/90]) appear to *increase in stiffness* during fatigue cycling, until about 80% of fatigue life, after which stiffness returns to the original undamaged value just before failure (Figures 7.12–7.13).

3. FE specimens that *do not* have plies or fibres oriented along the loading-axis ('matrix-dominant', e.g. [±45], [90]) exhibit the typical 3-stage *decreasing* stiffness expected of engineering fibre-composites (Figures 7.15–7.16).

4. The relationship between fatigue load level and degree of stiffening in fibre-dominant specimens cannot be conclusively identified due to contradictory reports from different studies [25; 50; 103] (Figures 7.12 and 7.14).

5. In contrast, the load-stiffening relationship is clearer for matrix-dominant FE specimens, where independent studies consistently show that higher loading amplitude generally results in larger loss of stiffness (Figure 7.17).

6. Further contradiction of Flax-epoxy stiffening behaviour in [0] and [0/90] specimens arises from studies on other NFCs, particularly Hemp-epoxy (HE) by de Vasconcellos et al. [116]. HE [0/90] specimens are found to show *decreasing* stiffness (Figure 7.18), in contrast to that reported for FE. Hemp fibres have similar hierarchical microstructure, constituent fractions, and even damage mechanisms similar to Flax. So the only remaining source of this differing behaviour seems to be the testing parameters applied. The reported HE specimens were fatigued at 1 Hz and R=0.01, whereas the FE specimens were tested at 5 Hz (higher frequency) and higher loading ratio R=0.1 (smaller stress amplitude).

7. Further controlled testing is necessary to identify the effect of test parameters on the apparent stiffening phenomenon in fibre-dominant Flax-composites, since the nature of modulus evolution has considerable impact on engineering design factors (e.g. developing progressive damage material models). Furthermore, such contradictorty data on mechanical behaviour compromises confidence in NFCs as potential replacements for synthetic fibre composites.

7.5 Limitations of existing fatigue studies and future work

The limitations of existing fatigue knowledge on NFCs, and future work to address these identified limitations are discussed:

1. From the survey of NFC fatigue studies conducted in this chapter, it can be concluded that existing knowledge of *fatigue endurance* under tension-tension stress-controlled cycling is substantial, though not comprehensive. Sufficient fatigue life data is available for Flax-epoxy (FE) composites from multiple sources to allow collective analysis of several common architectures, namely [0], [90], [0/90], [±45], and random-oriented short-fibre reinforced laminates. Data from these FE tests may also be applicable to composites of similar plant fibres, such as Sisal, Hemp, and Jute. However, most FE tests to date are tension-tension, at a nominal loading ratio of $R = 0.1$. Further testing is required to determine fatigue lives under different loading ratios, including tension-compression and compression-compression conditions, so that cost-saving fatigue life prediction tools such as *fatigue master curves* and comprehensive *constant fatigue life diagrams* may be developed [223]. Such approaches allow the theoretical prediction of constant-amplitude fatigue lives under a variety of loading ratios, which may be extrapolated to predict composite behaviour under complex, variable-amplitude or multiaxial operational loading in real engineering applications [224; 225].

2. While data on *fatigue life* is sizeable, the number of *progressive damage* studies available for various Flax-epoxy/NFC architectures is still limited. Further studies are necessary to confirm the evolution of material properties and damage indicators (e.g. residual stiffness, residual strength, mean strain, permanent strain, crack density, dissipated energy, etc). For such novel bio-materials as NFCs, 'reproducibility' is essential to induce confidence in reported data and encourage popular application.

3. It is noted earlier that reports of FE [0] stiffness evolution have conflicting aspects [25; 50; 103] – namely the relationship between load amplitude and stiffness increase. Such fibre-dependent behaviours must be clarified, since (i) these observations influence the development of predictive models, and (ii) fibre-direction properties are an important defining feature of NFCs when proposing a comparison with synthetic fibre composites.

4. The internal physical mechanisms proposed to explain the *composite stiffening* behaviour of fibre-dominant specimens are the same as those identified for *elementary fibre stiffening* discussed in Chapter 2: (i) reorientation of microfibrils in the S2 cell wall, and (ii) strain-induced crystallisation of amorphous cellulose in the fibre wall [25; 50; 103; 109; 110]. However, these conjectures are refuted by the finding that Hemp-composites, wherein the fibres have microstructure and damage mechanisms similar to Flax, *do not demonstrate fibre-direction stiffening* (Figure 7.18). Note that

all Flax-epoxy publications that report stiffening are based on tests conducted at the same 5 Hz, R=0.1 parameters, namely those of Bensadoun et al. [109; 110], Liang et al. [25; 50], and El Saw et al. [103]. It is advisable to now study stiffness evolution of the same Flax-epoxy composites under different fatigue loading conditions.

5. It is yet unclear why Hemp-reinforced composites would demonstrate exactly the opposite stiffness progression behaviour of Flax-reinforced specimens. Considering that Hemp and Flax fibres are mechanically comparable, the most significant difference between reported FE tests [25; 50; 103] and HE tests [116] are the fatigue-testing parameters applied. In the absence of newer information, it seems very likely that *the nature of stiffness evolution in NFCs is sensitive to the fatigue test parameters applied*. That is to say, variation in cycling amplitude, or frequency, or both, may influence the path of observable stiffness evolution towards an increase or decrease. If so, this is a serious source of error in studying NFC fatigue response, and must be controlled for in future studies. The implications of a fibre-composite configuration that does not lose its original stiffness under fatigue conditions, as is suggested by the independent findings of Liang et al. [25; 50] and El Sawi et al. [103] (Figures 7.12–7.13), are significant to the goal of promoting NFCs as alternatives to synthetic fibre composites, and therefore must be thoroughly verified.

6. Considering the limited number of studies available for Flax-epoxy alone, the unusual fatigue-stiffening phenomenon reported for its fibre-dominant laminates, the inconclusive relation between load amplitude and stiffening, and the possible influence of test parameters on observed progressive response, it is concluded that existing knowledge on Flax-epoxy fatigue damage is insufficient, ambiguous, therefore inadequate for engineering design consideration. Continued research on Flax-epoxy (and other comparable NFCs) is necessary to clarify their fatigue damage response with confidence.

7.6 Conclusion

This 'review and analysis' study was conducted since a necessity for a holistic examination of existing NFC fatigue studies was identified. All available on fatigue studies were examined, to the best of the author's knowledge: 6 publications on different Flax-epoxy composites, and 7 on other NFCs. From the collective examination of all fatigue reports on Flax, Hemp, and Jute composites, it may be concluded that mechanisms of fatigue-related degradation are the same in cellulosic plant fibre composites, and these mechanisms are similar to those identified from monotonic and quasi-static testing. Fatigue testing parameters (e.g. frequency, loading ratio) and structural variables (e.g. off-axis plies, moisture content, fibre crimp, 'out-of-plane' weaves in fabric) are all found to influence longevity. Strain amplitude and permanent deformation is continually increasing under constant stress-amplitude fatigue, and has been shown to be correlated to increasing internal crack density. To minimise the influence of different fibre-fractions in data across disparate studies, the stress in stress-life data can be normalised by composite density; therefore *specific S–N* plots enable fairer comparison of fatigue performance. Of all reported composites, epoxy-based matrix provides highest composite fatigue resistance, followed by polyester and polyethylene. The most durable FE laminates architectures in decreasing order are [0], [0/90], quasi-isotropic, twill-fabric reinforced, [±45], short-fibre reinforced, and [90]. FE [0/90], balanced-twill fabric reinforced, and quasi-isotropic laminates have comparable fatigue lives, and therefore may be interchangeable. Similar comparable performance is found between FE [±45] and short-fibre reinforced configurations. UD [0] laminates of Flax, Sisal, and Jute exceed Glass-reinforced [0/90] in specific fatigue endurance; while Flax- and Hemp-reinforced short-fibre and [±45] configurations show similar endurance to Glass-reinforced [±45] – thus indicating several opportunities to replace Glass-reinforcement by natural fibres. Laminates of matrix-governed behaviour consistently show progressive loss of stiffness from all reports. Contradictory reports of stiffness evolution is found in NFCs where behaviour is governed by fibre properties: (i) both directly proportional and inverse correlations have been reported between stress amplitude and stiffness change; and (ii) independent studies found FE specimens show progressive *stiffening* even while accumulating internal physical damage (cycled at 5 Hz, R=0.1), but similar fibre-dominant HE specimens show progressive *degradation* (cycled at 1 Hz, R=0.01).

NFC fatigue research is concluded to be still limited and ambiguous, and therefore insufficient for engineering design. Continued research (both original and duplication studies) are required to encourage confident application of NFCs in high-performance dynamically-loaded structures.

Chapter 8

Fatigue response, constant strain amplitude

This chapter describes original strain-amplitude controlled fatigue tests of Flax-epoxy laminates of four commonly-studied architectures, and of two Glass-epoxy laminates for comparative investigation. Fatigue endurance is tested and statistically modelled. The physical cracking damage in Flax-epoxy composites are observed and their mechanisms described. The cyclic fatigue response of these NFCs, and evolution of their damaged mechanical properties, are contrasted with equivalent Glass-epoxy composite performance, and with reported data from stress-amplitude controlled fatigue studies.

8.1 Introduction

The previous chapter identified a concerning limitation of NFC fatigue studies reported to date – there is reason to suspect that stiffness evolution measurements, particularly those of fibre-direction modulus, are sensitive to test parameters (frequency and/or loading amplitude), which may be responsible for the apparent *stiffening* observed in Flax-reinforced epoxy [0] and [0/90] specimens [25; 50; 103; 109; 110].

The cause of this remarkable stiffening behaviour in Flax-epoxy composite is now typically attributed to the same internal physical mechanisms identified for *elementary fibre stiffening* of ligno-cellulosic plant fibres, discussed in Chapter 2: (i) microfibrils *reorienting* towards loading-axis, and (ii) strain-induced *crystallisation* of initially amorphous cellulose [25; 50; 103; 109; 110]. But these proposals may be called to question by studies of comparable Hemp-reinforced epoxy compsites [116] that do not exhibit any stiffening when fatigued in the fibre-direction, despite Hemp fibre structure possessing similar microfibrillar arrangement and non-crystalline cellulose content. Furthermore, it is unlikely that (i) these fibre-specific physical mechanisms should continue for 80% of specimens' fatigue lives, some of which are in excess of 500,000–1,000,000 cycles, as reported in [25; 50; 103; 109; 110], (ii) and that the stiffening contributions of microfibrils and crystallising cellulose are not countered by the degrading effect of accumulating crack-damage in other parts of the composite, namely in fibre walls or along fibre-matrix interface (as are known to occur [50; 55; 95; 103; 116]).

As discussed in the previous chapter, in all NFC fatigue studies to date, the cyclic loading signal is stress-amplitude controlled, under which specimens demonstrate a continuously increasing deformation amplitude (strain amplitude) over fatigue life. It follows that specimens cycled at constant stress amplitude experienced progressively increasing *strain rates* as they accumulate damage and become more compliant (or less stiff). Since studies by Kim et al. [15], Poilâne et al. [198], and Fotouh et al. [94] have convincingly shown that NFC response (stiffness, strength, and failure strain) is sensitive to deformation rate (see Figure 8.1), it is reasoned that a changing strain rate introduces an additional (and, perhaps, unnecessary) variable in stress-controlled fatigue tests, which may have influenced the observed mechanical properties (e.g. aforementioned stiffness increase) and, subsequently, the conclusions derived from those observations.

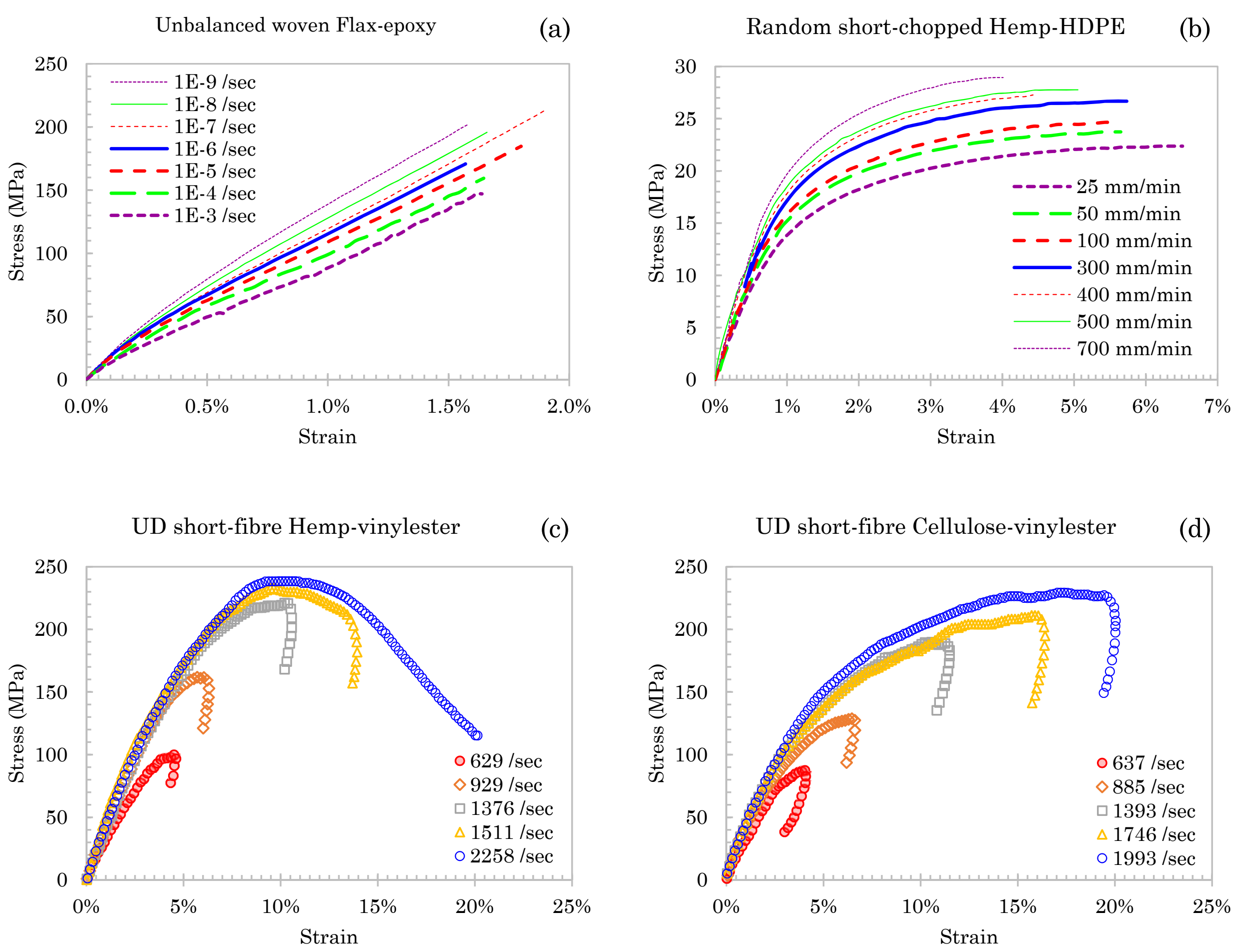

Figure 8.1: Influence of strain-rate on the uniaxial response of several NFCs: (a) Woven Flax/epoxy, from data in [198]; (b) Random oriented short-chopped (<5 mm) Hemp/HDPE, from data in [94]; (c) UD short-fibre (∼25.4 mm) Hemp/vinylester, from data in [15]; and (d) UD short-fibre (∼25.4 mm) Cellulose/vinylester, from data in [15].

The study detailed in this chapter initiates with the hypothesis that the fibre-direction stiffening in spite of damage, as reported in recent Flax-epoxy fatigue studies [25; 50; 103; 109; 110], is not an inherent material property of the natural fibre composite, but a consequence of the fatigue test method adopted.

In order to eliminate or limit the effect of a continuously varying strain rate, the mechanical tests in this chapter were conducted under a constant-amplitude strain, thereby enforcing a near-constant strain rate during the cyclic loading and unloading phases, throughout the duration of each fatigue test.

8.2 Materials and manufacturing

Commercially available unidirectional Flax fabric and E-Glass were used as reinforcement in a thermoset-polymer epoxy matrix. The manufacturing parameters were selected to produce a ~50-50% fibre-matrix composition in the eventual laminates. For a detailed description of the reinforcing fibres, epoxy-hardener matrix, and composite manufacturing, refer back to Chapter 4. Four Flax-epoxy laminates are studied for fatigue performance: unidirectional $[0]_{16}$, crossplies $[0/90]_{4S}$ and $[\pm 45]_{4S}$, and quasi-isotropic $[0/-45/90/45]_{2S}$. The crossply laminates are compared with equivalent stacking-sequence Glass-epoxy specimens that are also tested for fatigue: $[0/90]_{3S}$ and $[\pm 45]_{3S}$. The densities and constituent fractions of the tested composites are given in Table 4.1.

8.3 Experimental methods

8.3.1 Specimen preparation

All composite specimens were cut from the manufactured plates using a fine-cutting 0.35 mm diamond-edged saw, followed by grinding to produce a flat edge finish. Monotonic test specimens were prepared as detailed in Chapter 5. For fatigue testing, specimens with the same rectangular 250×25 mm dimensions were cut from the 4 mm thick manufactured plates. Laboratory trials indicated that specimens fitted with tapered Aluminium tabs (as was done for static testing in Chapter 5) often fractured near the grips during fatigue testing, while those with Flax-epoxy tabs (quasi-isotropic layup) always fractured in the middle gauge section. Specimen and tab dimensions are within the guidelines of fatigue testing standard ASTM D3479 [226].

8.3.2 Testing

All tests were carried out at room temperature and pressure in the same servo-hydraulic MTS 322 (Eden Prairie, MN, USA) test frame used for the static testing documented in previous chapters. In order to determine the relative failure strains of each composite chosen for fatigue study, displacement-controlled tests were conducted for baseline monotonic mechanical properties. These tests, including strain measurement, are identical in procedure to those documented in Chapter 5.

For fatigue tests, loading to enforce constant-amplitude strain was controlled via feedback from a 1.0-in (25.4 mm) gauge uniaxial extensometer. The typical fatigue test program conducted in this study is a combination of alternating fatigue and quasi-static stages, as demonstrated by the command waveform diagram Figure 8.2. In order to follow the evolution of residual 'static-condition' stiffness of the specimen, a typical test initiates with quasi-static cycle, followed by a fatigue regime that is periodically interrupted for

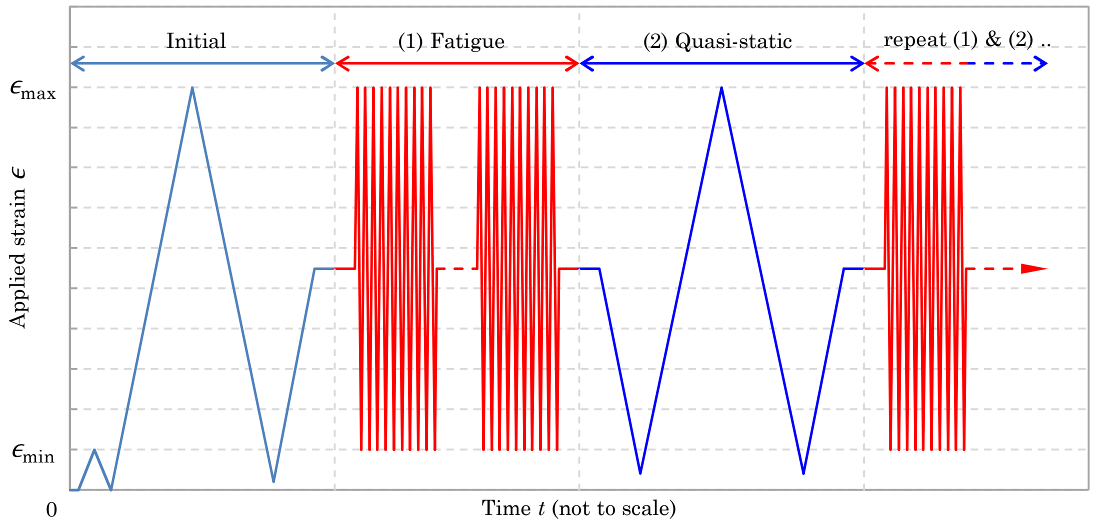

Figure 8.2: Strain signal waveform showing initial quasi-static cycles (2 mm/min), followed by fatigue cycling (5 Hz, $R_\epsilon = 0.1$) interrupted at intervals by one-and-half quasi-static cycle.

interim quasi-static tests. The quasi-static cycles were displacement-controlled at 2 mm/min (as was done for tests in Chapter 5), while the tensile-tensile-strain fatigue tests were run at a commanded frequency of 5 Hz and strain ratio $R_\epsilon = \frac{\epsilon_{\min}}{\epsilon_{\max}} = 0.1$. Before initiating the fatigue stage, the specimen is loaded up to the mean strain level, $\bar{\epsilon} = \frac{(\epsilon_{\max} - \epsilon_{\min})}{2}$. During the interim quasi-static stages, the specimen is typically brought down to a zero-force load (strain may be non-zero due to accumulated plasticity), then loaded to the maximum strain $\epsilon_{\max}$. All specimens are tested until failure, or up to a maximum of 2 million fatigue cycles if failure is not observed.

8.3.2.1 IR imaging

During fatigue testing, an Infra-red (IR) camera is used to image the specimen surface at intervals. The aim was to record the evolution of superficial temperature, and thereby indirectly observe the extent of emitted thermal energy as a result of progressive internal damage. The test setup with the IR camera is shown in Figure 8.3.

8.3.3 Data processing

To observe material properties evolution over the fatigue life, the following are measured from the response plots (also demonstrated in Figure 8.4):

- *Initial modulus* E_0 measured from the initial ramp-up response as shown in Figure 8.4(a), considered to be the stiffness of the undamaged material.
- *Fatigue secant modulus* E^{f}, i.e. slope of line passing through both extrema of the fatigue cycle hysteresis loop (ϵ_{max} and ϵ_{min} points), as shown in Figure 8.4.

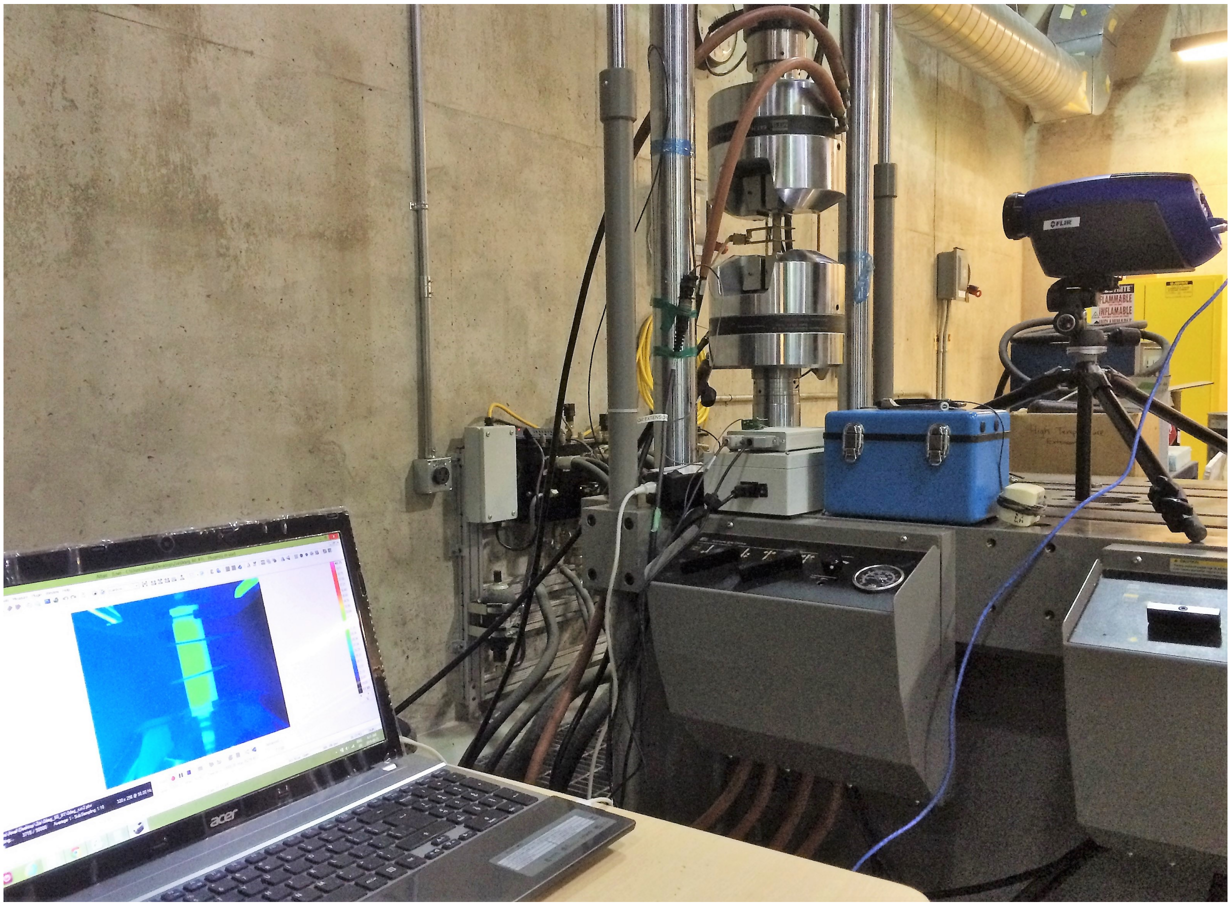

Figure 8.3: Fatigue test setup showing IR camera pointed directly at a mounted tensile specimen. The recorded thermal image is showing on the laptop screen.

- *Damage* D^{f} measured from fatigue cycles, is computed in terms of secant modulus degradation at cycle N (as defined by Hahn and Kim [85]), and given by (8.1). This is similar to the definition of static damage in (5.1).

$$D^{\mathrm{f}}(N) = 1 - \frac{E^{\mathrm{f}}(N)}{E_0} \tag{8.1}$$

- *Static secant modulus* E^{st}, i.e. slope of line passing through both extrema of the quasi-static cycle hysteresis loop, identical to that shown earlier in Figure 5.1.

- *Damage* D^{st} measured from the interim quasi-static cycles, as indicated in the waveform diagram Figure 8.2, is calculated as the secant modulus degradation, identical to the definition of static damage in (5.1).

$$D^{\mathrm{st}}(N) = 1 - \frac{E^{\mathrm{st}}(N)}{E_0} \tag{8.2}$$

- *Inelastic strain* component ϵ^p, measured at the intersection of secant modulus line and zero-stress axis.

- *Hysteresis energy density* U^{h} is the volumetric energy dissipated during a cycle, computed by measur-

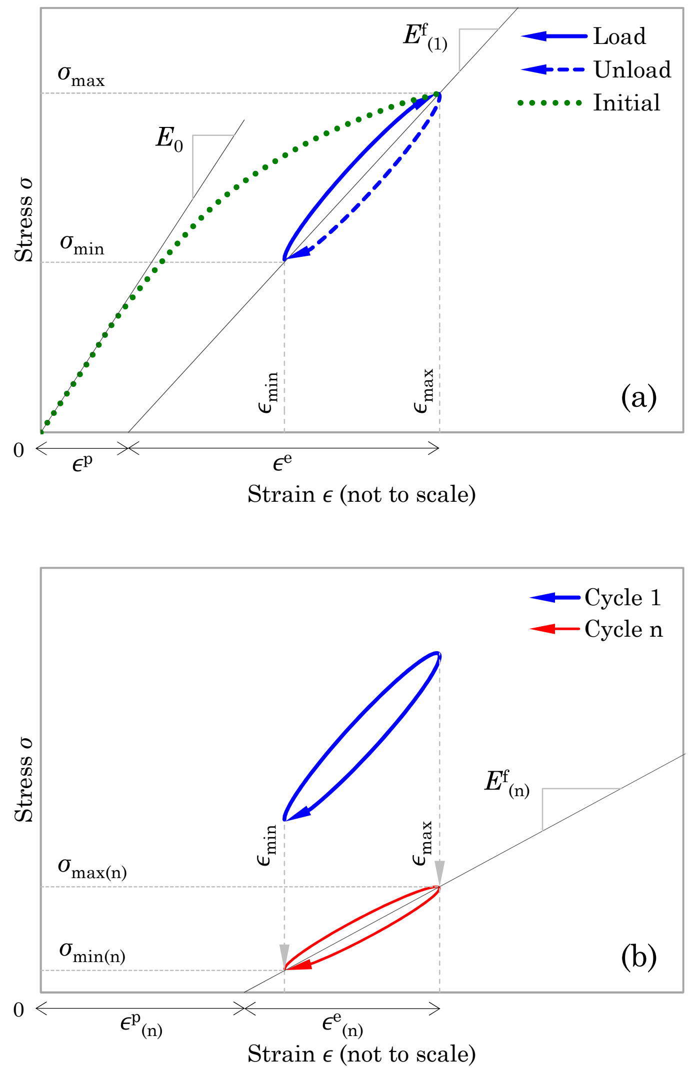

Figure 8.4: Representation of (a) initial ramp-up and fatigue Cycle 1 hysteretic loop, showing initial modulus E_0, stress amplitude, fatigue secant modulus E^{f}, elastic and inelastic strain components ϵ^{e} and ϵ^{p}; (b) Cycle n with same strain amplitude but shifted downwards, with degraded modulus (relaxed stress amplitude) and increased inelastic strain component.

ing the area enclosed by the hysteresis loop in stress-strain plot. This well-known concept represents dissipative processes in the composite related to viscoelasticity and/or internal damage.

- *Surface temperature* T^{S} as detected on the surface of the fatiguing specimens by the IR camera.

Note that under constant amplitude strain reversals, the stress levels required to maintain the commanded strain range tend to relax (demonstrated in Figure 8.4(b)) due to accumulating permanent deformation ϵ^{p}.

8.4 Results and discussion

8.4.1 Monotonic properties

The Flax-epoxy (FE) properties were already reported earlier in Chapter 5. Three tensile tests are conducted for each Glass-epoxy (GE) stacking sequence; their results listed alongside FE properties in Table 8.1.

Table 8.1: Tested mechanical properties of neat epoxy, laminates of Flax-epoxy (FE) and Glass-epoxy (GE)

	Epoxy cured[a]	FE $[0]_{16}$[a]	FE Quasi-isotropic[b,c]	FE $[0/90]_{4S}$[a]	FE $[\pm 45]_{4S}$[a]	GE $[0/90]_{3S}$	GE $[\pm 45]_{3S}$
Initial modulus E_0 (GPa)	3.03 ±0.46	31.42 ±1.47	13.09 ±1.44	16.69 ±0.72	6.42 ±0.41	26.49 ±3.26	14.57 ±0.10
Strength σ^{tu} (MPa)	67.17 ±2.45	286.70 ±13.30	124.60 ±3.25	155.78 ±9.56	74.28 ±3.56	380.61 ±11.83	88.89 ±1.12
Failure strain ε^{tu} (%)	3.61 ±0.23	1.53 ±0.07	1.70 ±0.02	1.57 ±0.08	11.04 ±0.40	1.98 ±0.02	2.52 ±0.04
Poisson's ratio ν_{LT}	0.403 ±.007	0.353 ±0.011	0.357 ±0.050	0.111 ±0.027	0.620 ±0.073	0.075 ±0.004	0.830 ±0.016

[a] from Table 5.6 in Chapter 5
[b] from Table 5.5 in Chapter 5
[c] $[0/+45/90/-45]_{2S}$

To aid comparison between the considered laminates, typical tensile loading response plots are shown altogether in Figure 8.5. All FE laminates that contain a 0° ply along the loading axis fail at similar

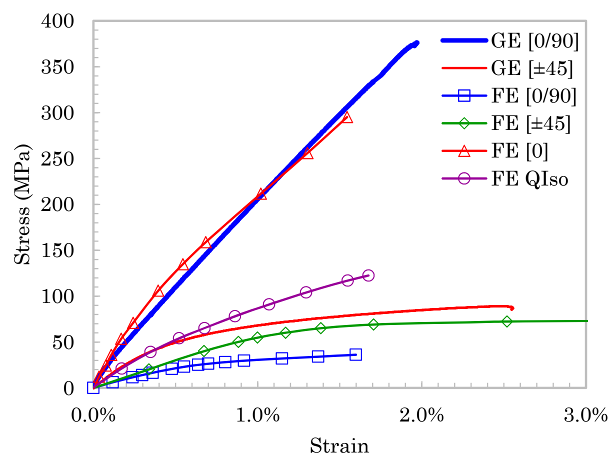

Figure 8.5: Typical monotonic tensile response of Flax-epoxy (FE) and Glass-epoxy (GE) laminates chosen for fatigue study. For clarity, only one curve per composite, and up to 3% strain, is shown.

strains (∼1.6-1.7%), suggesting that axial deformation and failure is fibre-dominant in [0], [0/90], and quasi-isotropic specimens. The strongest of the six is GE [0/90] at 376 MPa and 1.97% failure strain, with the closest comparable FE layup being [0]. The GE [0/90] response is mostly linear, initially at a modulus of 27 GPa then relatively constant at ∼20 GPa. In comparison, FE [0] response is nonlinear. Though the FE [0] is initially stiffer at 31 GPa, its tangential modulus of eventually degrades to become comparable to that of GE [0/90] (evident in Figure 8.5). The GE angled-crossply laminate [±45] has an initial modulus and failure strength of 15 GPa and 89 MPa, respectively. To this, the closest comparable FE layups are the quasi-isotropic (in terms of tangential modulus, at least up to ∼0.5% strain), and FE [±45] (in terms of failure strength and high-strain behaviour).

8.4.2 Fatigue life

Reviewing Figure 8.5, it is evident that the halfway-to-failure strain for most of the considered laminates is in the range of ∼1.0-1.2%. So, values from this range were chosen as the highest peak-strain level at which to start fatigue testing for all laminates. The peak strain levels are shown on the monotonic response curve of each test laminate in Appendix A.6, Figure A.8. For FE laminates, at least 5 replicate tests are conducted for each strain level, while a minimum of 3 per strain level are tested for GE. The fatigue lives of all tested specimens are listed in Appendix A.6, Table A.3. The resulting mean fatigue lives under the chosen peak strain levels are given in Table 8.2.

The typically wide scatter in specimen fatigue lives necessitate the application of statistical methods for data analysis and failure prediction [227]. To analyse strength and fatigue life data of fibre-composites, the two-parameter *Weibull* distribution and the *log-normal* distribution are the most frequently applied probability functions [219; 226–228]. For a comparison of different distribution functions used in analysis of fibre-composite fatigue life/strength, please refer to the work of Hwang and Han [227]. In this study on Flax-epoxy laminates, the log-normal distribution is chosen for fatigue life under constant strain amplitude, following recommended procedures in ASTM D3479 [226] and ASTM E739 [219].

The observed fatigue lives listed in Table 8.2 can be modelled by a linearised strain-life (ϵ-N) relationship per ASTM E739 [219]:

$$\log\left(N_{\mathrm{f}}\right) = A_{\epsilon} + B_{\epsilon}\left(\epsilon_{\max}\right) \tag{8.3}$$

where N_{f} is fatigue life, i.e. number of cycles until failure (dependent variable), $\epsilon_{\max}$ is the commanded *peak strain* (independent variable), A_{ϵ} and B_{ϵ} are material-specific parameters to be determined by fitting ϵ-N test data. Recall that (8.3) assumes a log-normal distribution of fatigue lives, and that the variance (scatter) of $\log(N_{\mathrm{f}})$ is assumed constant over the entire range of tested $\epsilon_{\max}$ levels.

Following ASTM E739 [219] and ASTM STP313 [229], the linear median trend and hyperbolic 95% confidence bounds are computed for all laminates. The modelled hypothesis of linearity in (8.3) was found acceptable for all laminates. The parameters of the linear model are given in Table 8.3. The observed fatigue lives, estimated median lives, and upper/lower confidence bounds for tested laminates are plotted in Figures 8.6–8.7. Samples that survived 2×10^{6} cycles (run-outs) are plotted with 'filled-in' markers. For ease of comparison, all charts are presented at the same axis ranges.

From Figures 8.7(a) and (b), the tested Flax-composites generally appear to have longer strain-fatigue lives than Glass-composites of the same stacking sequence. This observation is true at *all* tested strain levels for [0/90]. Also, the FE trend slope ($B_{\epsilon} = -376.76$) is nearly identical to that of GE ($B_{\epsilon} = -369.35$),

Table 8.2: Average fatigue lives of tested Flax-epoxy (FE) and Glass-epoxy (GE) laminates

Laminate	$\epsilon_{\max}$	mean N_f		St dev[a]	Laminate	$\epsilon_{\max}$	mean N_f		St dev[a]
FE $[0]_{16}$	1.08%	1,453	±	290	FE Quasi-iso[b]	1.28%	434	±	220
	0.94%	4,648	±	1,751		1.12%	3,393	±	1,875
	0.81%	17,670	±	6,819		0.96%	9,184	±	2,679
	0.67%	76,542	±	26,153		0.80%	55,177	±	29,959
	0.54%	218,482	±	68,499		0.64%	472,790	±	92,910
	0.40%	679,583	±	259,199		0.48%	1,111,979	±	362,062
	0.27%	>2,000,000				0.32%	>2,000,000		
FE $[0/90]_{4S}$	1.25%	523	±	194	FE $[\pm45]_{4S}$	1.30%	3,481	±	847
	1.09%	3,670	±	1,566		1.20%	8,321	±	2,723
	0.94%	8,608	±	4,484		1.10%	38,195	±	21,596
	0.78%	44,638	±	16,168		1.00%	100,843	±	49,998
	0.62%	186,172	±	162,022		0.90%	288,384	±	155,063
	0.47%	527,551	±	241,841		0.80%	1,250,226	±	579,593
	0.31%	>2,000,000				0.75%	>2,000,000		
GE $[0/90]_{3S}$	0.90%	4,916	±	1,847	GE $[\pm45]_{3S}$	1.05%	3,691	±	1,199
	0.80%	9,002	±	1,433		1.00%	17,285	±	8,163
	0.70%	18,109	±	8,272		0.90%	110,548	±	40,402
	0.60%	58,607	±	18,198		0.80%	487,440	±	198,831
	0.50%	125,531	±	49,607					
	0.40%	332,058	±	142,524					

[a] Population standard deviation
[b] $[0/+45/90/-45]_{2S}$

i.e. the FE log-lives exceed those of GE by a consistent relative proportion (see Figure 8.7(a)). For [±45], the longer survival of FE is true only for strain levels $\geq$ 0.8%. Below this, between 0.8-0.6% strain levels, extrapolating the median trends would suggest that both FE and GE [±45] have statistically similar fatigue lives (1–3$\times10^6$ cycles). Note, however, that since testing is terminated at 2$\times10^6$ cycles, there is no test data beyond this to allow a conclusive comparison of fatigue performance. A natural high-cycle fatigue limit cannot be identified for any of the FE specimens, as all composite log-lives consistently follow a linearly increasing trend with decreasing strain levels, eventually exceeding the maximum limit of 2$\times10^6$ cycles at a low enough strain amplitude. As such, the fatigue limit for each laminate is considered to be the lowest tested strain level at which a specimen survives 2$\times10^6$ cycles.

Table 8.3: Identified parameters of linearised strain-life relationship (8.3)

Laminate	n^a	Var^b	A_ϵ		CI$_{0.95}$^{c}	B_ϵ		CI$_{0.95}$^{c}
FE $[0]_{16}$	30	0.03218	7.472	±	0.226	-402.42	±	29.18
FE Quasi-iso^d	30	0.06826	7.480	±	0.329	-376.76	±	36.67
FE $[0/90]_{4S}$	32	0.05514	8.198	±	0.289	-433.55	±	31.71
FE $[\pm 45]_{4S}$	30	0.05505	9.822	±	0.572	-484.65	±	53.27
GE $[0/90]_{3S}$	18	0.04154	6.914	±	0.401	-369.35	±	59.63
GE $[\pm 45]_{3S}$	15	0.05620	12.632	±	1.294	-858.65	±	134.04

[a] total number of specimens tested to failure; not including run-outs
[b] variance s^2 of the normal distribution of $\log(N_\mathrm{f})$, where s is standard deviation
[c] 95% confidence interval
[d] quasi-isotropic laminate $[0/+45/90/-45]_{2S}$

The strain-life medians are all plotted collectively in Figure 8.8. It can be seen that the FE composites wherein response is fibre-dominant ([0], [0/90], and quasi-isotropic) produce plots that are closely placed and have similar slopes, suggesting their comparable fatigue endurance; while the FE [±45] plot is located further apart, demonstrating its considerably longer survival. From this study on fatigue lives, it can be inferred that:

1. on account of their longer strain-based fatigue lives, Flax-composites are comparable to, or exceed, Glass-composites of equivalent stacking sequence in longevity, and
2. on account of their linear $\epsilon_{\max}$-$\log(N)$ relationship, Flax-composites lend themselves to reliable fatigue failure prediction, and are therefore suitable for engineering components.

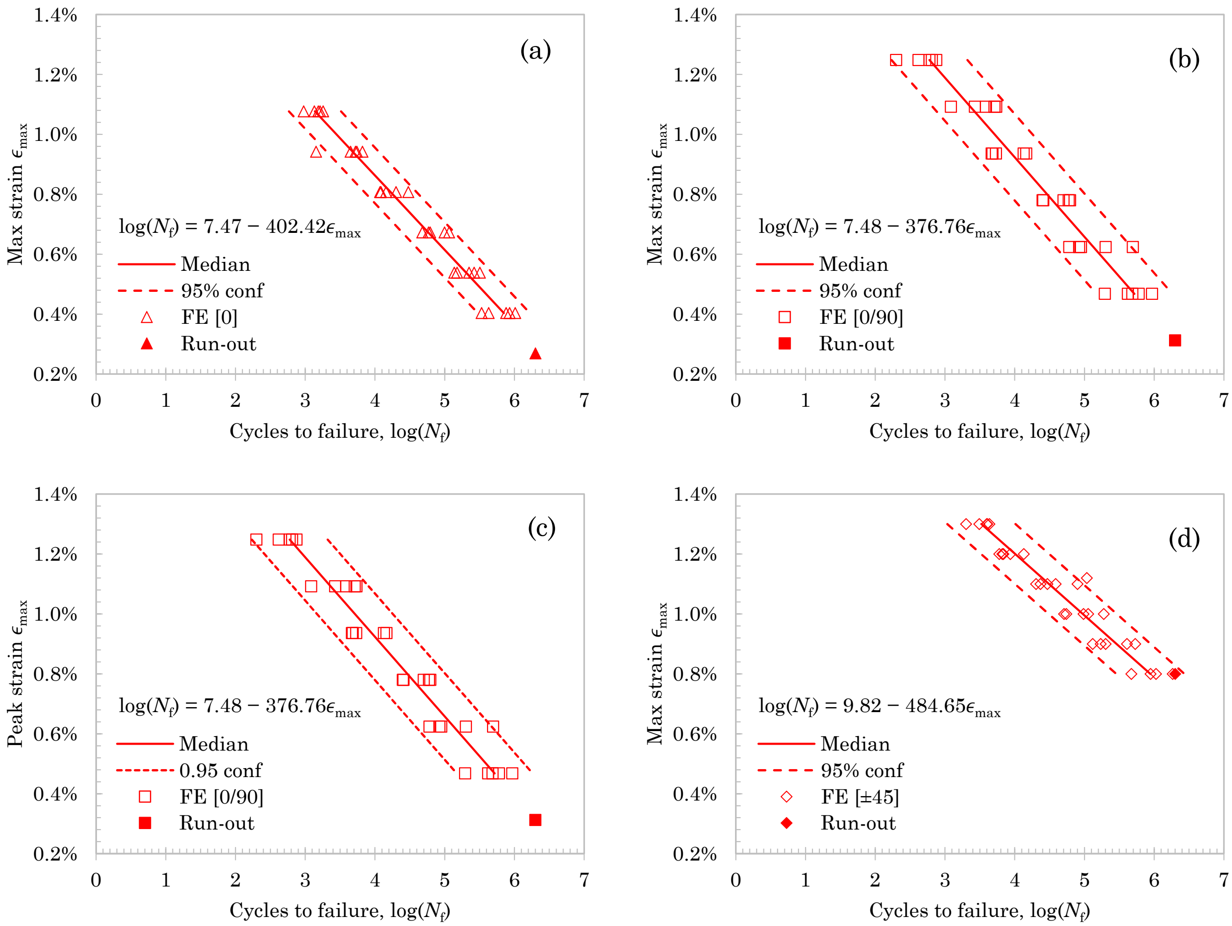

Figure 8.6: Strain-life (ϵ-N) curves for Flax-epoxy laminates (a) $[0]_{16}$, (b) $[0/90]_{4S}$, (c) Quasi-isotropic $[0/{+45}/90/{-45}]_{2S}$, and (d) $[\pm 45]_{4S}$, showing test data, median trend and 95% confidence bounds; *Run-out* = did not fail by $2{\times}10^6$ cycles.

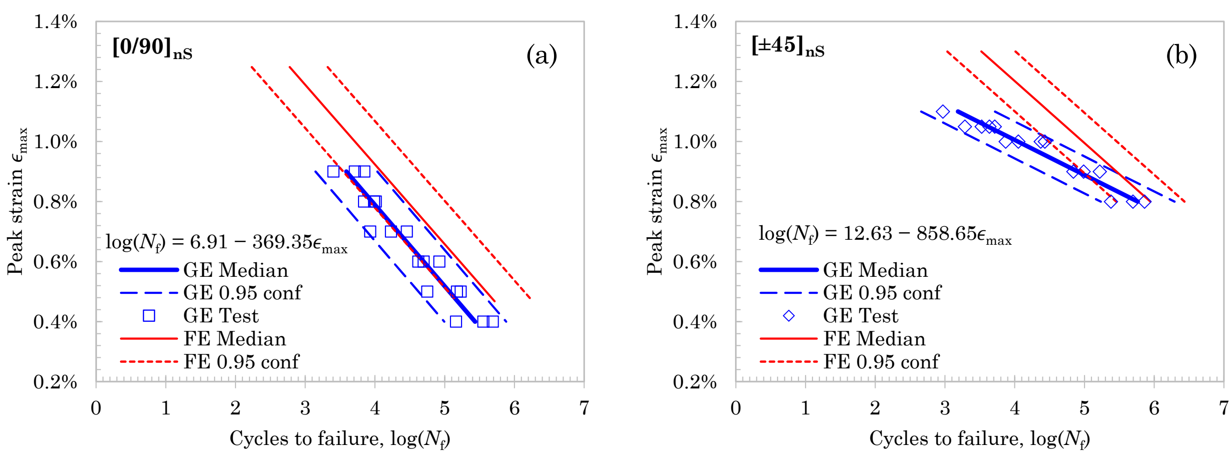

Figure 8.7: Strain-life (ϵ-N) curves for Glass-epoxy (GE) laminates (a) $[0/90]_{3S}$, and (b) $[\pm 45]_{3S}$, compared to equivalent Flax-epoxy (FE), showing GE test data, median trends and 95% confidence bounds.

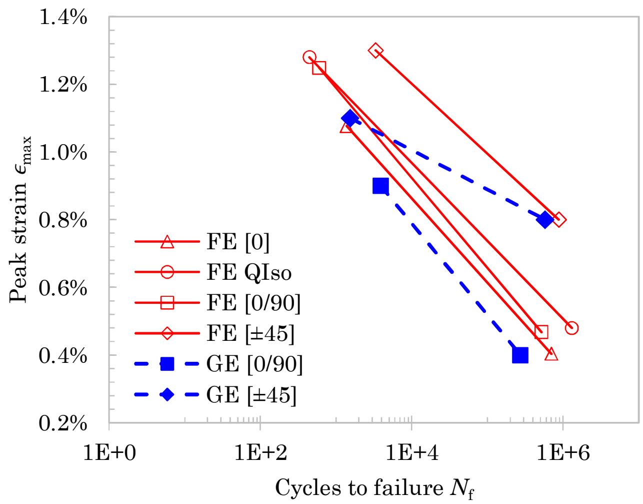

Figure 8.8: All Flax-epoxy (FE) and Glass-epoxy (GE) strain-life (ϵ-N) medians. Test data and confidence bounds not shown to preserve clarity.

8.4.3 Observed damage and failure mechanisms

8.4.3.1 Macrostructure failure and fracture

The failure mechanisms evident from an examination of fracture surfaces show much similarity with those well-known for quasi-static failure. Flax-epoxy (FE) [0] specimens (Figure 8.9) fail in sudden brittle fracture, with an uneven 'zig-zag' fracture surface with evidence of fibre pull-out (indicating debonding from surrounding matrix material) and fibre breakage.

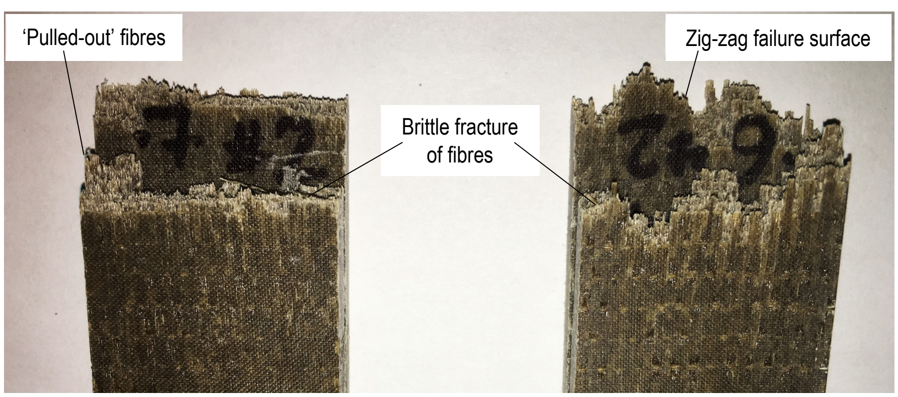

Figure 8.9: Fracture surface of and failure modes of Flax-epoxy [0] fatigue specimens.

The crossply [0/90] specimens (Figure 8.10) show the same evidence of brittle fibre breakage in 0° plies, and clean fibre-matrix separation along 90° plies. It is interesting to note that Glass-epoxy (GE) fracture is more violent compared to FE [0/90], evident from the fracture surfaces. At higher loading levels ($\epsilon_{max} > 0.6\%$), the GE specimens reveal a more severe fracture, where Glass fibres of outer 0° plies appear to debond along fibre length for considerable distances away from fracture site. This suggests that

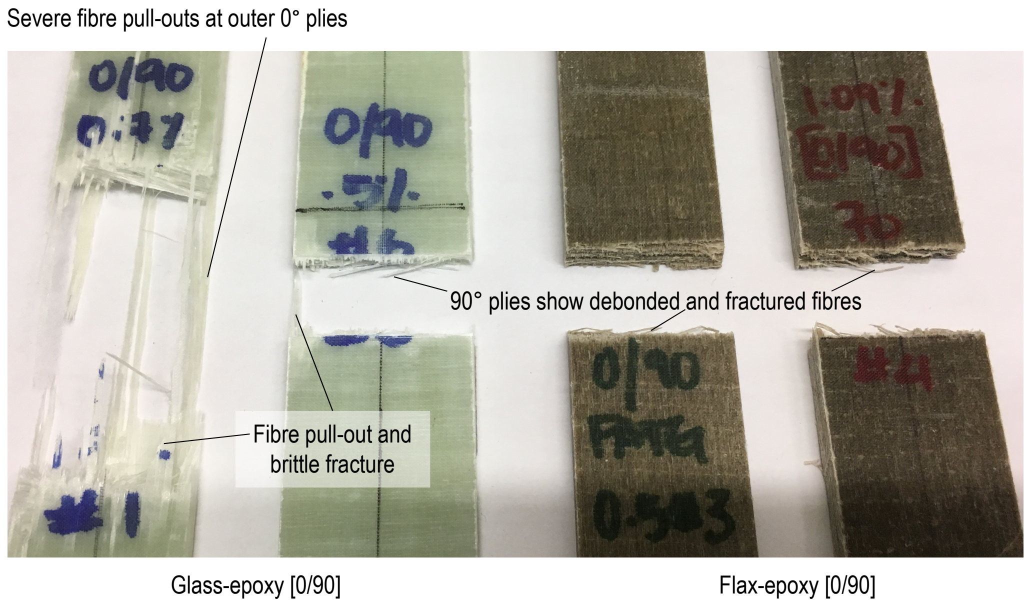

Figure 8.10: Fracture surface and failure modes of Glass-epoxy and Flax-epoxy [0/90] fatigue specimens. Glass-epoxy shows more violent fracture.

Glass fibres tend to debond from matrix first, before breakage, confirming that Glass fibre strength exceeds Glass-epoxy interfacial adhesion strength.

Angled-crossply [±45] specimens show similar behaviour as in monotonically tested specimens (Figure 8.11), with evidence of ply rotation towards loading axis that results in a ductile 'necking' at failure site, followed by delamination and fibre fracture. This is true for both FE and GE specimens. It is noted

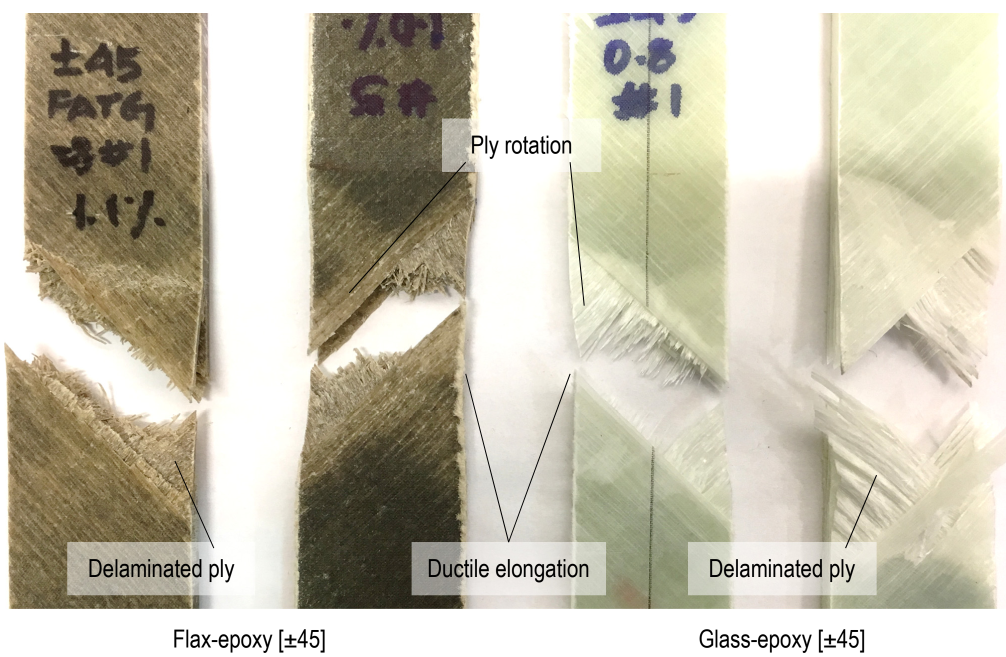

Figure 8.11: Fracture surface and failure modes of Flax-epoxy and Glass-epoxy [±45] fatigue specimens.

that at higher strain amplitude levels ($\epsilon_{\max} > 1.0\%$), FE [±45] specimens fracture before significant ply rotation and ductile elongation.

FE quasi-isotropic specimens show all above failure mechanisms, as can be seen in Figure 8.12.

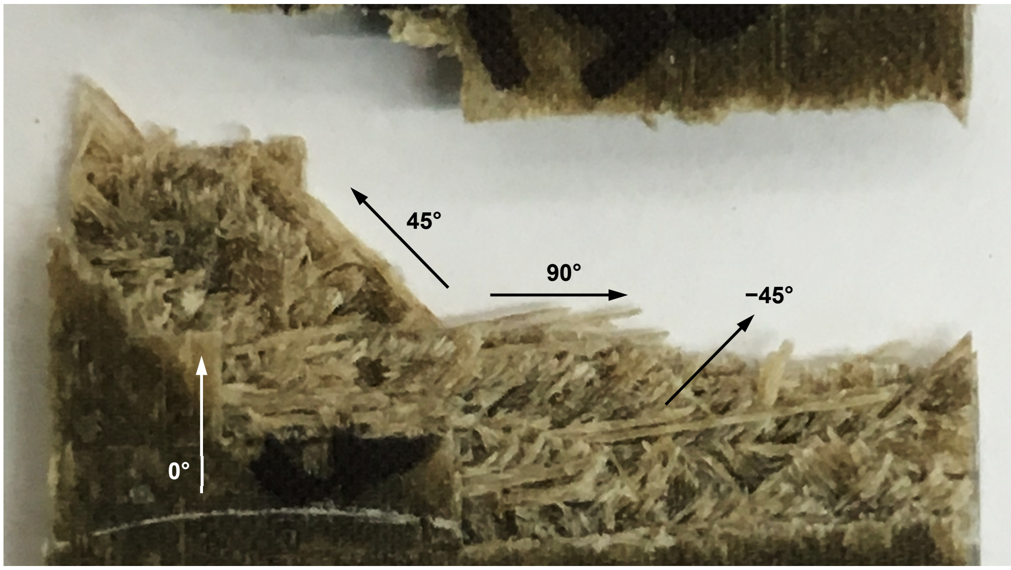

Figure 8.12: Fracture surface of Flax-epoxy quasi-isotropic $[0/45/90/-45]_{2S}$ specimens.

8.4.3.2 Microstructure damage

SEM micrography of specimen cross-sections at different stages of fatigue life reveal damage mechanisms and offer insight on developing failure conditions.

Flax-epoxy [0]. To examine physical damage characteristics under fibre-direction loading, FE [0] specimen cross-sections were imaged after they were fatigued up to 3,600 cycles ($0.2N_{\mathrm{f}}$) and 14,300 cycles ($0.8N_{\mathrm{f}}$) under a peak loading of $\epsilon_{\max}$=0.8%, shown in Figures 8.13(a) and (b), respectively. Damage during early life appears to be strictly cracks within fibre bundles (intra-bundle), indicating separation of elementary fibres due to a breakdown of pectic adhesion between them. The cracking is seen to be diffuse and evenly spread out amongst fibre bundles. At this stage, intra-bundle cracks do not seem to propagate beyond the fibre bundle (Figure 8.13(a)). After 80% of fatigue life, cracks are observed propagating around fibre bundles (circum-bundle), indicating degraded fibre-matrix bonding. Long and thick cracks are seen to result from the merging of both intra-bundle and circum-bundle cracks (Figure 8.13(b)).

It is noticed that, of all the compound-cracks, those weaving around fibre bundles, propagating along ply boundaries appear deeper and more severe. It is reasoned that the steady compounding of these interlaminar cracks over fatigue life eventually separates plies, compromising inter-ply load transfer. Saturation of interlaminar cracks cause fibres to carry a higher proportion of the tensile cyclic load, resulting in eventual brittle breakage of fibres and specimen fracture. This is in agreement with the 'zig-zag' fracture surface and fibre pull-outs evidenced in Figure 8.9. No cracks are observed to originate in the matrix-rich regions.

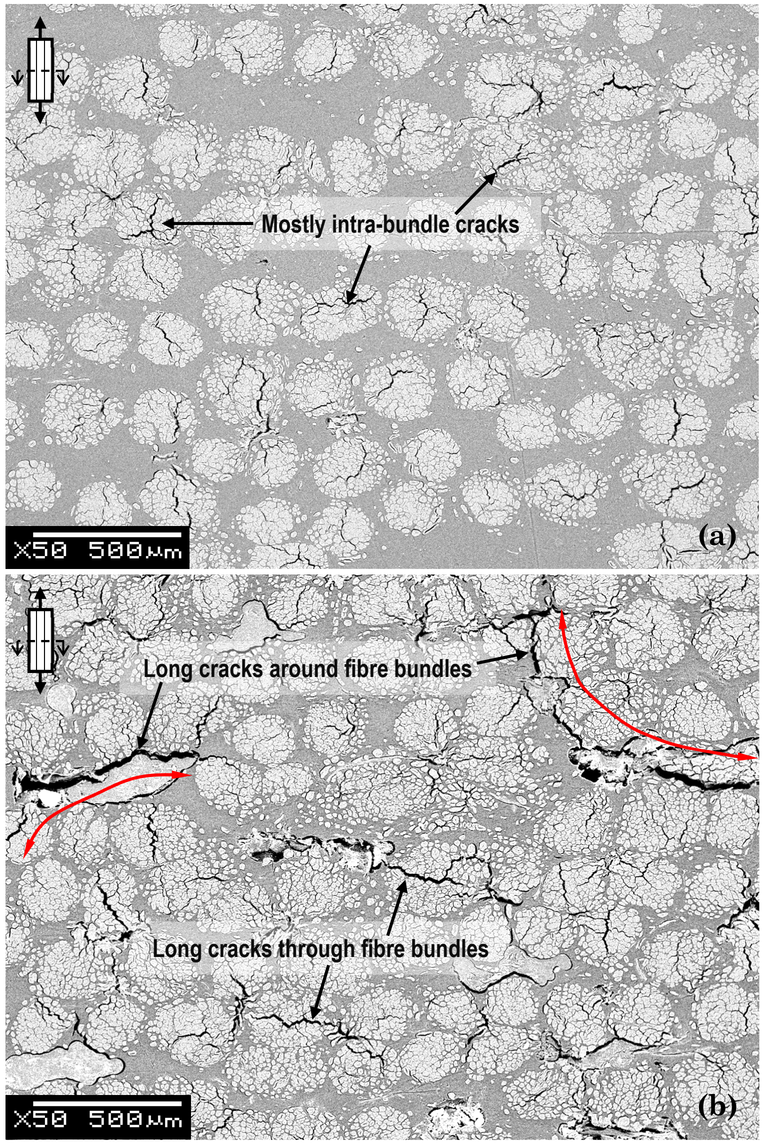

Figure 8.13: Flax-epoxy [0] cross-section at ×50 after (a) $0.2N_\mathrm{f}$, and (b) $0.8N_\mathrm{f}$, under ϵ_max=0.8% ($N_\mathrm{f} \simeq 17,891$ cycles).

Flax-epoxy and Glass-epoxy [0/90]. FE crossply specimens show diffuse intra-bundle cracking during early fatigue life in fibres of both orientations, similar to those found in FE [0]. After 80% of fatigue life under, in the 90° plies, intra-bundle cracks between adjacent fibre bundles are seen to merge, even across the matrix, and continue to propagate until interrupted by a laminar boundary, as seen in Figure 8.14(a). These cracks are perpendicular to the loading axis, as expected. Such 'through' cracks in 90° plies are only seen to originate from, and propagate through, fibre bundles – they are not typically seen around fibre bundles along fibre-matrix interface. This indicates that adhesion of elementary fibres is the weak link in these off-axis plies.

The 0° plies also show intra-bundle cracking that propagate toward laminar boundaries, and such cracks appear evenly distributed amongst fibre bundles. However, the major damage mode appears to be deep

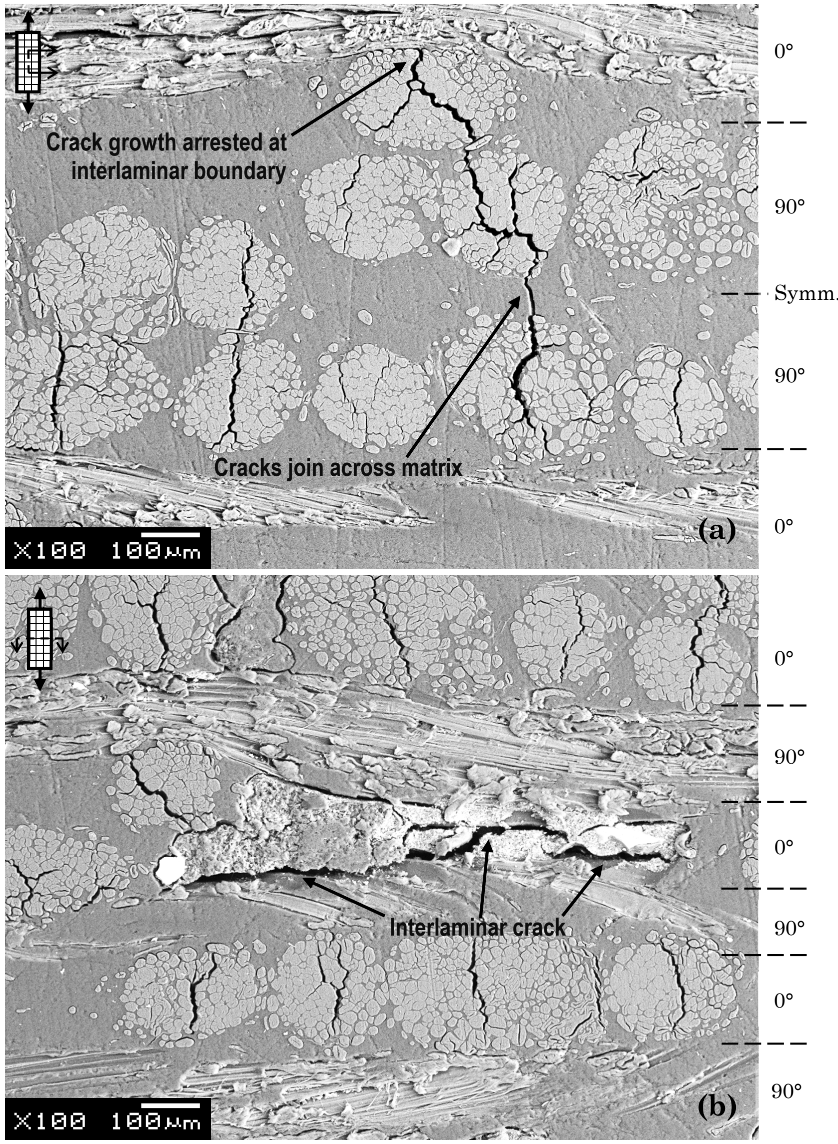

Figure 8.14: Flax-epoxy [0/90] imaged at ×100 across (a) longitudinal and (b) transverse cross-sections, after $0.8N_{\mathrm{f}}$ under $\epsilon_{\max}$=0.8% ($N_{\mathrm{f}} \simeq 53,654$ cycles).

fissures along the interface between between 0 and 90° plies (Figure 8.14(b)), indicating delamination. These interlaminar cracks propagate around fibre bundles, but also merge with through-cracks that originate from within bundles. It is reasoned that failure conditions develop when enough through-cracks in 90° plies and interlaminar separations accumulate, thereby forcing 0° plies to resist a higher fraction of cyclic tensile stress.

In contrast to the diffuse, nearly-even distribution of intra-fibre microcracks in Flax-epoxy [0/90], the equivalent layup Glass-epoxy specimens tend to favour the propagation of isolated major cracks that typically weave their way around Glass fibres until interrupted by ply boundaries, as shown in Figure 8.15. This may explain why GE [0/90] specimens failed more violently than FE under similar cyclic loading, as noted earlier (and shown in Figure 8.10): As the isolated, less-numerous through-cracks in GE 90° plies progress to ply boundaries and merge with interlaminar cracks, the outcome is a sudden failure of the off-axis plies, instead of a steady degradation of load-carrying capacity. As a result, the 0° plies are suddenly exposed to higher cyclic stresses, fracturing shortly after. The above observations suggest that

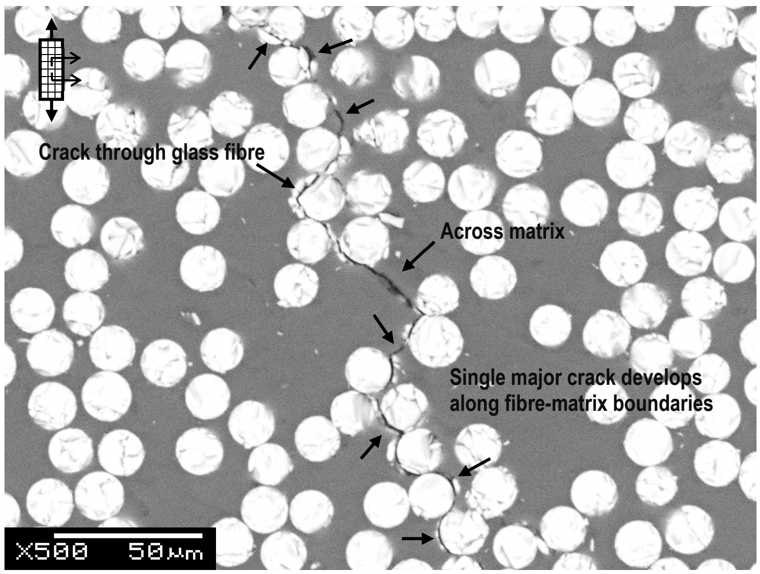

Figure 8.15: Glass-epoxy [0/90] imaged at $\times 500$ across longitudinal section, after $0.8N_\mathrm{f}$ under ϵ_max=0.8% ($N_\mathrm{f} \simeq 9,103$ cycles).

natural-fibre reinforcement is preferable for a less energetic failure of the composite.

Flax-epoxy and Glass-epoxy [±45]. Like in the UD laminates, FE [±45] also demonstrate intra-bundle cracks early during fatigue life. Interestingly, the transverse cross-sections of examined fatigue specimens did not indicate cracks along ply boundaries as was observed for monotonic and quasi-static tests (Figure 5.15, Chapter 5), even by 80% of fatigue life. Instead, the longer cracks appear to be a result of merging between adjacent intra-bundle cracks, which seem to split a ply in half through the fibre bundles – as shown in Figure 8.16(a). In general, intra-bundle cracks are observed to remain confined within fibre bundles unless they are in close proximity to another fibre bundle crack, in which case they merge into a longer crack along ply width.

The longitudinal section, however, showed both intra-bundle and circum-bundle cracks, as shown in Figure 8.16(b). Furthermore, long cracks are seen perpendicular to the loading axis, propagating along fibre-matrix interface around Flax fibre bundles. As can be seen, these perpendicular-to-loading interfacial cracks propagate into matrix-rich regions, and are expected to progress under cyclic tensile loading until they merge with other cracks. These mechanisms support the observation of separated fibres and delamination on the fracture surfaces of FE [±45] specimens (Figure 8.11).

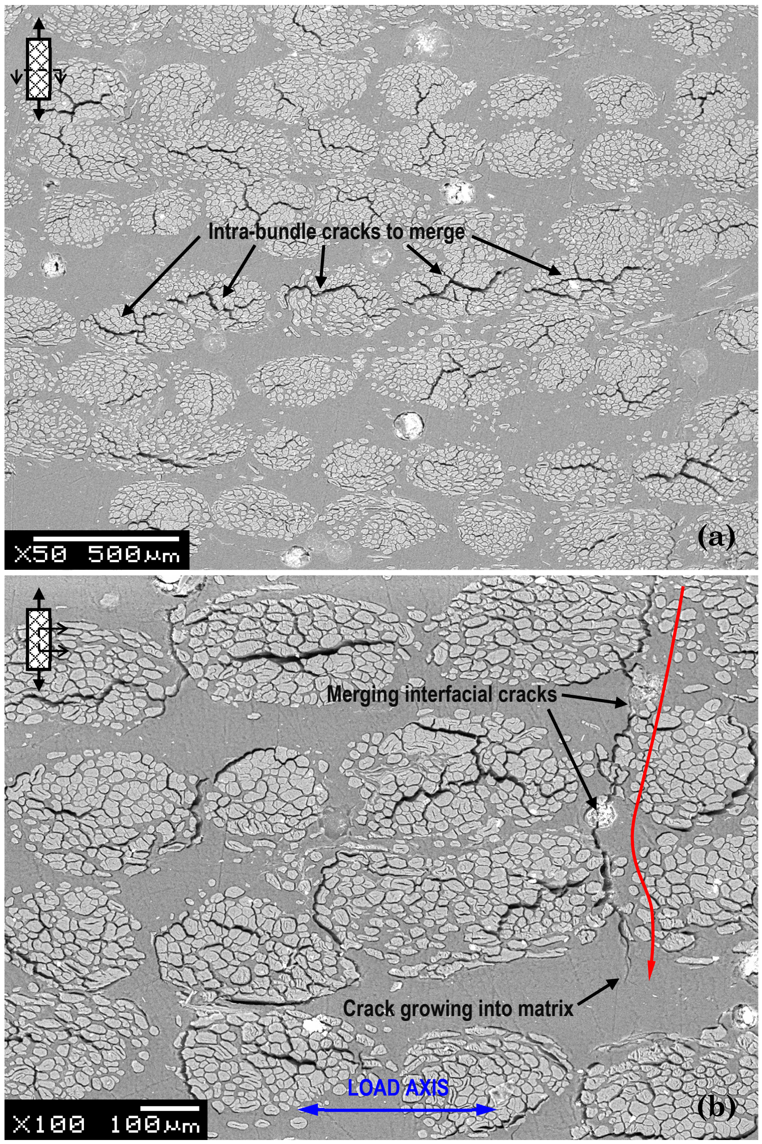

Figure 8.16: Flax-epoxy [±45] imaged across (a) transverse section at ×50 and (b) longitudinal section at ×100, after $0.8N_\mathrm{f}$ under $\epsilon_{\max}$=1.0% ($N_\mathrm{f} \simeq 94,515$ cycles).

Examination of the GE [±45] transverse sections after $0.8N_\mathrm{f}$ show only localised crescent-shaped interfacial cracks around one side of Glass fibres, typically on the side opposite to direction of ply rotation, as seen in Figure Similar to the GE [0/90] case, isolated major cracks propagate around fibres, unlike the diffuse cracking seen in Flax-specimens. In both GE or FE specimens, no crack appears to initiate in the matrix-rich regions. 8.17.

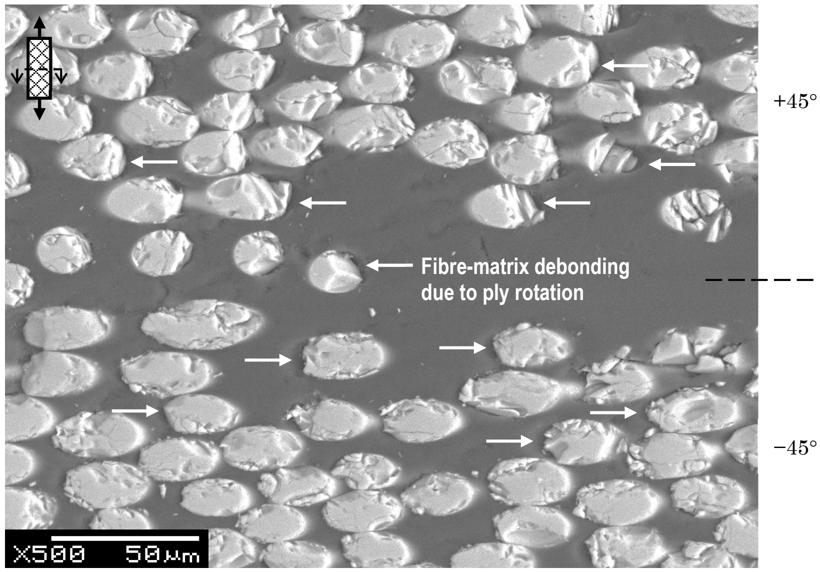

Figure 8.17: Glass-epoxy [±45] imaged across transverse cross-section at ×500, after $0.8N_\mathrm{f}$ under ϵ_max=1.0% ($N_\mathrm{f} \simeq 11,105$ cycles).

8.4.4 Fatigue response and hysteresis energy

As described earlier through Figures 8.2-8.4, the fatigue test regime begins with a quasi-static loading run (from which the initial undamaged moduli are computed), followed by fatigue cycling at constant strain amplitude. As examples of evolving fatigue response, typical stress-strain plots for all tested laminates are shown at the same loading amplitude (from ϵ_min ∼0.08% to peak ϵ_max ∼0.8%) in Figures 8.18(a)-(f). Note the clear relaxation of stress, and decrease of secant modulus, over fatigue life.

Recall that *hysteresis energy* is the energy dissipated during a fatigue cycle, and this energy per unit volume (energy density) is quantified by the area enclosed within a hysteresis loop, representing dissipative processes in the composite related to viscoelasticity and/or internal damage. Upon examining the hysteretic response of all tested laminates at different stages of fatigue life under the same strain-amplitude, shown in Figure 8.18, it is found that FE [0], [0/90], and quasi-isotropic specimens exhibit only a marginal decrease in loop area, while that of FE [±45] is nearly constant. GE [0/90] specimens clearly show increasing loop area, indicating increased energy dissipation (i.e. increased damage); while GE [±45] specimens show a reducing loop area, indicating that the most intensive damage events occur during early fatigue life. To aid comparison between the tested laminates, the typical cyclic response of all laminates are plotted in the same chart in Figures 8.19(a)-(b). It is evident that, while there is certainly a degradation of secant

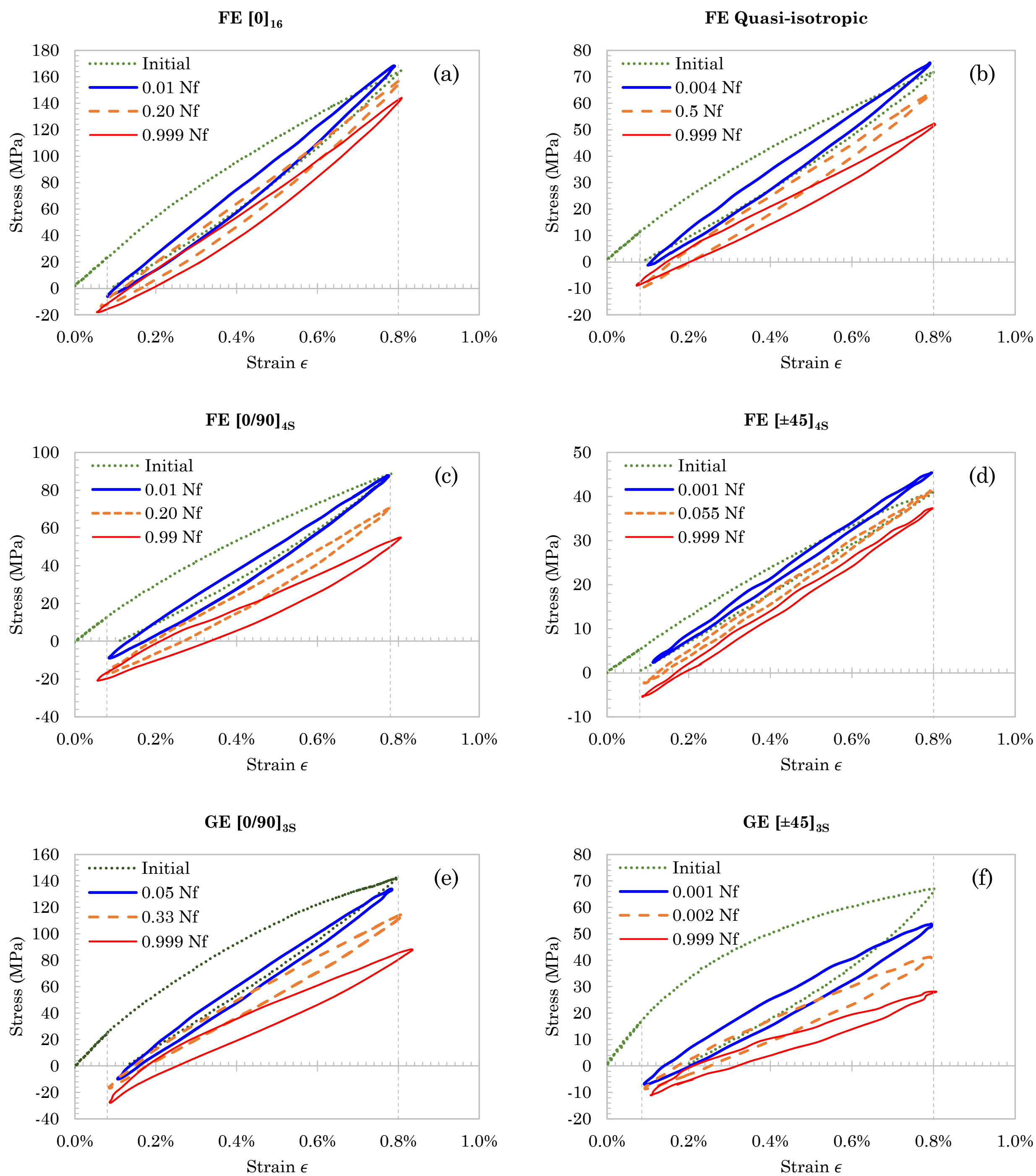

Figure 8.18: Typical example response plots of Flax-epoxy (FE) and Glass-epoxy (GE) laminates cycled at $\epsilon_{\max}$ ~0.8%, showing initial quasi-static response (dotted line), and progression of fatigue cycle moduli and hysteresis loops over fatigue life.

modulus for all specimens over their fatigue life, the change in hysteresis loop area is significantly more pronounced in Glass-epoxy specimens than in Flax-epoxy.

The above hysteretic behaviour at all strain-loading levels, can be followed from evolution plots of

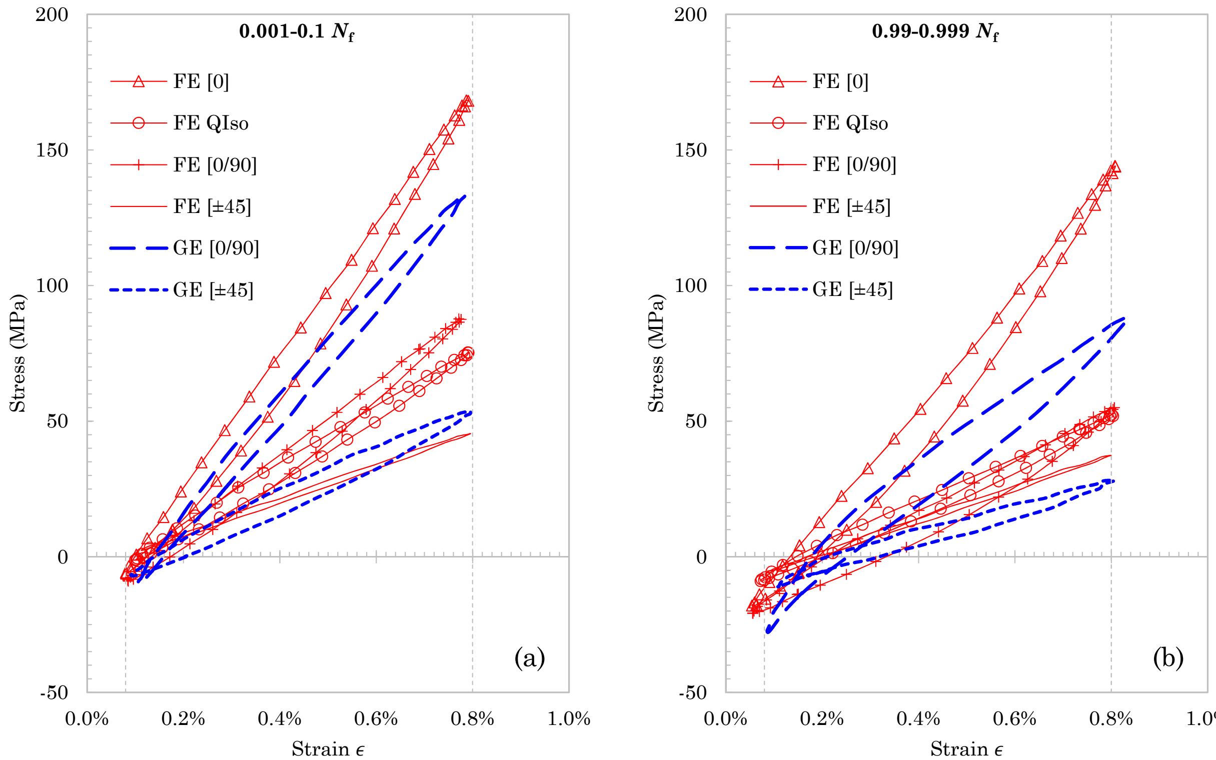

Figure 8.19: Comparison of typical response under constant strain amplitude ($\epsilon_{\min}$ ~0.08% to $\epsilon_{\max}$ ~0.8%) at the (a) beginning, and (b) end, of fatigue life.

hysteresis energy density, shown in Figure 8.20. As noted earlier, hysteresis energy is an indication of internal dissipative processes related to viscoelasticity or damage, or both. For all FE specimens, dissipated energy tends to generally decrease over strain-controlled fatigue life after an initial peak during early fatigue life (this peak dissipation may be barely discernible at low load levels, but is more prominent at higher load levels). In fact, at low peak strain levels, the energy density appears nearly constant for most of fatigue life (Figure 8.20). This suggests that damage events are more energetic at the very beginning of fatigue cycling, but progressively decreases in intensity until end-of-life. For all FE specimens, it is observed that the period 0.2–0.8N_f is of a 'plateaued' trend, suggesting hysteresis size in this period is more influenced by constant reversible viscous processes within the composite than accumulating irreversible damage. The relationship between loading level and dissipation energy is somewhat directly proportional for all tested composites, as can be seen in Figures A.9 and 8.21.

GE specimens, in contrast to FE, demonstrate a continuously evolving energy dissipation (Figure 8.20). GE [0/90] specimens show an increasing trend, with the bulk of increase occurring during early fatigue life, while GE [±45] show a decreasing trend at all tested load levels. This suggests that damage activity becomes increasingly intensive in GE [0/90], but less energetic in GE [±45], as fatigue cycling progresses. Since FE specimens tend to show an almost constant level of dissipation at many load levels, even until just before failure, hysteresis energy may not prove a useful indicator of progressive damage, or failure criterion, for Flax-composites, as it might for Glass-composites.

Figure A.9 shows that higher load amplitudes result in higher magnitudes of energy, at any stage of

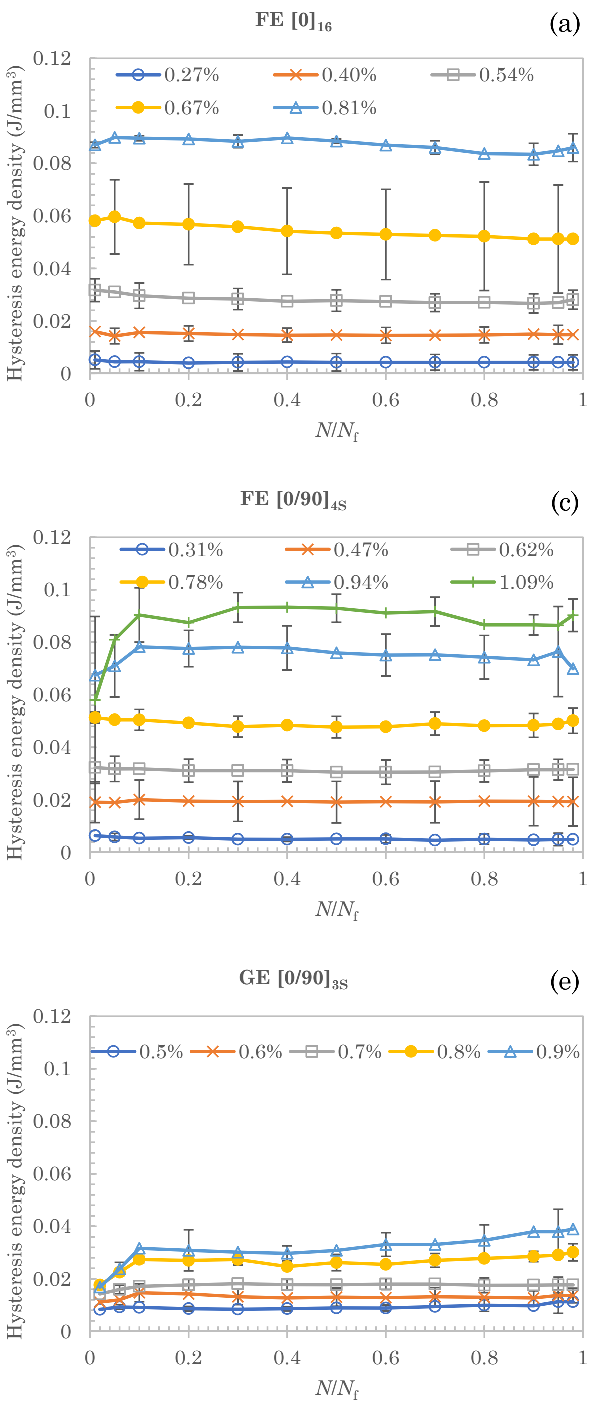

Figure 8.20: Hysteresis energy per unit volume U^h dissipated over fatigue life for tested $\epsilon_{\max}$ levels. The mean trendlines until just before failure ($\sim$0.98 N_f) are shown with standard deviation bars.

fatigue life. From the same figure, it is also noted that the change in hysteresis energy density (ΔU^h) between $0.1N_\mathrm{f}$ and $0.9N_\mathrm{f}$ is negligible at low loading levels, and marginal at higher loading levels, for all tested laminates *except* GE [±45]. To fairly compare energy densities dissipated under *any* given load amplitude for all tested specimens, the trends at early and late fatigue life are shown superimposed in Figure 8.21. Amongst the FE specimens, the highest energy densities at most strain amplitudes appear

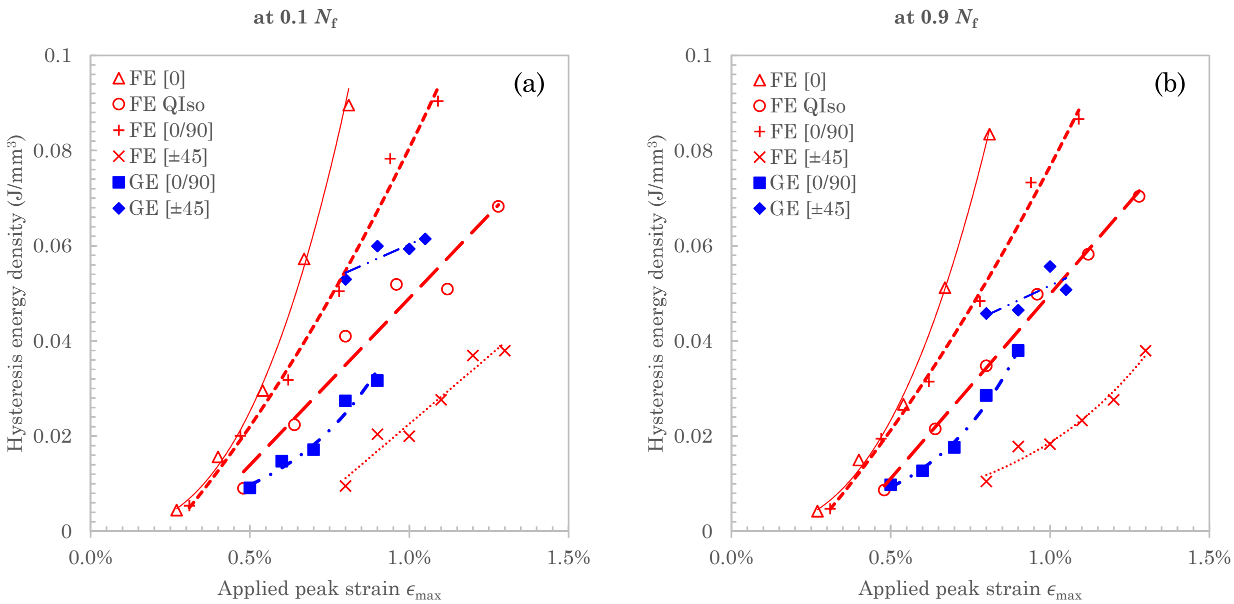

Figure 8.21: Comparison of hysteresis energy U^h trends across all tested laminates (a) at the beginning of fatigue life (0.1 N_f), and (b) towards the end (0.9 N_f).

to be for FE [0], followed by [0/90], quasi-isotropic, and [±45], in order of reducing magnitude. This indicates that hysteresis energy (and consequently composite internal damage intensity) under strain-controlled conditions is proportionally related the amount of fibrous reinforcement along loading direction (i.e. number of 0° plies in the laminate). It follows that fibre-related mechanisms, such as microfibril reorientation, movement of amorphous cellulose, and fibre wall cracking, may contribute more to the observed dissipation than matrix-related, interface-related, or delamination mechanisms.

To compare with Glass-composites, FE [0/90] specimens clearly exhibit higher energy magnitudes than GE specimens of the same layup (Figure 8.21). Since the response in [0/90] specimens is governed by fibre-properties (i.e. fibre-dominant), the higher energy dissipation in FE indicates that fibre damage is more energetic in the NFC, than in the synthetic Glass-composite. In contrast, for the matrix-dominant [±45] layup, GE hysteresis energy is found to be significantly higher than that in FE specimens, and the difference exists throughout the fatigue life. This may be an indication of more severe interfacial debonding or delamination in GE composites, and of better fibre-matrix adhesion in FE.

The hysteresis energy evolution trends reported for specimens under *stress*-amplitude controlled fatigue, shown in Figure 8.22, are markedly different from those of strain-amplitude controlled fatigue observed in this study. It is noted that the stress-controlled hysteresis energy data in Figure 8.22 has considerable fluctuations and large standard deviations bars, compared to the data reported in this study. The 'noisy' data may have resulted from the strain estimation method adopted in the source study [50]. Strain was not measured by a dedicated transducer, but estimated from actuator crosshead displacement – which is a less-precise method of recording specimen deformation.

Fibre-dominant specimens FE [0] and [0/90] shows *continuously decreasing* energy density under stress-

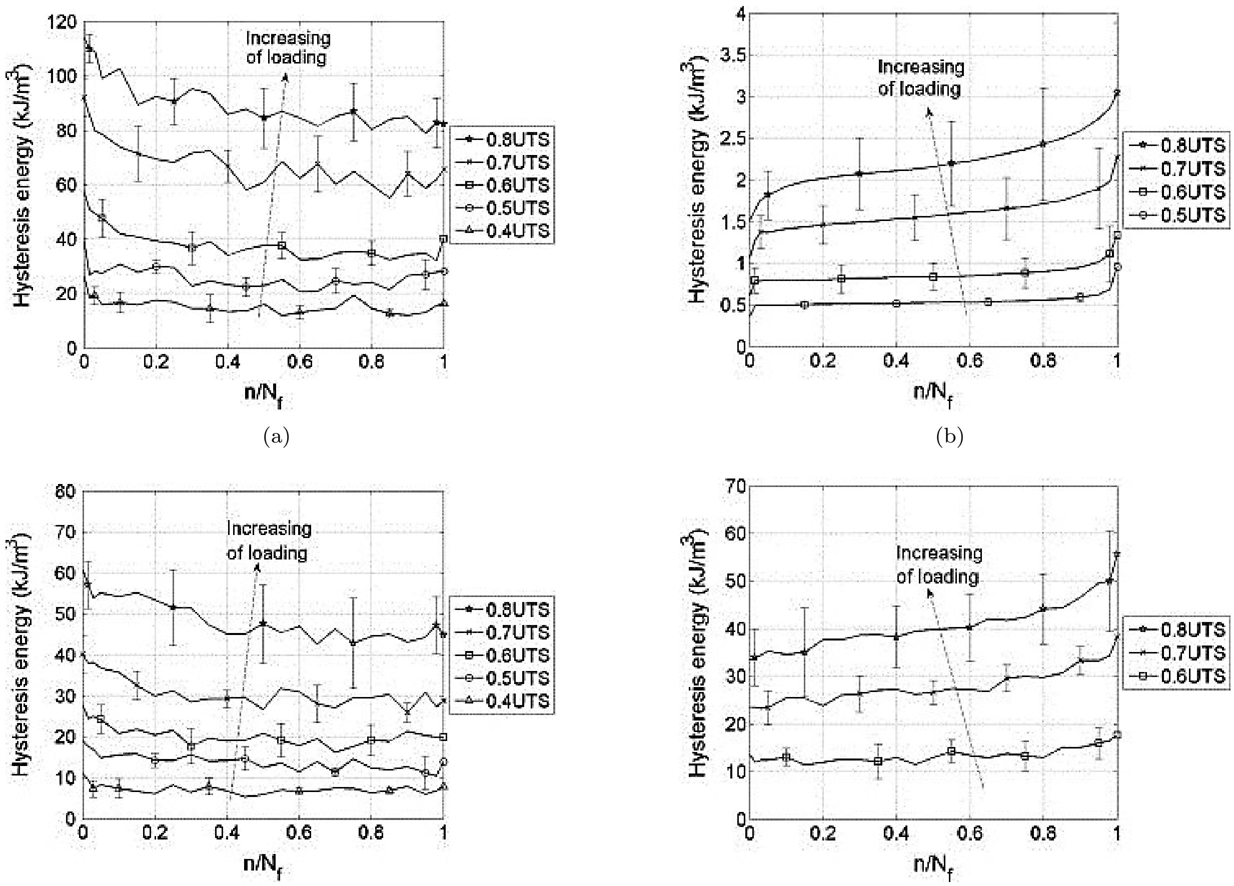

(a) (b) (c) (d)

Figure 8.22: Hysteresis energy density evolution under stress-amplitude controlled fatigue of Flax-epoxy laminates: (a) $[0]_{12}$, (b) $[90]_{12}$, (c) $[0/90]_{3S}$, and (d) $[\pm 45]_{3S}$. Reproduced with permission from [50].

controlled tests (Figures 8.22(a) and 8.22(c)) – this behaviour is somewhat different from the strain-controlled trends found by the present study (Figures 8.20(a) and (c)). Matrix-dominant specimens FE [90] and [±45] show a *continuously increasing* trend (Figures 8.22(b) and 8.22(d)) under stress-controlled fatigue. This is also unlike the trend seen for strain-controlled specimens (Figure 8.20(d)), where the hysteresis energy is initially increasing during early fatigue life (up to 0.05–$0.1N_\mathrm{f}$), nearly constant for the majority of fatigue life between 0.2–$0.8N_\mathrm{f}$, and decreasing thereafter. Considering that the reported stress-controlled specimens were of the same Flax-reinforced epoxy composite, the trends of hysteresis energy progression should not be dissimilar, since the internal viscous or damaging mechanisms are the same. The different observations, therefore, are attributed to the difference in applied fatigue control mode. It is reasoned that, as specimen strain rate is continually increasing in a stress-controlled test (unlike in a strain-controlled test), the changing strain rate proves an additional variable influencing the time-dependent visco-elastoplastic mechanisms within Flax microstructure. Therefore, hysteresis energy evolution measured from a stress-controlled test may not be a reliable indicator of internal damage, but instead is a consequence of rate-dependent viscous mechanisms.

8.4.5 Inelasticity

Permanent deformation in NFCs are a result of several mechanisms discussed earlier in the introductory Chapter 2: irreversible damage like transverse cracking in fibre walls and fibre-matrix interfacial debonding, reorganisation of Flax fibre microconstituents such as separation of elementary fibres and irreversible extension of hellically-would microfibrils due to 'stick-slip' mechanisms, and inherent material inelastic phenomena like matrix polymer plasticity. Permanent deformation, as quantified by the inelastic component of strain response, is found to progressively accumulate over fatigue life for all tested specimens, as shown in Figure 8.23. Recall that, before fatigue cycling, the specimens were subjected to an initial quasi-static tensile ramp-up to the peak strain level, followed by complete unloading, as shown earlier in Figure 8.2 (this was done to measure initial static-condition properties). So, fatigue testing began with pre-existing permanent deformation in the specimen, which is reflected in the non-zero inelastic strain at N=0 in the evolution trends.

For all laminate configurations, under all tested load levels, it appears that the bulk of permanent deformation occurs within the first 10% of fatigue life (before $0.1N_\mathrm{f}$). Inelastic strains are higher at higher load amplitudes, as expected. This is similar to that in the case of stress-controlled fatigue, shown earlier in Figure 2.26. An interesting observations is that, for fibre-dominant FE laminates ([0], [0/90], and quasi-isotropic), there appears to be exist a threshold loading level below which the inelastic strain response does not vary significantly. For instance, for FE [0], the trends for loading below ϵ_max=0.54% appear to overlap (Figure 8.23(a)). Likewise for FE quasi-isotropic at ϵ_max ≤0.64% (Figure 8.23(b)), and for FE [0/90] at ϵ_max ≤0.47% (Figure 8.23(c)). This suggests that inelasticity-causing mechanisms, perhaps fibre-related, are less active during cycling at these lower amplitudes. This reasoning is supported by the observation that these 'threshold' strain levels happen to be located at the transition region of the laminate's monotonic response curve (see Figure A.8), indicating a period before significant developments of internal damaging mechanisms. Furthermore, investigation of inelasticity evolution during quasi-static loading (Chapter 5) of FE [0], [90], and [±45] show that inelastic mechanisms are minimal below these threshold levels (static inelasticity charts reproduced here in Figure 8.24).

The relationship between increase in applied strain amplitude and change in inelastic strain is concisely demonstrated by Figure 8.25 for each tested laminate. 2.26. The FE specimens generally show a nonlinear increasing relationship at higher loading levels, whereas GE show a linear relationship, between applied strain level and resulting inelasticity. From the chart, it becomes evident that the ductile [±45] layups of both GE and FE are prone to the most severe permanent deformation over fatigue life, followed by FE quasi-isotropic, FE [0/90], and GE [0/90], in decreasing order of inelasticity. The angled-crossply [±45] specimens of both FE and GE show considerable ply rotation as they fatigue, and delamination is a prominent failure mode in such specimens – so both characteristics contribute towards the high inelastic accumulation. Still, it is interesting to observe that GE [±45] are more susceptible to inelastic deformation than FE laminates of the same architecture, suggesting that interlaminar strength is higher in FE under fatigue conditions.

The trends for FE [0/90] and FE quasi-isotropic overlap in Figure 8.25, so either one can be more susceptible to inelasticity than the other, depending on the applied strain level. Of all the FE specimens, FE [0] accumulates the least permanent strain, suggesting that fibre-direction damage mechanisms (microfibril reorientation, fibre cracking, fibre-matrix debonding) do not contribute as much to permanent deformation

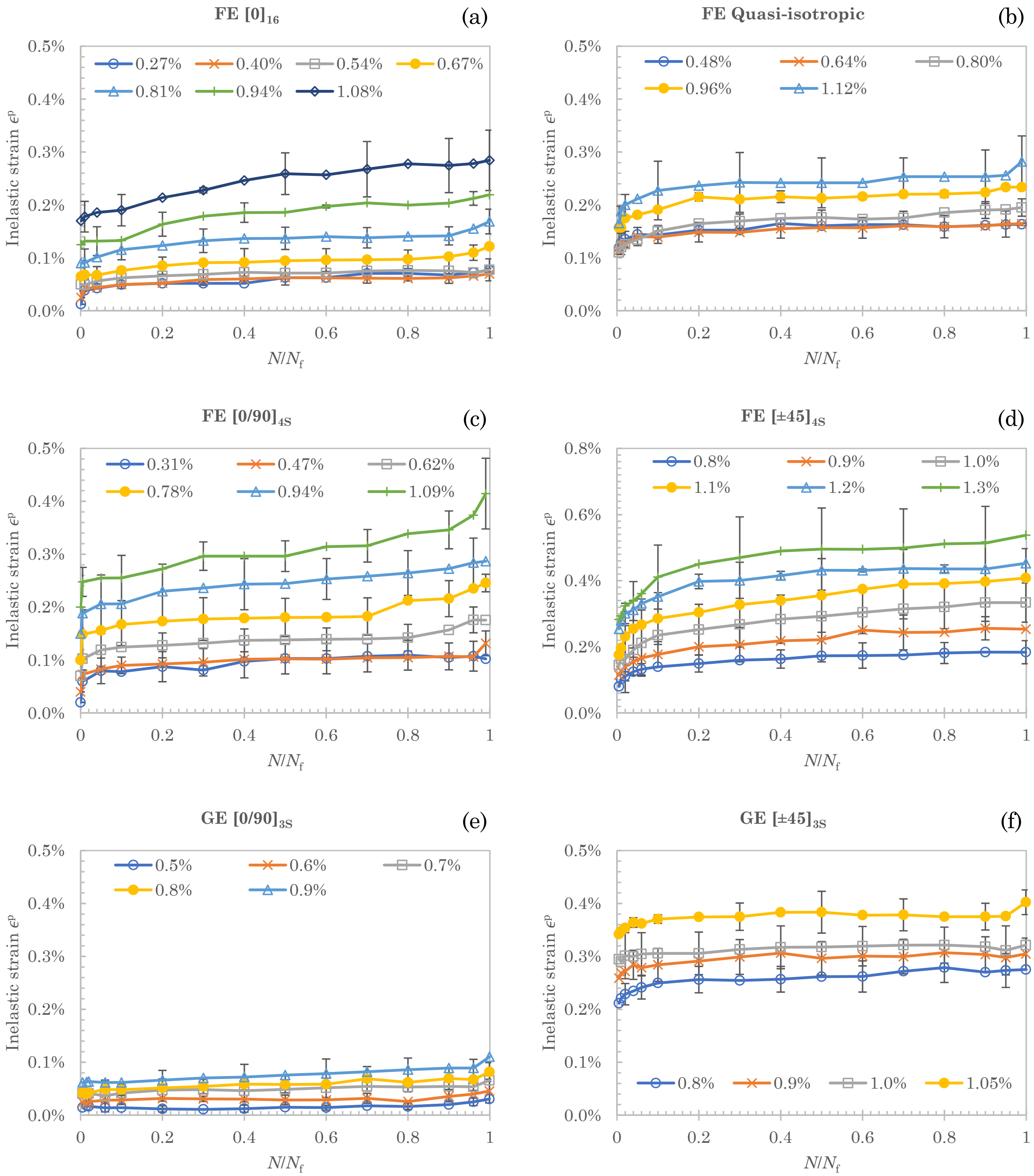

Figure 8.23: Accumulated permanent strain ϵ^p over fatigue life for tested $\epsilon_{\max}$ levels. The mean trendlines are shown with standard deviation bars.

as delamination-related mechanisms in crossply and quasi-isotropic layups. GE [0/90] accumulates the least amount of inelastic accumulation over strain-controlled fatigue life, at any applied strain amplitude. This is consistent with its monotonic linear-brittle response (Figure 8.5). As such, GE [0/90] is more resistant to inelasticity than all FE fibre-dominant layups.

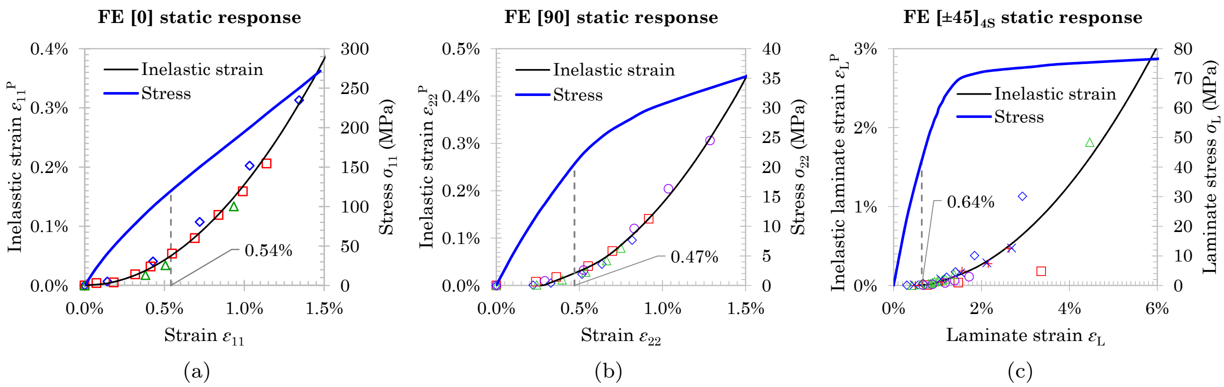

Figure 8.24: Inelastic strain evolution during quasi-static tensile loading for Flax-epoxy (FE) laminates (a) [0], (b) [90], and (c) [±45], from Chapter 5.

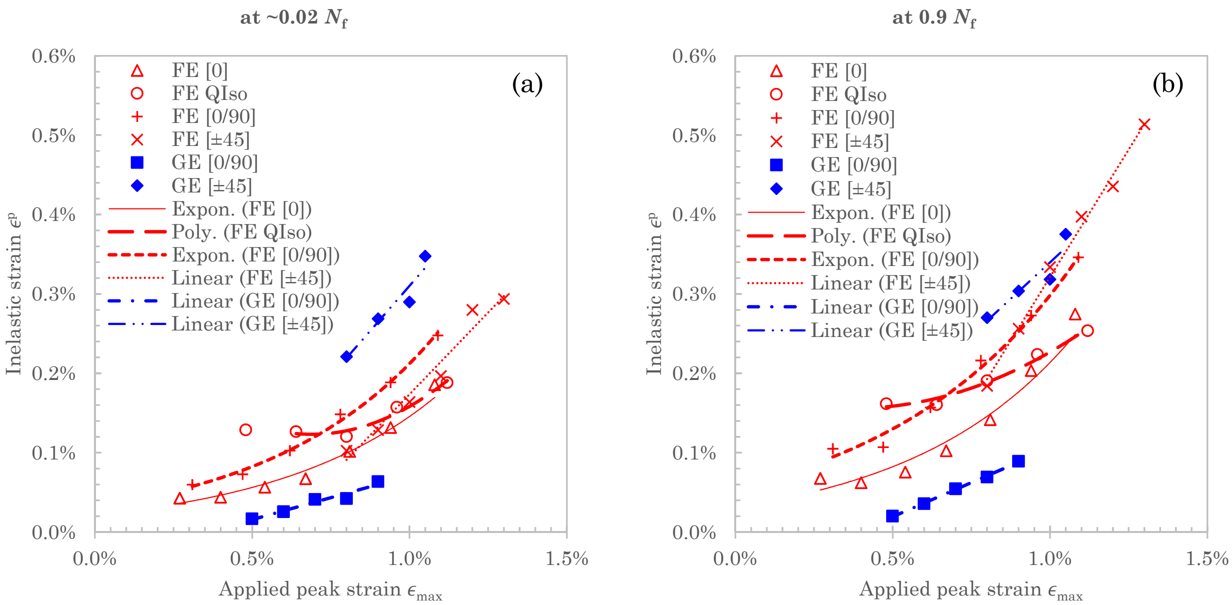

Figure 8.25: Observed trend of permanent strain ϵ^{p} over applied ϵ_{max} levels (a) at the beginning of fatigue life ($\sim$0.02 N_f), and (b) towards the end (0.9 N_f)

8.4.6 Peak stress

Under strain-amplitude controlled fatigue, the stress-amplitude tends to 'relax' both in magnitude and mean value. The evolution of peak stress σ_{max} is a measure of this stress-relaxation, shown for all tested laminate configurations in Figure 8.26. The peak stress shows a net reduction from beginning to end of fatigue life, and in nearly all tested cases the majority of reduction occurs early, before $0.1N_f$. Cyclic stabilisation of stress is observed in fibre-dominant FE laminates (those with 0° ply along loading direction), in the period 0.2-0.8 N_f. So, it is useful to note that, for future tests, control can be switched from strain to load mode (pseudo-strain control) as long as strain response is monitored periodically, and the load command is adjusted to ensure strain limits are within desired tolerance. For the results reported here, however, the tests were always conducted purely under strain-amplitude control. Similar stabilisation does

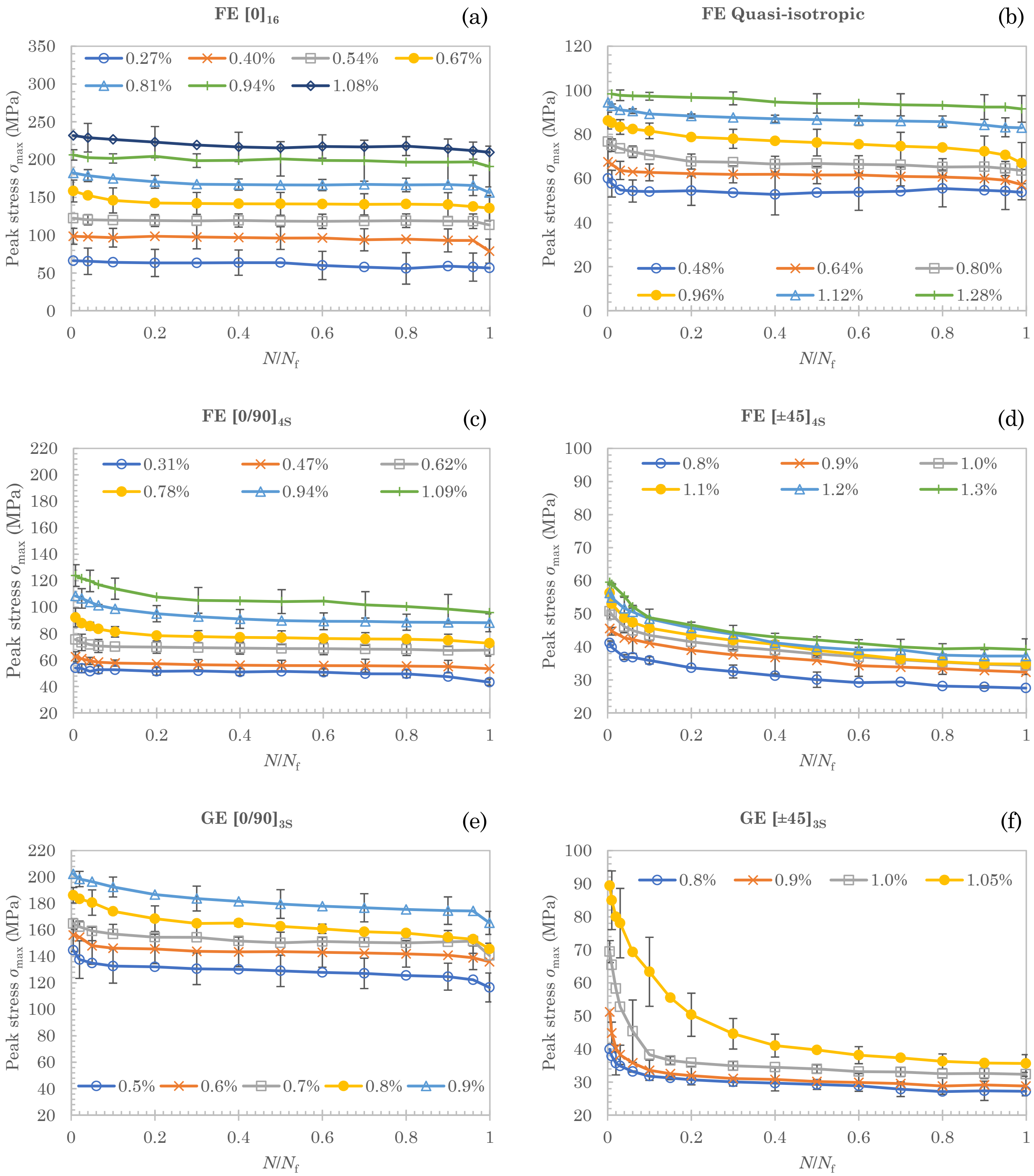

Figure 8.26: Peak stress $\sigma_{\max}$ evolution over fatigue life for tested $\epsilon_{\max}$ levels. The mean trendlines are shown with standard deviation bars.

not seem to occur for the [±45] layup of both FE and GE, where the peak stress is continuously decreasing.

The correlation between applied strain level and peak stress response can be examined from Figure 8.27. During early fatigue life (Figure 8.27(a)), GE [0/90] consistently carries the highest tensile stress

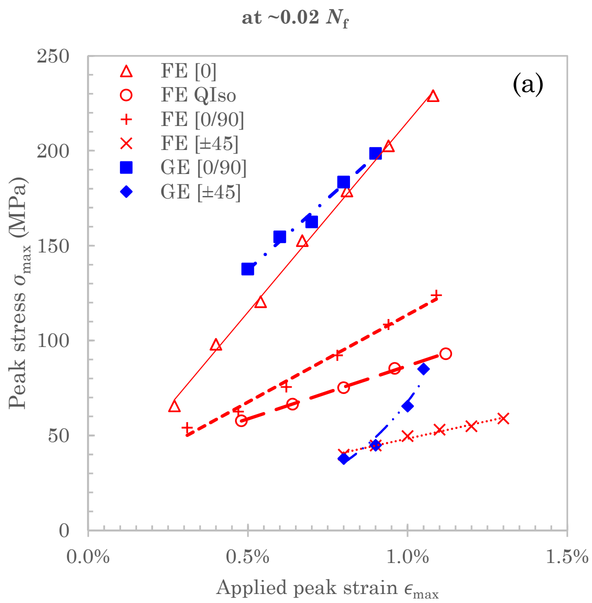

Figure 8.27: Observed trend of peak stress $\sigma_{\max}$ over applied $\epsilon_{\max}$ levels (a) at the beginning of fatigue life ($\sim$0.02 $N_{\rm f}$), and (b) towards the end (0.9 $N_{\rm f}$).

for the same strain amplitude deformation as other tested specimens (though FE [0] is a close second). This is expected, since GE [0/90] has the highest static tensile strength. For similar reasons, GE [±45] also withstands higher stressing than the FE specimens of same architecture, during early fatigue life. However, it is interesting to note that towards the end of fatigue life (Figure 8.27(b)), GE [0/90] peak stresses appear to match those of FE [0], and the same similarity is also found between GE and FE [±45] specimens.

It must be noted that the GE specimens have a different fibre volume fraction than FE (see Table 4.1), so a more insightful comparison may be derived by converting peak stress values to *specific* peak stress – i.e. dividing by composite density. Figure 8.28 revises and re-presents the data from Figure 8.27 to demonstrate correlation between specific peak stress and applied strain levels. It can now be seen that FE [0] withstands higher peak stresses *per unit density*, than GE [0/90], throughout constant strain-amplitude fatigue life. Similarly, the density-normalised peak stress carried by FE [±45] is also comparable to that of GE [±45], for all tested strain-amplitudes.

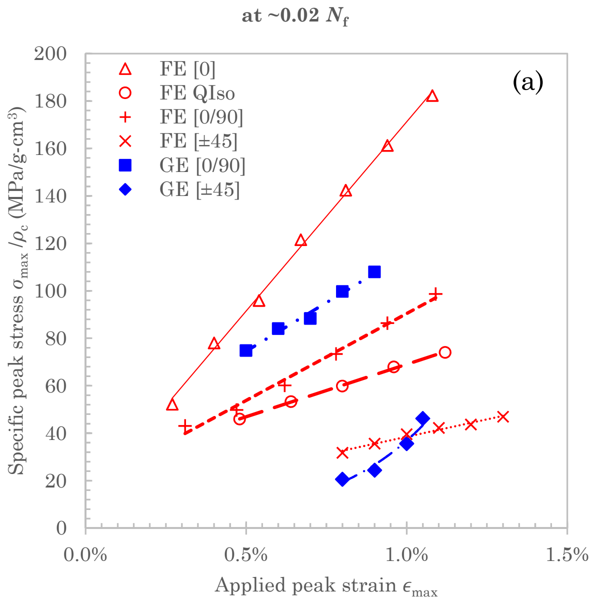

Figure 8.28: *Specific* peak stress $\sigma_{\max}/\rho_c$ (i.e. peak stress normalised for composite density) over applied $\epsilon_{\max}$ levels (a) at the beginning of fatigue life ($\sim$0.02 N_f), and (b) towards the end (0.9 N_f).

8.4.7 Stiffness and damage

8.4.7.1 Stiffness evolution measured from fatigue cycles

Figure 8.29 shows the evolution of stiffness in all tested laminates. Recall that secant modulus E^f of a fatigue cycle is normalised by initial undamaged modulus E_0, both measured from fatigue response data as previously indicated in Figure 8.4. All specimens, including those of fibre-dominant FE, show a net loss of stiffness. With the exception of the angled-crossply [±45] laminates, the stiffness degradation matches the expected typical 3-stage evolution of fibre-composites, discussed in the previous chapter and shown in Figure 7.11(b). The matrix-dominant [±45] also show a loss of stiffness, but the trend appears to have 2 stages, and is missing the third stage of rapid-degradation just before failure. The loss of stiffness appears to be proportional to the applied strain amplitude for all tested FE and GE laminates. For fibre-dominant specimens under lower strain loading levels ($\epsilon_{\max} < 0.8\%$), after an initial reduction, the modulus appears to remain constant past 0.1-0.2N_f. In the matrix-dominant specimens, modulus degradation is continuous throughout fatigue cycling, though more rapid during the first half of fatigue life.

The degrading stiffness of FE [0] and [0/90] seen here under strain-amplitude controlled fatigue is completely contradictory to the *increasing* trend observed for the same laminates under stress-controlled fatigue, reported in the work of Liang et al. [25; 50], El Sawi et al. [103], and Bensadoun et al. [109; 110]. This *stiffening* phenomenon under stress-controlled fatigue was discussed in the previous chapter Section 7.3.1. It was reported that FE [0] specimens experienced up to 2–11% modulus increase (see Figure 7.12), depending on the applied stress-amplitude, and that FE [0/90] showed 1–4% modulus increase (see Figure 7.13). In contrast, under constant strain amplitude test of the present study, a modulus loss of up to 30% under the highest strain-amplitude levels is evidenced for the same composites (Figures 8.29(a) and (c)).

As discussed in the introductory section of this chapter, the stiffening of fibre-dominant FE specimens

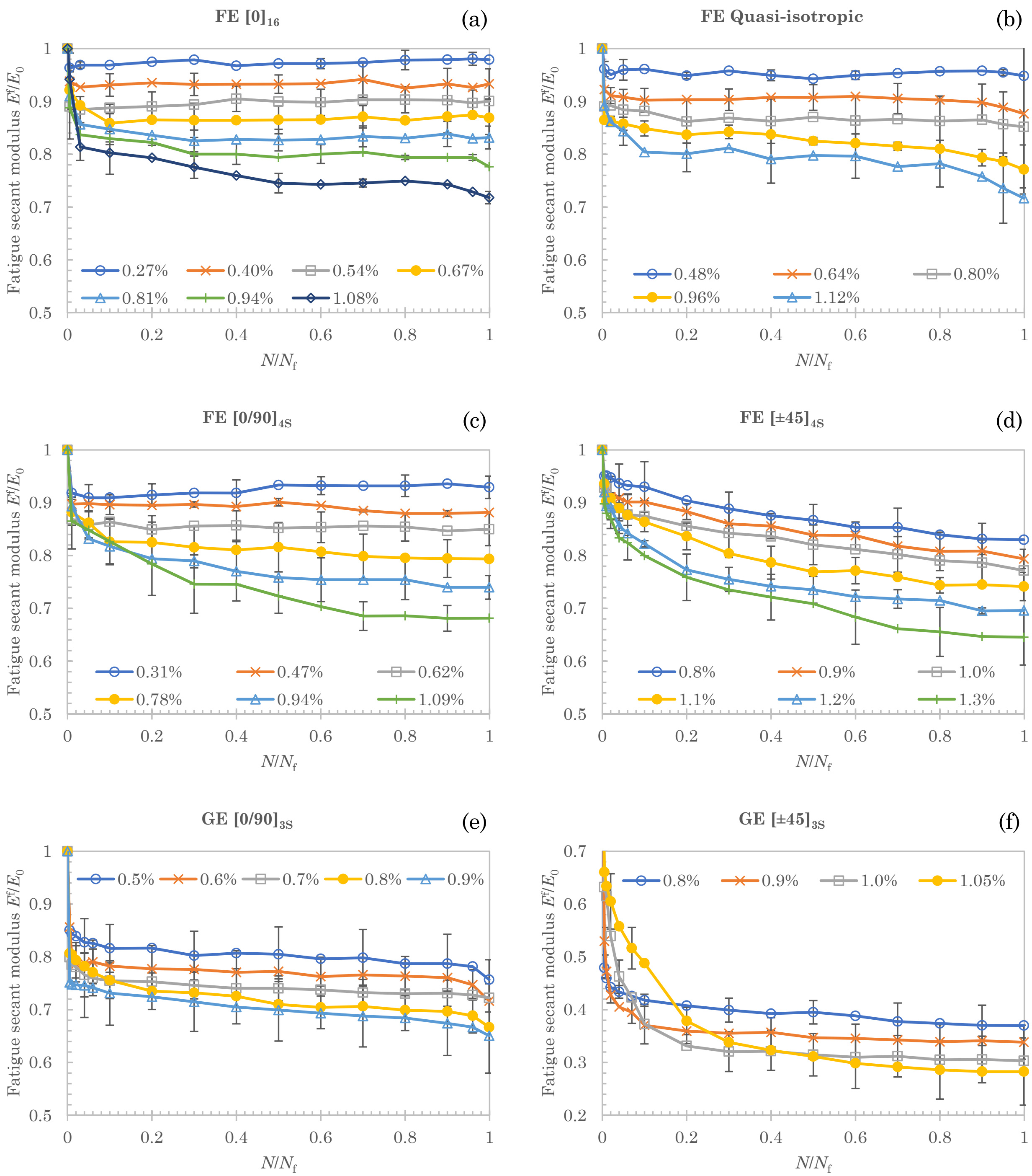

Figure 8.29: Evolution of normalised secant modulus E^{f} measured from *fatigue* cycles for tested $\epsilon_{\max}$ levels. The mean trendlines are shown with standard deviation bars.

in reported studies was attributed to structural reorganisation of, and within, Flax fibres that enhanced stiffness, i.e. straightening of initial 'waviness' of flax fibres, movement of microfibrils toward loading axis (reorientation), and rearrangement of irregularly-folded cellulose polymer chains into regular straight chains parallel to loading axis (crystallisation) [25; 50; 103; 109; 110]. However, these mechanisms still exist when the same specimens are tested under strain-controlled fatigue, and therefore should exert the same stiffening influence on specimen modulus – but this is not evidenced in the present study. Considering that measureable NFC material properties have been shown to be sensitive to strain-rate (refer back to Figure 8.1), it is thus concluded that composite stiffening reported by stress-controlled fatigue studies is not solely due to structural changes in the natural fibre, and therefore not an inherent physical property of NFC material, but is more likely a result of increasing strain-amplitude, and consequently strain-rate, over fatigue life.

8.4.7.2 Damage measured from fatigue cycles

Damage D^{f}, based on loss of secant modulus of fatigue cycles, is calculated via relation (8.1). Since the damage D^{f} is defined in terms of normalised modulus, damage increase and stiffness loss are interchangeable metrics, and damage evolution is a reflection of the stiffness trends shown earlier in Figure 8.29. The evolution of this stiffness-based definition of damage is given in Appendix A.6, Figure A.10.

In fibre-dominant specimens of FE, damage evolution is continuous at higher strain loading levels, but generally near-constant after an initial increase. This indicates their internal damaging mechanisms are more intense during early fatigue life, before $0.2N_{\mathrm{f}}$. Since specimen response is governed by fibre-properties, the near-constant damage after $0.2N_{\mathrm{f}}$ may indicate that fibre-specific damage mechanisms are either negligible, or simply do not have an effect on specimen modulus which fibre-specific damage may be. Unlike its FE counterpart, GE [0/90] shows a continuously increasing damage trend after $0.2N_{\mathrm{f}}$ at all applied strain levels. Matrix dominant [±45] specimens of both FE and GE also show rapid stiffness damage during early life, but subsequently continue with a less-steep increasing trend.

It is noteworthy that the Glass-reinforced specimens appear to sustain more stiffness damage than equivalent Flax-reinforced specimens. This is more clearly demonstrated by Figure 8.30, which plots the relationship between measured stiffness damage and applied peak strain, over different stages of fatigue life. It is seen that the extent of damage is directly proportional to applied strain loading, for all tested specimens. GE specimens are found to consistently suffer more damage than FE, throughout fatigue life, for all tested strain amplitudes. GE [±45] shows the most damage, up to 60-75% loss of stiffness by late fatigue life. The next most damaging laminate is GE [0/90] sustains up to 20-35% stiffness loss. Amongst the FE laminates, the most susceptible to damage proves to be FE [0/90], followed by [0], [±45], and quasi-isotropic laminates. During early fatigue life, FE angled-crossply [±45] is found to be the least damaging in terms of stiffness loss, but by mid fatigue life quasi-isotropic specimens sustain the same degradation of stiffness as [±45].

The implication of these findings is that, since Flax-reinforced laminates tend to lose much less of their original stiffness than equivalent Glass-epoxy, they may be considered against Glass-epoxy for applications where drastic loss of relative stiffness is not desired.

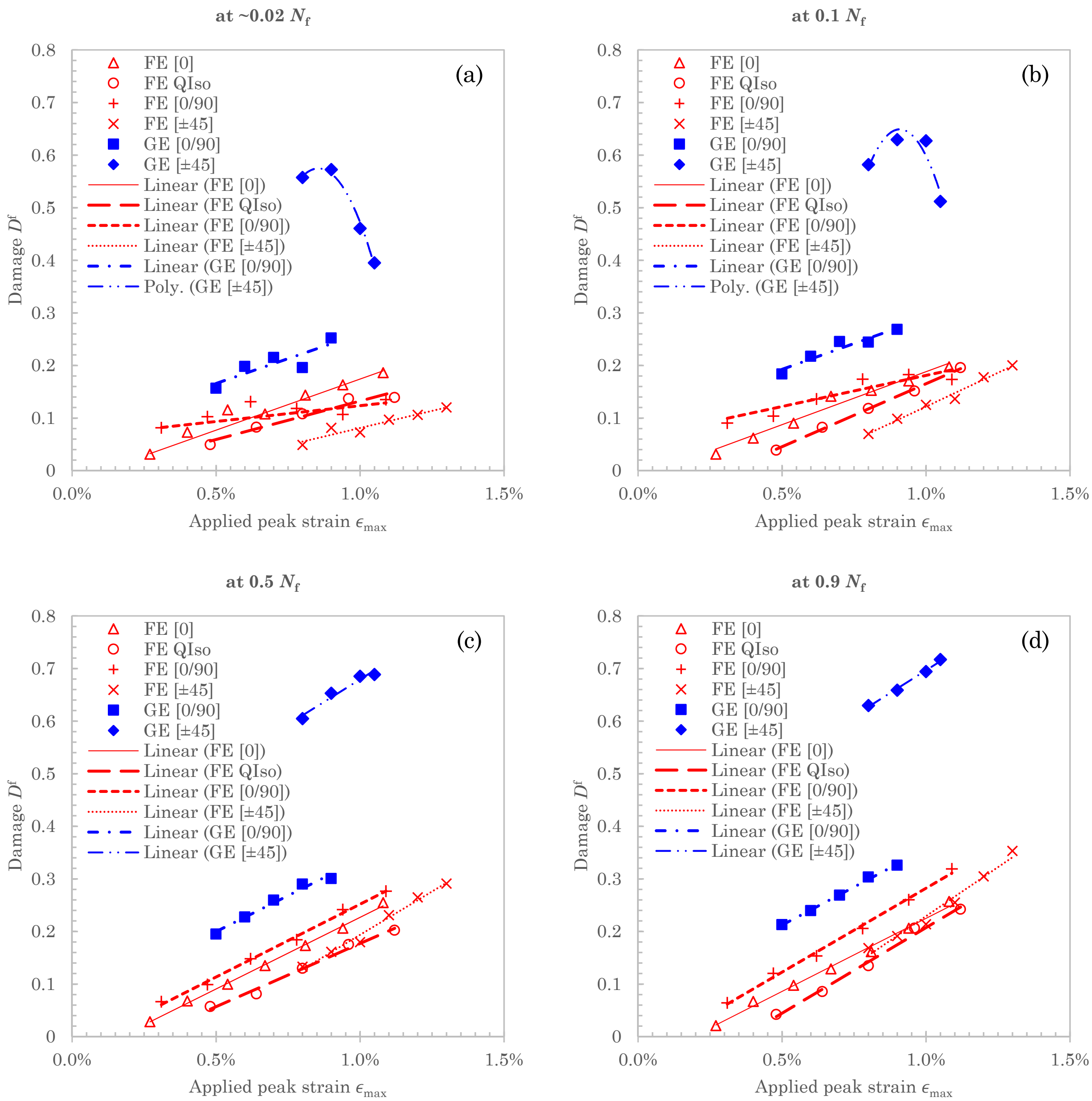

Figure 8.30: Observed trend of damage D^{f} over applied $\epsilon_{\max}$ levels (a) at the beginning ~0.02 N_{f}, (b) early 0.1 N_{f}, (c) mid 0.5 N_{f}, and (d) late fatigue life 0.9 N_{f}.

8.4.7.3 Damage measured from quasi-static cycles

Per test plan, fatigue cycling was interrupted at intervals to conduct quasi-static load-unload cycle at a constant 2 mm/min displacement rate. This loading rate, of course, is slower than that experienced during 5 Hz fatigue cycling. These interrupted static tests were conducted in order to compare the fatigue and static-condition secant moduli (therefore, damage), and investigate the influence of testing strain-rate on modulus measurement.

The 'static' damage D^{st} is calculated in terms of normalised static-condition secant modulus, per relation (8.2). Evolution of D^{st} over fatigue life for tested FE specimens are given in Appendix A.6, Figure A.11. By inspection, the static damage trends correlate well with those measured from fatigue cycles shown in Figure A.10. A direct comparison of the measured damage magnitudes during early and late fatigue life can be made from Figure 8.31, where static and fatigue values are plotted against applied peak strain.

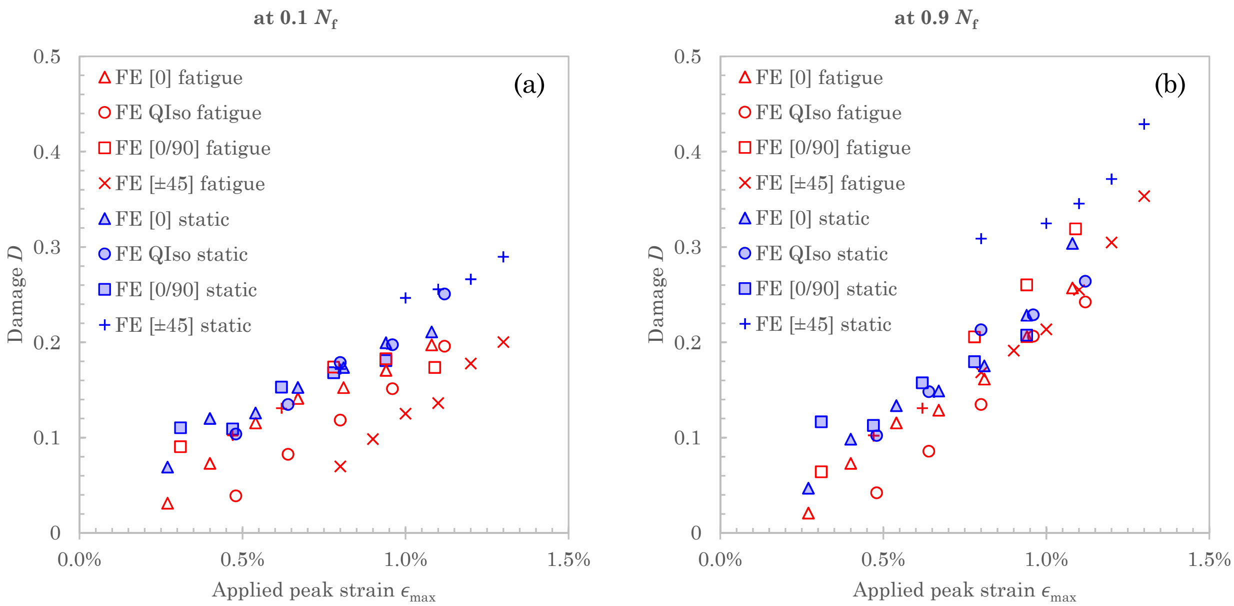

Figure 8.31: Comparison of damage trends measured from fatigue and quasi-static cycles for Flax-epoxy (FE) laminates (a) at the beginning of fatigue life (0.1 N_f), and (b) towards the end (0.9 N_f).

It can be seen that static damage values are consistently *higher* than those from fatigue. In other words, stiffness measured from static cycles (slower strain rate) are *lower* than that from fatigue cycles (quicker strain rate), confirming that increased strain rate results in a higher-estimated modulus.

8.4.8 Temperature

Under cyclic loading, a portion of mechanical energy transferred into the test specimen is either 'stored' in the material or dissipated as heat or acoustic emissions [230; 231]. Heat emissions manifest as surface temperature (T^S) that can be recorded by infra-red (IR) camera, as done in this study. Full-field images of specimen surface temperature were taken at intervals throughout fatigue test duration until failure. During fatigue cycling, the observed surface temperature fluctuated in sync and in proportion to cyclic loading, indicating that some fraction of total temperature change ($\Delta T = T^S - T_0$) is a consequence of the immediate rate of mechanical work done on the specimen, i.e. thermoelastic heating. Still, while fluctuating, the general trend of surface temperature was of a progressive increase, indicating that some fraction of total temperature change is associated 'stored' energy that is steadily increasing. It was observed that the location of eventual fracture generated the highest temperatures, allowing the easy identification of failure-prone areas. This indicates there exists yet another fraction of temperature change that is directly proportional to the intensity of local damage phenomena. As such, the highest surface temperatures on a full-field surface image may be considered reliable indicators of localised internal damage intensity.

Evolution trends of the *highest peak* surface temperature (highest = highest temperature over specimen 2D surface; peak = temperature at peak cycle strain) detected on tested specimens are shown in Figure 8.32. Note that laboratory room temperature was T_0 ∼23℃. A correlation is observed between peak temperature and strain loading level, as shown in Figure 8.33. As expected, all specimens exhibited a steadily rising superficial temperature over fatigue life. The evolution profile is typically of 3 stages, where the initial and final stage is of accelerated temperature rise, and the middle stage is of either steadily rising or constant temperature.

It is observed that, amongst the FE fibre-dominant laminates ([0], [0/90], and quasi-isotropic), increasing peak load levels typically result in higher surface temperatures during most of fatigue life. However, such a correlation cannot be conclusively observed for GE [0/90] specimens (Figure 8.33(e)), where the data suggests that peak temperatures generated may be independent of strain loading level. For the matrix-dominant [±45] laminates, temperature and peak strain also appear to have a directly proportional relationship, with the specific exception of FE [±45] where the proportional trend no longer holds after $\epsilon_{\max}$=1.2% (see Figures 8.32(d) and 8.33(d)). This anomaly for FE [±45] may suggest that the major heat-releasing damage mechanisms already occurred during the initial static cycle that strained the specimen to 1.2%. Note that the monotonic response of this layup also reveals a change in tangent modulus at ϵ=1.2%, indicating that degrading damage mechanisms occur at this strain loading.

8.5 Further discussion

The observed fatigue lives were statistically examined, and found to follow a consistent trend that can be modelled by a linearised strain-life (ϵ–N) relationship (8.3), for each tested laminate. Fibre-dominant specimens (wherein behaviour is governed by fibre properties) appear to have closely matching fatigue lives, whereas the lone matrix-dominant layup [±45] showed significantly longer endurance at the same strain loading levels. Fatigue longevity of Flax-reinforced [0/90] and [±45] specimens are observed to exceed those of Glass-reinforced specimens of the same architecture. Several mechanical properties and progressive phenomena are followed throughout fatigue life: stiffness damage, inelastic strain, hysteresis energy, and surface temperature. Most of these trends demonstrate a 2 or 3-stage evolution, where the first stage is a short period of accelerated evolution, followed by a constant or less-rapid evolution that covers majority of fatigue life, with a possible third stage of accelerated progression just before failure.

SEM examination of microstructure reveal evenly-distributed intra-bundle cracking early during fatigue life of all FE specimens, which is thought to contribute to the initial rapid degradation of mechanical properties and increase in energetic phenomena (hysteresis energy, temperature). Later life ($0.8N_{\mathrm{f}}$) damage mechanisms include continuous cracking around fibre bundles along interfacial boundaries, merging of multiple intra-bundle cracks across matrix regions between adjacent bundles, and interlaminar cracks that may have resulted for merged intra-bundle or circum-bundle cracks. In contrast to the diffuse damage evidenced in Flax-epoxy, Glass-reinforced specimens developed isolated single major cracks weaving along interfacial boundaries. Fatigue damage evolution trends show that both GE laminate configurations consistently suffer higher damage (i.e. more severe relative stiffness loss) than the FE. At intervals, fatigue

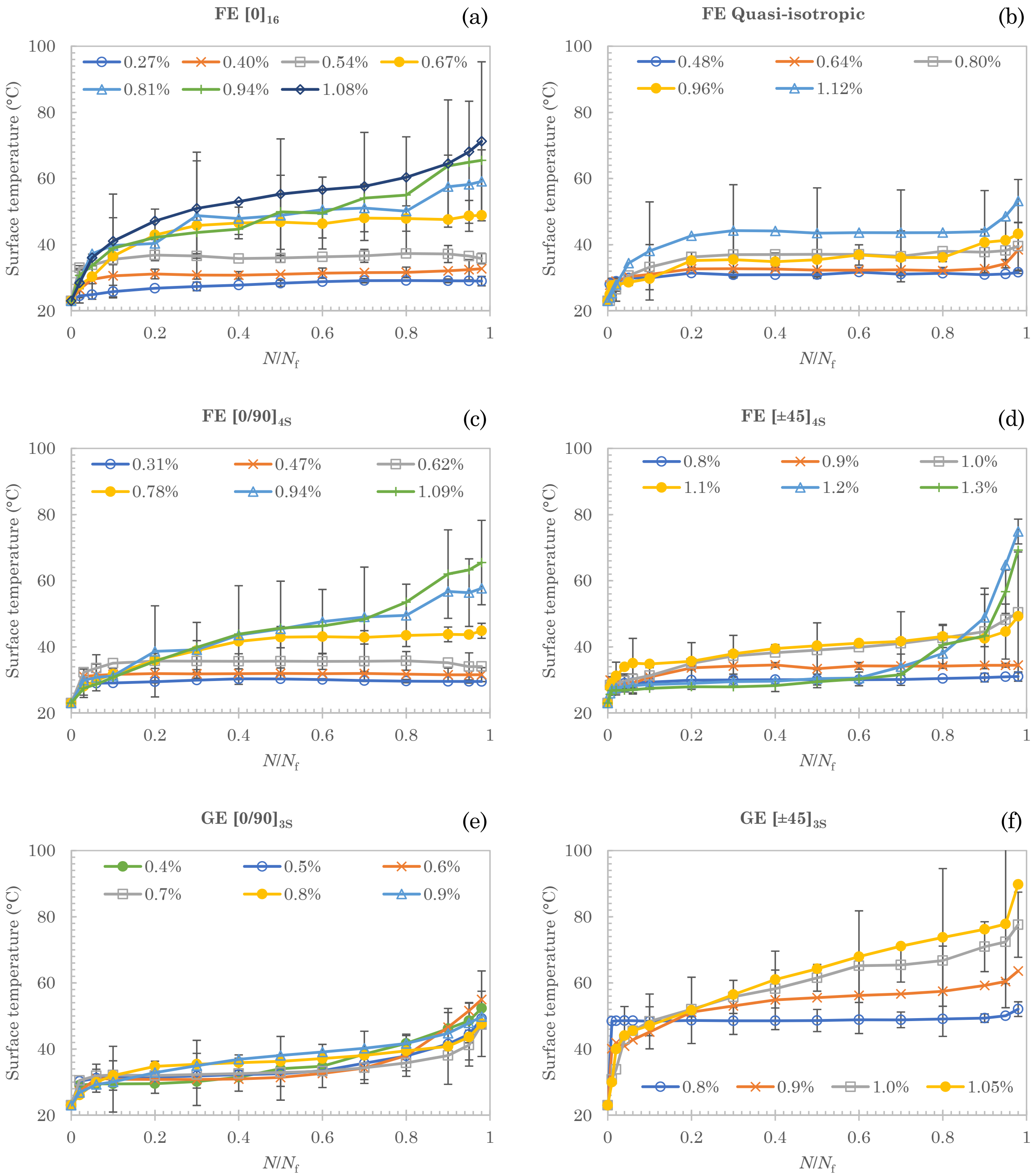

Figure 8.32: Temperature of specimen surface over fatigue life for tested $\epsilon_{\max}$ levels. The mean trendlines until just before failure ($\sim$0.98 N_{f}) are shown with standard deviation bars.

cycling was interrupted for a quasi-static load-unload cycle, which revealed that residual stiffness measured under static conditions (lower strain-rate) are generally higher than that measured under fatigue conditions (higher strain-rate), after the same duration of fatigue history – further confirmation that fatigue stiffening

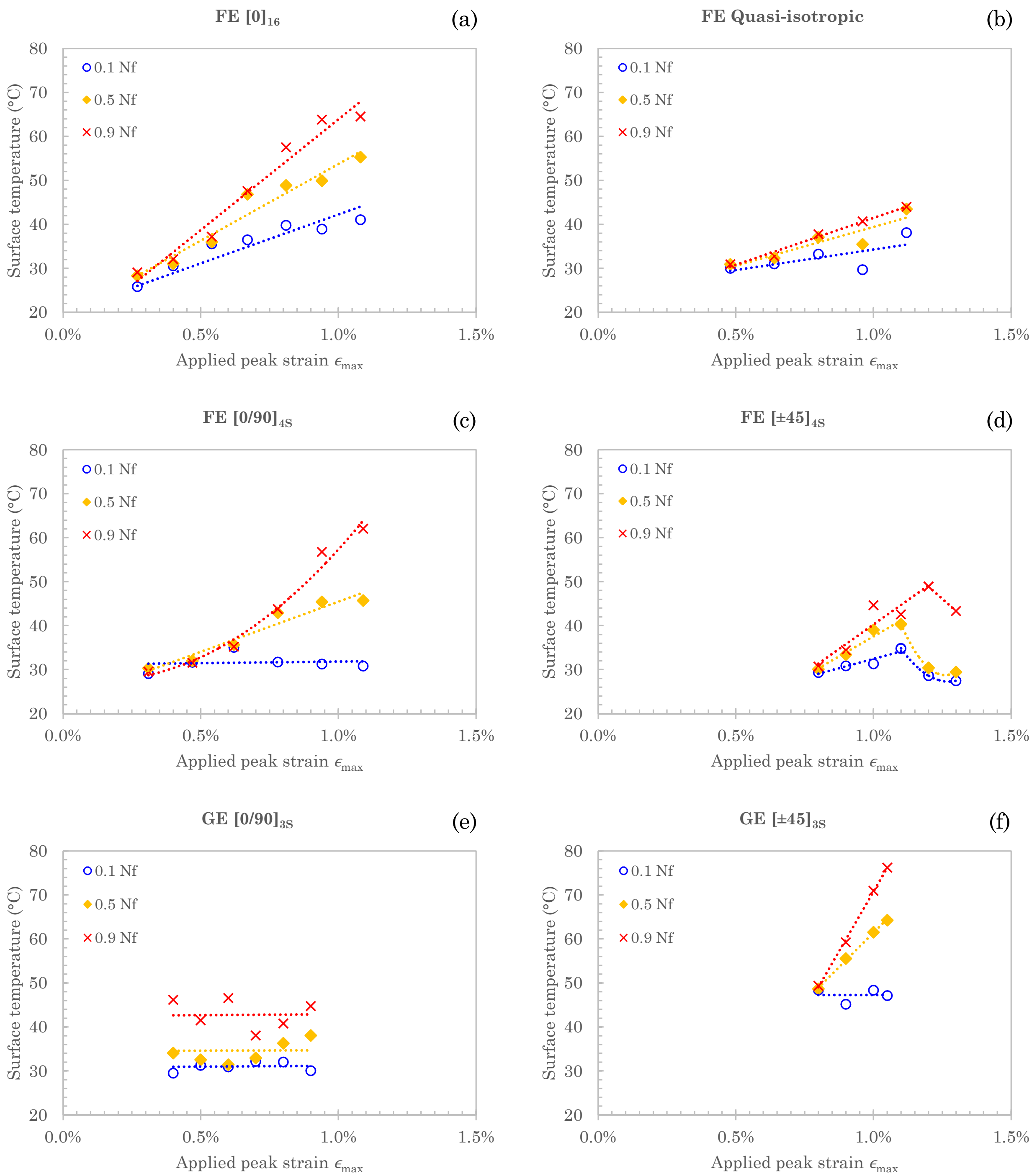

Figure 8.33: Observed trends of surface temperature over applied $\epsilon_{\max}$ levels at early (0.1 N_{f}), mid (0.5 N_{f}), and late (0.9 N_{f}) fatigue life.

observed in spite of damage in stress-controlled studies may be a function of test parameters. GE [±45] specimens are seen to accumulate more permanent strain than FE at the same loading levels (confirming observation from stress-controlled studies [25; 50]), but the reverse is observed for [0/90] laminate. Absolute peak stress in FE [0] specimens are similar to those measured in GE [0/90], however when normalised for density, FE [0] is found to exceed GE [0/90]. The same comparison holds true for between GE and FE [±45]. The energy-based phenomena (hysteresis, surface temperature) trends suggest fibre-direction energy dissipation is higher in FE than GE, which is consistent with micrography observations of fibre damage in Flax but none in Glass. Off-axis GE trends show much higher energy dissipation than FE, suggesting that non-fibre-related mechanisms, e.g. fibre-matrix debonding and delamination, are more intensive in GE specimens than in FE.

8.5.1 Future work

1. In this study (where loading ratio was $R_\epsilon = 0.1$, as cycling progressed and the specimens accumulated permanent extension, the enforcement of a constant minimum strain eventually resulted in compressive minimum stresses (see Figure 8.19). It may be advisable in future strain-controlled testing to apply larger loading ratios, e.g. $R_\epsilon \geq 0.2$, to ensure that there is no departure into compressive loading. Furthermore, testing may be conducted for a range of strain loading ratios, including tension-compression and compression-compression, to study Flax-epoxy performance in comparison to Glass-composites.

2. It is common for realistic engineering applications to involve variable amplitude cyclic loading. Future research on Flax-composite performance may be tested under a spectrum loading regime that is representative of a specific application, e.g. biomechanical prosthetics.

3. This study did not investigate the fatigue response of [90] laminates (which would have provide insight on 'transverse' fatigue strength), since engineering components made of laminates are rarely designed to be loaded perpendicular to the fibre axis. However, in the interest of obtaining a complete dataset of FE fatigue performance in all orthotropic directions, testing of [90] may be desirable. Furthermore, off-axis testing at a range of fibre orientations may also be of interest.

4. Future 'durability' studies may involve fatigue testing of Flax-epoxy laminates after structural distress, e.g. water ageing, high-temperature exposure, impact loading, etc. Post-fatigue microstructure observations in such studies may reveal different damage mechanisms, or evolution at different intensities, than that observed in this study.

8.6 Conclusion

This study conducted *constant strain-amplitude* fatigue tests on select Flax-epoxy laminates (unidirectional $[0]_{16}$, crossply $[0/90]_{4S}$, angled-crossply $[\pm45]_{4S}$, and quasi-isotropic $[0/45/90/-45]_{2S}$), and presents original data on their response under strain-controlled tension-tension cycling (5 Hz cycling frequency, load ratio $R_\epsilon = \frac{\epsilon_{\min}}{\epsilon_{\max}}$=0.1). Strain-amplitude control was chosen in order to maintain a constant strain rate during fatigue cycling, since it was shown in previous studies that loading strain-rate has a significant influence on measured stiffness and strength. Considering the superior stiffness damage resistance, lower inelastic strains and damage-related energy dissipation in off-axis configurations, and higher specific stress transfer in FE specimens compared to GE, Flax proves to be a serious alternative to Glass for mechanical reinforcement against fatigue degradation in engineering structures.

Chapter 9

Modelling progressive fatigue damage

This chapter develops an analytical means to model laminate-scale progressive fatigue damage and failure in NFCs, based on the stiffness degradation and inelastic strain data from the preceding chapter. Model parameters are identified for the four laminate architectures tested, and the simulated predictions are critically compared with experimental data.

9.1 Introduction

It is well known that fatigue is a major failure type in engineering structures that are subjected to frequent, repetitive loading. Compared to homogeneous and isotropic materials like metals, fatigue damage in fibre reinforced composites are significantly more complex and varied [128]. On account of their multi-scale, hierarchical structure, fibre composites demonstrate multiple damage mechanisms during fatigue, each of which may initiate at different stages of fatigue life, develop at different growth rates, and interact in complex ways that vary the composite material properties. In metals, fatigue damage accumulation tends to be gradual where initial accumulation is barely measurable (Figure 9.1(a)), and material stiffness can be considered unaffected during operational loading (i.e. constant relationship between load and deformation can be assumed), thereby allowing the prediction of fatigue behaviour through linear elastic analyses and fracture mechanics [232]. In contrast, fibre composites may demonstrate rapid stiffness degradation at a very early stage of fatigue loading (even for moderate strains), followed by a period of steady damage accumulation in the various phases of the composite [131]. Figure 9.1 compares the characteristic damage evolution trends for metals with fibre-composites. The previous chapter found that the growth of stiffness damage in Flax-epoxy composites under strain-controlled fatigue followed a similar evolution curve as Figure 9.1(b).

Predicting fatigue behaviour in composites reinforced by natural fibres is further complicated by the non-homogeneous nature of the fibre itself, in addition to the the differing micro- and meso-structural damaging phenomena that can evolve co-dependently or independently of each other. This chapter contributes to the fatigue response modelling of NFCs by proposing damage and inelasticity evolution functions, based on the constant-strain amplitude and constant-frequency cyclic tests documented in Chapter 8.

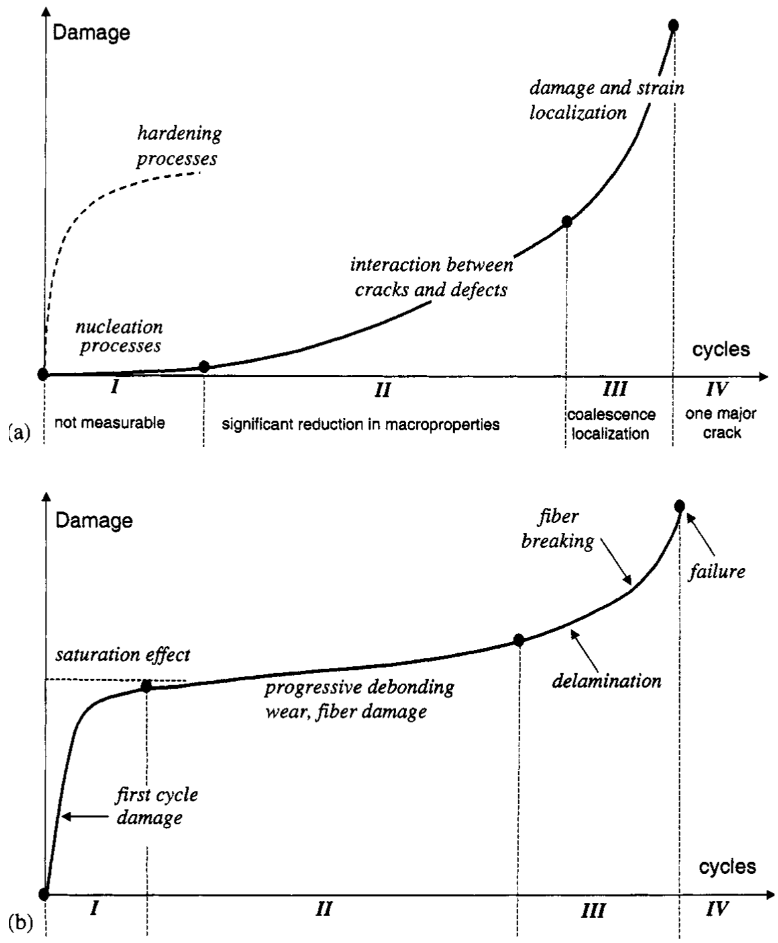

Figure 9.1: Typical fatigue damage evolution profiles in (a) metals, and (b) fibre reinforced composites. Reproduced with permission from [131].

9.1.1 Fatigue damage modelling techniques

Though engineering composites serve as replacements for metals, the already-validated methods for metal fatigue modelling are not directly applicable for fibre-composites, on account of their different fatigue behaviour [213]. Furthermore, the plethora of composite configurations that arise from combining different fibres and matrix materials, in different layup orientation sequences, and manufactured by different methods, complicates the development of all-encompassing modelling techniques. Fibre-composites, including NFCs, exhibit anisotropic material properties, that are different under tensile and compressive loading, and are sensitive to parameters such as loading rate, loading frequency, mean stress or strain, and ambient temperature/humidity conditions. To account for all these variables and simulate their influence on composite behaviour in a comprehensive modelling framework has proven a near-impossible task [213].

The enduring popularity of composites in engineering, notwithstanding their complexity of fatigue response, has resulted in a diverse array of failure modelling approaches for specific behaviours of specific subsets of fibre-composites, evident from the abundant literature in this field. The primary damage mechanisms that lead to fatigue failures are now well identified (e.g. micro-cracking, interfacial cracking, progressive delamination, fibre fracture etc. [233]), however we remain deficient in understanding what causes damage to follow its unique trajectories at specific growth speeds under a given loading scenario [234]. This compels research to be broken down to address damage mechanisms individually, and to still rely on heavily empirical strategies where proposed theories are validated for a limited range of loading conditions. Attempts to find a unifying theory and comparative examinations of several failure and damage theories have concluded that no single approach is dominant, and that the effectiveness of each is greatly dependent on the case studied [235–237]. In the midst of such modelling challenges for even the traditional engineering composites (i.e. Carbon or Glass reinforced), the fatigue simulation of NFCs is uniquely disadvantaged due to their relative novelty and considerably scant fatigue data – which previous chapters have attempted to remedy by analysing existing stress-controlled fatigue data (Chapter 7) and reporting original strain-amplitude controlled behaviour (Chapter 8).

The current general consensus seems to classify fatigue modelling techniques into (i) fatigue criteria-based life prediction models, (ii) phenomenological (residual stiffness or strength) models , and (iii) mechanistic progressive damage models [232; 234; 238]. *Life prediction* models typically predict the fatigue failure of a laminate based on fitting stress-life or strain-life plots generated experimentally. Well-known examples of such models are Wöhler and Basquin curves, etc. *Fatigue failure criteria* are mathematical polynomial relationships based on orthotropic failure strengths (or strains) that are able to predict the fatigue life of a multi-orientation laminate. Such methods are not based on any actual degradation mechanisms, and are purely empirical relationships that have been shown to reproduce experimentally observed fatigue lives with reasonable accuracy. *Phenomenological* models are able to describe the evolution of macroscopic material properties, typically in terms of modulus or residual strength. *Mechanistic* models strategies that simulate the evolution of individual damage phenomena, such as delaminations or matrix microcracks, in order to predict the material properties over the complete fatigue life. An excellent review of existing fatigue life models, strength and stiffness-based models, and progressive damage modelling techniques is compiled between the work of Degrieck and van Paepegem [232], and Sevenois and van Paepegem [234].

The growth of damage zones within a composite structure leads to a continuous redistribution of stress and stress concentrations, so the prediction of evolving material properties requires modelling a nonlinear history of successive damage states [232]. The damage state in a fibre-composite may be estimated by measuring the progress of one or more relevant *damage indicators* or *metrics*. The evolution of several material properties of Flax-epoxy composites were studied in the previous Chapter 8 (e.g. hysteresis energy, inelastic strain, stiffness, surface temperature), all of which are experimentally measurable using non-destructive techniques. It was shown in Chapter 5 that stiffness degradation of NFCs are not correlated with accumulating permanent strain (particularly in the fibre-direction), indicating that mechanisms that degrade stiffness and those that result in permanent deformation should be treated separately in order to simulate the damage state of NFC material. Therefore, following the static response modelling philosophy adopted in Chapter 6, the chosen indicators of fatigue damage in this study are stiffness and inelastic strain component of total strain.

Existing published data on plant-based NFCs are only from *stress*-controlled fatigue studies, which do not lend themselves to reliable stiffness-based predictive modelling, since material stiffness from such tests are sometimes found to *increase* over fatigue life (specifically in fibre-direction) despite evidence of internal material degradation [25; 50; 103; 109; 110]. This stiffening phenomenon did not manifest in *strain*-

controlled tests documented in Chapter 8, strongly suggesting that hitherto reported NFC fatigue-stiffening was a function of test parameters, and is not an inherent material property. As such, strain-controlled experimental data are perhaps more appropriate and meaningful for fatigue damage modelling in NFCs.

Most existing criteria and models of fibre-composite fatigue were developed for stress-controlled cycling loading, and do not typically treat inelastic strain as a damage parameter. In the absence of relevant, applicable models, this study initiates the task of developing a method to predict damage growth under constant strain-amplitude fatigue. The proposed solution is essentially a phenomenological laminate-scale approach, whereby an evolution function is proposed to simulate stiffness and cumulative inelastic strain as functions of fatigue cycle and applied strain, combined with the strain-life (ϵ–N) relationships determined in Chapter 8 to predict fatigue life. To aid the immediate application of the proposed relationship for rapid prototyping of Flax-fibre based components, model parameters are identified for the considered laminates, which are some of the most common stacking-sequence configurations in engineering applications.

9.2 Materials, manufacturing, and methods

The representative NFCs considered in this study are the Flax-epoxy laminates for which fatigue data were tested in Chapter 8: unidirectional $[0]_{16}$, crossplies $[0/90]_{4\mathrm{S}}$ and $[\pm 45]_{4\mathrm{S}}$, and quasi-isotropic $[0/\text{-}45/90/45]_{2\mathrm{S}}$. Other plant fibre based ligno-cellulosic NFCs, like those of Hemp, Sisal, and Jute, are expected to demonstrate similar nonlinear damage behaviour as the considered Flax-reinforced specimens, on account of their similar fibre properties, common hierarchical microstructure arrangement, and similar cellulose content and crystallinity [115; 239]. While the model parameters identified in later sections apply specifically to Flax-epoxy laminates, the form of the proposed evolution function should remain applicable to other NFCs.

Plates of these Flax-epoxy laminates were manufactured from commercially available Flax fabric and epoxy material as detailed in sections 4.2.1, 4.2.2, and 4.3. Composite constituent fractions and densities are listed in Table 4.1. Rectangular 250×25-mm test specimens were cut from these manufactured plates and prepared for fatigue testing as detailed in section 4.5. Fatigue tests were conducted under constant strain amplitude of ratio $R_\epsilon = \frac{\epsilon_{\mathrm{min}}}{\epsilon_{\mathrm{max}}} = 0.1$, and frequency 5 Hz, using equipment detailed in section 8.3.2. The number of tested specimens for each laminate configuration, and their mean fatigue lifetimes are listed in Table 8.2. Experimental fatigue damage D^{f} as a function of fatigue cycle N was calculated in terms of secant modulus E^{f} normalised by initial undamaged static modulus E_0, per relation (8.1) repeated here:

$$D^{\mathrm{f}}(N) = 1 - \frac{E^{\mathrm{f}}(N)}{E_0} \tag{8.1}$$

The above moduli, and inelastic strain, ϵ^p were measured from stress-strain response plots as shown in Figure 8.4.

9.3 Proposed model for strain-controlled fatigue

As noted earlier, the chosen damage indicators of fatigue secant modulus E^{f} and inelastic strain ϵ^p were measured from laminate response data as shown in Figure 8.4. The evolution of these metrics for Flax-epoxy laminates under constant strain-amplitude fatigue are shown in Figures A.10 and 8.23, respectively.

9.3.1 Progressive evolution function

An analytical function is proposed to model the evolution of damage metrics at the scale of the laminate, based on the shape and form of the experimentally observed trends. In doing so, this approach follows the modelling philosophy adopted in the works of Mao and Mahadevan [240] for UD and woven graphite-epoxy, Giancane et al. [241] for UD glass-epoxy, and Kennedy et al. [242] for fibre-direction modulus degradation in quasi-isotropic glass-epoxy laminates, wherein nonlinear stiffness degradation was modelled by a macroscale function that described uniaxial laminate-scale damage over fatigue life.

On examining the increasing tends for secant damage and inelastic strain of Flax-epoxy laminates (Figures A.10 and 8.23), a *hyperbolic* relation is evident with respect to fatigue duration N_{f} for all strain loading levels, where D^{f} and ϵ^p initially accumulate rapidly, followed by an extended period at constant or gently increasing magnitude. A Hill-equation-type function is found to fit the evolution profile of both damage metrics. So, to express damaged-condition material property X as a function of fatigue cycles N for a given peak strain loading level $\epsilon_{\max}$, the following relation is proposed:

$$\mathrm{X}\left(N, \epsilon_{\max}\right) = \frac{\lambda}{\left(\dfrac{\kappa}{\hat{N}}\right)^{n} + 1} \tag{9.1}$$

where

$$\left.\begin{array}{lll} \hat{N} & = N/N_{\mathrm{f}} & \text{is the normalised number of cycles,} \\ & & N_{\mathrm{f}} \text{ is the fatigue life of the laminate} \\ \lambda & = c_1\left(\epsilon_{\max}\right)^p & \text{is a shape-limiting parameter} \\ & & \text{that is a function of } \epsilon_{\max} \text{ raised to power } p \\ & & \text{and is dependent on coefficient } c_1 \\ \kappa & = c_2\left(\epsilon_{\max}\right)^p & \text{is also a function of } \epsilon_{\max} \text{ raised to power } p \\ & & \text{and is dependent on coefficient } c_2 \end{array}\right\} \tag{9.2}$$

and where c_1, c_2, n, and p are parameters, unique to the laminate, that have to be identified.

Substituting (9.2) into (9.1) gives the fully expanded form of the proposed numerical model, with the four parameters to be identified shown in red:

$$\mathrm{X}_{\mathrm{num}}\left(N, \epsilon_{\max}\right) = \frac{c_1 \epsilon_{\max}^{p}}{\left[\dfrac{c_2 \epsilon_{\max}^{p}}{N/N_{\mathrm{f}}}\right]^{n} + 1} \tag{9.3}$$

9.3.2 Failure

Under strain-amplitude controlled fatigue, all evolving mechanical properties observed experimentally for the considered Flax-epoxy laminates – permanent strain (Figure 8.23), peak stress (Figure 8.26), stiffness (Figure 8.29) – demonstrate some degree of stabilisation or plateauing well before fatigue failure. As the value of these material properties reach near-constant levels by $0.5N_\mathrm{f}$ and may not change much even by just-before-failure, they do not make for reliable indicators of *imminent* failure, and therefore cannot be utilised as failure criteria for the case of constant strain-amplitude fatigue.

As such, it appears the best phenomenological means of predicting NFC failure under strain-controlled fatigue is to estimate fatigue life N_f from empirically-derived relationships between applied strain load level and fatigue life, as was done in Chapter 8. For the considered Flax-epoxy laminates, the strain-life (ϵ–N) data and modelled medians were shown in Figure 8.6. The fatigue life trends were found to be well simulated by a linearised relationship (8.3) between ϵ_max and $\log(N_\mathrm{f})$, repeated here:

$$\log\left(N_\mathrm{f}\right) = A_\epsilon + B_\epsilon\left(\epsilon_\mathrm{max}\right) \tag{8.3}$$

Parameters A_ϵ and B_ϵ of the linear relation (8.3) for the tested Flax-epoxy laminates were already identified and listed in Table 8.3.

9.3.3 Sensitivity of parameters

A sensitivity study is conducted to determine the limits of the proposed evolution function (9.3) and its parameters. The following charts in Figure 9.2 demonstrate the effect of varying each unknown parameter on the predicted damage evolution.

It is observed that:

- The predicted plots are most sensitive to power parameters n and p, followed by c_1 and c_2, in that order.
- Negative values of c_1 and p produce negative predictions of limiting parameter λ, and therefore X (Figure 9.2(a)), which is not desired for simulating increasing damage (i.e. degrading stiffness) or increasing inelasticity phenomena. For the Flax-composites considered in this study, therefore, c_1 must be positive.
- Parameters c_2 and p must be positive (see Figures 9.2(b) and (c)).
- Values of $-1 \leq n \leq 1$ produce a generally bi-linear (2-stage) curve, whereas values of $n > |1|$ produce a sigmoidal evolution curve with three distinct stages (Figure 9.2(d)). Also, $n = 0$ produces a flat curve for X, and positive values of n result in an *increasing* trend for X. Since most of the experimentally observed evolutions for inelastic strain and fatigue damage resemble the 2-stage bilinear increasing trends (Figures A.10 and 8.23), parameter n is best limited to the range $0 \leq n \leq 1$.

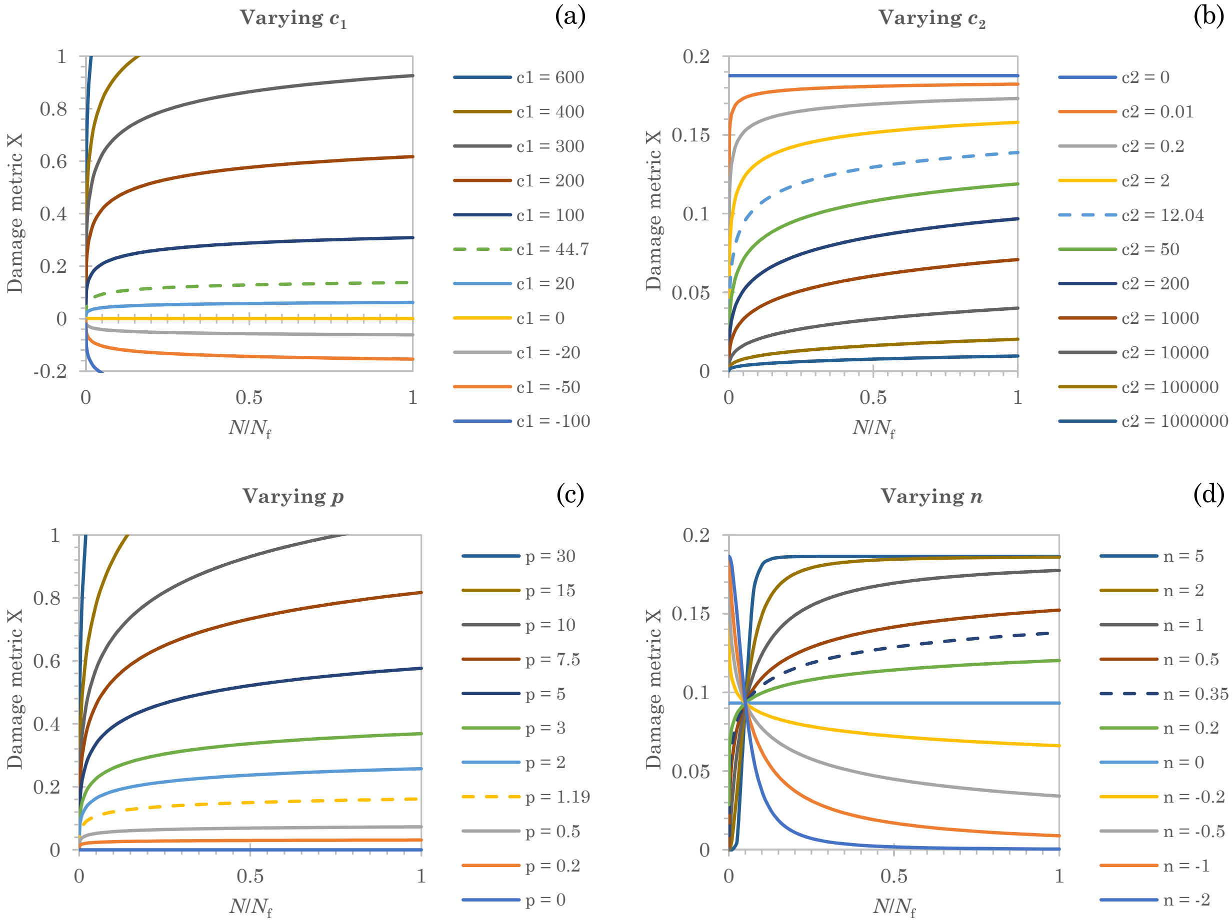

Figure 9.2: Sensitivity to parameters in proposed fatigue damage evolution function (9.3). As an example, prediction for damage D^{f} in $[0/90]_{\mathrm{nS}}$ laminate tested at $\epsilon_{\max}$=1.0% (parameters $\{c_1, c_2, n, p\} = \{45, 12, 0.35, 1.19\}$) is shown as the benchmark curve (broken lines).

9.3.4 Parameter identification

The four parameters of the proposed fatigue damage evolution model are identified by applying a classical nonlinear optimisation procedure, specifically the generalised reduced gradient (GRG) algorithm available as a built-in solver in commercial MS Excel software.

For each unique laminate stacking sequence, the cost function z_f is formulated to minimise the difference between experimentally observed value and simulation-predicted value over the fatigue life N_{f} for all k tested peak strain levels $\epsilon_{\max}$, as follows:

$$z_f(\mathbf{p}) = \frac{\sum\limits_{i=1}^{k} \sum\limits_{\hat{N}=0}^{1} \left(\mathrm{X}_{\mathrm{num}}(\mathbf{p}) - \mathrm{X}_{\mathrm{exp}}\right)^2}{\sum\limits_{i=1}^{k} \sum\limits_{\hat{N}=0}^{1} \left(\mathrm{X}_{\mathrm{exp}}\right)^2} \tag{9.4}$$

where

$$\left.\begin{array}{rl}\mathbf{p} & \text{is the parameter set } [c_1, c_2, n, p] \\ \mathrm{X}_{\mathrm{num}} & \text{is the predicted value of material property X calculated using (9.3)} \\ \mathrm{X}_{\mathrm{exp}} & \text{is the experimentally observed value of material property X} \\ \hat{N} & \text{is the normalised fatigue cycles } \frac{N}{N_{\mathrm{f}}} \\ k & \text{is the total number of fatigue tests conducted for subject laminate} \\ i & \text{is the index for each fatigue test}\end{array}\right\} \tag{9.5}$$

Considering the sensitivity study described in the previous section, it is evident that the identified parameters should fall within certain limits in order to efficiently search for a parameter set that produces the global minima for cost function z_f. The GRG algorithm is therefore instructed to minimise the cost function (9.4) by guessing parameters $\mathbf{p}$ within the following basic constraints:

$$\begin{array}{rcl} & c_1 & \geq 0 \\ & c_2 & > 0 \\ & p & \geq 0 \\ 1 \geq & n & \geq 0 \end{array} \tag{9.6}$$

9.4 Results and Discussion

The parameters identified for damage and inelastic strain evolution are listed in Table 9.1.

Table 9.1: Identified parameters of evolution function (9.3) for damage and inelastic strain in tested Flax-epoxy laminates

		Damage evolution				Inelastic strain evolution			
Laminate	Ply sequence	c_1	c_2	n	p	c_1	c_2	n	p
UD fibre-direction	$[0]_{16}$	34	3.83	0.71	1.33	9.0	40	0.25	2.33
Cross-ply	$[0/90]_{4S}$	45	12.0	0.35	1.19	1.8	60	0.15	1.30
Angled cross-ply	$[\pm 45]_{4S}$	77	163	0.35	2.24	11.8	65	0.22	2.44
Quasi-isotropic	$[0/+45/90/-45]_{2S}$	42	5.49	0.25	1.60	0.32	0.79	0.20	1.00

Recall that the above evolution function (9.3) is formulated in terms of normalised fatigue life $\frac{N}{N_{\mathrm{f}}}$. The fatigue life N_{f} (i.e. number of cycles to failure) at any applied strain loading can be estimated from the strain-life relation (8.3). Parameters for this ϵ–N relationship were already identified in Chapter 8 and listed in Table 8.3, repeated here:

Since the fatigue loading is strain-controlled, and the enforced axial deformation is the same for all plies in the tested specimen, it can be reasoned that damage variable D^{f} (that is based on a *normalised* secant modulus, relative to initial undamaged modulus) and inelastic strain response ϵ^p should not be significantly influenced by the number of plies (or number of repeating orientation sequences), as long as the overall layup is symmetrical and specimen laminate thickness remains small with respect to its

Table 9.2: Identified parameters of linearised strain-life relationship (8.3) for Flax-epoxy laminates, from Chapter 8

Laminate	A_ϵ		$\mathrm{CI}_{0.95}$ [a]	B_ϵ		$\mathrm{CI}_{0.95}$ [a]
$[0]_{16}$	7.472	±	0.226	-402.42	±	29.18
$[0/90]_{4S}$	8.198	±	0.289	-433.55	±	31.71
$[\pm 45]_{4S}$	9.822	±	0.572	-484.65	±	53.27
$[0/+45/90/-45]_{2S}$	7.480	±	0.329	-376.76	±	36.67

[a] 95% confidence interval

length or width. So, the parameters in Table 9.1 should hold for all low-thickness Flax-epoxy laminates in engineering structures.

9.4.1 Damage evolution

The simulated and experimental damage evolutions are shown superimposed for all considered Flax-epoxy laminates in Figures 9.3–9.6

FE [0]. For [0] laminate (Figure 9.3), the predicted evolutions appear in good agreement with the experimental, for all strain loading levels, however the correlation is least for the lowest and highest load levels $\epsilon_{\max}$=0.27% and $\epsilon_{\max}$=1.08%, respectively. For $\epsilon_{\max}$=0.27%, the experimentally observed damage

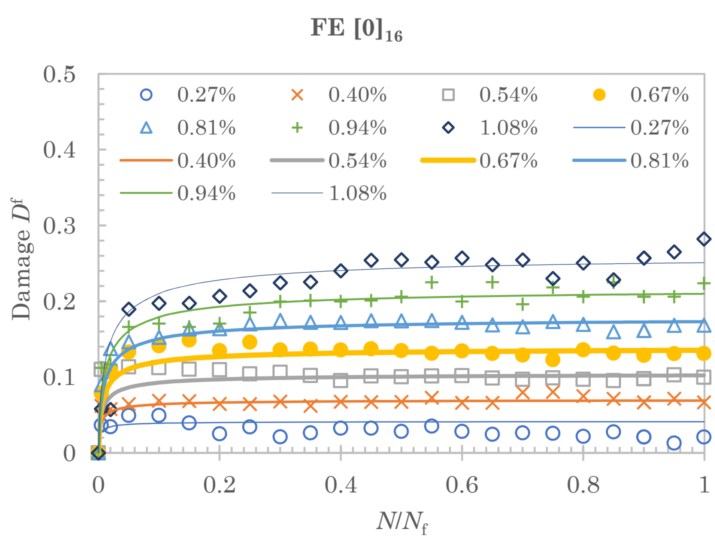

Figure 9.3: Evolution of fatigue damage D^{f} in Flax-epoxy [0] laminate under various applied $\epsilon_{\max}$ levels, showing experimentally derived (discrete datapoints) and simulated (continuous line) trends.

trend appears to generally decrease after $0.1N_{\mathrm{f}}$, which the simulated evolution function is not formulated to capture. However, this is more likely indicative of error in experimental data. It must be noted that the experimentally determined datapoints are actually the mean from several tests on specimens of the same laminate, with a non-zero standard deviation, as indicated by the error bars in the originally reported data (see Figure A.10(a)). For the case of $\epsilon_{\max}$=1.08%, the averaged experimental data is observed to fluctuate, which may be on account of signal noise in the original measurements. Still, when considered altogether, the damage evolution datasets for FE [0] appears well-captured, indicating the suitability of the proposed evolution function and the identified parameters.

FE quasi-isotropic. For the quasi-isotropic specimen data (Figure 9.4), good correlation is seen between the predicted and experimental curves for most of fatigue life, however the experimental trends for $\epsilon_{\max}$=0.96%, 0.64%, and 1.12% load levels appear to move away from the simulated trend after $0.8N_{\mathrm{f}}$. This is because the form of the proposed evolution function does not allow for a rapid increase at the end

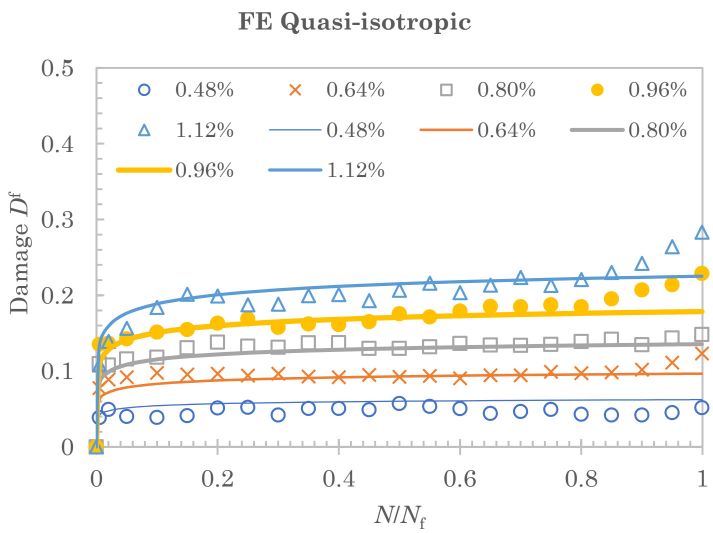

Figure 9.4: Evolution of fatigue damage D^{f} in Flax-epoxy quasi-isotropic laminate under various applied $\epsilon_{\max}$ levels, showing experimentally derived (discrete datapoints) and simulated (continuous line) trends.

of fatigue life, and therefore dos not capture such spurts of accelerated damage towards end-of-life as seen for $\epsilon_{\max}$=0.96%, 0.64%, and 1.12%. However, as will be seen in the subsequent paragraphs, the evolution function remains suitable for a majority of damage and inelasticity trends observed experimentally.

The inability of the proposed function to capture accelerated trends after $0.8N_{\mathrm{f}}$ means it underestimates stiffness-degradation damage after this stage, and this discrepancy gets larger as N increases beyond $0.8N_{\mathrm{f}}$. For example, under loading level $\epsilon_{\max}$=0.96%, the experimental mean damage at 0.999 N_{f} is $D^{\mathrm{f}}_{\mathrm{exp}}$=0.2288, but predicted damage is $D^{\mathrm{f}}_{\mathrm{num}}$=0.1785. This is an underestimation of 22%. Similarly, for $\epsilon_{\max}$=1.12%, $D^{\mathrm{f}}_{\mathrm{exp}}$=0.2833 at 0.999 N_{f}, while $D^{\mathrm{f}}_{\mathrm{num}}$=0.2252 – a difference of 21%. Considering this, it may be advisable, when incorporating this evolution function into larger models of composite structures, to either limit its application to $\leq 0.8N_{\mathrm{f}}$ – which still covers a substantial portion of a load-bearing component's useful damage-tolerant life.

FE [0/90]. For FE [0/90] laminate (Figure 9.5), the predicted curves agree well with the experimental data, and the least correlation appears to be for the lowest and highest loading levels $\epsilon_{\max}$=0.31% and

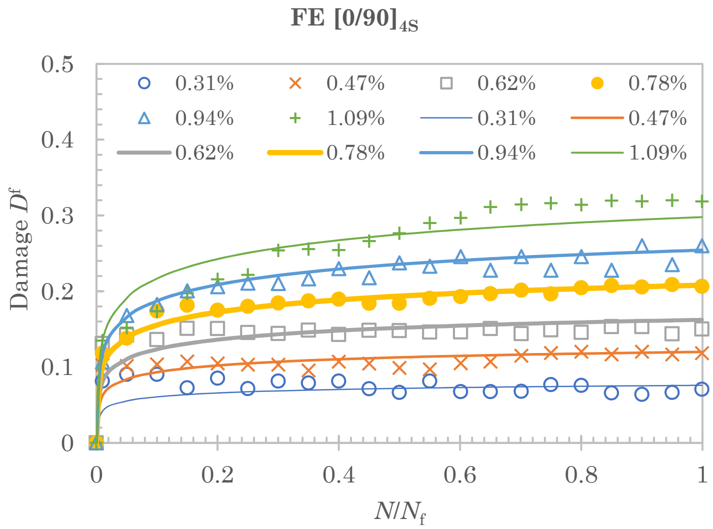

Figure 9.5: Evolution of fatigue damage D^{f} in Flax-epoxy $[0/90]_{\mathrm{nS}}$ laminate under various applied $\epsilon_{\max}$ levels, showing experimentally derived (discrete datapoints) and simulated (continuous line) trends.

$\epsilon_{\max}$=1.09%, respectively – as was also noticed in the case of FE [0]. For $\epsilon_{\max}$=0.31%, early-life predictions (before $0.2N_{\mathrm{f}}$) are underestimated, while for $\epsilon_{\max}$=1.09% they are overestimated. As discussed for the FE [0] case, noise in the original experimental datasets from which mean trends are estimated can account for the fluctuating trends. However, when observed collectively, the experimental datasets are well-captured by the proposed evolution function and identified parameters.

FE [±45]. The predictions for angled-crossply [±45] laminate are very good, as seen in Figure 9.6. The

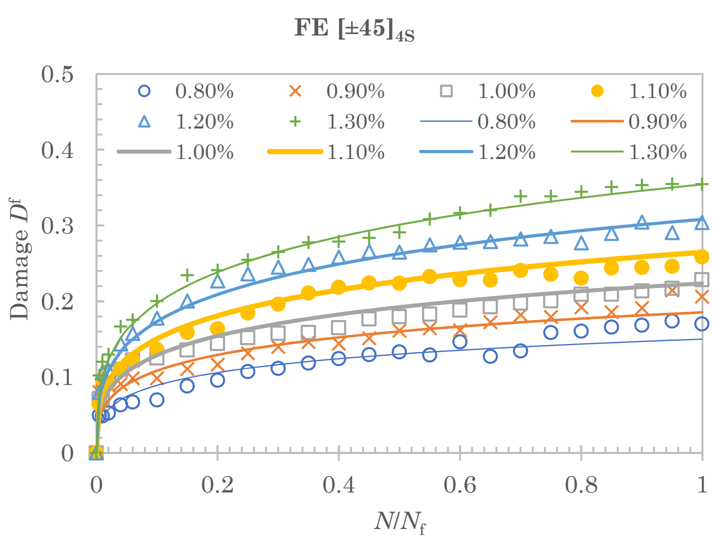

Figure 9.6: Evolution of fatigue damage D^{f} in Flax-epoxy $[\pm 45]_{\mathrm{nS}}$ laminate under various applied $\epsilon_{\max}$ levels, showing experimentally derived (discrete datapoints) and simulated (continuous line) trends.

evolution function is successfully able to vary the damage rates depending on strain loading level, and thereby attain very good agreement during early-life rapid damaging stage.

It can be concluded that the form of the proposed evolution function is suitable to describe the damage progression observed under constant strain-amplitude fatigue cycling of all the Flax-epoxy laminates considered, for most of fatigue life. An observed limitation, however, is that laminates and loading levels that exhibit a rapid increase in damage before just before failure cannot be captured accurately, and may result in up to ∼20% underestimation in predicted damage.

9.4.2 Inelastic strain accumulation

The simulated inelastic strain response is shown superimposed on experimental datapoints for all considered Flax-epoxy laminates in Figures 9.7–9.10.

FE [0]. For [0] specimens, the simulated evolution of inelastic strain shows very good correlation with experimental data, but only for load levels $\epsilon_{\max} \geq 0.54\%$ (Figure 9.7). It is noted that, for loading

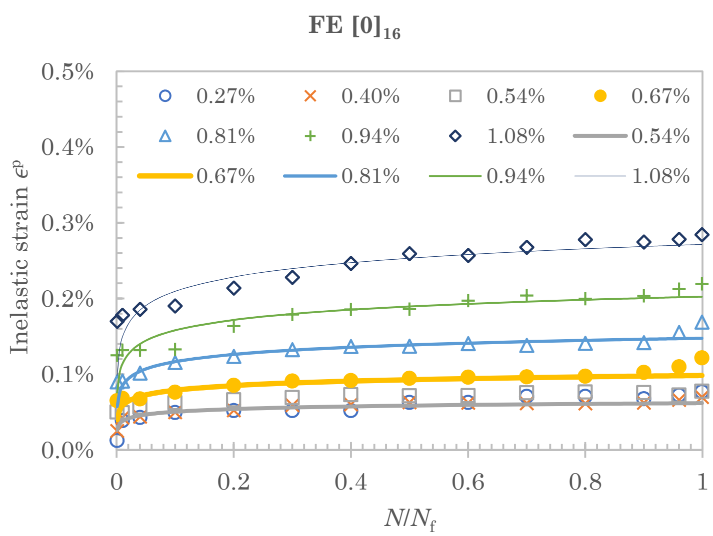

Figure 9.7: Evolution of inelastic strain ϵ^{p} in Flax-epoxy [0] laminate under various applied $\epsilon_{\max}$ levels, showing experimentally derived (discrete datapoints) and simulated (continuous line) trends.

levels below 0.5%, there does not seem to be much difference in experimentally-observed permanent strain between different loading amplitudes – as can be seen in the nearly identical trends trends for $\epsilon_{\max}$=0.4% and 0.27% (also reported in Chapter 8, Figure 8.23(a)). This is interesting, as it suggests that internal mechanisms of permanent deformation in the composite (or in the Flax fibre) are not yet intensively activated under lower peak strains below ∼0.5% (evidence supporting this reasoning was further discussed in preceding chapter section 8.4.5).

So, from the strain-controlled test data available, it appears that the peak cyclic strain of $\epsilon_{\max}$ ≃0.5% is a *threshold*, below which the influence of varying loading amplitude on permanent deformation is undetectable, for FE [0] specimens. To reflect this characteristic, simulated inelastic strains for loading levels *below* the threshold (i.e. for ϵ_{max}=0.27–0.54%) are considered equal to those predicted *for* the threshold ϵ_{max}=0.54%, and this assumption is supported by experimental evidence.

There is some divergence between predicted and experimental data towards the end of fatigue life. Particularly after $0.95N_{\text{f}}$, the experimental data indicates an accelerated rise. This is not captured by the model, resulting in an underestimated prediction of inelastic strain. As an example, for ϵ_{max}=0.67% (largest observed deviation) the prediction at end of life is $\epsilon^{p}_{\text{num}}$=0.0983%, but the experimental observation is $\epsilon^{p}_{\text{exp}}$=0.1217% – a difference of 19%.

FE quasi-isotropic. Inelastic strain data for the quasi-isotropic specimens appear well-captured by the prediction of proposed evolution function (Figure 9.8). Again, a threshold loading level is identified at

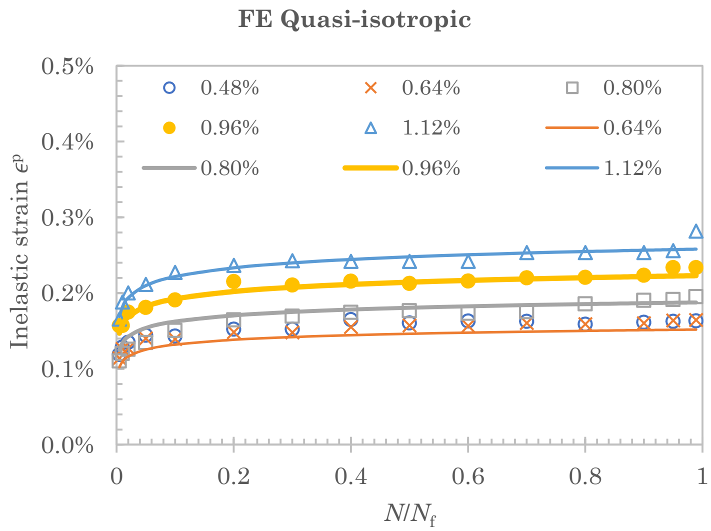

Figure 9.8: Evolution of inelastic strain ϵ^{p} in Flax-epoxy quasi-isotropic $[0/{+45}/90/{-45}]_{\text{nS}}$ laminate under various applied ϵ_{max} levels, showing experimentally derived (discrete datapoints) and simulated (continuous line) trends.

ϵ_{max}=0.64%, below which the experimental data appears identical (compare data for ϵ_{max}=0.64% and 0.48%). As was assumed in the case of FE [0], prediction for loading below the threshold (i.e. for ϵ_{max}=0.48–0.64%) is considered to be the same as that for the threshold ϵ_{max}=0.64%, based on the experimental evidence.

FE [0/90]. Predictions for [0/90] laminate are in good agreement with experimental for most of fatigue life, i.e. up to $\sim 0.9N_{\text{f}}$, after which the prediction is underestimated (Figure 9.9). As in the case of FE [0], the proposed evolution function is unable to capture the rapid rise in accumulation that occurs at end of fatigue life. The discrepancy in prediction appears to increase at higher loading levels. For example, at the loading level of ϵ_{max}=0.62%, predicted inelastic strain at end of life ($0.99N_{\text{f}}$) is $\epsilon^{p}_{\text{num}}$=0.1587%, but the experimental inelastic strain is $\epsilon^{p}_{\text{exp}}$=0.1755%, which is a difference of 9.6%. At the higher ϵ_{max}=1.09%, $\epsilon^{p}_{\text{num}}$=0.3139%, but $\epsilon^{p}_{\text{exp}}$=0.4146% – a difference of 24%. These differences that arise towards the end of life suggest that the application of proposed evolution function should be limited to fatigue duration of up to $\simeq 0.9N_{\text{f}}$.

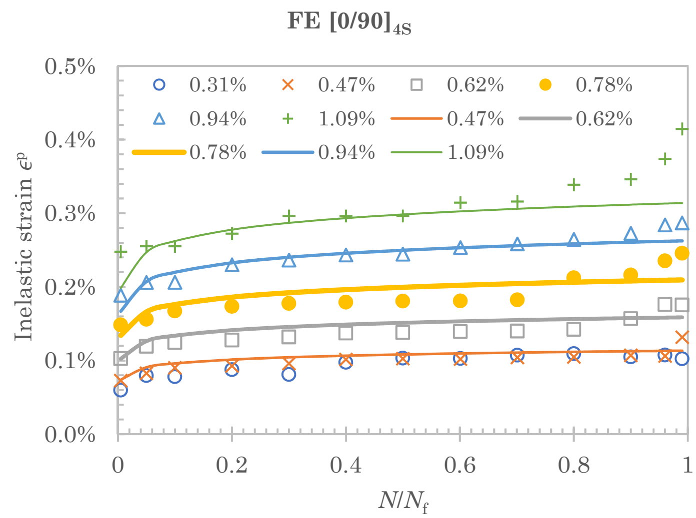

Figure 9.9: Evolution of inelastic strain ϵ^p in Flax-epoxy $[0/90]_{nS}$ laminate under various applied ϵ_{max} levels, showing experimentally derived (discrete datapoints) and simulated (continuous line) trends.

Also, as was observed for the other fibre-dominant laminates ([0] and quasi-isotropic), a threshold loading level is identified at ϵ_{max}=0.47%, since experimental data for this loading appears unchanged from that for ϵ_{max}=0.31%. As such, the simulated trend for ϵ_{max}=0.31% is considered to be the same as for ϵ_{max}=0.47%.

FE [±45]. The predictions for angled-crossply [±45] are in very good agreement with experimental data, as can be seen from Figure 9.10. The proposed evolution function is able to successfully capture the high

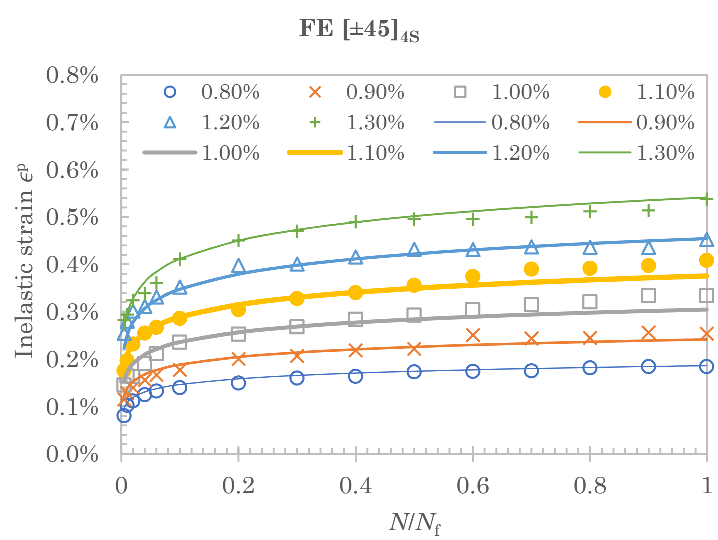

Figure 9.10: Evolution of inelastic strain ϵ^p in Flax-epoxy $[\pm 45]_{nS}$ laminate under various applied ϵ_{max} levels, showing experimentally derived (discrete datapoints) and simulated (continuous line) trends.

accumulation rates during early fatigue life for the different loading levels, and follows through with steadily reducing-rate predictions for the rest of fatigue life, as required. This indicates that the proposed function and identified parameters are representative of [±45] laminate behaviour under constant strain-amplitude fatigue.

9.4.3 Stress at failure

As was seen in the preceding sections, the proposed evolution function (9.1) is sometimes unable to capture latter-lifedamage and permanent strain in the considered NFCs (i.e. after 0.8–0.9N_f). This limitation appears most pronounced in laminates where response is fibre-dominant, namely $[0]_\mathrm{nS}$, $[0/90]_\mathrm{nS}$, and quasi-isotropic $[0/45/90/-45]_\mathrm{nS}$, where inelastic strain and sometimes damage may be underestimated. As such, it is possible for a discrepancy in predicted damage state after $0.9N_\mathrm{f}$ to be doubly-compounded, if both stiffness damage and inelastic strain are underestimated.

As a validation check for the predictive potential of the proposed evolution model, and to study the implications of a possible double-underestimation on the simulated response of these laminates, the cyclic *peak stress* at any given stage of fatigue life can be calculated from damage and inelastic strain predictions, and compared with reported peak stress observed experimentally.

The peak stress σ_max may be derived from (8.1), where fatigue damage D^f is defined in terms secant modulus of fatigue cycle E^f normalised by initial undamaged static modulus E_0:

$$D^\mathrm{f} = 1 - \frac{E^\mathrm{f}}{E_0} \tag{9.7}$$

But, from the definition of E^f in Figure 8.4:

$$E^\mathrm{f} = \frac{\sigma_\mathrm{max}}{\epsilon^e} \tag{9.8}$$

where ϵ^e is the elastic portion of peak cycle strain ϵ_max, related to inelastic strain ϵ^p by

$$\epsilon^e = \epsilon_\mathrm{max} - \epsilon^p \tag{9.9}$$

So, D^f may be expressed as:

$$D^\mathrm{f} = 1 - \frac{\sigma_\mathrm{max}}{E_0\left(\epsilon_\mathrm{max} - \epsilon^p\right)} \tag{9.10}$$

Therefore, in terms of peak stress:

$$\sigma_\mathrm{max} = E_0\left(1 - D^\mathrm{f}\right)\left(\epsilon_\mathrm{max} - \epsilon^p\right) \tag{9.11}$$

As it was observed the the maximum discrepancy between simulated and experimental trends occur just before failure, a comparison of calculated peak stress at failure (e.g. at $0.99N_\mathrm{f}$) with the experimentally observed stress should further demonstrate the extent of discrepancy in computed material response. This is done and the results are shown in Table 9.3.

It can be seen from Table 9.3 that, for all cases considered, the mean error in predicted peak stress at $0.99N_\mathrm{f}$ is ∼10%. The highest magnitude of discrepancy is 30%, which occurs for [0/90] at its lowest loading level ϵ_max=0.31%. The least discrepancy is 1%, for [±45] at ϵ_max=1.0%. It appears that predictions for

Table 9.3: Comparison of predicted and experimental peak stress $\sigma_{\max}$ at end of fatigue life ($0.999N_\mathrm{f}$) for Flax-epoxy laminates

Laminate	E_0 [a] (MPa)	$\epsilon_{\max}$ (%)	$D^\mathrm{f}_\mathrm{num}$	ϵ^P_num (%)	$\sigma_{\max,\mathrm{num}}$ [b] (MPa)	$\sigma_{\max,\exp}$ [c] (MPa)	Discrepancy [d]
$[0]_{16}$	30,000	0.27	0.0411	0.0618	73.76	56.68	6%
		0.40	0.0690	0.0618	102.73	78.96	20%
		0.54	0.1021	0.0618	128.82	113.59	13%
		0.67	0.1353	0.0983	148.31	135.80	9%
		0.81	0.1731	0.1475	164.36	156.37	5%
		0.94	0.2098	0.2023	174.87	190.90	-8%
		1.08	0.2509	0.2713	181.73	209.68	-13%
$[0/90]_{4\mathrm{S}}$	16,700	0.31	0.0759	0.1134	30.34	43.31	-30%
		0.47	0.1200	0.1134	52.41	53.42	-2%
		0.62	0.1623	0.1587	64.54	67.52	-4%
		0.78	0.2080	0.2095	75.46	72.74	4%
		0.94	0.2542	0.2625	84.38	88.20	-4%
		1.09	0.2978	0.3139	91.02	95.92	-5%
QIso [e]	13,100	0.48	0.0623	0.1519	40.30	53.77	-25%
		0.64	0.0966	0.1519	57.76	61.11	-5%
		0.80	0.1355	0.1877	69.34	63.58	9%
		0.96	0.1785	0.2230	79.31	66.97	18%
		1.12	0.2252	0.2580	87.50	83.00	5%
$[\pm45]_{4\mathrm{S}}$	6,400	0.80	0.1501	0.1860	33.40	27.55	21%
		0.90	0.1854	0.2413	34.34	32.36	6%
		1.00	0.2236	0.3044	34.56	34.35	1%
		1.10	0.2645	0.3753	34.11	34.78	-2%
		1.20	0.3081	0.4541	33.03	37.22	-11%
		1.30	0.3541	0.5409	31.38	39.21	-20%

[a] Nominal values, based on experimental data (see Chapter 5)
[b] Calculated per (9.11)
[c] Note, this is the mean value of three or more fatigue tests, reported in Chapter 8.
[d] Calculated with respect to experimental peak stress: $\frac{\sigma_\mathrm{num}-\sigma_\mathrm{exp}}{\sigma_\mathrm{exp}}$
[e] Quasi-isotropic laminate $[0/+45/90/-45]_{2\mathrm{S}}$

the lowest levels of strain amplitude cycling tend to be the most discrepant. It must be stressed that the experimental data considered in this exercise is the *mean* of three or more fatigue tests. The standard deviations from the original data have not been factored here in this non-statistical validation exercise.

Considering the above, it can be concluded that the single evolution function (9.1), proposed for both progressive damage and for inelasticity, is a good analytical model for replicating experimental observations of Flax-epoxy laminates under constant strain-amplitude fatigue.

9.5 Further discussion

The approach proposed here combines a macroscale analytical function with empirically determined strain-life relationship to model progressive material degradation and failure in Flax-epoxy laminates under uniaxial constant strain-amplitude fatigue. The approach is, therefore, phenomenological, per classification in [232]. Stiffness degradation (or, *residual stiffness*) and permanent deformation are chosen as indicators of the fatigue damage state, following the findings of earlier quasi-static studies (Chapter 5) that indicated that stiffness loss in NFCs may not necessarily be correlated with permanent strain. In formulating a semi-empirical means in terms of relevant damage variables to capture overall composite damage response, it is similar in approach to many existing phenomenological techniques proposed for stress-controlled fatigue [232; 234]. Typically, models based on *residual stiffness* are advantageous because modulus can be measured by non-destructive methods, unlike for *residual strength* techniques. Furthermore strength-based methods may be unsuitable for NFC materials, since 'post-fatigue' strength studies by Bensadoun et al. [109; 110] found no detectable loss of strength in many Flax-epoxy laminate architectures (including short-fibre and twill-fabric reinforced) even after 500,000 tension-tension cycles at 0.3UTS.

Observing that most existing laminate-scale models were developed for stress-controlled fatigue [232; 234], incorporating stress-specific parameters, the proposed evolution function (9.1) is constructed as a function of applied cyclic *peak strain* and fatigue cycles. A convenient feature of this is that a single function is able to well-emulate both stiffness damage and inelastic strain evolution trends at all tested loading levels. The model has been shown to successfully reproduce the behaviour of four common laminates layups, including off-axis [±45] configuration, so it appears robust. Given sufficient experimental data, the model parameters can be determined by heuristic methods. Though the evolution function was developed to capture overall laminate response, it may be incorporated at the ply scale in (mesoscale or quasi-mesoscale) as part of a larger model framework for a composite structure, as was done by Kennedy et al. [242].

An obvious limitation of the proposed macroscale approach is that it is not based on individual damage mechanisms, and therefore cannot track different damage modes at the constituent- or ply-level. The parameters identified for each laminate in this study are, so far, unique to each laminate and its loading conditions (5 Hz, tension-tension R_ϵ=0.1), so fresh experimental data is required for other configurations to determine the nature of their progressive response and fatigue life. Nevertheless, the proposed evolution function serves as an expedient, computationally inexpensive, and flexible means to approximate laminate stiffness loss and permanent strain under strain-controlled fatigue, supported by extensive experimental data.

9.5.1 Future work

To the best of the author's knowledge, this is one of the first attempts to offer, and demonstrate application of, a numerical relationship for the progression of fatigue damage in natural fibre composites. There is much scope for expanding the capabilities of the model, including:

- So far, fatigue data from FE [0] tests allowed derivation of fibre-direction stiffness degradation and inelasticity, and similarly FE $[\pm45]_{\mathrm{nS}}$ tests can enable the derivation of shear-related stiffness loss and inelasticity. In order to upgrade the proposed macroscale approach to a mesoscale model wherein the damage behaviour can be further clarified in all orthotropic components, fatigue testing of FE [90] specimens should be conducted, so that fatigue damage and inelasticity can be quantified in 'transverse', or perpendicular to fibre, direction. This may allow the use of proposed evolution function for a multi-orientation laminate.

- As a control study, and to further expand to a constituent-level model, *neat epoxy* specimens can be fatigue tested under the same strain-amplitude control conditions. This should provide a baseline against which origins of damaging behaviour in composites can be studied, as was done for static-condition loading in Chapter 5. Insight from a comparative fatigue study of internal damage in neat epoxy and its composites can justify further discretisation of damage variables into components representing fibre, matrix, and interface degradation.

- The proposed evolution equation (9.3) is formulated in terms of peak cyclic strain $\epsilon_{\max}$, and the parameters identified are specific to tension-tension fatigue cycling at load ratio R_ϵ=0.1. It is possible to rearrange the function in terms of strain loading ratio $R_\epsilon = \frac{\epsilon_{\min}}{\epsilon_{\max}}$. This allows evaluating the proposed function for fatigue under different load ratios, including tension-compression and compression-compression. It is expected that the shape of evolution trends under different loading ratios will be similar to that of R_ϵ=0.1 modelled in this study, so the evolution function as proposed should remain applicable, given new parameters are identified.

9.6 Conclusion

Several recent independent studies on cellulosic plant fibre NFCs had shown that, under stress-controlled fatigue, the composite stiffness along fibre-direction appears to *increase*, up to 8-12%, and never dropping below original undamaged stiffness even while accumulating significant permanent strain and observable cracking damage [25; 50; 103; 109; 110]. It was argued in Chapters 7–8, based on contradictory evidence, that this stiffening is unlikely to be a fundamental material property, but instead is a consequence of stress-based testing parameters. As such, existing stress-controlled data may be unsuitable to develop stiffness-based fatigue damage models for NFCs, so original strain-controlled test data – which show no evidence of stiffening – are utilised in this study to develop a predictive fatigue model. An analytical approach is proposed to model NFC laminate damaging behaviour under constant strain-amplitude fatigue, based on uniaxial experimental observations reported in Chapter 8. The approach combines a growth function to model progressive material degradation, with empirically determined strain-life relationship to predict failure, in Flax-epoxy laminates. Laminate level behaviour is simulated for four commonly-studied configurations: unidirectional [0], quasi-isotropic $[0/45/90/-45]_{\mathrm{nS}}$, and cross-plies $[0/90]_{\mathrm{nS}}$ and $[\pm45]_{\mathrm{nS}}$. Laminate stiffness and permanent strain are chosen as damage indicators to be modelled. A single evolution function is proposed, in terms of cyclic peak strain and fatigue longevity, to simulate both the evolution of stiffness degradation and of accumulating inelastic strain. As such, the modelling approach is phenomenological. It was observed from Chapter 8 that, under constant strain-amplitude fatigue, mechanical properties like stiffness, cyclic peak stress, and inelastic strain may reach a constant value well before failure – so they are unsuitable as indicators of imminent failure, i.e. as failure criteria. Therefore, laminate failure is not predicted by applying criteria based on material properties, but from the strain-life (ϵ–N) relationships determined from fatigue tests. Model parameters were identified for the four laminate stacking sequences studied. The predicted evolution is found to well-capture the experimental trends for stiffness damage and inelastic accumulation at all tested load levels, for all considered Flax-epoxy laminates.

Chapter 10

In conclusion

The work compiled in this dissertation is a result of recognising the limited mechanical data and behaviour-prediction tools available for natural fibre composites (NFCs) like Flax-reinforced composites, under both static and cyclic fatigue conditions.

10.1 Research contributions

Static response, mechanical. Tensile, compressive, and shear in-plane orthotropic mechanical properties (modulus, strength, failure strain, Poisson's ratio, nonlinear loading response) of Flax-epoxy under monotonic/quasi-static conditions are extensively tested (based on response of UD [0], transverse-UD [90], and angled-crossply $[\pm 45]_{\mathrm{nS}}$ specimens) and reported. Laminate properties of several 'standard' symmetrical stacking sequences (off-axis-UD [45], crossply $[0/90]_{\mathrm{nS}}$, and quasi-isotropic $[0/45/90/{-45}]_{\mathrm{nS}}$) are also tested and reported. The tensile moduli and strength properties are found to be within the reported range in other publications, indicating that the composites fabricated for the present studies are well-representative of Flax-epoxy behaviour. Flax fibre modulus and strength are back-estimated from composite properties, and also found to be within range of published reports. These mechanical data serve to corroborate available information and/or augment them with new data on Flax-composites (compression, shear, off-axis, Poisson's ratios), thereby increasing confidence in reported material properties and enabling meaningful preliminary design and prototyping using Flax-laminates.

Static response, progressive damage. The effect of internal damage on mechanical degradation is investigated by following the changes in material stiffness and permanent deformation, and by SEM observation of internal microstructure post-loading. Damage is defined in terms of relative loss of stiffness along orthotropic coordinates, and the inelastic component of total strain is a measure of accumulating permanent deformation. The evolution of damage and inelastic strain until specimen failure is measured and charted along fibre-direction, perpendicular to fibre-direction, and in-plane shear, under tensile and compressive loading. All evolutions are found to be nonlinear, and stiffness loss mechanisms appear not necessarily associated with those of inelastic accumulation. Constituent-level damage mechanisms are identified by specimen micrography after successive loading stages before failure, after failure. The SEM observations are correlated with measured stiffness and inelastic strain evolution. The findings provide insight on material degradation, and its effect on orthotropic properties of Flax-epoxy composite. The well-quantified *damage indicators* allow prediction of their initiation and progression trends, and their contribution to specimen failure, which serves to enable the sophisticated design of damage-tolerant NFC structures.

Static response model. A mesoscale model of static-condition NFC response is developed based on the damage and inelastic strain evolutions identified for Flax-epoxy composites. The thermodynamically-consistent ply-scale damage mechanics model is able to capture interim stiffness damage and accumulated permanent deformation, thereby allowing prediction of complex loading/unloading paths to eventual failure. Appropriately chosen state variables and thermodynamic potentials allow for the development of damage-coupled elastic and inelastic evolution laws, which are then incorporated in the constitutive law for orthotropic ply response. For a multi-ply laminate, simulated response for individual plies can be homogenised to predict global response. Model parameters are specifically identified for Flax-epoxy composite. Considering that existing damage mechanics models based on synthetic fibre (Carbon, Glass, etc.) behaviour tend to ignore fibre-direction progressive damage and inelasticity, and are therefore unsuitable for NFC laminates, the proposed mesomodel offers a well-validated, robust means of numerically replicating the highly-nonlinear NFC behaviour in all in-plane orthotropic directions.

Fatigue response, stress-amplitude controlled. As fatigue is an important failure mode in high-performance engineering composites, research of NFC response under cyclic loading is essential to encourage confidence in their mechanical durability and dynamic capabilities. Studies to date on NFC fatigue are limited, compared to those for Carbon or Glass fibre composites. Existing studies are all recent, and all test NFCs by *constant stress-amplitude* cycling. There is considerable variation in the reported fibre architectures (UD, crossply, woven twill-fabric, short-fibre, etc.), fibre content, and fatigue testing parameters (loading frequency/rate, stress ratio, etc.). So, in order to establish current state-of-the-art on NFC fatigue, a holistic review and analysis of these disparate studies is conducted. Stress-life (S-N) data on different NFCs are analysed and found to be well-modelled by linearised, 2-parameter, stress/log-life relationships. *Specific* stress-life (i.e. density normalised) is proposed to be a fairer measure of comparing fatigue endurance between different NFCs that minimises the influence of fibre content. Compiled evidence suggests that Flax, Jute, and Sisal fibre reinforcement offer comparable fatigue resistance. Several laminate configurations reinforced by natural fibres are found to exceed, or be similar to, Glass-reinforced laminates in fatigue endurance. Progressive fatigue damage is reviewed by examining reports of residual strain and stiffness. Contradictory reports of stiffness evolution is found for NFCs where behaviour is governed by fibre properties, wherein fibre-direction modulus is seen to increase or decrease over fatigue life depending on test parameters. This 'review and analysis' study finds that while available fatigue life data is fairly substantial (so cycles-to-failure can be statistically modelled), existing knowledge of damage initiation and progression is deficient or ambiguous, therefore inadequate for engineering design consideration.

Fatigue response, strain-amplitude controlled. To remedy the identified limitations of, and uncertainties in, available NFC fatigue reports, original *constant strain-amplitude* tests are conducted. Previous

NFC studies showed that increasing strain-rate results in a stiffer, stronger response. Strain-amplitude control eliminates variation in strain-rate, therefore limit any influence of loading rate on measured longevity or progressive damage. Four commonly-studied laminate configurations were tested for Flax-epoxy (FE): unidirectional [0], crossply $[0/90]_{\mathrm{nS}}$, angled-crossply $[\pm 45]_{\mathrm{nS}}$, and quasi-isotropic $[0/45/90/-45]_{\mathrm{nS}}$. In addition, Glass-epoxy (GE) $[0/90]_{\mathrm{nS}}$ and $[\pm 45]_{\mathrm{nS}}$ were also tested to enable a comparative investigation. Longevity of Flax-reinforced [0/90] and [±45] specimens are observed to exceed equivalent Glass-reinforced specimens. No fatigue-stiffening behaviour is observed in [0] or [0/90] Flax-epoxy specimens, contradicting reports from published stress-controlled fatigue studies. Fatigue lives for all laminates are found to follow a predictable trend, modelled by a linearised strain-life (ϵ–N) relationship. Physical cracking damage is observed by destructive SEM micrography, and the mechanisms are found to be similar to those identified for quasi-static loading. Evolutions of stiffness damage, inelastic strain, hysteresis energy, and surface temperature are measured over fatigue life, and discussed in relation to observed damage mechanisms. At any given loading level, Glass-laminates consistently suffer more stiffness loss than Flax-laminates. On account of superior stiffness damage resistance, lower inelastic strains and damage-related energy dissipation in off-axis configurations, and higher specific stress transfer in FE specimens, Flax is indeed an alternative to Glass for fatigue-tolerant engineering structures. In keeping strain-amplitude constant, this study offers clarity on reported NFC stiffening phenomena, and produces evolution data better suited for progressive damage modelling.

Fatigue response model. As existing models of fatigue life and progressive fatigue damage are formulated in terms of stress-controlled parameters, a strain-based approach is proposed specifically for strain-controlled fatigue response of NFCs. Stiffness-degradation and permanent strain are chosen as indicators of progressive damage. An analytical 4-parameter growth function is proposed that can capture macroscale (laminate-level) evolution as a function of peak cyclic strain and fatigue cycle count. As all externally-observable damage-indicating properties are seen to reach constant values well before failure, material properties do not appear to be reliable as failure criteria under strain-controlled fatigue – so laminate failure is predicted by applying strain-life (ϵ–N) relationships. A single evolution function is found to well-represent damage and inelastic strain progression. Model parameters are identified for the tested Flax-epoxy laminates ([0], $[0/90]_{\mathrm{nS}}$, $[\pm 45]_{\mathrm{nS}}$, and $[0/45/90/-45]_{\mathrm{nS}}$). The predictions of proposed evolution function show good agreement with experimental data, by closely emulating the different evolution rates at different strain loading levels. The proposed approach offers a convenient, computationally-inexpensive, phenomenological method to replicate macroscale fatigue response.

10.2 Future work

The primary motivation all research in this dissertation was to encourage the replacement of Glass-composites by those reinforced by natural fibres like Flax. To that end, the opportunities for further research are numerous, especially considering that natural fibre composites are still a relatively new competitor for traditional synthetic fibre composites. Possible future work for each sub-objective covered in this dissertation has been discussed in the respective chapters:

- Scope for quasi-static progressive damage model expansion was discussed in Section 6.5.

- The limitations of existing knowledge of NFC fatigue, which are opportunities for future investigation, were discussed in Section 7.5. In addition, continued stress-controlled studies may be advisable for compression-compression, and bending fatigue loading.
- Further research on strain-amplitude controlled fatigue performance was discussed in Section 8.5.1.
- Improvements to the proposed progressive fatigue damage modelling approach were discussed in Section 9.5.1.

Furthermore, using the experimental data and modelling techniques proposed in this work, future research can involve studying the mechanical feasibility of Flax-composites in targeted structural applications where Glass-composites are typically employed, e.g. in secondary structure of aircraft, piping, construction materials, or load-bearing application where a high strength-to-weight ratio is desirable, e.g. sporting equipment, protective gear, prosthetic implants, fracture stabilising plates, etc.

10.3 Concluding remarks

The combined contribution of this dissertation provides much-needed original data on the damaged-condition mechanical behaviour of Flax-epoxy and other NFCs under a variety of loading conditions, clarifies contradictory aspects of critical NFC behaviour, and proposes numerical methods to replicate observed progressive damage and failure in NFCs. In so doing, the work is a humble advancement in the pursuit of establishing renewable, non-toxic, environmentally sustainable natural fibre alternatives for high-performance structural engineering applications.

Appendix A

A.1 Acoustic emission (AE) measurement of fatigue damage

Acoustic emission measurement of fatigue damage events related to matrix, fibre, and interface in Hemp-epoxy [0/90] and [±45] laminates are shown in Figure A.1 [116].

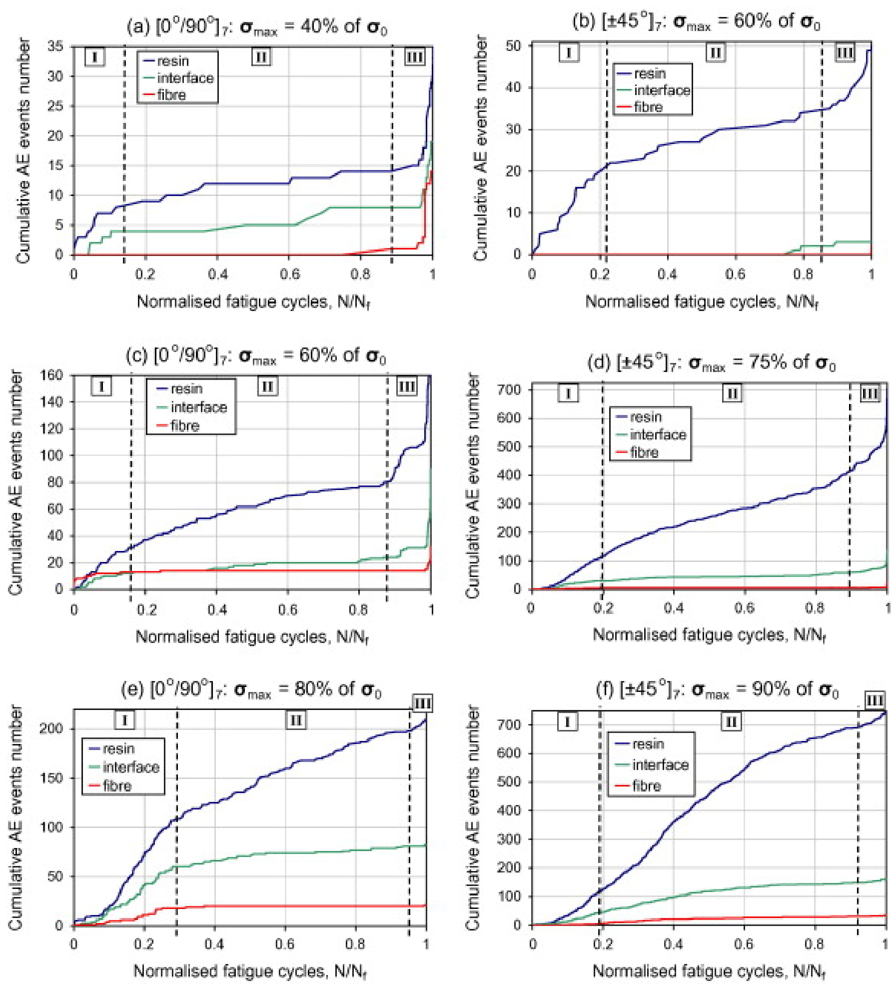

Figure A.1: Cumulative trends of acoustic emission (AE) events, recorded for two Hemp-epoxy laminates (*left* [0/90], *right* [±45]) fatigued at different stress amplitudes, and sorted according to source fibre, matrix, or interface cracking. Reproduced with permission from [116].

A.2 Structural reorganisation in elementary fibres under tension

The sequence of shear-induced crystallisation, stick-slip sliding, and eventual permanent microfibril reorientation is shown schematically in Figure A.2, and summarily tabulated in Table A.1.

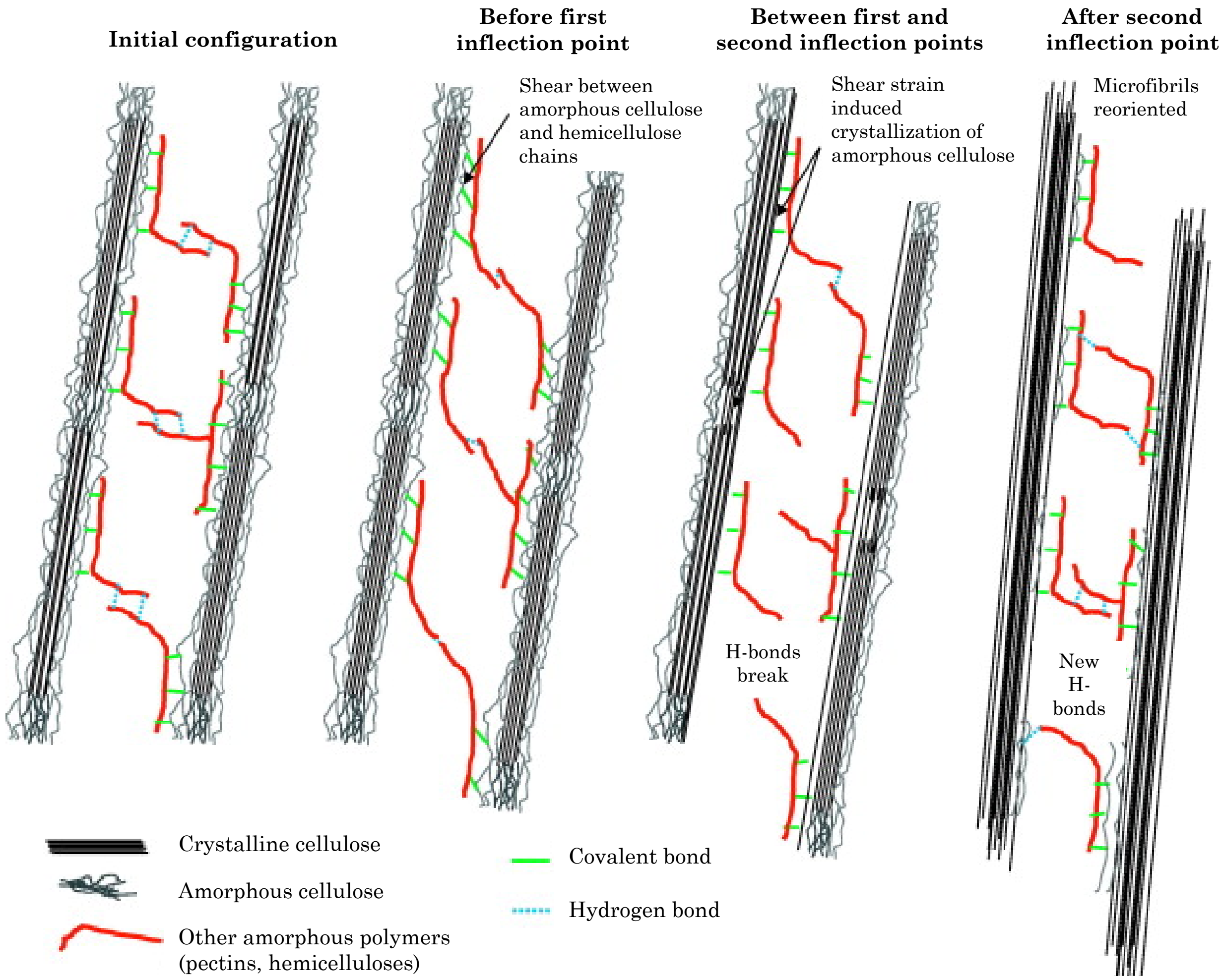

Figure A.2: Schematic showing sequence of reorganisation amongst constituent polymers of elementary fibres under tensile loading, with reference to nonlinear monotonic response shown in Figure 2.23. Adapted and reproduced with permission from [65].

Table A.1: Sequence of damage mechanisms expected in elementary Flax fibre under tensile deformation with reference to nonlinear monotonic response shown in Figure 2.23, based on Hemp fibre study [65].

Stress-strain response curve	Observed mechanical response	Proposed damage events and mechanisms
Before 1st inflection point	1st linear segment with near-constant tangent modulus	Elastic deformation of microfibrils and amorphous matrix
	Unchanging, or some increase in, secant modulus of hysteresis loop	Shear forces between microfibrils and surrounding matrix
	Some permanent strain	Possibly some reorientation and reduction in MFA
At 1st inflection point	Decrease in tangent modulus after ~0.5% strain ('yield' point)	Matrix shear flow threshold reached, bonds within amorphous polymer chains break, viscous flow initiates
Between 1st and 2nd inflection points	2nd linear segment with decreased tangent modulus	Vicous flow of amorphous polymers continues, 'stick-slip' mechanisms underway
	Increasing secant modulus	Strain-induced crystallisation (rearrangement into straight chains) of previously amorphous cellulose
	Significantly increased permanent strain	Spiral spring-like extension of helical microfibrils
		Continued reorientation of microfibrils towards loading axis, reduction in MFA
At 2nd inflection point	Increase in tangent modulus after ~1.4% strain	Maximum flow point of amorphous matrix reached
	Bulging defect locations become less visible	Saturation point of crystallisation for amorphous cellulose
		Locally 'micro-compressed' kink band regions are fully extended
After 2nd inflection point	3rd linear segment (possibly even somewhat parabolic) with increased tangent modulus	Microfibrils actively sliding and reorienting, or almost taut along loading axis; MFA approaching minimum
	Increasing secant modulus	Microfibrils and crystalline cellulose separate from amorphous matrix
	Increasing permanent strain	Cracks initiate in outer primary cell wall, probably localised around defect locations
Failure	Loss of load-carrying capacity	Microfibrils fracture
	Defect locations on microfibril are evidently preferred crack-propagation routes	All other cell walls also tear, catastropic fibre fracture

A.3 Mechanical testing setup

Figure A.3: Mechanical test frame and IR camera setup.

A.4 Quasi-static response, progressive loading

Epoxy specimens accumulate the least amount of permanent deformation of all specimens under the same loading mode, even though their failure strain is considerably higher, as shown in the tensile example in Figure A.4.

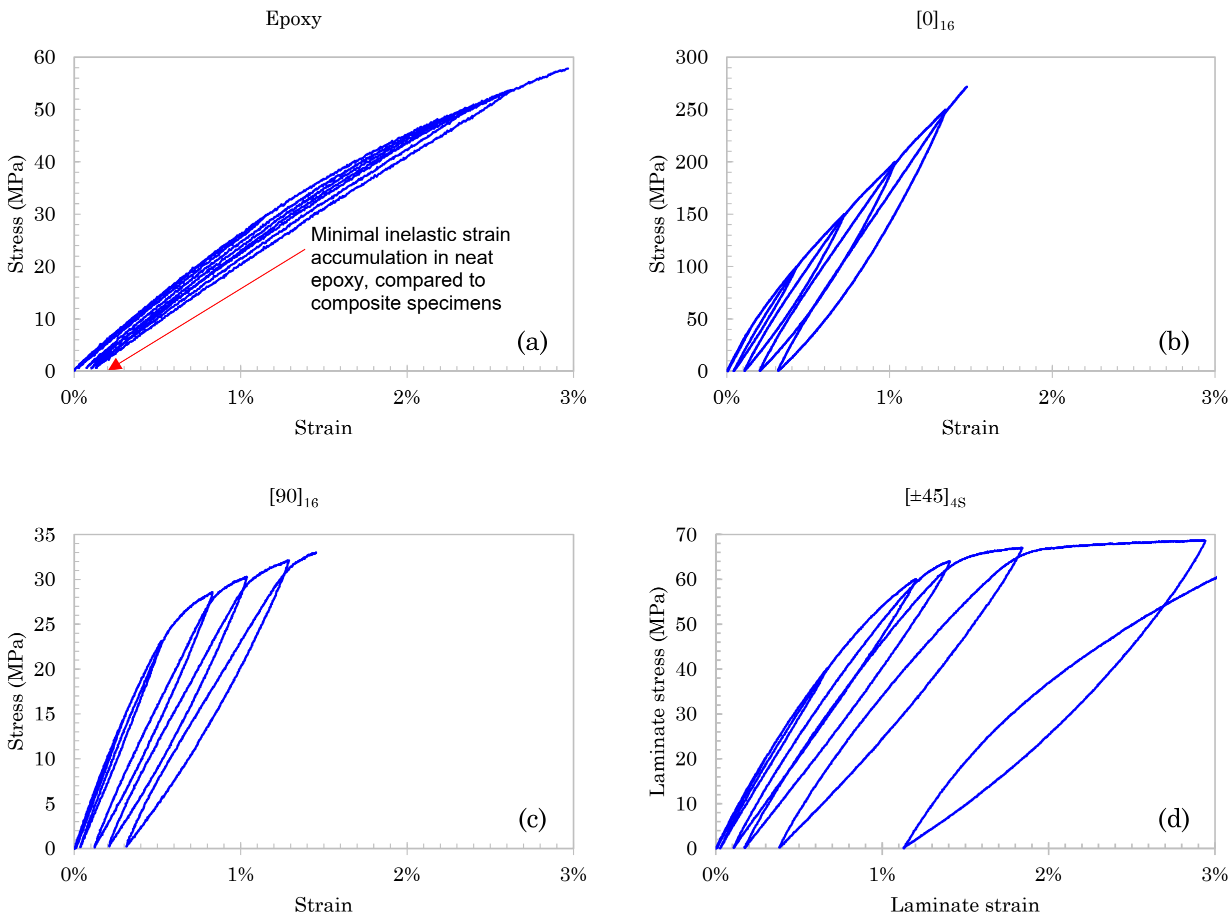

Figure A.4: Tensile load-unload response plots showing neat epoxy accumulates the least residual strain, though has a higher failure strain than [0] or [90].

The damage and inelastic strain accumulation behaviour for neat epoxy and Flax-epoxy composite (along the in-plane orthotropic directions) are summarised in Table A.2.

Table A.2: Summary of Flax-epoxy in-plane stiffness and inelasticity evolution behaviour (T = tension, C = compression, FE = UD Flax-epoxy ply)

		Stiffness evolution			Permanent strain accumulation		
	Type	Initiation strain	Progression, damage rate	Damage D at failure	Initiation strain	Progression, accumulation rate	Permanent strain ε^p at failure
Neat epoxy	T	0.3%	Continuous, constant degradation proportional to applied strain	0.413	0.63%	Continuously increasing rate	0.29%
	C	0.3%	Continuously increasing degradation rate	0.319	0.47%	Continuous, constant accumulation proportional to applied strain	0.15%
FE *11*[a]	T	0	Sigmoidal profile. Initial rate slow up to 0.3% strain, followed by rapid degradation until 0.9% strain. No further degradation until failure.	0.183	0	Continuously increasing rate	0.40%
	C	0.09%	Continuous degradation; logarithmic profile. Initial rate rapid up to 0.6% strain	0.378	0	Continuously increasing rate	0.60%
FE *22*[b]	T	0.2%	Continuous, constant degradation proportional to applied strain	0.465	0.3%	Continuously increasing rate	0.44%
	C	0	Continuous, constant degradation proportional to applied strain	0.493	0	Continuous, constant accumulation proportional to applied strain	0.31%
FE *12*[c]		$\gamma_{12} = 0.4\%$ ($\varepsilon_L = 0.25\%$)[d]	Continuous degradation; logarithmic profile. Initial rate rapid, significant reduction after 3% shear strain	0.631	0	Continuously increasing rate	$\gamma_{12}^p = 1.32\%$ at $\gamma_{12} = 5\%$; and $\gamma_{12}^p = 5.4\%$ at $\gamma_{12} = 10\%$[e]

[a] fibre-direction
[b] in-plane transverse
[c] in-plane shear
[d] γ_{12} is shear strain, ε_L is the corresponding [±45] laminate axial strain
[e] γ_{12} is shear strain, γ_{12}^p is inelastic component of shear strain

A.5 Fatigue response, constant stress-amplitude

Chapter 7 discussed the density-normalised *specific* stress-life plots for NFCs under stress-amplitude controlled fatigue. The corresponding S–N plots (not normalised) for several laminate architectures are given here for reference.

The fatigue life data for Flax-epoxy (FE) short-fibre and quasi-isotropic laminates are presented in Figure A.5. This corresponds to the density-normalised specific fatigue life given earlier in Figure 7.3.

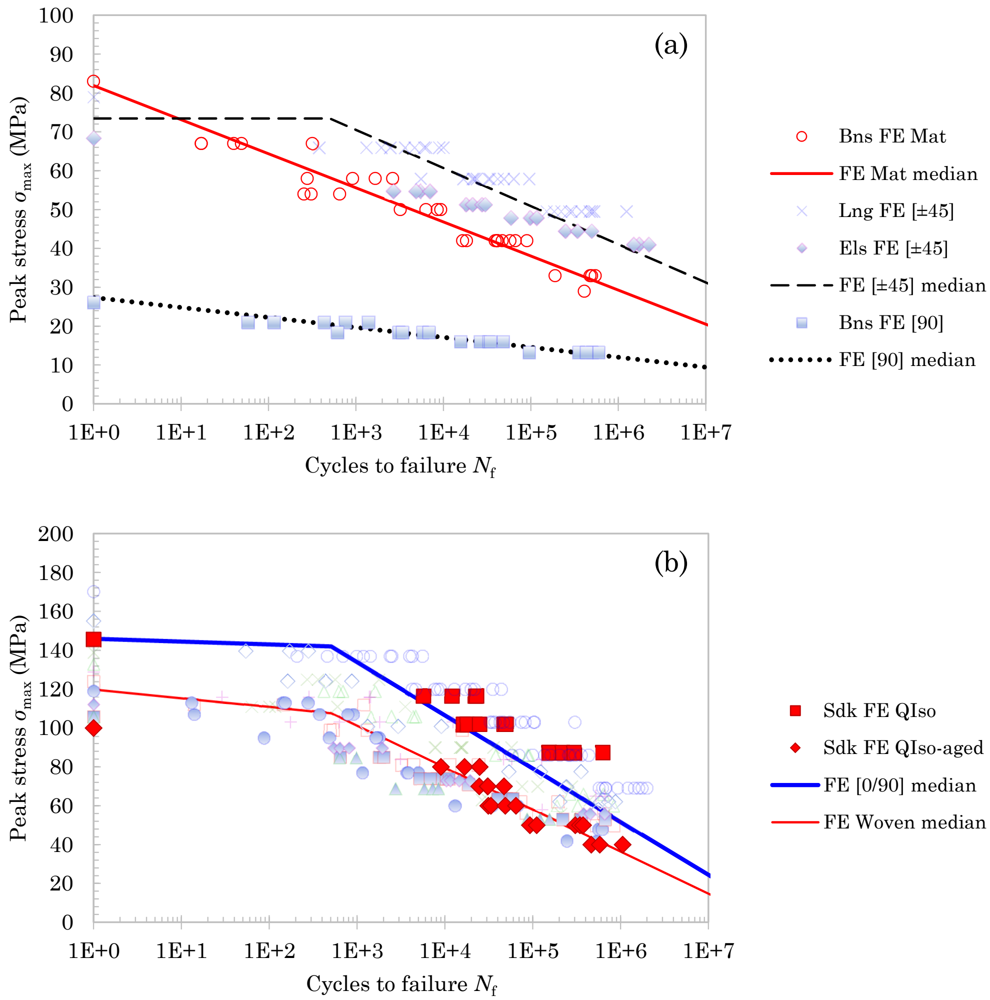

Figure A.5: Reported fatigue life data for: (a) Short-fibre random mat FE laminate, superimposed on data for FE [±45] laminates; and (b) Quasi-istotropic FE laminate $[0_2/90_2/\pm45]_S$, superimposed on data for biaxial FE laminates. Data adapted from Sodoke et al. [112] (Sdk), Liang et al. [25; 50] (Lng), El Sawi et al. [103] (Els), and Bensadoun et al. [109; 110] (Bns).

The fatigue life plots for unidirectional [0] FE laminates are presented in Figure A.5. This corresponds to the density-normalised specific fatigue life given earlier in Figure 7.2.

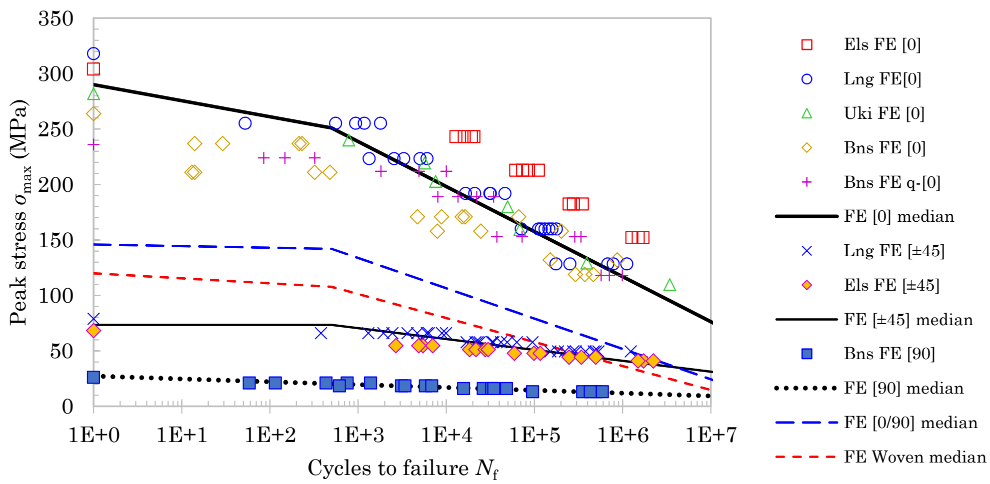

Figure A.6: Reported fatigue life data for Flax-epoxy (FE) [0], $[\pm45]_{nS}$, and [90] laminates. Data adapted from from El Sawi et al. [103] (Els), Liang et al. [25; 50] (Lng), Ueki et al. [106] (Uki), Bensadoun et al. [109; 110] (Bns), and Asgarinia et al. [108] (Asg).

The fatigue life data for short-fibre and angled-crossply [±45] laminates of Flax-epoxy and Glass-epoxy (GE) are presented in Figure A.7. This corresponds to the density-normalised specific fatigue life given earlier in Figure 7.5.

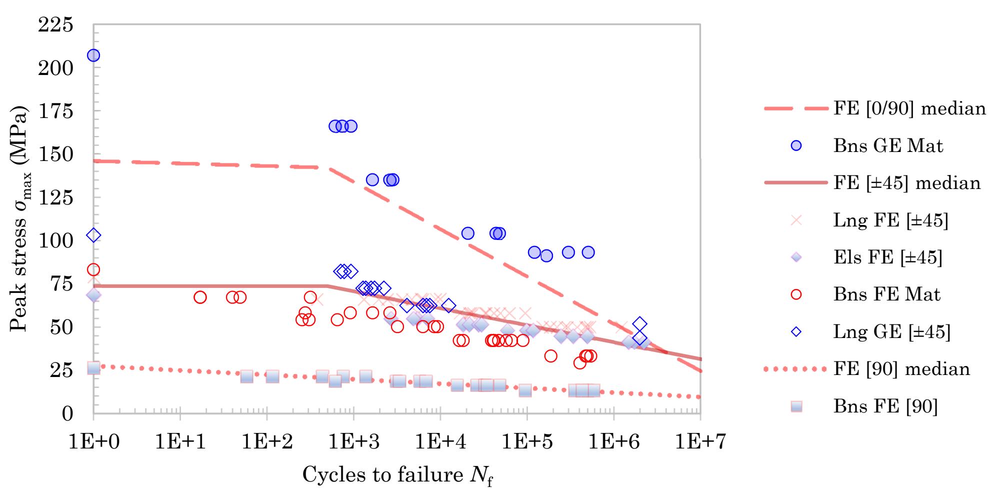

Figure A.7: Comparison of reported fatigue lives for $[\pm45]_{nS}$ and short-fibre-mat Flax-epoxy (FE) and Glass-epoxy (GE) laminates. For clarity, only median trendlines for FE are shown. GE data adapted from Liang et al. [25; 50] (Lng and Bensadoun et al. [109; 110] (Bns).

A.6 Fatigue response, constant strain-amplitude

The chosen peak strain levels $\epsilon_{\max}$ for constant strain-amplitude fatigue testing are shown on the monotonic response curves of each laminate, in Figure A.8. The cycles to failure N for all tested specimens at all loading levels ($\epsilon_{\max}$) are listed in Table A.3.

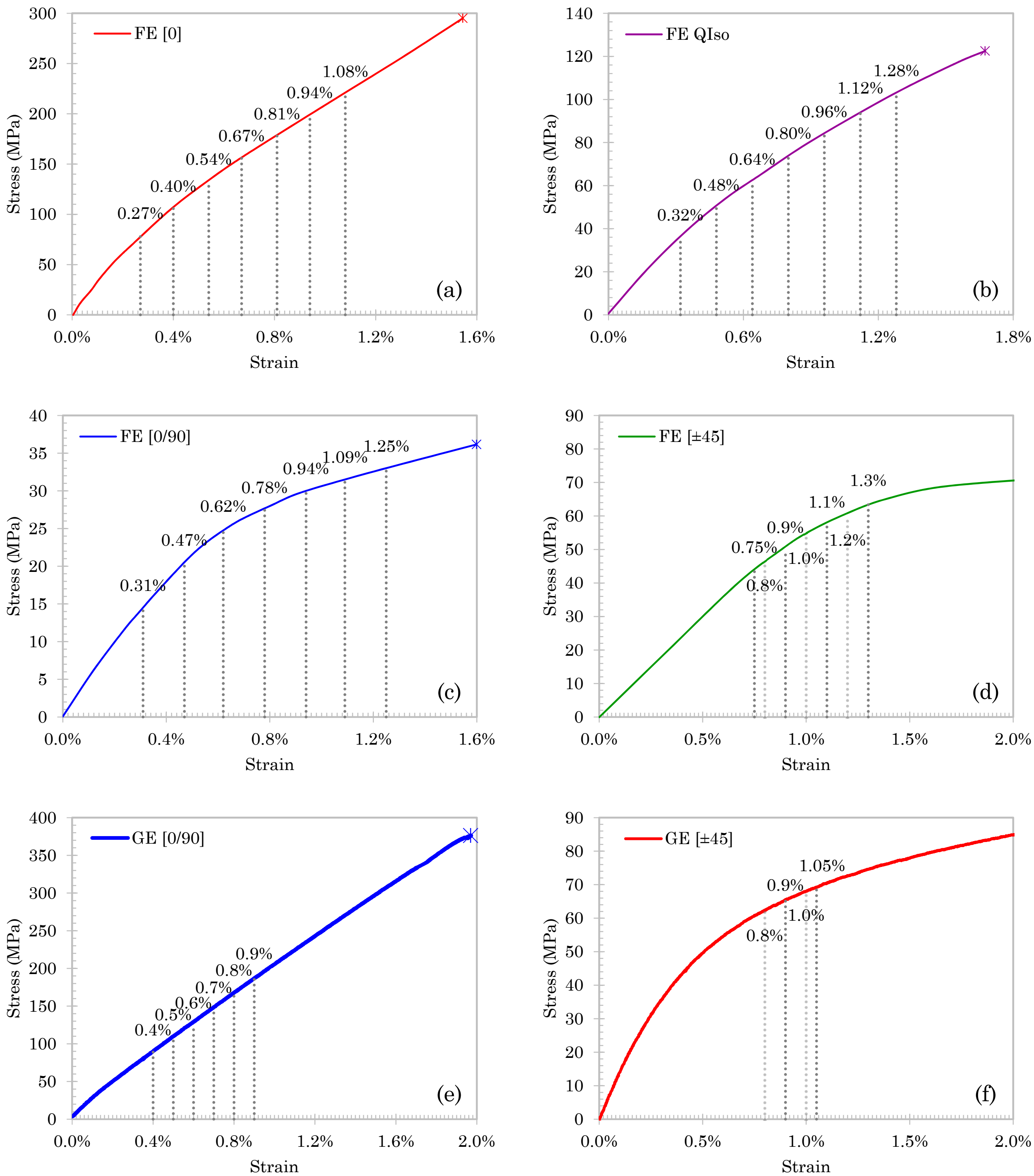

Figure A.8: Monotonic response curves showing chosen peak strain levels for strain-amplitude controlled fatigue testing of Flax-epoxy (FE) and Glass-epoxy (GE) laminates.

Table A.3: Fatigue lives (cycles to failure, N) of tested Flax-epoxy (FE) and Glass-epoxy (GE) specimens

FE [0]			FE QIso			FE [0/90]			FE [±45]			GE [0/90]			GE [±45]		
ϵ_{max}	N	$\log(N)$	ϵ_{max}	N	$\log(N)$	ϵ_{max}	N	$\log(N)$	ϵ_{max}	N	$\log(N)$	ϵ_{max}	N	$\log(N)$	ϵ_{max}	N	$\log(N)$
1.08%	950	2.978	1.28%	410	2.613	1.25%	648	2.812	1.30%	2,000	3.301	0.90%	2,544	3.406	1.10%	932	2.969
1.08%	1,800	3.255	1.28%	277	2.442	1.25%	600	2.778	1.30%	4,329	3.636	0.90%	5,155	3.712	1.05%	1,929	3.285
1.08%	1,351	3.131	1.28%	269	2.430	1.25%	200	2.301	1.30%	3,958	3.597	0.90%	7,049	3.848	1.05%	5,153	3.712
1.08%	1,536	3.186	1.28%	862	2.936	1.25%	751	2.876	1.30%	4,026	3.605	0.80%	9,731	3.988	1.05%	4,325	3.636
1.08%	1,628	3.212	1.28%	350	2.544	1.25%	418	2.621	1.30%	3,092	3.490	0.80%	10,275	4.012	1.05%	3,358	3.526
0.94%	4,456	3.649	1.12%	1,500	3.176	1.09%	1,220	3.086	1.20%	13,479	4.130	0.80%	7,000	3.845	1.00%	7,403	3.869
0.94%	1,428	3.155	1.12%	6,961	3.843	1.09%	5,132	3.710	1.20%	6,000	3.778	0.70%	28,737	4.458	1.00%	23,534	4.372
0.94%	5,483	3.739	1.12%	2,763	3.441	1.09%	3,879	3.589	1.20%	8,633	3.936	0.70%	17,031	4.231	1.00%	11,251	4.051
0.94%	6,611	3.820	1.12%	3,269	3.514	1.09%	2,685	3.429	1.20%	6,858	3.836	0.70%	8,560	3.932	1.00%	26,950	4.431
0.94%	5,260	3.721	1.12%	2,474	3.393	1.09%	5,435	3.735	1.20%	6,633	3.822	0.60%	83,938	4.924	0.90%	97,064	4.987
0.81%	14,401	4.158	0.96%	7,548	3.878	0.94%	4,810	3.682	1.12%	108,090	5.034	0.60%	49,884	4.698	0.90%	165,375	5.218
0.81%	11,822	4.073	0.96%	10,800	4.033	0.94%	4,684	3.671	1.10%	23,322	4.368	0.60%	42,000	4.623	0.90%	69,205	4.840
0.81%	12,159	4.085	0.96%	13,258	4.122	0.94%	5,400	3.732	1.10%	79,525	4.901	0.50%	170,238	5.231	0.80%	495,485	5.695
0.81%	19,973	4.300	0.96%	8,856	3.947	0.94%	14,658	4.166	1.10%	20,158	4.304	0.50%	56,356	4.751	0.80%	240,000	5.380
0.81%	29,996	4.477	0.96%	5,457	3.737	0.94%	13,489	4.130	1.10%	38,562	4.586	0.50%	150,000	5.176	0.80%	726,835	5.861
0.67%	47,585	4.677	0.80%	35,500	4.550	0.78%	25,167	4.401	1.10%	29,409	4.468	0.40%	491,598	5.692			
0.67%	115,489	5.063	0.80%	115,000	5.061	0.78%	59,585	4.775	1.00%	50,949	4.707	0.40%	358,965	5.555			
0.67%	61,818	4.791	0.80%	24,496	4.389	0.78%	25,734	4.411	1.00%	96,887	4.986	0.40%	145,612	5.163			
0.67%	99,358	4.997	0.80%	59,632	4.775	0.78%	62,384	4.795	1.00%	112,763	5.052						
0.67%	58,458	4.767	0.80%	41,258	4.616	0.78%	50,320	4.702	1.00%	188,788	5.276						
0.54%	137,000	5.137	0.80%	37,363	4.572	0.62%	84,000	4.924	1.00%	54,827	4.739						
0.54%	150,040	5.176	0.64%	249,000	5.396	0.62%	89,408	4.951	0.90%	170,856	5.233						
0.54%	263,281	5.420	0.64%	350,000	5.544	0.62%	60,705	4.783	0.90%	131,050	5.117						
0.54%	319,027	5.504	0.64%	177,152	5.248	0.62%	201,589	5.304	0.90%	533,698	5.727						
0.54%	223,064	5.348	0.64%	421,058	5.624	0.62%	495,159	5.695	0.90%	200,588	5.302						
0.40%	426,467	5.630	0.64%	401,258	5.603	0.47%	196,319	5.293	0.90%	405,726	5.608						
0.40%	852,140	5.931	0.64%	1,238,273	6.093	0.47%	487,347	5.688	0.80%	470,082	5.672						
0.40%	336,912	5.528	0.48%	1,273,262	6.105	0.47%	420,138	5.623	0.80%	1,062,000	6.026						
0.40%	1,023,658	6.010	0.48%	605,212	5.782	0.47%	932,684	5.970	0.80%	1,833,621	6.263						
0.40%	758,739	5.880	0.48%	952,143	5.979	0.47%	601,269	5.779	0.80%	885,428	5.947						
0.27%	2,000,000	6.301	0.48%	1,695,847	6.229	0.31%	2,000,000	6.301	0.80%	2,000,000	6.301						
			0.48%	1,033,431	6.014												
			0.32%	2,000,000	6.301												

The proportional relationship between loading level and dissipation energy can be observed in Figure A.9.

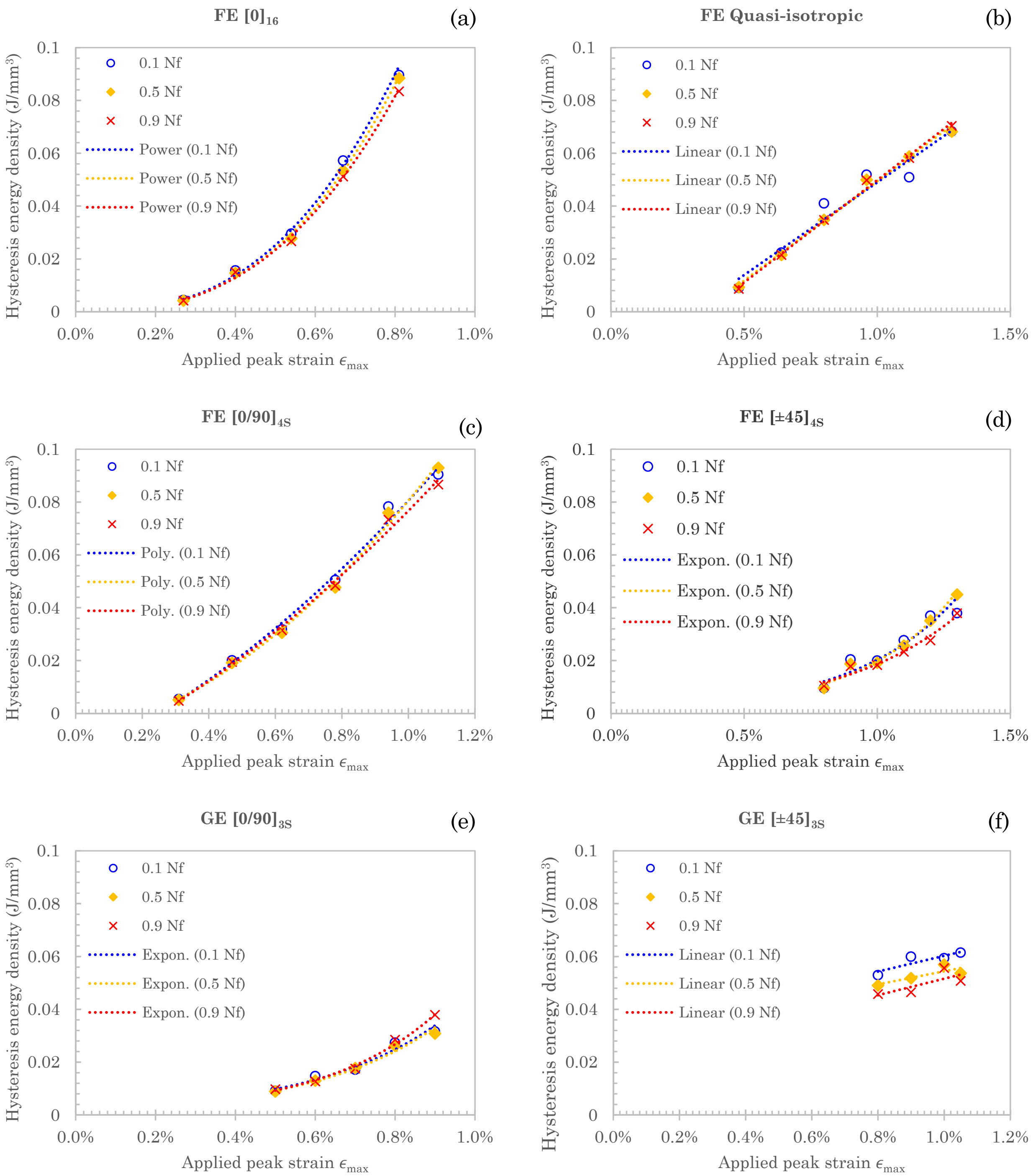

Figure A.9: Observed trends of hysteresis energy density U^h over applied $\epsilon_{\max}$ levels at early (0.1 N_f), mid (0.5 N_f), and late (0.9 N_f) fatigue life.

Since fatigue damage is defined in terms of normalised modulus, damage increase and stiffness loss are interchangeable metrics, and damage evolution is a reflection of the stiffness trends shown earlier in Figure 8.29.

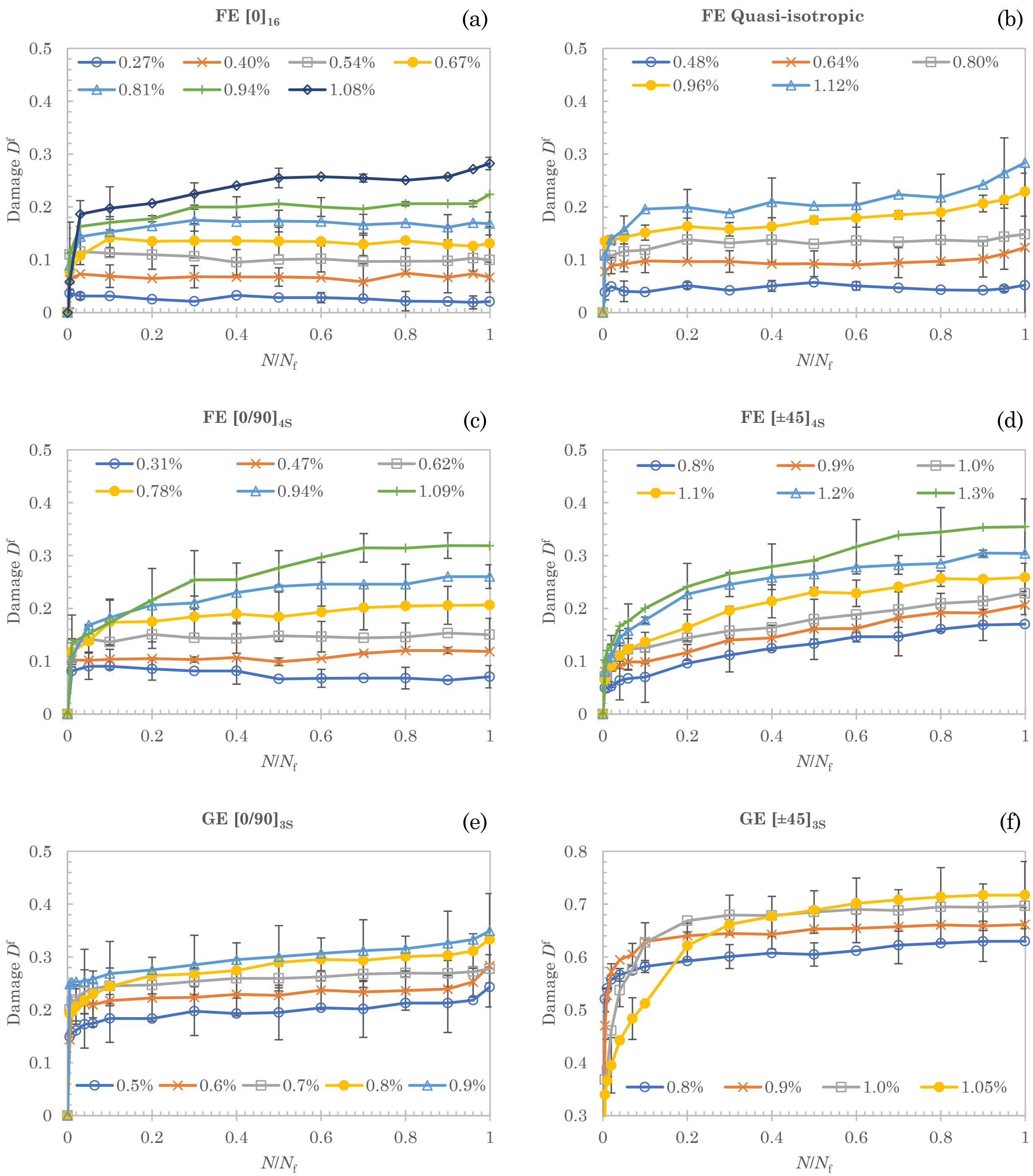

Figure A.10: Damage D^{f} evolution measured from *fatigue* cycles for tested $\epsilon_{\max}$ levels. The mean trendlines are shown with standard deviation bars.

The 'static' damage evolution trends for Flax-epoxy, i.e. modulus degradation measured from static cycles, are shown in Figure A.11. These 'static' trends are similar to to those measured from fatigue cycles, given earlier in Figure A.10.

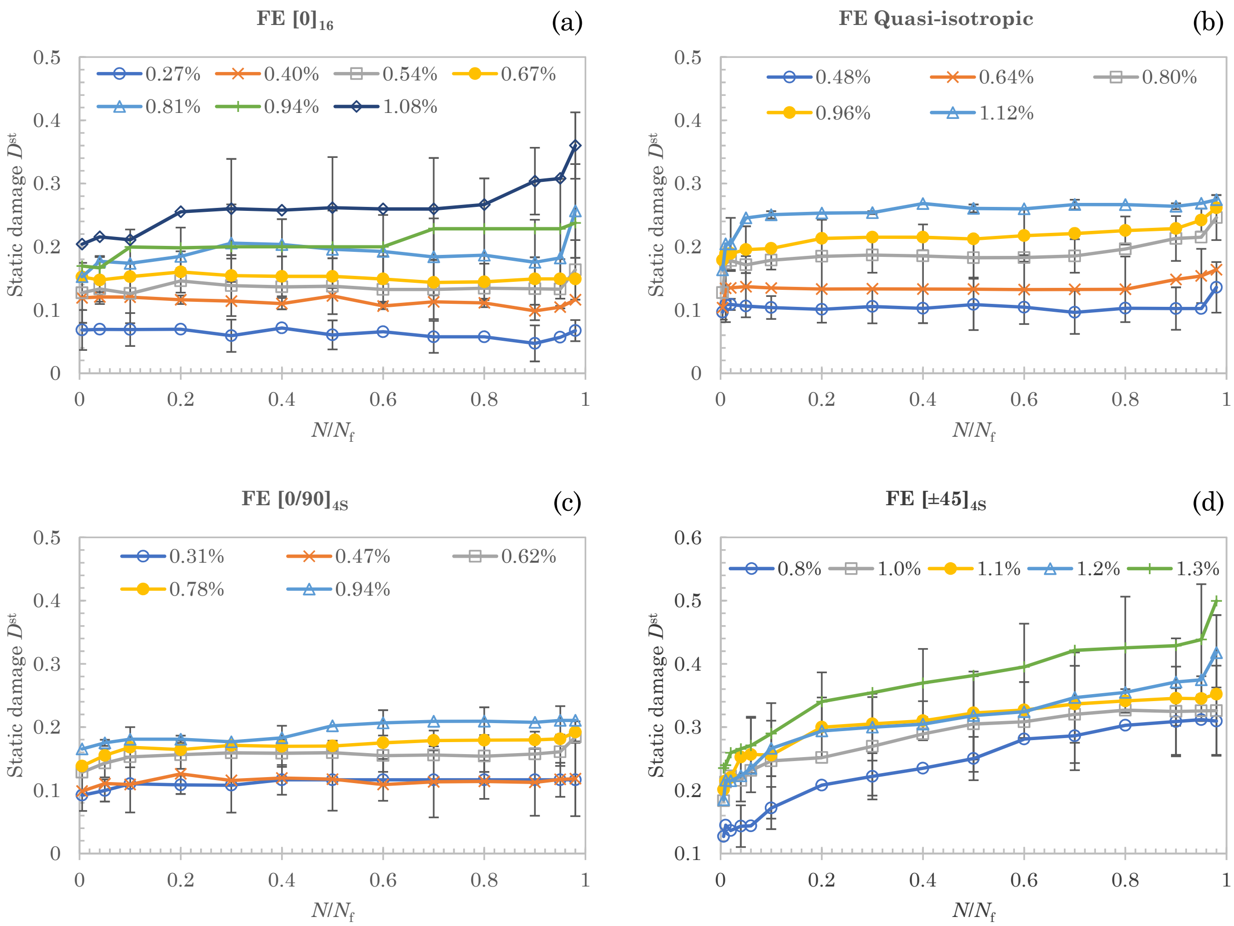

Figure A.11: Damage D^{st} measured from the intermediate *quasi-static* cycles for Flax-epoxy (FE) laminates. The mean trendlines are shown with standard deviation bars.

References

[1] D. U. Shah, Developing plant fibre composites for structural applications by optimising composite parameters: a critical review, Journal of Material Science 48 (18) (2013) 6083–6107. doi:10.1007/s10853-013-7458-7.

[2] D. U. Shah, Natural fibre composites: Comprehensive Ashby-type materials selection charts, Materials Design 62 (2014) 21–31. doi:10.1016/j.matdes.2014.05.002.

[3] P. Wambua, J. Ivens, I. Verpoest, Natural fibres: Can they replace glass in fibre reinforced plastics?, Composites Science and Technology 63 (9) (2003) 1259–1264. doi:10.1016/S0266-3538(03)00096-4.

[4] S. V. Joshi, L. T. Drzal, A. K. Mohanty, S. Arora, Are natural fiber composites environmentally superior to glass fiber reinforced composites?, Composites Part A: Applied Science and Manufacturing 35 (3) (2004) 371–376. doi:10.1016/j.compositesa.2003.09.016.

[5] K. G. Satyanarayana, G. G. C. Arizaga, F. Wypych, Biodegradable composites based on lignocellulosic fibers An overview, Progress in Polymer Science 34 (9) (2009) 982–1021. doi:doi:10.1016/j.progpolymsci.2008.12.002.

[6] K. L. Pickering, M. G. A. Efendy, T. M. Le, A review of recent developments in natural fibre composites and their mechanical performance, Composites Part A: Applied Science and Manufacturing 83 (2016) 98–112. doi:10.1016/j.compositesa.2015.08.038.

[7] D. B. Dittenber, H. V. S. GangaRao, Critical review of recent publications on use of natural composites in infrastructure, Composites Part A: Applied Science and Manufacturing 43 (8) (2012) 1419–1429. doi:10.1016/j.compositesa.2011.11.019.

[8] K. Murali Mohan Rao, K. Mohana Rao, A. V. Ratna Prasad, Fabrication and testing of natural fibre composites: Vakka, sisal, bamboo and banana, Materials Design 31 (1) (2010) 508–513. doi:10.1016/j.matdes.2009.06.023.

[9] H. M. G. van der Werf, L. Turunen, The environmental impacts of the production of hemp and flax textile yarn, Industrial Crops and Products 27 (1) (2008) 1–10. doi:10.1016/j.indcrop.2007.05.003.

[10] D. N. Saheb, J. P. Jog, Natural fiber polymer composites: A review, Advances in Polymer Technology 18 (4) (1999) 351–363. doi:10.1002/(SICI)1098-2329(199924)18:4<351::AID-ADV6>3.0.CO;2-X.

[11] J. Summerscales, N. Dissanayake, A. Virk, W. Hall, A review of bast fibres and their composites. Part 2 Composites, Composites Part A: Applied Science and Manufacturing 41 (10) (2010) 1336–1344. doi:10.1016/j.compositesa.2010.05.020.

[12] M.-P. Ho, H. Wang, J.-H. Lee, C.-K. Ho, K.-T. Lau, J. Leng, D. Hui, Critical factors on manufacturing processes of natural fibre composites, Composites Part B: Engineering 43 (8) (2012) 3549–3562. doi:10.1016/j.compositesb.2011.10.001.

[13] D. U. Shah, D. Porter, F. Vollrath, Can silk become an effective reinforcing fibre? A property comparison with flax and glass reinforced composites, Composites Science and Technology 101 (2014) 173–183. doi:10.1016/j.compscitech.2014.07.015.

[14] S. K. Garkhail, R. W. H. Heijenrath, T. Peijs, Mechanical properties of natural-fibre-mat-reinforced thermoplastics based on flax fibres and polypropylene, Applied Composite Materials 7 (5-6) (2000) 351–372. doi:10.1023/A:1026590124038.

[15] W. Kim, A. Argento, E. Lee, C. Flanigan, D. Houston, A. Harris, D. F. Mielewski, High strain-rate behavior of natural fiber-reinforced polymer composites, Journal of Composite Materials 46 (9) (2012) 1051–1065. doi:10.1177/0021998311414946.

[16] A. Stamboulis, C. Baillie, T. Peijs, Effects of environmental conditions on mechanical and physical properties of flax fibers, Composites Part A: Applied Science and Manufacturing 32 (8) (2001) 1105–1115. doi:10.1016/S1359-835X(01)00032-X.

[17] A. Le Duigou, P. Davies, C. Baley, Environmental impact analysis of the production of flax fibres to be used as composite material reinforcement, Journal of Biobased Materials and Bioenergy 5 (1) (2011) 153–165. doi:10.1166/jbmb.2011.1116.

[18] T. Corbière-Nicollier, B. Gfeller Laban, L. Lundquist, Y. Leterrier, J. A. E. Månson, O. Jolliet, Life cycle assessment of biofibres replacing glass fibres as reinforcement in plastics, Resources, Conservation and Recycling 33 (4) (2001) 267–287. doi:10.1016/S0921-3449(01)00089-1.

[19] M. Pervaiz, M. M. Sain, Carbon storage potential in natural fiber composites, Resources, Conservation and Recycling 39 (4) (2003) 325–340. doi:10.1016/S0921-3449(02)00173-8.

[20] S. Gonzlez-Garca, A. Hospido, G. Feijoo, M. T. Moreira, Life cycle assessment of raw materials for non-wood pulp mills: Hemp and flax, Resources, Conservation and Recycling 54 (11) (2010) 923–930. doi:10.1016/j.resconrec.2010.01.011.

[21] H. L. Bos, M. J. A. van den Oever, O. C. J. J. Peters, Tensile and compressive properties of flax fibres for natural fibre reinforced composites, Journal of Material Science 37 (8) (2002) 1683–1692. doi:10.1023/A:1014925621252.

[22] S. Liang, P.-B. Gning, L. Guillaumat, Quasi-static behaviour and damage assessment of flax/epoxy composites, Materials Design 67 (2015) 344–353. doi:10.1016/j.matdes.2014.11.048.

[23] C. Baley, Analysis of the flax fibres tensile behaviour and analysis of the tensile stiffness increase, Composites Part A: Applied Science and Manufacturing 33 (7) (2002) 939–948. doi:10.1016/S1359-835X(02)00040-4.

[24] H. L. Bos, A. M. Donald, In situ ESEM study of the deformation of elementary flax fibres, Journal of Material Science 34 (13) (1999) 3029–3034. doi:10.1023/A:1004650126890.

[25] S. Liang, P.-B. Gning, L. Guillaumat, A comparative study of fatigue behaviour of flax/epoxy and glass/epoxy composites, Composites Science and Technology 72 (5) (2012) 535–543. doi:10.1016/j.compscitech.2012.01.011.

[26] B. Lamy, C. Baley, Stiffness prediction of flax fibers-epoxy composite materials, Journal of Material Science Letters 19 (11) (2000) 979–980. doi:10.1023/A:1006776423764.

[27] B. Lamy, C. Pomel, Influence of fiber defects on the stiffness properties of flax fibers-epoxy composite materials, Journal of Material Science Letters 21 (15) (2002) 1211–1213. doi:10.1023/A:1016524619867.

[28] B. Madsen, H. Lilholt, Physical and mechanical properties of unidirectional plant fibre compositesan evaluation of the influence of porosity, Composites Science and Technology 63 (9) (2003) 1265–1272. doi:10.1016/S0266-3538(03)00097-6.

[29] B. Madsen, A. Thygesen, H. Lilholt, Plant fibre composites porosity and volumetric interaction, Composites Science and Technology 67 (78) (2007) 1584–1600. doi:10.1016/j.compscitech.2006.07.009.

[30] B. Madsen, A. Thygesen, H. Lilholt, Plant fibre composites porosity and stiffness, Composites Science and Technology 69 (78) (2009) 1057–1069. doi:10.1016/j.compscitech.2009.01.016.

[31] J. Gassan, A study of fibre and interface parameters affecting the fatigue behaviour of natural fibre composites, Composites Part A: Applied Science and Manufacturing 33 (3) (2002) 369–374. doi:10.1016/S1359-835X(01)00116-6.

[32] M. Assarar, D. Scida, A. El Mahi, C. Poilne, R. Ayad, Influence of water ageing on mechanical properties and damage events of two reinforced composite materials: Flax fibres and glass fibres, Materials Design 32 (2) (2011) 788–795. doi:10.1016/j.matdes.2010.07.024.

[33] R. H. Newman, Auto-accelerative water damage in an epoxy composite reinforced with plain-weave flax fabric, Composites Part A: Applied Science and Manufacturing 40 (10) (2009) 1615–1620. doi:10.1016/j.compositesa.2009.07.010.

[34] D. Scida, M. Assarar, C. Poilâne, R. Ayad, Influence of hygrothermal ageing on the damage mechanisms of flax-fibre reinforced epoxy composite, Composites Part B: Engineering 48 (2013) 51–58. doi:10.1016/j.compositesb.2012.12.010.

[35] K. Oksman, L. Wallstrm, L. A. Berglund, R. D. de Toledo Filho, Morphology and mechanical properties of unidirectional sisal-epoxy composites, Journal of Applied Polymer Science 84 (13) (2002) 2358–2365. doi:10.1002/app.10475.

[36] C. Bonnafous, F. Touchard, L. Chocinski-Arnault, Damage mechanisms in hemp-fibre woven fabric composite, and comparison with glass-fibre composite, Polymers & Polymer Composites 19 (7) (2011) 543–552.

[37] D. U. Shah, P. J. Schubel, M. J. Clifford, Can flax replace E-glass in structural composites? A small wind turbine blade case study, Composites Part B: Engineering 52 (2013) 172–181. doi:10.1016/j.compositesb.2013.04.027.

[38] A. Shahzad, D. H. Isaac, Fatigue properties of hemp and glass fiber composites, Polymer Composites 35 (10) (2014) 1926–1934. doi:10.1002/pc.22851.

[39] N. Saba, M. Jawaid, O. Y. Alothman, M. T. Paridah, A review on dynamic mechanical properties of natural fibre reinforced polymer composites, Construction and Building Materials 106 (2016) 149–159. doi:10.1016/j.conbuildmat.2015.12.075.

[40] M. A. Aziz, P. Paramasivam, S. L. Lee, Prospects for natural fibre reinforced concretes in construction, International Journal of Cement Composites and Lightweight Concrete 3 (2) (1981) 123–132. doi:10.1016/0262-5075(81)90006-3.

[41] M. A. Mansur, M. A. Aziz, A study of jute fibre reinforced cement composites, International Journal of Cement Composites and Lightweight Concrete 4 (2) (1982) 75–82. doi:10.1016/0262-5075(82)90011-2.

[42] H. S. Ramaswamy, B. M. Ahuja, S. Krishnamoorthy, Behaviour of concrete reinforced with jute, coir and bamboo fibres, International Journal of Cement Composites and Lightweight Concrete 5 (1) (1983) 3–13. doi:10.1016/0262-5075(83)90044-1.

[43] L. Yan, N. Chouw, Experimental study of flax FRP tube encased coir fibre reinforced concrete composite column, Construction and Building Materials 40 (2013) 1118–1127. doi:10.1016/j.conbuildmat.2012.11.116.

[44] L. Yan, S. Su, N. Chouw, Microstructure, flexural properties and durability of coir fibre reinforced concrete beams externally strengthened with flax FRP composites, Composites Part B: Engineering 80 (2015) 343–354. doi:10.1016/j.compositesb.2015.06.011.

[45] L. Yan, Plain concrete cylinders and beams externally strengthened with natural flax fabric reinforced epoxy composites, Materials and Structures 49 (6) (2016) 2083–2095. doi:10.1617/s11527-015-0635-1.

[46] L. Yan, N. Chouw, K. Jayaraman, Flax fibre and its composites – A review, Composites Part B: Engineering 56 (2014) 296–317. doi:10.1016/j.compositesb.2013.08.014.

[47] P.-O. Hagstrand, K. Oksman, Mechanical properties and morphology of flax fiber reinforced melamine-formaldehyde composites, Polymer Composites 22 (4) (2001) 568–578. doi:10.1002/pc.10560.

[48] K. Charlet, J.-P. Jernot, M. Gomina, L. Bizet, J. Brard, Mechanical properties of flax fibers and of the derived unidirectional composites, Journal of Composite Materials 44 (24) (2010) 2887–2896. doi:10.1177/0021998310369579.

[49] K. Charlet, Contribution to the study of flax fibre reinforced unidirectional composites: Relationships between the fibre microstructure and its mechanical properties, PhD dissertation, Université de Caen, Basse-Normandie, France (May 2008).
URL https://hal.archives-ouvertes.fr/tel-01133091

[50] S. Liang, P.-B. Gning, L. Guillaumat, Properties evolution of flax/epoxy composites under fatigue loading, International Journal of Fatigue 63 (2014) 36–45. doi:10.1016/j.ijfatigue.2014.01.003.

[51] K. Charlet, S. Eve, J. Jernot, M. Gomina, J. Breard, Tensile deformation of a flax fiber, Procedia Engineering 1 (1) (2009) 233–236. doi:10.1016/j.proeng.2009.06.055.

[52] C. Clark, Flax stem cross-section, showing locations of underlying tissues (Sep. 2008).
URL http://commons.wikimedia.org/wiki/File:Labeledstemforposter_copy_new.jpg

[53] H. L. Bos, K. Molenveld, W. Teunissen, A. M. van Wingerde, D. R. V. van Delft, Compressive behaviour of unidirectional flax fibre reinforced composites, Journal of Material Science 39 (6) (2004) 2159–2168. doi:10.1023/B:JMSC.0000017779.08041.49.

[54] K. Charlet, C. Baley, C. Morvan, J. P. Jernot, M. Gomina, J. Brard, Characteristics of Hermés flax fibres as a function of their location in the stem and properties of the derived unidirectional composites, Composites Part A: Applied Science and Manufacturing 38 (8) (2007) 1912–1921. doi:10.1016/j.compositesa.2007.03.006.

[55] G. Romhány, J. Karger-Kocsis, T. Czigány, Tensile fracture and failure behavior of technical flax fibers, Journal of Applied Polymer Science 90 (13) (2003) 3638–3645. doi:10.1002/app.13110.

[56] B. Madsen, E. K. Gamstedt, Wood versus plant fibers: Similarities and differences in composite applications, Advances in Materials Science and Engineering 2013 (2013) 1–14. doi:10.1155/2013/564346.

[57] A. K. Bledzki, J. Gassan, Composites reinforced with cellulose based fibres, Progress in Polymer Science 24 (2) (1999) 221–274. doi:10.1016/S0079-6700(98)00018-5.

[58] L. J. Gibson, The hierarchical structure and mechanics of plant materials, Journal of The Royal Society Interface (2012) rsif20120341doi:10.1098/rsif.2012.0341.

[59] NEUROtiker, Structure of Cellulose (chain conformation) (Oct. 2007).
URL https://commons.wikimedia.org/wiki/File:Cellulose_Sessel.svg

[60] J. W. S. Hearle, The fine structure of fibers and crystalline polymers. III. Interpretation of the mechanical properties of fibers, Journal of Applied Polymer Science 7 (4) (1963) 1207–1223. doi:10.1002/app.1963.070070403.

[61] P. S. Mukherjee, K. G. Satyanarayana, An empirical evaluation of structure-property relationships in natural fibres and their fracture behaviour, Journal of Material Science 21 (12) (1986) 4162–4168. doi:10.1007/BF01106524.

[62] A. Bourmaud, C. Morvan, A. Bouali, V. Placet, P. Perr, C. Baley, Relationships between microfibrillar angle, mechanical properties and biochemical composition of flax fibers, Industrial Crops and Products 44 (2013) 343–351. doi:10.1016/j.indcrop.2012.11.031.

[63] B. Madsen, M. Aslan, H. Lilholt, Fractographic observations of the microstructural characteristics of flax fibre composites, Composites Science and Technology 123 (2016) 151–162. doi:10.1016/j.compscitech.2015.12.003.

[64] A. Day, K. Ruel, G. Neutelings, D. Crnier, H. David, S. Hawkins, B. Chabbert, Lignification in the flax stem: Evidence for an unusual lignin in bast fibers, Planta 222 (2) (2005) 234–245. doi:10.1007/s00425-005-1537-1.

[65] V. Placet, O. Cissé, M. Lamine Boubakar, Nonlinear tensile behaviour of elementary hemp fibres. Part I: Investigation of the possible origins using repeated progressive loading with in situ microscopic observations, Composites Part A: Applied Science and Manufacturing 56 (2014) 319–327. doi:10.1016/j.compositesa.2012.11.019.

[66] L. Salmén, Micromechanical understanding of the cell-wall structure, Comptes Rendus Biologies 327 (9) (2004) 873–880. doi:10.1016/j.crvi.2004.03.010.

[67] G. Davies, D. Bruce, Effect of environmental relative humidity and damage on the tensile properties of flax and nettle fibers, Textile Research Journal 68 (9) (1998) 623–629. doi:10.1177/004051759806800901.

[68] J. Andersons, E. Poriķe, E. Spārniņš, The effect of mechanical defects on the strength distribution of elementary flax fibres, Composites Science and Technology 69 (13) (2009) 2152–2157. doi:10.1016/j.compscitech.2009.05.010.

[69] M. Hughes, Defects in natural fibres: their origin, characteristics and implications for natural fibre-reinforced composites, Journal of Material Science 47 (2) (2011) 599–609. doi:10.1007/s10853-011-6025-3.

[70] A. Lefeuvre, A. Bourmaud, C. Morvan, C. Baley, Elementary flax fibre tensile properties: Correlation between stressstrain behaviour and fibre composition, Industrial Crops and Products 52 (2014) 762–769. doi:10.1016/j.indcrop.2013.11.043.

[71] I. Pillin, A. Kervoelen, A. Bourmaud, J. Goimard, N. Montrelay, C. Baley, Could oleaginous flax fibers be used as reinforcement for polymers?, Industrial Crops and Products 34 (3) (2011) 1556–1563. doi:10.1016/j.indcrop.2011.05.016.

[72] R. Joffe, J. Andersons, L. Wallström, Strength and adhesion characteristics of elementary flax fibres with different surface treatments, Composites Part A: Applied Science and Manufacturing 34 (7) (2003) 603–612. doi:10.1016/S1359-835X(03)00099-X.

[73] C. Baley, Influence of kink bands on the tensile strength of flax fibers, Journal of Material Science 39 (1) (2004) 331–334. doi:10.1023/B:JMSC.0000007768.63055.ae.

[74] J. Andersons, E. Spārniņš, R. Joffe, L. Wallström, Strength distribution of elementary flax fibres, Composites Science and Technology 65 (34) (2005) 693–702. doi:10.1016/j.compscitech.2004.10.001.

[75] M. Aslan, G. Chinga-Carrasco, B. F. Sørensen, B. Madsen, Strength variability of single flax fibres, Journal of Material Science 46 (19) (2011) 6344–6354. doi:10.1007/s10853-011-5581-x.

[76] G. Coroller, A. Lefeuvre, A. Le Duigou, A. Bourmaud, G. Ausias, T. Gaudry, C. Baley, Effect of flax fibres individualisation on tensile failure of flax/epoxy unidirectional composite, Composites Part A: Applied Science and Manufacturing 51 (2013) 62–70. doi:10.1016/j.compositesa.2013.03.018.

[77] R. W. Kessler, U. Becker, R. Kohler, B. Goth, Steam explosion of flax – a superior technique for upgrading fibre value, Biomass and Bioenergy 14 (3) (1998) 237–249. doi:10.1016/S0961-9534(97)10040-X.

[78] T. Stuart, Q. Liu, M. Hughes, R. D. McCall, H. S. S. Sharma, A. Norton, Structural biocomposites from flax – Part I: Effect of bio-technical fibre modification on composite properties, Composites Part A: Applied Science and Manufacturing 37 (3) (2006) 393–404. doi:10.1016/j.compositesa.2005.06.002.

[79] N. Zafeiropoulos, G. Dijon, C. Baillie, A study of the effect of surface treatments on the tensile strength of flax fibres: Part I. Application of Gaussian statistics, Composites Part A: Applied Science and Manufacturing 38 (2) (2007) 621–628. doi:10.1016/j.compositesa.2006.02.004.

[80] S. Alix, E. Philippe, A. Bessadok, L. Lebrun, C. Morvan, S. Marais, Effect of chemical treatments on water sorption and mechanical properties of flax fibres, Bioresource and Technology 100 (20) (2009) 4742–4749. doi:10.1016/j.biortech.2009.04.067.

[81] J. L. Thomason, J. Carruthers, J. Kelly, G. Johnson, Fibre cross-section determination and variability in sisal and flax and its effects on fibre performance characterisation, Composites Science and Technology 71 (7) (2011) 1008–1015. doi:10.1016/j.compscitech.2011.03.007.

[82] K. Charlet, J.-P. Jernot, M. Gomina, J. Brard, C. Morvan, C. Baley, Influence of an Agatha flax fibre location in a stem on its mechanical, chemical and morphological properties, Composites Science and Technology 69 (9) (2009) 1399–1403. doi:10.1016/j.compscitech.2008.09.002.

[83] V. Placet, F. Trivaudey, O. Cissé, V. Gucheret-Retel, M. L. Boubakar, Diameter dependence of the apparent tensile modulus of hemp fibres: A morphological, structural or ultrastructural effect?, Composites Part A: Applied Science and Manufacturing 43 (2) (2012) 275–287. doi:10.1016/j.compositesa.2011.10.019.

[84] J. Keckes, I. Burgert, K. Frühmann, M. Mller, K. Kölln, M. Hamilton, M. Burghammer, S. V. Roth, S. Stanzl-Tschegg, P. Fratzl, Cell-wall recovery after irreversible deformation of wood, Nature Materials 2 (12) (2003) 810–813. doi:10.1038/nmat1019.

[85] H. Hahn, R. Kim, Fatigue behavior of composite laminate, Journal of Composite Materials 10 (2) (1976) 156–180. doi:10.1177/002199837601000205.

[86] D. Sinclair, A bending method for measurement of the tensile strength and Young's modulus of glass fibers, Journal of Applied Physics 21 (5) (1950) 380–386. doi:10.1063/1.1699670.

[87] J. H. Greenwood, P. G. Rose, Compressive behaviour of Kevlar 49 fibres and composites, Journal of Materials Science 9 (11) (1974) 1809–1814. doi:10.1007/BF00541750.

[88] T. Peijs, R. J. M. van Vught, L. E. Govaert, Mechanical properties of poly(vinyl alcohol) fibres and composites, Composites 26 (2) (1995) 83–90. doi:10.1016/0010-4361(95)90407-Q.

[89] S. J. Deteresa, R. S. Porter, R. J. Farris, Experimental verification of a microbuckling model for the axial compressive failure of high performance polymer fibres, Journal of Materials Science 23 (5) (1988) 1886–1894. doi:10.1007/BF01115735.

[90] M. Hughes, J. Carpenter, C. Hill, Deformation and fracture behaviour of flax fibre reinforced thermosetting polymer matrix composites, Journal of Materials Science 42 (7) (2007) 2499–2511. doi:10.1007/s10853-006-1027-2.

[91] A. Corigliano, Damage and Fracture Mechanics Techniques for Composite Structures (3.09), in: Numerical and Computational Methods, Vol. 3 of Comprehensive Structural Integrity, Elsevier Pergamon, Amsterdam; San Diego CA, 2003, pp. 459–539. doi:10.1016/B0-08-043749-4/03041-X.

[92] J.-M. Berthelot, Composite Materials: Mechanical Behaviour and Structural Analysis, Springer-Verlag, Berlin Heidelberg, 1999.
URL http://link.springer.com/10.1007/978-1-4612-0527-2

[93] C. Bathias, An engineering point of view about fatigue of polymer matrix composite materials, International Journal of Fatigue 28 (10) (2006) 1094–1099. doi:10.1016/j.ijfatigue.2006.02.008.

[94] A. Fotouh, J. D. Wolodko, M. G. Lipsett, Fatigue of natural fiber thermoplastic composites, Composites Part B: Engineering 62 (2014) 175–182. doi:10.1016/j.compositesb.2014.02.023.

[95] G. Romhány, J. Karger-Kocsis, T. Czigány, Tensile fracture and failure behavior of thermoplastic starch with unidirectional and cross-ply flax fiber reinforcements, Macromolecular Materials and Engineering 288 (9) (2003) 699–707. doi:10.1002/mame.200300040.

[96] R. H. Newman, M. A. Battley, J. E. P. Carpenter, M. J. L. Guen, Energy loss in a unidirectional flax-polyester composite subjected to multiple tensile loadunload cycles, Journal of Material Science 47 (3) (2012) 1164–1170. doi:10.1007/s10853-011-5713-3.

[97] W. S. Williams, D. A. Steffens, R. Bacon, Bending behavior and tensile strength of carbon fibers, Journal of Applied Physics 41 (12) (1970) 4893–4901. doi:10.1063/1.1658559.

[98] H. Spatz, L. Köhler, K. J. Niklas, Mechanical behaviour of plant tissues: Composite materials or structures?, Journal of Experimental Biology 202 (23) (1999) 3269–3272.

[99] L. Köhler, T. Speck, H.-C. Spatz, Micromechanics and anatomical changes during early ontogeny of two lianescent Aristolochia species, Planta 210 (5) (2000) 691–700. doi:10.1007/s004250050669.

[100] L. Köhler, H.-C. Spatz, Micromechanics of plant tissues beyond the linear-elastic range, Planta 215 (1) (2002) 33–40. doi:10.1007/s00425-001-0718-9.

[101] D. Kretschmann, Natural materials: Velcro mechanics in wood, Nature Materials 2 (12) (2003) 775–776. doi:10.1038/nmat1025.

[102] O. M. Astley, A. M. Donald, The tensile deformation of flax fibres as studied by X-ray scattering, Journal of Materials Science 38 (1) (2003) 165–171. doi:10.1023/A:1021186421194.

[103] I. El Sawi, Z. Fawaz, R. Zitoune, H. Bougherara, An investigation of the damage mechanisms and fatigue life diagrams of flax fiber-reinforced polymer laminates, Journal of Material Science 49 (5) (2014) 2338–2346. doi:10.1007/s10853-013-7934-0.

[104] G. Fargione, A. Geraci, G. La Rosa, A. Risitano, Rapid determination of the fatigue curve by the thermographic method, International Journal of Fatigue 24 (1) (2002) 11–19. doi:10.1016/S0142-1123(01)00107-4.

[105] J. Montesano, Z. Fawaz, H. Bougherara, Use of infrared thermography to investigate the fatigue behavior of a carbon fiber reinforced polymer composite, Composite Structures 97 (2013) 76–83. doi:10.1016/j.compstruct.2012.09.046.

[106] Y. Ueki, H. Lilholt, B. Madsen, Fatigue behaviour of uni-directional flax fibre/epoxy composites, in: Proceedings of the 20th International Conference on Composite Materials, ICCM20 Secretariat, Copenhagen, Denmark, 2015.
URL http://findit.dtu.dk/en/catalog/2289420365

[107] I. El Sawi, H. Bougherara, R. Zitoune, Z. Fawaz, Influence of the manufacturing process on the mechanical properties of flax/epoxy composites, Journal of Biobased Materials and Bioenergy 8 (1) (2014) 69–76. doi:10.1166/jbmb.2014.1410.

[108] S. Asgarinia, C. Viriyasuthee, S. Phillips, M. Dub, J. Baets, A. Van Vuure, I. Verpoest, L. Lessard, Tension-tension fatigue behaviour of woven flax/epoxy composites, Journal of Reinforced Plastics and Composites 34 (11) (2015) 857–867. doi:10.1177/0731684415581527.

[109] F. Bensadoun, K. A. M. Vallons, L. B. Lessard, I. Verpoest, A. W. Van Vuure, Fatigue behaviour assessment of flaxepoxy composites, Composites Part A: Applied Science and Manufacturing 82 (2016) 253–266. doi:10.1016/j.compositesa.2015.11.003.

[110] F. Bensadoun, In-service behaviour of Flax fibre reinforced composites for high performance applications, PhD dissertation, Katholieke Universiteit Leuven, Leuven, Belgium (Jul. 2016).
URL https://lirias.kuleuven.be/bitstream/123456789/541393/1/PhD+thesis_Farida+Bensadoun.pdf

[111] K. Vallons, S. V. Lomov, I. Verpoest, Fatigue and post-fatigue behaviour of carbon/epoxy non-crimp fabric composites, Composites Part A: Applied Science and Manufacturing 40 (3) (2009) 251–259. doi:10.1016/j.compositesa.2008.12.001.

[112] F. K. Sodoke, L. Toubal, L. Laperrière, Hygrothermal effects on fatigue behavior of quasi-isotropic flax/epoxy composites using principal component analysis, Journal of Material Science 51 (24) (2016) 10793–10805. doi:10.1007/s10853-016-0291-z.

[113] A. N. Towo, M. P. Ansell, Fatigue of sisal fibre reinforced composites: Constant-life diagrams and hysteresis loop capture, Composites Science and Technology 68 (34) (2008) 915–924. doi:10.1016/j.compscitech.2007.08.021.

[114] A. N. Towo, M. P. Ansell, Fatigue evaluation and dynamic mechanical thermal analysis of sisal fibrethermosetting resin composites, Composites Science and Technology 68 (34) (2008) 925–932. doi:10.1016/j.compscitech.2007.08.022.

[115] D. U. Shah, P. J. Schubel, M. J. Clifford, P. Licence, Fatigue life evaluation of aligned plant fibre composites through SN curves and constant-life diagrams, Composites Science and Technology 74 (2013) 139–149. doi:10.1016/j.compscitech.2012.10.015.

[116] D. S. de Vasconcellos, F. Touchard, L. Chocinski-Arnault, Tensiontension fatigue behaviour of woven hemp fibre reinforced epoxy composite: A multi-instrumented damage analysis, International Journal of Fatigue 59 (2014) 159–169. doi:10.1016/j.ijfatigue.2013.08.029.

[117] C. Bonnafous, F. Touchard, L. Chocinski-Arnault, Multi scale analysis by acoustic emission of damage mechanisms in natural fibre woven fabrics/epoxy composites., in: EPJ Web of Conferences, Vol. 6, EDP Sciences, Poitiers, France, 2010, p. 20009. doi:10.1051/epjconf/20100620009.

[118] A. Fotouh, Characterization and Modeling of Natural-Fibres-Reinforced composites (Moisture Absorption Kinetics, Monotonic Behaviour and Cyclic Behaviour), PhD dissertation, University of Alberta, Edmonton, AB, Canada (Nov. 2014). doi:10.7939/R3NS0M479.
URL https://era.library.ualberta.ca/files/qf85nc982

[119] T. Yuanjian, D. H. Isaac, Impact and fatigue behaviour of hemp fibre composites, Composites Science and Technology 67 (15) (2007) 3300–3307. doi:10.1016/j.compscitech.2007.03.039.

[120] Y. Huang, R. J. Young, Effect of fibre microstructure upon the modulus of PAN- and pitch-based carbon fibres, Carbon 33 (2) (1995) 97–107. doi:10.1016/0008-6223(94)00109-D.

[121] X. Huang, Fabrication and properties of carbon fibers, Materials 2 (4) (2009) 2369–2403. doi:10.3390/ma2042369.

[122] P. Ladevèze, E. Le Dantec, Damage modelling of the elementary ply for laminated composites, Composites Science and Technology 43 (3) (1992) 257–267. doi:10.1016/0266-3538(92)90097-M.

[123] E. Le Dantec, Contribution à la modélisation du comportement des composites stratifies, PhD dissertation, Université Pierre et Marie Curie - Paris 6, France (July 1989).

[124] C. T. Herakovich, Damage Mechanics, Chapter 9.5, in: Mechanics of Fibrous Composites, John Wiley & Sons, Inc, New York, NY, 1998, pp. 332–361.
URL http://ca.wiley.com/WileyCDA/WileyTitle/productCd-0471106364.html

[125] C. T. Herakovich, Mechanics of composites: A historical review, Mechanics Research Communications 41 (2012) 1–20. doi:10.1016/j.mechrescom.2012.01.006.

[126] V. D. Azzi, S. W. Tsai, Anisotropic strength of composites, Experimental Mechanics 5 (9) (1965) 283–288. doi:10.1007/BF02326292.

[127] S. W. Tsai, E. M. Wu, A general theory of strength for anisotropic materials, Journal of Composite Materials 5 (1) (1971) 58–80. doi:10.1177/002199837100500106.

[128] Z. Hashin, A. Rotem, A fatigue failure criterion for fiber reinforced materials, Journal of Composite Materials 7 (4) (1973) 448–464. doi:10.1177/002199837300700404.

[129] M. R. Garnich, V. M. K. Akula, Review of degradation models for progressive failure analysis of fiber reinforced polymer composites, Applied Mechanics Reviews 62 (1) (2008) 010801–010801. doi:10.1115/1.3013822.

[130] S. M. Spottswood, A. N. Palazotto, Progressive failure analysis of a composite shell, Composite Structures 53 (1) (2001) 117–131. doi:10.1016/S0263-8223(00)00183-5.

[131] J.-L. Chaboche, Damage Mechanics (2.04), in: Numerical and Computational Methods, Vol. 2 of Comprehensive Structural Integrity, Elsevier Pergamon, Amsterdam; San Diego CA, 2003, pp. 213–284. doi:10.1016/B0-08-043749-4/02085-1.

[132] J. Lemaitre, J.-L. Chaboche, Damage Mechanics, Chapter 7, in: Mechanics of Solid Materials, Cambridge University Press, 1990, pp. 346–450.

[133] E. J. Barbero, L. d. Vivo, A constitutive model for elastic damage in fiber-reinforced PMC laminae, International Journal of Damage Mechanics 10 (1) (2001) 73–93. doi:10.1106/6PQ6-31JW-F69K-74LU.

[134] E. J. Barbero, P. Lonetti, An inelastic damage model for fiber reinforced laminates, Journal of Composite Materials 36 (8) (2002) 941–962. doi:10.1177/0021998302036008549.

[135] P. Maimí, P. P. Camanho, J. A. Mayugo, C. G. Dávila, A continuum damage model for composite laminates: Part I Constitutive model, Mechanics of Materials 39 (10) (2007) 897–908. doi:10.1016/j.mechmat.2007.03.005.

[136] E. Abisset, F. Daghia, P. Ladevèze, On the validation of a damage mesomodel for laminated composites by means of open-hole tensile tests on quasi-isotropic laminates, Composites Part A: Applied Science and Manufacturing 42 (10) (2011) 1515–1524. doi:10.1016/j.compositesa.2011.07.004.

[137] A. K. Gupta, B. P. Patel, Y. Nath, Continuum damage modeling of composite laminated plates using higher order theory, Composite Structures 99 (2013) 141–151. doi:10.1016/j.compstruct.2012.11.038.

[138] D. Notta-Cuvier, F. Lauro, B. Bennani, An original approach for mechanical modelling of short-fibre reinforced composites with complex distributions of fibre orientation, Composites Part A: Applied Science and Manufacturing 62 (2014) 60–66. doi:10.1016/j.compositesa.2014.03.016.

[139] A. K. Gupta, B. P. Patel, Y. Nath, Nonlinear static analysis of composite laminated plates with evolving damage, Acta Mechanica 224 (6) (2013) 1285–1298. doi:10.1007/s00707-013-0875-5.

[140] P. Ladevèze, A damage computational method for composite structures, Computers and Structures 44 (12) (1992) 79–87. doi:10.1016/0045-7949(92)90226-P.

[141] O. Allix, P. Ladevèze, Interlaminar interface modelling for the prediction of delamination, Composites Structures 22 (4) (1992) 235–242. doi:10.1016/0263-8223(92)90060-P.

[142] L. Daudeville, P. Ladevèze, A damage mechanics tool for laminate delamination, Composites Structures 25 (1) (1993) 547–555. doi:10.1016/0263-8223(93)90203-3.

[143] O. Allix, P. Ladevèze, E. Vittecoq, Modelling and identification of the mechanical behaviour of composite laminates in compression, Composites Science and Technology 51 (1) (1994) 35–42. doi:10.1016/0266-3538(94)90154-6.

[144] O. Allix, P. Ladevèze, A. Corigliano, Damage analysis of interlaminar fracture specimens, Composites Structures 31 (1) (1995) 61–74. doi:10.1016/0263-8223(95)00002-X.

[145] A. Gasser, P. Ladevèze, M. Poss, Damage mechanisms of a woven SiC/SiC composite: Modelling and identification, Composites Science and Technology 56 (7) (1996) 779–784. doi:10.1016/0266-3538(96)00020-6.

[146] P. Casari, P. Ladevèze, T.-W. Chou, Damage modeling and characterization of a three-dimensional woven composite, in: ICCM-12, Paris, 1999.
URL http://www.iccm-central.org/Proceedings/ICCM12proceedings/site/htmlpap/pap717.htm

[147] A. F. Johnson, Modelling fabric reinforced composites under impact loads, Composites Part A: Applied Science and Manufacturing 32 (9) (2001) 1197–1206. doi:10.1016/S1359-835X(00)00186-X.

[148] O. Allix, A composite damage meso-model for impact problems, Composites Science and Technology 61 (15) (2001) 2193–2205. doi:10.1016/S0266-3538(01)00113-0.

[149] S. Guinard, O. Allix, D. Guédra-Degeorges, A. Vinet, A 3D damage analysis of low-velocity impacts on laminated composites, Composites Science and Technology 62 (4) (2002) 585–589. doi:10.1016/S0266-3538(01)00153-1.

[150] C. Knipprath, A. A. Skordos, A. K. Pickett, A simplified discrete finite element model for non-crimp fabric composites, in: ECCM-13, Stockholm, 2008.
URL https://dspace.lib.cranfield.ac.uk/handle/1826/3067

[151] N. Feld, O. Allix, E. Baranger, J.-M. Guimard, A micromechanics-based mesomodel for unidirectional laminates in compression up to failure, Journal of Composite Materials 46 (23) (2012) 2893–2909. doi:10.1177/0021998311434170.

[152] F. Daghia, P. Ladevèze, Identification and validation of an enhanced mesomodel for laminated composites within the WWFE-III, Journal of Composite Materials 47 (20-21) (2013) 2675–2693. doi:10.1177/0021998313494095.

[153] A. Chilali, W. Zouari, M. Assarar, H. Kebir, R. Ayad, Analysis of the mechanical behaviour of flax and glass fabrics-reinforced thermoplastic and thermoset resins, Journal of Reinforced Plastics and Composites 35 (16) (2016) 1217–1232. doi:10.1177/0731684416645203.

[154] D. Schueler, N. Toso-Pentecôte, H. Voggenreiter, Simulation of high velocity impact on composite structures - Model implementation and validation, Applied Composite Materials 23 (4) (2016) 857–878. doi:10.1007/s10443-016-9489-0.

[155] J. Lemaitre, How to use damage mechanics, Nuclear Engineering and Design 80 (2) (1984) 233–245. doi:10.1016/0029-5493(84)90169-9.

[156] N. S. Ottosen, M. Ristinmaa, Thermodynamic Framework for Constitutive Modeling, Ch. 21, in: The Mechanics of Constitutive Materials, 1st Edition, Elsevier Science Ltd, Oxford, 2005, pp. 551–589. doi:10.1016/B978-008044606-6/50021-7.

[157] J. Lemaitre, R. Desmorat, Background on Continuum Damage Mechanics, Ch. 1, in: Engineering Damage Mechanics: Ductile, Creep, Fatigue and Brittle Failures, Springer, Berlin, Heidelberg, 2005, pp. 1–76. doi:10.1007/b138882.

[158] N. S. Ottosen, M. Ristinmaa, The Mechanics of Constitutive Materials, 1st Edition, Elsevier Science Ltd, Oxford, 2005.
URL http://www.sciencedirect.com/science/book/9780080446066

[159] G. A. Holzapfel, Balance of Energy in Continuum Thermodynamics, Ch. 4.5, in: Nonlinear Solid Mechanics: A Continuum Approach for Engineering, John Wiley & Sons, Ltd, Chichester, UK, 2000, pp. 161–166.
URL http://ca.wiley.com/WileyCDA/WileyTitle/productCd-0471823198.html

[160] J. Lemaitre, J.-L. Chaboche, Mechanics of Solid Materials, Cambridge University Press, 1990.

[161] Huang Jinsong, Griffiths D. V., Return mapping algorithms and stress predictors for failure Analysis in geomechanics, Journal of Engineering Mechanics 135 (4) (2009) 276–284. doi:10.1061/(ASCE)0733-9399(2009)135:4(276).

[162] J. Lemaitre, R. Desmorat, Engineering Damage Mechanics: Ductile, Creep, Fatigue and Brittle Failures, Springer, Berlin, Heidelberg, 2005. doi:10.1007/b138882.

[163] E. Bodros, I. Pillin, N. Montrelay, C. Baley, Could biopolymers reinforced by randomly scattered flax fibre be used in structural applications?, Composites Science and Technology 67 (34) (2007) 462–470. doi:10.1016/j.compscitech.2006.08.024.

[164] K. Oksman, M. Skrifvars, J. F. Selin, Natural fibres as reinforcement in polylactic acid (PLA) composites, Composites Science and Technology 63 (9) (2003) 1317–1324. doi:10.1016/S0266-3538(03)00103-9.

[165] P. Lodha, A. N. Netravali, Characterization of Phytagel® modified soy protein isolate resin and unidirectional flax yarn reinforced 'green' composites, Polymer Composites 26 (5) (2005) 647–659. doi:10.1002/pc.20128.

[166] N. M. Barkoula, S. K. Garkhail, T. Peijs, Biodegradable composites based on flax/polyhydroxybutyrate and its copolymer with hydroxyvalerate, Industrial Crops and Products 31 (1) (2010) 34–42. doi:10.1016/j.indcrop.2009.08.005.

[167] J. Modniks, J. Andersons, Modeling elastic properties of short flax fiber-reinforced composites by orientation averaging, Computational Materials Science 50 (2) (2010) 595–599. doi:10.1016/j.commatsci.2010.09.022.

[168] J. A. Foulk, W. Y. Chao, D. E. Akin, R. B. Dodd, P. A. Layton, Enzyme-retted flax fiber and recycled polyethylene composites, Journal of Polymers and the Environment 12 (3) (2004) 165–171. doi:10.1023/B:JOOE.0000038548.73494.59.

[169] B. S. Kaith, A. S. Singha, S. Kumar, S. Kalia, Mercerization of Flax Fiber Improves the Mechanical Properties of Fiber-Reinforced Composites, International Journal of Polymeric Materials 57 (1) (2007) 54–72. doi:10.1080/00914030701328843.

[170] K. Oksman, High quality flax fibre composites manufactured by the resin transfer moulding process, Journal of Reinforced Plastics and Composites 20 (7) (2001) 621–627. doi:10.1177/073168401772678634.

[171] I. Van de Weyenberg, T. Chi Truong, B. Vangrimde, I. Verpoest, Improving the properties of UD flax fibre reinforced composites by applying an alkaline fibre treatment, Composites Part A: Applied Science and Manufacturing 37 (9) (2006) 1368–1376. doi:10.1016/j.compositesa.2005.08.016.

[172] J. Andersons, R. Joffe, Estimation of the tensile strength of an oriented flax fiber-reinforced polymer composite, Composites Part A 42 (9) (2011) 1229–1235. doi:10.1016/j.compositesa.2011.05.005.

[173] C. Baley, F. Busnel, Y. Grohens, O. Sire, Influence of chemical treatments on surface properties and adhesion of flax fibrepolyester resin, Composites Part A: Applied Science and Manufacturing 37 (10) (2006) 1626–1637. doi:10.1016/j.compositesa.2005.10.014.

[174] C. Baley, Y. Perrot, F. Busnel, H. Guezenoc, P. Davies, Transverse tensile behaviour of unidirectional plies reinforced with flax fibres, Materials Letters 60 (24) (2006) 2984–2987. doi:10.1016/j.matlet.2006.02.028.

[175] D. U. Shah, Damage in biocomposites: Stiffness evolution of aligned plant fibre composites during monotonic and cyclic fatigue loading, Composites Part A: Applied Science and Manufacturing 83 (2016) 160–168. doi:10.1016/j.compositesa.2015.09.008.

[176] P.-B. Gning, S. Liang, L. Guillaumat, W. J. Pui, Influence of process and test parameters on the mechanical properties of flax/epoxy composites using response surface methodology, Journal of Material Science 46 (21) (2011) 6801–6811. doi:10.1007/s10853-011-5639-9.

[177] LINEO NV, Advanced Flax - FlaxPly (2014).
URL http://lineo.eu/products

[178] Z. Mahboob, I. El Sawi, R. Zdero, Z. Fawaz, H. Bougherara, Tensile and compressive damaged response in Flax fibre reinforced epoxy composites, Composites Part A: Applied Science and Manufacturing 92 (2017) 118–133. doi:10.1016/j.compositesa.2016.11.007.

[179] ASTM D3171, Test Methods for Constituent Content of Composite Materials, Tech. Rep. ASTM D3171-15, ASTM International, West Conshohocken, PA (2011). doi:10.1520/D3171-15.
URL https://www.astm.org/Standards/D3171.htm

[180] S. Phillips, J. Baets, L. Lessard, P. Hubert, I. Verpoest, Characterization of flax/epoxy prepregs before and after cure, Journal of Reinforced Plastics and Composites 32 (11) (2013) 777–785. doi:10.1177/0731684412473359.

[181] ASTM D3039, Test Method for Tensile Properties of Polymer Matrix Composite Materials, Tech. Rep. ASTM D3039 / D3039M-14, ASTM International, West Conshohocken, PA (2014). doi:10.1520/D3039_D3039M-14.
URL https://www.astm.org/Standards/D3039.htm

[182] ASTM D638, Test Method for Tensile Properties of Plastics, Tech. Rep. ASTM D638-14, ASTM International, West Conshohocken, PA (2010). doi:10.1520/D0638-14.
URL https://www.astm.org/Standards/D638.htm

[183] Correlated Solutions, The VIC-2D™ System (2014).
URL http://www.correlatedsolutions.com/vic-2d/

[184] S. M. Panamoottil, R. Das, K. Jayaraman, Anisotropic continuum damage model for prediction of failure in flax/polypropylene fabric composites, Polymer Composites 37 (8) (2016) 2588–2597. doi:10.1002/pc.23453.

[185] M. Kersani, S. Lomov, A. Van Vuure, A. Bouabdallah, I. Verpoest, Damage in flax/epoxy quasi-unidirectional woven laminates under quasi-static tension, Journal of Composite Materials 49 (4) (2015) 403–413. doi:10.1177/0021998313519282.

[186] D. U. Shah, P. J. Schubel, M. J. Clifford, P. Licence, The tensile behavior of off-axis loaded plant fiber composites: An insight on the nonlinear stressstrain response, Polymer Composites 33 (9) (2012) 1494–1504. doi:10.1002/pc.22279.

[187] M. Berges, R. Lger, V. Placet, V. Person, S. Corn, X. Gabrion, J. Rousseau, E. Ramasso, P. Ienny, S. Fontaine, Influence of moisture uptake on the static, cyclic and dynamic behaviour of unidirectional flax fibre-reinforced epoxy laminates, Composites Part A: Applied Science and Manufacturing 88 (2016) 165–177. doi:10.1016/j.compositesa.2016.05.029.

[188] ASTM D3518, Standard Test Method for In-Plane Shear Response of Polymer Matrix Composite Materials by Tensile Test of a ±45 degree Laminate, Tech. Rep. ASTM D3518 / D3518M-13, ASTM International, West Conshohocken, PA (Sep. 2013). doi:10.1520/D3518_D3518M.
URL https://www.astm.org/Standards/D3518.htm

[189] Z. Mahboob, Y. Chemisky, F. Meraghni, H. Bougherara, Mesoscale modelling of tensile response and damage evolution in natural fibre reinforced laminates, Composites Part B: Engineering 119 (2017) 168–183. doi:10.1016/j.compositesb.2017.03.018.

[190] A. Thuault, B. Domengès, I. Hervas, M. Gomina, Investigation of the internal structure of flax fibre cell walls by transmission electron microscopy, Cellulose 22 (6) (2015) 3521–3530. doi:10.1007/s10570-015-0744-6.

[191] I. M. De Rosa, C. Santulli, F. Sarasini, Acoustic emission for monitoring the mechanical behaviour of natural fibre composites: A literature review, Composites Part A: Applied Science and Manufacturing 40 (9) (2009) 1456–1469. doi:10.1016/j.compositesa.2009.04.030.

[192] M. Rask, B. Madsen, B. F. Sørensen, J. L. Fife, K. Martyniuk, E. M. Lauridsen, In situ observations of microscale damage evolution in unidirectional natural fibre composites, Composites Part A: Applied Science and Manufacturing 43 (10) (2012) 1639–1649. doi:10.1016/j.compositesa.2012.02.007.

[193] A. G. Facca, M. T. Kortschot, N. Yan, Predicting the elastic modulus of natural fibre reinforced thermoplastics, Composites Part A: Applied Science and Manufacturing 37 (10) (2006) 1660–1671. doi:10.1016/j.compositesa.2005.10.006.

[194] A. G. Facca, M. T. Kortschot, N. Yan, Predicting the tensile strength of natural fibre reinforced thermoplastics, Composites Science and Technology 67 (1112) (2007) 2454–2466. doi:10.1016/j.compscitech.2006.12.018.

[195] J. Andersons, J. Modniks, E. Spārniņš, Modeling the nonlinear deformation of flax-fiber-reinforced polymer matrix laminates in active loading, Journal of Reinforced Plastics and Composites 34 (3) (2015) 248–256. doi:10.1177/0731684414568043.

[196] S. M. Panamoottil, R. Das, K. Jayaraman, Towards a multiscale model for flax composites from behaviour of fibre and fibre/polymer interface, Journal of Composite Materials 51 (6) (2016) 859–873. doi:10.1177/0021998316654303.

[197] G. Z. Voyiadjis, A. R. Venson, Experimental damage investigation of a SiC-Ti aluminide metal matrix composite, International Journal of Damage Mechanics 4 (4) (1995) 338–361. doi:10.1177/105678959500400403.

[198] C. Poilâne, Z. E. Cherif, F. Richard, A. Vivet, B. Ben Doudou, J. Chen, Polymer reinforced by flax fibres as a viscoelastoplastic material, Composites Structures 112 (2014) 100–112. doi:10.1016/j.compstruct.2014.01.043.

[199] J. Sliseris, L. Yan, B. Kasal, Numerical modelling of flax short fibre reinforced and flax fibre fabric reinforced polymer composites, Composites Part B: Engineering 89 (2016) 143–154. doi:10.1016/j.compositesb.2015.11.038.

[200] J. C. Simo, J. W. Ju, Strain- and stress-based continuum damage modelsI. Formulation, Mathematical and Computer Modelling 12 (3) (1989) 378. doi:10.1016/0895-7177(89)90117-9.

[201] D. G. Luenberger, Y. Ye, Linear and Nonlinear Programming, 4th Edition, Vol. 228 of International Series in Operations Research & Management Science, Springer International Publishing, Switzerland, 2016. doi:10.1007/978-3-319-18842-3.

[202] J. C. Simo, T. J. R. Hughes, Computational Inelasticity, Vol. 7 of Interdisciplinary Applied Mathematics, Springer-Verlag, New York, 1998.
URL http://link.springer.com/10.1007/b98904

[203] G. Chatzigeorgiou, N. Charalambakis, Y. Chemisky, F. Meraghni, Periodic homogenization for fully coupled thermomechanical modeling of dissipative generalized standard materials, International Journal of Plasticity 81 (2016) 18–39. doi:10.1016/j.ijplas.2016.01.013.

[204] J. C. Simo, R. L. Taylor, A return mapping algorithm for plane stress elastoplasticity, International Journal for Numerical Methods in Engineering 22 (3) (1986) 649–670. doi:10.1002/nme.1620220310.

[205] SMART+ Smart Materials Algorithms and Research Tools.
URL http://github.com/smartplus-team/smartplus

[206] A. Bensoussan, J.-L. Lions, G. Papanicolaou, Asymptotic Analysis for Periodic Structures, Vol. 374, American Mathenmatical Society Chelsea Publishing, Providence, Rhode Island, 2011.

[207] E. Sanchez-Palencia, Non-Homogeneous Media and Vibration Theory, Vol. 127 of Lecture Notes in Physics, Springer Berlin Heidelberg, Berlin, Heidelberg, 1980.
URL http://link.springer.com/10.1007/3-540-10000-8

[208] G. Chatzigeorgiou, Y. Chemisky, F. Meraghni, Computational micro to macro transitions for shape memory alloy composites using periodic homogenization, Smart Materials and Structures 24 (3) (2015) 035009. doi:10.1088/0964-1726/24/3/035009.

[209] Y. Chemisky, F. Meraghni, N. Bourgeois, S. Cornell, R. Echchorfi, E. Patoor, Analysis of the deformation paths and thermomechanical parameter identification of a shape memory alloy using digital image correlation over heterogeneous tests, International Journal of Mechanical Sciences 9697 (2015) 13–24. doi:10.1016/j.ijmecsci.2015.03.007.

[210] C. Knipprath, Mechanical performance of binder yarn composites, PhD thesis, Cranfield University, Cranfield, UK (May 2010).
URL http://dspace.lib.cranfield.ac.uk/handle/1826/6774

[211] Z. Mahboob, H. Bougherara, Fatigue of flax-epoxy and other plant fibre composites: Critical review and analysis, Composites Part A: Applied Science and Manufacturing 109 (2018) 440–462. doi:10.1016/j.compositesa.2018.03.034.

[212] S. W. Case, K. L. Reifsnider, Fatigue of Composite Materials (4.16), in: Cyclic Loading and Fatigue, Vol. 4 of Comprehensive Structural Integrity, Elsevier Pergamon, Amsterdam; San Diego CA, 2003, pp. 405–441. doi:10.1016/B0-08-043749-4/04100-8.

[213] A. P. Vassilopoulos, T. Keller, Fatigue of Fiber-reinforced Composites, Engineering Materials and Processes, Springer, London, 2011.
URL http://link.springer.com/10.1007/978-1-84996-181-3

[214] A. P. Vassilopoulos (Ed.), Fatigue Life Prediction of Composites and Composite Structures, Composites Science and Engineering, Woodhead Publishing, CRC Press, 2010.
URL http://www.sciencedirect.com/science/book/9781845695255

[215] A. H. Abdullah, S. K. Alias, N. Jenal, K. Abdan, A. Ali, Fatigue behavior of kenaf fibre reinforced epoxy composites, Engineering Journal 16 (5) (2012) 105–114. doi:10.4186/ej.2012.16.5.105.

[216] H. Katogi, Y. Shimamura, K. Tohgo, T. Fujii, Fatigue Behavior of Unidirectional Jute Spun Yarn Reinforced PLA, Advanced Composite Materials 21 (1) (2012) 1–10. doi:10.1163/156855111X610226.

[217] A. E. Ismail, M. A. C. A. Aziz, Fatigue strength of woven kenaf fiber reinforced composites, IOP Conference Series: Materials Science and Engineering 100 (1) (2015) 012037. doi:10.1088/1757-899X/100/1/012037.

[218] Y. Dobah, M. Bourchak, A. Bezazi, A. Belaadi, F. Scarpa, Multi-axial mechanical characterization of jute fiber/polyester composite materials, Composites Part B: Engineering 90 (2016) 450–456. doi:10.1016/j.compositesb.2015.10.030.

[219] ASTM E739, Standard Practice for Statistical Analysis of Linear or Linearized Stress-Life (S-N) and Strain-Life (ϵ-N) Fatigue Data, Tech. Rep. ASTM E739-10(2015), ASTM International, West Conshohocken, PA (2015). doi:10.1520/E0739-10R15.
URL https://www.astm.org/Standards/E739.htm

[220] T. Munikenche Gowda, A. C. B. Naidu, R. Chhaya, Some mechanical properties of untreated jute fabric-reinforced polyester composites, Composites Part A: Applied Science and Manufacturing 30 (3) (1999) 277–284. doi:10.1016/S1359-835X(98)00157-2.

[221] W. Van Paepegem, J. Degrieck, A new coupled approach of residual stiffness and strength for fatigue of fibre-reinforced composites, International Journal of Fatigue 24 (7) (2002) 747–762. doi:10.1016/S0142-1123(01)00194-3.

[222] W. Van Paepegem, Fatigue damage modelling of composite materials with the phenomenological residual stiffness approach (Chapter 4), in: A. P. Vassilopoulos (Ed.), Fatigue Life Prediction of Composites and Composite Structures, Woodhead Publishing Series in Composites Science and Engineering, Woodhead Publishing, 2010, pp. 102–138. doi:10.1533/9781845699796.1.102.

[223] M. Kawai, Fatigue life prediction of composite materials under constant amplitude loading (Chapter 6), in: A. P. Vassilopoulos (Ed.), Fatigue Life Prediction of Composites and Composite Structures, Woodhead Publishing Series in Composites Science and Engineering, Woodhead Publishing, 2010, pp. 177–219. doi:10.1533/9781845699796.2.177.

[224] A. P. Vassilopoulos, R. P. L. Nijssen, Fatigue life prediction of composite materials under realistic loading conditions (variable amplitude loading) (Chapter 9), in: Fatigue Life Prediction of Composites and Composite Structures, Woodhead Publishing Series in Composites Science and Engineering, Woodhead Publishing, 2010, pp. 293–333. doi:10.1533/9781845699796.2.293.

[225] M. Quaresimin, R. Talreja, Fatigue of fiber reinforced composites under multiaxial loading (Chapter 10), in: A. P. Vassilopoulos (Ed.), Fatigue Life Prediction of Composites and Composite Structures, Woodhead Publishing Series in Composites Science and Engineering, Woodhead Publishing, 2010, pp. 334–389. doi:10.1533/9781845699796.2.334.

[226] ASTM D3479, Test Method for Tension-Tension Fatigue of Polymer Matrix Composite Materials, Tech. Rep. ASTM D3479 / D3479M-12, ASTM International, West Conshohocken, PA (2013). doi:10.1520/D3479_D3479M-12.
URL https://www.astm.org/Standards/D3479.htm

[227] W. Hwang, K. S. Han, Statistical study of strength and fatigue life of composite materials, Composites 18 (1) (1987) 47–53. doi:10.1016/0010-4361(87)90007-3.

[228] R. Talreja, Estimation of Weibull parameters for composite material dtrength and fatigue life data, in: K. N. Lauraitis (Ed.), ASTM STP 723 Fatigue of Fibrous Composite Materials, Americal Society for Testing and Materials, Philadelphia, PA, 1981, pp. 291–311.

[229] A. C. E.-. on Quality Control of Materials, Manual on Fitting Straight Lines, Manual ASTM STP313, American Society for Testing and Materials, Philadelphia, PA (Mar. 1962).

[230] M. Naderi, A. Kahirdeh, M. M. Khonsari, Dissipated thermal energy and damage evolution of Glass/Epoxy using infrared thermography and acoustic emission, Composites Part B: Engineering 43 (3) (2012) 1613–1620. doi:10.1016/j.compositesb.2011.08.002.

[231] M. Naderi, M. M. Khonsari, On the role of damage energy in the fatigue degradation characterization of a composite laminate, Composites Part B: Engineering 45 (1) (2013) 528–537. doi:10.1016/j.compositesb.2012.07.028.

[232] J. Degrieck, W. Van Paepegem, Fatigue damage modeling of fibre-reinforced composite materials: Review, Applied Mechanics Reviews 54 (4) (2001) 279–300. doi:10.1115/1.1381395.

[233] S. Subramanian, K. L. Reifsnider, W. W. Stinchcomb, A cumulative damage model to predict the fatigue life of composite laminates including the effect of a fibre-matrix interphase, International Journal of Fatigue 17 (5) (1995) 343–351. doi:10.1016/0142-1123(95)99735-S.

[234] R. D. B. Sevenois, W. Van Paepegem, Fatigue Damage Modeling Techniques for Textile Composites: Review and Comparison With Unidirectional Composite Modeling Techniques, Applied Mechanics Reviews 67 (2) (2015) 020802–020802–12. doi:10.1115/1.4029691.

[235] U. Icardi, S. Locatto, A. Longo, Assessment of recent theories for predicting failure of composite laminates, Applied Mechanics Reviews 60 (2) (2007) 76–86. doi:10.1115/1.2515639.

[236] N. L. Post, S. W. Case, J. J. Lesko, Modeling the variable amplitude fatigue of composite materials: A review and evaluation of the state of the art for spectrum loading, International Journal of Fatigue 30 (12) (2008) 2064–2086. doi:10.1016/j.ijfatigue.2008.07.002.

[237] J. A. Pascoe, R. C. Alderliesten, R. Benedictus, Methods for the prediction of fatigue delamination growth in composites and adhesive bonds A critical review, Engineering Fracture Mechanics 112 (2013) 72–96. doi:10.1016/j.engfracmech.2013.10.003.

[238] G. P. Sendeckyj, Life prediction for resin-matrix composite materials, in: Fatigue of Composite Materials, 1st Edition, Vol. 4 of Composite Materials Series, Elsevier Science Publishers BV, Amsterdam, The Netherlands, 1991, pp. 431–483.
URL https://www.elsevier.com/books/fatigue-of-composite-materials/reifsnider/978-0-444-70507-5

[239] K. Joseph, S. Thomas, C. Pavithran, M. Brahmakumar, Tensile properties of short sisal fiber-reinforced polyethylene composites, Journal of Applied Polymer Science 47 (10) (1993) 1731–1739. doi:10.1002/app.1993.070471003.

[240] H. Mao, S. Mahadevan, Fatigue damage modelling of composite materials, Composite Structures 58 (4) (2002) 405–410. doi:10.1016/S0263-8223(02)00126-5.

[241] S. Giancane, F. W. Panella, V. Dattoma, Characterization of fatigue damage in long fiber epoxy composite laminates, International Journal of Fatigue 32 (1) (2010) 46–53. doi:10.1016/j.ijfatigue.2009.02.024.

[242] C. R. Kennedy, C. M. . Brdaigh, S. B. Leen, A multiaxial fatigue damage model for fibre reinforced polymer composites, Composite Structures 106 (Supplement C) (2013) 201–210. doi:10.1016/j.compstruct.2013.05.024.